# TDFD
## TÜRK DOĞA ve FEN DERGİSİ

### TURKISH JOURNAL OF NATURE AND SCIENCE
# TJNS
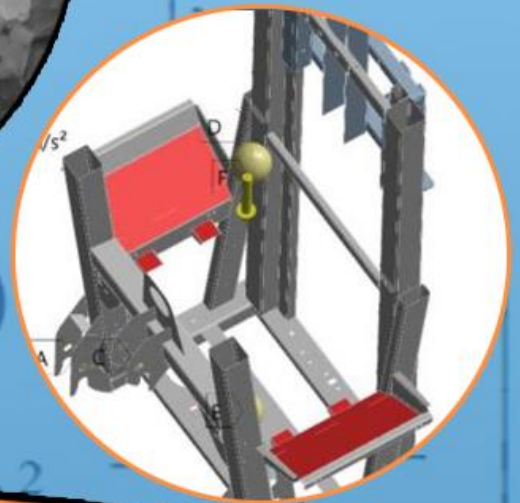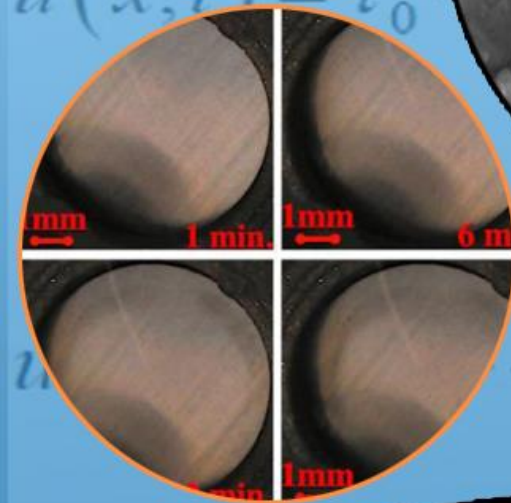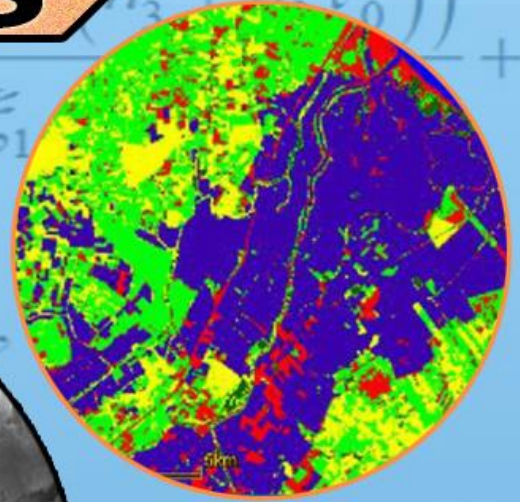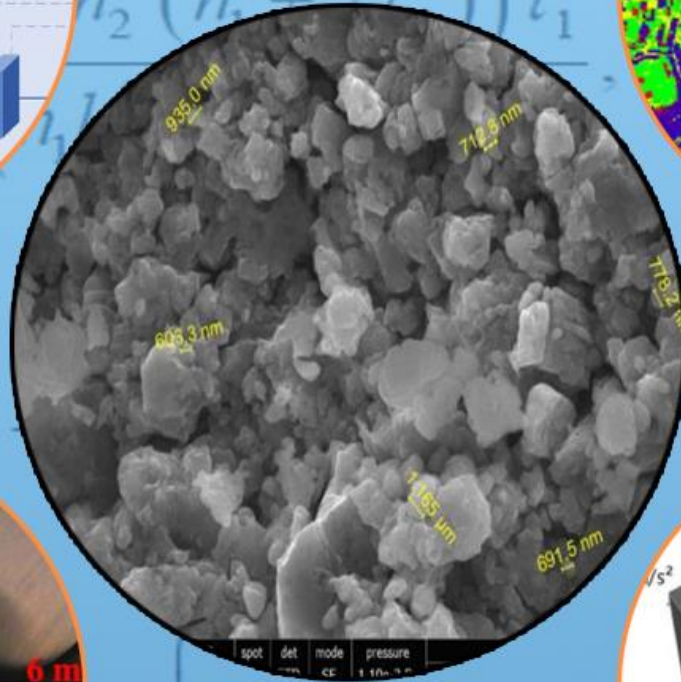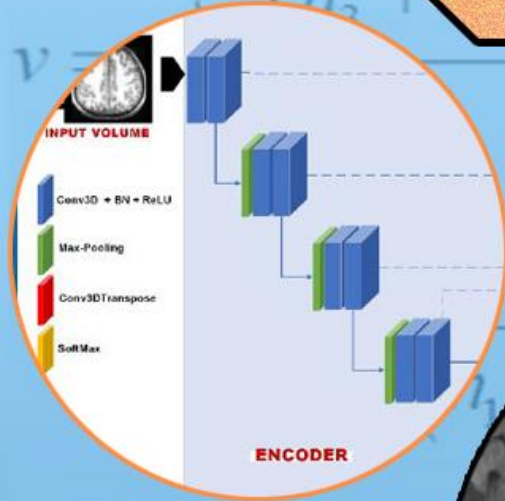
# TÜRK DOĞA VE FEN DERGİSİ

## Amaç

Türk Doğa ve Fen Dergisi, Dergipark tarafından yayınlanan Bingöl Üniversitesi Fen Bilimleri Enstitüsüne ait ulusal ve hakemli bir dergidir. Türk Doğa ve Fen Dergisi, Türkiye ve dünyanın her yerinden gelen doğa ve fen bilimlerinin her alanında özgün, yayımlanmamış, yayımlanmak üzere başka yere gönderilmemiş makale, derleme ve sempozyum değerlendirmesi gibi çalışmaların bilim alemine sunulması amacıyla kurulmuştur.

## Kapsam

Türk Doğa ve Fen Dergisinde Mühendislik, Ziraat, Veterinerlik, Fen ve Doğa Bilimleri alanlarından olmak üzere Türkçe ve İngilizce hazırlanmış orijinal makale, derleme ve sempozyum değerlendirmesi gibi çalışmalar yayımlanır. Türk Doğa ve Fen Dergisi sadece online sistemde yayınlanmakta olup ayrıca kağıt baskısı bulunmamaktadır.

## *Merhaba…*

Türk Doğa ve Fen Dergisi, Dergipark tarafından yayınlanmakta olup Bingöl Üniversitesi Fen Bilimleri Enstitüsüne aittir. Bahar ve güz dönemi olmak üzere yılda iki defa çıkarılan ulusal hakemli bir dergi olarak ilk sayısını 2012 bahar döneminde yayımlamıştır. Türk Doğa ve Fen Dergisi, Türkiye ve dünyanın her yerinden gelen doğa ve fen bilimlerinin her alanında özgün, yayımlanmamış, yayımlanmak üzere başka yere gönderilmemiş makale, derleme ve sempozyum değerlendirmesi gibi çalışmaların bilim alemine sunulması amacıyla kurulmuştur. İlk sayısından bugüne kesintisiz olarak faaliyetlerini sürdürmektedir.

Türk Doğa ve Fen Dergisi sadece online sistemde yayınlanmakta olup ayrıca kağıt baskısı bulunmamaktadır. Dergimize gelen her çalışma öncelikle Turnitin intihal programında taranmaktadır. Dergimizde editörlerin, hakemlerin ve yazarların, uluslararası yayım etik kurallarına uyması ve makalelerin yazım kurallarına uyumlu olması zorunluluğu vardır.

Yazarlar yayımlanmak üzere dergimize gönderdikleri çalışmaları ile ilgili telif haklarını zorunlu olarak Bingöl Üniversitesi Türk Doğa ve Fen Dergisi'ne devretmiş sayılırlar. Yazarlardan herhangi bir ücret talep edilmemektedir. Yazarların değerlendirmeleri, dergimizin resmi görüşü olarak kabul edilemez. Çalışmaların her türlü sorumluluğu yazarlarına aittir. Araştırma ürünleri için etik kurul raporu gerekli ise, çalışma üzerinde bu raporun alınmış olduğu belirtilmeli ve kurul raporu sisteme kaydedilmelidir. Araştırma ile ilgili intihal, atıf manipülasyonu, sahte veri uydurma vb. suistimallerin tespit edilmesi halinde yayım ve etik ilkelerine göre davranılır. Bu durumda çalışmanın yayımlanmasını önlemek, yayımdan kaldırmak ya da başka işlemler yapmak için gerekli işlemler takip edilmektedir.

Dergimizde, kaynak gösteriminde uluslararası Vancouver sistemine geçilmiştir. Ayrıca dergimiz, Creative Commons ile lisanslanmak suretiyle dergimizde yayımlanan makalelerin paylaşımı, kaynak gösterimi ve yayımlanmasında dergi ve yazar haklarını korumaya almıştır. 2018 yılı güz döneminden itibaren makaleler, uluslararası yazar kimlik numarası ORCID No'su ile yayımlanmaktadır.

Dergi ekibi, dergimizin ulusal ve uluslararası indekslerce taranan bir dergi olması yönünde çalışmalarını titizlikle sürdürmektedir. Dergimize gösterilen ilgi bu yönde bizleri teşvik etmeye devam edecektir.

**Prof. Dr. Zafer ŞİAR**

Bingöl Üniversitesi, Fen-Edebiyat Fakültesi, Matematik Bölümü
E-Mail: zsiar@bingol.edu.tr

**Prof. Dr. Uğur ÇAKILCIOĞLU**

Munzur Üniversitesi, Pertek Sakine Genç Meslek Yüksekokulu, Bitki Morfolojisi
ve Anatomisi Bölümü
E-Mail: ucakilcioglu@yahoo.com

**Doç. Dr. Kamuran DİLSİZ**

Bingöl Üniversitesi, Fen-Edebiyat Fakültesi, Fizik Bölümü
E-Mail: kdilsiz@bingol.edu.tr

**Doç. Dr. Şükran KONCA**

Bakırçay Üniversitesi, Mühendislik ve Mimarlık Fakültesi, Temel Bilimler,
Matematik Bölümü
E-Mail: sukran.konca@bakircay.edu.tr

**Doç. Dr. İdris YAZGAN**

Kastamonu Üniversitesi, Fen Edebiyat Fakültesi, Biyoloji

E-Mail: idrisyazgan@gmail.com

**Doç. Dr. Abdulcabbar YAVUZ**

Gaziantep Üniversitesi, Mühendislik Fakültesi, Metalurji ve Malzeme Mühendisliği
E-Mail: ayavuz@gantep.edu.tr

**Doç. Dr. Bünyamin ALIM**

Bayburt Üniversitesi, Teknik Bilimler Meslek Yüksekokulu, Elektrik ve Enerji
Bölümü
E-Mail: balim@bayburt.edu.tr

**Dr. Öğr. Üyesi Mustafa Şükrü KURT**

Erzurum Teknik Üniversitesi, Fen Fakültesi, Temel Bilimler
E-Mail: mustafa.kurt@erzurum.edu.tr

**Dr. Öğr. Üyesi Sinan SAĞIR**

Karamanoğlu Mehmetbey Üniversitesi, Fizik

E-Mail: sinansagir@kmu.edu.tr / sinan.sagir@cern.ch

**Doç. Dr. Murat AYDEMİR**

Erzurum Teknik Üniversitesi, Fen Fakültesi, Temel Bilimler

E-Mail: murat.aydemir@erzurum.edu.tr

## Mühendislik Bilimleri

**Doç. Dr. Özgür ÖZGÜN**

Bingöl Üniversitesi, Sağlık Bilimleri Fakültesi, İş Sağlığı ve Güvenliği Bölümü
E-Mail: oozgun@bingol.edu.tr

**Prof. Dr. Figen KOREL**

İzmir Yüksek Teknoloji Enstitüsü, Gıda Mühendisliği Bölümü
E-Mail: figenkorel@iyte.edu.tr

**Prof. Dr. Kubilay ASLANTAŞ**

Afyon Kocatepe Üniversitesi, Teknoloji Fakültesi, Makine Mühendisliği Bölümü
E-Mail: aslantas@aku.edu.tr

**Prof. Dr. Hamit Özkan GÜLSOY**

Marmara Üniversitesi, Teknoloji Fakültesi, Metalurji ve Malzeme Mühendisliği
Bölümü
E-Mail: ogulsoy@marmara.edu.tr

**Prof. Dr. Ali Adnan HAYALOĞLU**

İnönü Üniversitesi, Mühendislik Fakültesi, Gıda Mühendisliği Bölümü
E-Mail: adnan.hayaloglu@inonu.edu.tr

**Prof. Dr. Barbara SAWICKA**

University of Life Sciences in Lublin, Department of Plant Production Technology
and Commodities Sciences
E-Mail: barbara.sawicka@gmail.com

**Prof. Dr. İbrahim GÜNEŞ**

Giresun Üniversitesi, Mühendislik Fakültesi, İnşaat Mühendisliği Bölümü
E-Mail: ibrahim.gunes@giresun.edu.tr

**Doç. Dr. Sırma YEĞİN**

Ege Üniversitesi, Mühendislik Fakültesi, Gıda Mühendisliği Bölümü
E-Mail: sirma.yegin@ege.edu.tr

**Doç. Dr. Hasan OĞUL**

Sinop Üniversitesi, Mimarlık ve Mühendislik Fakültesi, Nükleer Enerji
Mühendisliği
E-Mail: hogul@sinop.edu.tr

**Doç. Dr. Murat YILMAZTEKİN**

İnönü Üniversitesi, Mühendislik Fakültesi, Gıda Mühendisliği Bölümü
E-Mail: murat.yilmaztekin@inonu.edu.tr

**Doç. Dr. Ferhat AYDIN**

Sakarya Uygulamalı Bilimler Üniversitesi, Teknoloji Fakültesi, İnşaat
Mühendisliği Bölümü
E-Mail: ferhata@subu.edu.tr

**Dr. Öğr. Üyesi Nurullah DEMİR**

Bingöl Üniversitesi, Mühendislik ve Mimarlık Fakültesi, Gıda Mühendisliği
Bölümü
E-Mail: ndemir@bingol.edu.tr

**Dr. Öğr. Üyesi Ahmet GÜNER**

Bingöl Üniversitesi, Mühendislik ve Mimarlık Fakültesi, Elektrik ve Elektronik
Mühendisliği Bölümü
E-Mail: aguner@bingol.edu.tr

**Dr. Öğr. Üyesi Tahir AKGÜL**

Sakarya Uygulamalı Bilimler Üniversitesi, Teknoloji Fakültesi, İnşaat
Mühendisliği Bölümü
E-Mail: tahirakgul@subu.edu.tr

**Dr. Erhan Sulejmani**

University of Tetova, Faculty of Food Technology and Nutrition
E-Mail: erhan.sulejmani@unite.edu.mk

**Dr. Hacène Medjoudj**

Larbi Ben M'Hidi University of Oum El Bouaghi, Food Science Department
E-Mail: medjoudjh@yahoo.com

**Dr. Avinash Lakshmikanthan**

Nitte Meenakshi Institute of Technology, Department of Mechanical Engineering,
Karnataka, India
E-Mail: avinash.laks01@gmail.com

**Dr. Manjunath Patel GC**

PES Institute of Technology and Management, Department of Mechanical
Engineering, Karnataka, India
E-Mail: manju09mpm05@gmail.com

## Sağlık Bilimleri

### Doç. Dr. Aydın Şükrü BENGÜ

Bingöl Üniversitesi, Sağlık Hizmetleri Meslek Yüksekokulu, Tıbbi Hizmetler ve
Teknikler
E-Mail: abengu@bingol.edu.tr

### Dr. Öğr. Üyesi Dilhun Keriman ARSERİM UÇAR

Bingöl Üniversitesi, Sağlık Bilimleri Fakültesi, Beslenme ve Diyetetik Bölümü
E-Mail: dkucar@bingol.edu.tr

### Dr. Öğr. Üyesi Abdullah TUNÇ

Bingöl Üniversitesi, Sağlık Bilimleri Fakültesi, İş Sağlığı ve Güvenliği Bölümü
E-Mail: atunc@bingol.edu.tr

### Dr. Öğr. Üyesi Ramazan GÜNDOĞDU

Bingöl Üniversitesi, Sağlık Hizmetleri Meslek Yüksekokulu, Eczane Hizmetleri
E-Mail: rgundogdu@bingol.edu.tr

### Dr. Alexander HERGOVICH

UCL Cancer Institute, Faculty of Medical Sciences, Department of Cancer Biology,
UCL, London, UK
E-Mail: a.hergovich@uc.ac.uk

## Dr. Valenti GOMEZ

UCL Cancer Institute, Faculty of Medical Sciences, Department of Oncology, UCL, London, UK
E-Mail: valentin.gomez@ucl.ac.uk

## Veterinerlik Bilimleri

### Doç. Dr. Cüneyt ÇAĞLAYAN

Bilecik Şeyh Edebali Üniversitesi, Tıp Fakültesi, Temel Tıp Bilimleri Bölümü, Tıbbi Biyokimya Anabilim Dalı
E-Mail: cuneyt.caglayan@bilecik.edu.tr

### Prof. Dr. Fatih Mehmet KANDEMİR

Atatürk Üniversitesi, Veteriner Fakültesi, Veteriner Hekimliği Temel Bilimler
E-Mail: fmehmet.kandemir@atauni.edu.tr

### Doç. Dr. Akın KIRBAŞ

Bozok Üniversitesi, Veteriner Fakültesi, Klinik Bilimler Bölümü
E-Mail: akindahiliye55@yahoo.com

### Doç. Dr. Emrah Hicazi AKSU

Atatürk Üniversitesi, Veteriner Fakültesi, Klinik Bilimler Bölümü
E-Mail: emrahaksu@atauni.edu.tr

## Ziraat Bilimleri

### Dr. Öğr. Üyesi Zeynep DUMANOĞLU

Bingöl Üniversitesi, Ziraat Fakültesi, Biyosistem Mühendisliği Bölümü
E-Mail: zdumanoglu@bingol.edu.tr

### Prof. Dr. Kağan KÖKTEN

Bingöl Üniversitesi, Ziraat Fakültesi, Tarla Bitkileri Bölümü
E-Mail: kahafe1974@yahoo.com

### Prof. Dr. Mustafa SÜRMEN

Adnan Menderes Üniversitesi, Ziraat Fakültesi, Tarla Bitkileri Bölümü
E-Mail: mustafa.surmen@adu.edu.tr

**Prof. Dr. Banu YÜCEL**

Ege Üniversitesi, Ziraat Fakültesi, Hayvan Yetiştirme Anabilim Dalı, Zootekni Bölümü
E-Mail: banu.yucel@ege.edu.tr


**Doç. Dr. Hakan İNCİ**

Bingöl Üniversitesi, Ziraat Fakültesi, Zootekni Bölümü
E-Mail: hinci@bingol.edu.tr

## TEKNİK EDİTÖRLER

**Dr. Nimetullah KORKUT**

Bingöl Üniversitesi, BİNUZEM, Bilgisayar Teknolojileri
E-Mail: nkorkut@bingol.edu.tr


**Öğr. Gör. MEHMET VURAL**

Bingöl Üniversitesi, Genç Meslek Yüksek Okulu, Bilgisayar Teknolojileri
E-Mail: mvural@bingol.edu.tr

## DİL EDİTÖRÜ

**Öğr. Gör. Dr. Ahmet KESMEZ**
Bingöl Üniversitesi, Yabancı Diller Yüksekokulu, İngilizce Bölümü
E-Mail: akesmez@bingol.edu.tr

**Türk Doğa ve Fen Dergisi**
**Turkish Journal of Nature and Science**

www.dergipark.gov.tr/tdfd

# İÇİNDEKİLER/CONTENTS

| | |
|---|---|
| **Effects of Silica Aerogel Produced From Boron Wastes To Compressive Strength And Thermal Performance Of Environmentally Friendly Bricks**<br><br>**Arzu ÇAĞLAR[1*]** [ID]<br><br>[1] Kırsehir Ahi Evran University, Engineering-Architecture Faculty, Architecture Department, Kırsehir, Türkiye<br>Arzu ÇAĞLAR ORCID No: 0000-0003-3928-8059<br><br>*Corresponding author: arzu.caglar@ahievran.edu.tr*<br><br> | **24** |
| **Determination of Some Quality Parameters of Filtered Blossom Honey Obtained from Bingöl and Its Districts**<br><br>**Buket ARICI[1*]** [ID] **, İsa GÖKÇE[2]** [ID]<br><br>[1] Bingöl University, Central Laboratory Application and Research Center, Bingöl, Türkiye<br>[2] Tokat Gaziosmanpaşa University, Pharmacy Faculty, Department of Biochemistry, Bingöl, Türkiye<br>Buket ARICI ORCID No: 0000-0003-2570-0524<br>İsa GÖKÇE ORCID No: 0000-0002-5023-9947<br><br>*Corresponding author: barici@bingol.edu.tr*<br><br> | **33** |
| **Evaluation of Glucose, AST, ALT, Urea and Albumin Parameters in Children with Rotavirus Diagnosis**<br><br>**Veysel TAHİROĞLU[1*]** [ID] **, Cihat ÖZTÜRK[2]** [ID]<br><br>[1] Şırnak University, Faculty of Health Sciences, Department of Nursing, Şırnak, Türkiye<br>[2] Kırşehir Ahi Evran University, Faculty of Medicine, Department of Medical Microbiology, Kırşehir, Türkiye<br>Veysel TAHİROĞLU ORCID No: 0000-0003-3516-5561<br>Cihat ÖZTÜRK ORCID No: 0000-0003-2868-2317<br><br>*Corresponding author: veysel.tahiroglu@sirnak.edu.tr*<br><br> | **41** |
| **Transfer Learning for Detection of Casting Defects Model In Scope of Industrial 4.0**<br><br>**Hayriye TANYILDIZ[1]** [ID] **, Canan BATUR ŞAHİN[1*]** [ID]<br><br>[1] Faculty of Engineering and Natural Sciences, Malatya Turgut Ozal University, Malatya 44210, Türkiye<br>Hayriye TANYILDIZ ORCID No: 0000-0002-6300-9016<br>Canan BATUR ŞAHİN ORCID No: 0000-0002-2131-6368<br><br>*Corresponding author: canan.batur@ozal.edu.tr*<br><br> | **45** |

| | |
|---|---|
| **Prevalence of Cryptosporidium, Eimeria Species and Gastrointestinal Helminths in Lambs and Sheeps in Erzurum Region** Barış SARI[1] , İbrahim BALKAYA[2] , Gencay Taşkın TAŞÇI[1] , Mükremin Özkan ARSLAN[3] , Sezin Beyza KÜÇÜKLER[2*] [1]Departman of Parasitology, Veterinary Faculty, Kafkas University, Kars, Türkiye [2] Departman of Parasitology, Veterinary Faculty, Ataturk University, Erzurum, Türkiye [3] Departman of medical Parasitology, Medicine Faculty, Kafkas University, Kars, Türkiye Barış SARI ORCID No: 0000-0001-9978-2513 İbrahim BALKAYA ORCID No: 0000-0002-1103-2812 Gencay Taşkın TAŞÇI ORCID No: 0000-0002-8590-1101 Mükremin Özkan ARSLAN ORCID No: 0000-0002-6447-5561 Sezin Beyza KÜÇÜKLER ORCID No: 0009-0005-3772-6395 *Corresponding author: sezinbeyzakucukler@gmail.com | **105** |
| **The Effect Of Corset On Postoperative Pain Following Lumbar Disc Herniations** Hidayet Safak CINE[1*] [1] Istanbul Medeniyet University Goztepe Prof. Dr. Suleyman Yalcin City Hospital, Neurosurgery Department, Istanbul, Türkiye Hidayet Safak CINE ORCID No: 0000-0002-0808-5921 *Corresponding author: cinesafak@gmail.com | **112** |
| **The Effect of Alumina Additive on the Properties of Sheep Hydroxyapatite** Süleyman Serdar PAZARLIOĞLU[1*] [1] Marmara University, Technology Faculty, Metallurgy and Materials Science and Engineering Department, İstanbul, Türkiye Süleyman Serdar PAZARLIOĞLU ORCID No: 0000-0002-7870-8418 *Corresponding author: spazarlioglu@marmara.edu.tr | **118** |
| **Synthesis of $Li_7P_3S_{11}$ Solid Electrolyte for All-Solid-State Lithium-Sulfur Batteries** Çağrı Gökhan TÜRK[1,2] , Mahmud TOKUR[2,3,4*] [1]Sakarya University, Institute of Natural Sciences, Sakarya, Türkiye [2]Sakarya University, Research, Development and Application Center, Sakarya, Türkiye [3]Sakarya University, Department of Metallurgical & Materials Engineering, Sakarya, Türkiye [4]NESSTEC Energy & Surface Technologies A.S., Technology Development Zones, Sakarya, Türkiye Çağrı Gökhan TÜRK ORCID No: 0000-0001-9940-6948 Mahmud TOKUR ORCID No: 0000-0003-3612-5350 *Corresponding author: mtokur@sakarya.edu.tr | **128** |

# Türk Doğa ve Fen Dergisi
# Turkish Journal of Nature and Science
**www.dergipark.gov.tr/tdfd**

# Some Micronutrient Values and Some Quality Traits in Husk and Groats of Oat Genotypes

Leyla IDIKUT [1], Songul CIFTCI [2], Gulay ZULKADIR [3*], Ziya DUMLUPINAR [4], Ali OZKAN [5], Meryem Delal YAMAN [6]

[1] Kahramanmaraş Sutcu Imam University, Agriculture of Faculty, Agronomy Department, Kahramanmaras, Turkey
[2] Kahramanmaraş Sutcu Imam University, Agriculture of Faculty, Agronomy Department, Kahramanmaras, Turkey
[3] Mersin University, Applied Technology and Management School of Silifke, Organic Farming Menengment Department, Mersin, Turkey
[4] Kahramanmaraş Sutcu Imam University, Agriculture of Faculty, Agricultural Biotechnology of Department, Kahramanmaras, Turkey
[5] Gaziantep University, Fine Arts of Faculty, Gastronomy and Culinary Arts of Department, Gaziantep, Turkey
[6] Gaziantep University, Engineering, Food Engineering of Faculty, Gaziantep, Turkey

Leyla IDIKUT ORCID No: 0000-0002-0685-7158
Songul CIFTCI ORCID No: 0000-0002-5157-2709
Gulay ZULKADIR ORCID No: 0000-0003-3488-4011
Ziya DUMLUPINAR ORCID No: 0000-0003-3119-6926
Ali OZKAN ORCID No: 0000-0001-7652-8176
Meryem Delal YAMAN ORCID No: 0000-0003-4340-7153

*Corresponding author: gulayzulkadir@gmail.com

**Keywords**
Oats,
Seed,
Husk,
Groat characters,
Elements

**Abstract:** Oat is one of the important cereal crops due to its high nutritional content and versatile usage in human diet and animal feed. Therefore, it was aimed to examine some nutritional values in grain (groat and husk) and, some quality traits of five commercial oat varieties and six advanced oat lines under Kahramanmaraş conditions in 2016-2017 cropping year. The experiments were arranged in a randomized complete block design with four replications. According to the results, thousand seeds (groat + husk) weight was found as 26.17 to 45.51 g, test weight (groat + husk) was 47.80 to 54.30 kg, crude protein ratio of grain was 13.97 to 16.55%, groat percentage was 66.31% to 73.33%, husk ratio was 26.67% to 33.68%, iron content of groat was 22.75 to 39.44 mg kg$^{-1}$, iron content of husk was 54.06 to 90.27 mg kg$^{-1}$, zinc content in groat was 28.09 to 66.21 mg kg$^{-1}$, zinc content of husk was 14.04 to 36.59 mg kg$^{-1}$, calcium content in groat was 83.30 to 191.50 mg kg$^{-1}$, the calcium content of husk was 313.7 to 442.30 mg kg$^{-1}$. When genotypes were evaluated according to the examined characteristics, it was noted that TL137 genotype was the best in terms of both thousand grain weight and test weight, but it was low in protein ratio was low. TL576, Fetih, Kirk-lar and Kahraman genotypes were determined to be the highest genotypes in terms of groat percent-age. It was observed that the iron content in groat of Sari, TL139 and TL452 genotypes was high, but the iron content of Kahraman and TL42 genotypes was low in both groat and husk. It was noted that TL452 genotype had low both zinc and calcium content in groat.

# Yulaf Genotiplerinin Kabuk ve İç Tanelerindeki Bazı Mikro Besin Değerleri ve Bazı Kalite Özellikleri

**Anahtar Kelimeler**
Yulaf,
Tohum,
Kabuk,
Tane karakterleri,
Elementler

**Öz:** Yulaf, yüksek besin içeriği ve insan beslenmesinde ve hayvan yemlerinde çok yönlü kullanımı nedeniyle önemli tahıl bitkilerinden biridir. Bu nedenle, 2016-2017 üretim yılında Kahramanmaraş koşullarında beş ticari yulaf çeşidi ve altı ileri yulaf hattının tanelerinde (dane ve kavuz) bazı besin değerleri ile bazı kalite özelliklerinin incelenmesi amaçlanmıştır. Deneme tesadüf blokları deneme desenine göre dört tekerrürlü olarak düzenlenmiştir. Sonuçlara göre bin tane (dane+kavuz) ağırlığı 26.170 ile 45.510 g, hektolitre ağırlığı (dane+kavuz) 47.80 ile 54.30 kg, tanede ham protein oranı 13.97% ile 16.55%, kavuzsuz tane oranı 66.31% ile 73.33%, kavuz oranı 26.67 ila 33.68 mg kg$^{-1}$, danede demir içeriği 22.75 ila 39.44 mg kg$^{-1}$, kavuzda demir içeriği 54.06 ila 90.27 mg kg$^{-1}$, danede çinko içeriği 28.09 ila 66.21 mg kg$^{-1}$, kavuzda çinko içeriği 14.04 ila 36.59 mg kg$^{-1}$, danede kalsiyum içeriği 83.30 ila 192.50 mg kg$^{-1}$, kavuzda kalsiyum içeriği 313.7 ila 442.30 mg kg$^{-1}$ olarak bulunmuştur. İncelenen özelliklere göre genotipler değerlendirildiğinde TL137 genotipinin hem bin tane ağırlığı hem de test ağırlığı bakımından en iyi olduğu ancak protein oranlarının düşük olduğu dikkat çekmiştir. TL576, Fetih, Kırklar ve Kahraman genotiplerinin dane oranı bakımından en yüksek genotipler olduğu belirlenmiştir. Sarı, TL139 ve TL452 genotiplerinin danede demir içeriğinin yüksek olduğu, Kahraman ve TL42 genotiplerinin ise hem dane hem de kavuzda demir içeriğinin düşük olduğu görülmüştür. TL452 genotipinin danede hem çinko hem de kalsiyum içeriğinin düşük olduğu kaydedilmiştir.

1

# 1. INTRODUCTION

Oat (*Avena sativa* L.) is an important cereal crop. It is used as grain and forage crop. The characters of covering and protecting on soil of oat create diversification for sustainable agriculture. Oat is known as a rich plant in terms of protein, fat, starch, vitamins (especially vitamin E) and nutrients. Also, it has the soluble fibers that has hypocholesterolemic properties. The high nutritional value of the oat plant is due to the high amount of mineral substances (2.90-3.40%) [1]. Oat contains high protein (12.40- 24.40%), fat (2-12%), vitamins and mineral (54 mg Ca, 4.7 mg Fe, 117 mg Mg, 523 mg P, 429 mg K, 2 mg Na, 4 mg Zn in 100 grams,) substances [2; 3]. Although oat grains used for animal feed, it is recently uses as a multipurpose crop in human nutrition and industry has made it possible for oat to be among the prominent plants in the grain group [4]. Decker et al. [5] stated that husks of cereals as significant quantity of agricultural by-products represent with low digestibility and a high lignocellulose content. And also husks that finely milled could be used as a human food source. Additionally, it could be used in animal bedding and feeding purposes [6]. Barbieri et al. [7] stated that wheat husks were produced 10 million tons in Europe. When the husk currently re-searched potential utilization options, it is hoped that it will take place in many different composite material in the future [6]. Thereby oat husks will be improving the circular economy of agricultural as by-products so a lignocellulose material that have the potential for assessment. Although oat is consumed as whole grain cereal, it is used as breakfast products, oat-cookies, beverages and granola bars across the world, due to the health benefits. It is also a very good source of energy due to high rate of fat than other grains [8]. However, it has a well-balanced amino-acid composition, compared to other cereal grains [9]. In general, the unsaturation oil ratio of cereal lipids are range between 70-86% [10].

Oat has high protein content and the avenin seed storage protein in their seeds formed an important raw material source for alternative feed production in animal nutrition due to their high composition of lipids, unsaturated fatty acids, soluble fiber, essential amino acids, minerals, vitamins [11]. Oat grains are considered beneficial for health in terms of human nutrition [12]. It is an important plant due to its properties such as lowering cholesterol, decreasing heart disease, high fiber and iron con-tent, and lowering blood sugar levels in terms of human health [4].

Since oat products are used in the industry, it has an important cultivation area in the world. Oat crops might be grown in cool and rainy climates [12]. According to the data of 2021, oats yielded 23.6 million tons of which 9.6 million hectares were cultivated in the world. It was recorded that 208 thousand tons of product was obtained by planting 132.9 thousand ha in Turkey [13]. Over time, the richness of seed properties (protein, oil, vitamins and minerals) has increased the interest in oats [14]. In this study, it was aimed to determine some groat and husk characteristics of 11 oat genotypes and to determine the oat genotypes showing superiority in terms of the examined charac-teristics.

# 2. MATERIAL AND METHOD

In the study, 5 oat varieties (Kirklar, Fetih, Sari and Kahraman were belong to Avena sativa L. species and Arslanbey was belongs to Avena byzantina C. Koch species) and six local oat genotypes (TL38, TL137, TL139, TL576, TL42 and TL452 belongs to Avena sativa L.) were used as the material in the experiment. The trial was carried out in the 2016-2017 growing season under the conditions of Kahramanmaras province. Kahramanmaras region, where the experiment was conducted is located in the Eastern Mediterranean Region between the coordinates of 37°35'4.92" North latitude and 36°55'35.08" East longitude of Turkey. The sowing date was on 19.01.2017. It was planted late, due to the climatic conditions. The reason for this was the lack of sufficient rainfall in November and the excess of precipitation in December. Genotypes were planted with a drill between 20 cm row space, 5 m row length, 400 seed m², as 6 rows in per plot. The experiment was arranged in a randomized complete block design with four replications. The fertilizer was applied 7 kg da $^{-1}$ nitrogen and phosphorus with planting (20-20-0: N; P; K). In addition, 7 kg da-1 nitrogen was applied as top dressing at the beginning of the jointing stage. Herbicide (2,4-D amin) was applied for weed control. The relative humidity value varied between 65.9% and 42.9%, the average temperature values were the lowest 3.8 °C and the highest 26.4 °C, and the total precipitation was 408.7 mm.

Some climatic values of the months in which the research was carried out are given in the Table 1 [14]. Soil of the test area was clay-loam. It was determined that the soil was slightly alkaline (7.76), excessively lime (24.48%), slightly salty (0.32%), less in terms of phosphorus (3.2 kg da$^{-1}$), sufficient in potassium (98.64 kg da$^{-1}$), medium level in organic matter (2.28%) [15]. In the study, the thousand seeds (groat+husk) weight, crude protein ratios, test weight (groat+husk), groat percentage, husk ratio, iron content in groat, zinc content in groat, calcium content in groat, iron content of husk, zinc content of husk and calcium content of husk characters of oat genotypes were investigated. The weight of one thousand seeds was calculated by counting 100 grains four times and then dividing by four and multiplying by ten. The test weight was determined by measuring with the test pot and then weighing. After milling oat groats into flour, the crude protein ratios from samples taken as flour was made using the WINISI package program on the FOSS 6500 NIR system device. Groat percentage was measured with weighing the de-hulled grains. The husk ratio was calculated using the husk to groat+husk ratio. Determinations of the iron, zinc, calcium were realized by atomic absorption spectrometry (AAS) after microwave digestion.

2

**Table 1.** Some important climatic data of trial site in 2016-2017

| Months | Average Relative Humidity (%) | Average Temperature (℃) | Precipitation (mm) | Maximum Temperature (℃) | Minimum Temperature (℃) |
|---|---|---|---|---|---|
| October | 40.1 | 20.5 | 10.7 | 32.5 | 9.2 |
| November | 49.5 | 11.1 | 36.8 | 23.7 | 0.3 |
| December | 67.9 | 4.5 | 105.0 | 15.2 | -4.5 |
| January | 65.9 | 3.8 | 126.7 | 7.9 | 1.9 |
| February | 44.0 | 7.4 | 3.7 | 13.0 | 2.2 |
| March | 55.4 | 12.2 | 74.5 | 17.7 | 7.4 |
| April | 49.0 | 15.8 | 67.8 | 21.8 | 10.0 |
| May | 55.0 | 19.6 | 105.0 | 26.0 | 14.5 |
| June | 42.9 | 26.4 | 3.1 | 33.3 | 19.9 |

The variance analysis and the average of the data obtained in the experiment were analysed in the SAS statistical package program. Mean data belong to the cultivars were grouped by Duncan's multiple comparison test [17].

## 3. RESULTS AND DISCUSSION

The thousand seeds weight, test weight, crude protein ratio were showed in the Table 2. The groat percentage, ratio of husk, iron content in groat, iron content of husk were given in the Table 3. The zinc and calcium content of groat, zinc and calcium content of husk were given in the Table 4.

In the study, the differences among oat genotypes were found statistically insignificant in terms of thousand seeds weight. The average thousand seeds weight was found to be 34.92 g. The highest thousand seeds weight was obtained on TL137 genotype with 45.51 g, and the lowest thousand seeds weight was obtained on TL139 genotype with 26.17 g (Table 2).

As a result of the study, the weight of thousand seeds of oat genotypes varied among 26.17 to 45.51 g. It was noted that TL 137 line had a higher thousand seeds weight than the registered cultivars. Other lines had a lower thousand seeds weight than registered cultivars (Figure 1). Previously, many researchers reported that thousand seeds weight in oat genotypes ranged from 16.32 g to 42.62 g (Sahin et al. [18, 19, 20, 21]. The cited thousand seeds weights were found to be largely consistent with our research findings.

As seen in the Table 2, the variation among the genotypes was for significantly different for test weight (p<0.01). The average test weight was determined as 50.30 kg. The highest test weight was recorded in Kirklar genotype with 54.30 kg and the lowest test weight was recorded in TL576 genotype with 47.80 kg.
In the study, the test weight of oat genotypes was observed between 47.80 - 54.30 kg. Test weight is an important factor determining the quality of oat grain [22]. It was noted that TL 42, TL 137 and TL139 lines showed close values to Kahraman, Sari, Aslanbey cultivars and did not differ statistically (Figure 1). This shows that oat lines performed as successful as registered varieties. Test weights in previous studies were found by Sari et al. [4] 50.3- 57.7 kg in lines and 45.4 - 51.4 kg in standard varieties, Erbas [23] 34.5 - 51.0 kg, Sahin [24] 36.6 - 49.7 kg. As stated by many researchers, growing conditions, genetic factors, grain fullness, climate, environment, soil and relationships between these factors are the properties that affect the test weight [19; 24; 22; 14].

It is determined that oat genotypes are statistically significant in terms of crude protein ratio (p<0.01). The average crude protein ratio among genotypes was found 15.34%. It was noted that the highest protein rate was on TL38 genotype with 16.55%, and the lowest protein rate was on Arslanbey genotype with 13.97% (Table 2).

The grain crude protein ratio among oat genotypes ranged from 13.97% to 16.55%. In terms of protein in grain, TL38 and TL42 lines were not significantly different from Kahraman cultivar with the highest crude protein ratio among registered cultivars, and they were in the same group. Crude protein ratio in previous studies were determined 12.60% [18], and by Topkara [26] the average of genotypes as 14.98% and the average of varieties as 14.60%, 11.9-15.8% for landrace and improved oats varieties [27]. In earlier works, the crude protein ratio was determined in Triticale 10.80% to 19.20% [28; 29], 19.40% in barley, 8.8% in millet and 13.3% in rye [30]. It has been reported that the crude protein ratio depends on the environment and genotype [14; 29]. Exclusively, there was negative relationship between grain yield and crude protein ratio of cereals [29]. Generally, higher protein content in grain of oat is desired. It is determined that the protein content of oat grain is high and therefore it is an important plant in terms of human nutrition [18].

**Table 2.** Mean data of the oat genotypes for thousand seeds weight, test weight, crude protein ratio

| Genotypes | Thousand Seeds Weight (g) | Test Weight (kg) | Crude Protein Ratios (%) |
|---|---|---|---|
| TL38 | 31.18 | 48.80 cd | 16.55 a |
| TL42 | 29.10 | 50.20 b-d | 16.43 a |
| TL137 | 45.51 | 51.60 a-c | 14.15 cd |
| TL139 | 26.17 | 50.20 b-d | 14.67 b-d |
| TL452 | 33.98 | 48.30 cd | 15.00 bc |
| TL576 | 27.26 | 47.80 d | 15.45 b |
| Fetih | 35.74 | 48.70 cd | 15.52b |
| Sari | 38.71 | 50.80 b-d | 15.47 b |
| Arslanbey | 39.84 | 49.60 b-d | 13.97 d |
| Kirklar | 38.39 | 54.30 a | 14.95 cb |
| Kahraman | 38.24 | 53.00 ab | 16.52 a |
| General Means | 34.92 | 50,30 | 15.34 |
| C.V. (%) | 7.06 | 4.24 | 4.01 |
| P<0.001 | ns | ** | ** |

** significant at 0.01 level, ns: not significant, C.V. : Coefficient of Variation.
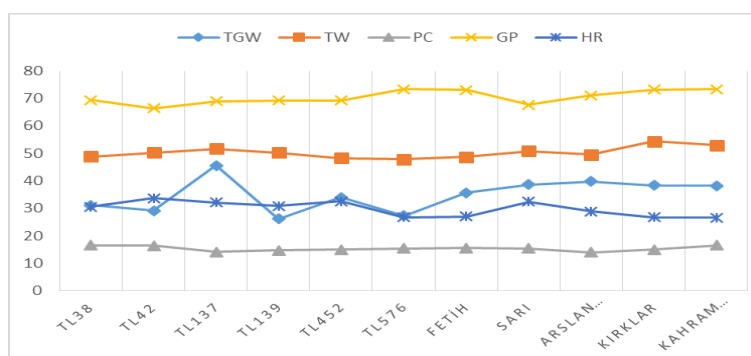


**Figure 1.** Thousand seeds weight, test weight, crude protein ratio, groat percentage and husk ratio of oat genotypes. TWG; thousand seeds weight, TW; test weight, PR; crude protein ratio, GP; groat percentage, HR; husk ratio

It was observed that oat genotypes had a statistically significant (p<0.01) variation for the groat percentage. The means of groat percentage of oat genotypes was found as 70.39%. The highest was recorded on the Kahraman genotype with 73.33%, and the lowest groat percentage was recorded on the TL42 genotype with 66.31% (Table 3).

The groat percentage of oat genotypes were determined to be among 66.31% to 73.33%. It was seen that TL 576 line, Kahraman and Kirklar varieties had the highest grain/groat+ husk ratio and were statistically in the same group. In previous studies, it found that the mean of the groat percentage of genotypes varied between 67.4% and 81.1% [23].

It has been determined that the husk ratios of oat genotypes are statistically significant (p<0.01). As can be seen in the Table 3, among the genotypes, the average of husk ratio was recorded to be 29.85%. It was determined that the highest of husk ratio was on TL42 genotype with 33.68%, while the lowest of husk ratio was on Kahraman genotype with 26.67%.

In this study, the husk ratio of oat genotypes varies between 26.67% and 33.68%. Average husk ratio of oat genotypes, Sahin et al. [18] found it to be 27.1%. Kahraman et al. [21] found 20.6–39.2% in Kirklareli location and 17.0-39.5% in Edirne location. Bedoic et al. [31] were determined that after the grain harvested was obtained 25-32% husks of oat seed. Our findings were showed that the ratio of groat and husk varied as depending on the variety and growing conditions. The similar findings in previous studies were also recorded.

It was observed that the differences among genotypes for the iron content of groat and iron content of husk were statistically significant (p<0.01). It was determined that the average iron content in groat was 34.05 mg kg⁻¹ and the average iron content of husk was 71.82 mg kg⁻¹. It was observed that the highest groat iron content was on the Sari genotype with 39.44 mg kg⁻¹, while the lowest iron content was on the TL38 genotype with 22.75 mg kg⁻¹. The highest iron content of husk was determined on the Arslanbey genotype with 90.25 mg kg⁻¹, while the lowest iron content of husk was determined on the TL42 genotype with 54.06 mg kg⁻¹ (Table 3).

Iron content in groat of oat genotypes was found between 22.75 - 39.44 mg kg⁻¹ and iron ratio of husk between 54.06 and 90.25 mg kg⁻¹. It has been determined that the iron content in the oat grain is significantly lower than that in the husk. It was seen that TL 139 and TL 452 lines used in the research had higher values than other varieties in terms of iron content in groat, except for the Sari variety. TL 38, TL 137 and TL 139 lines used in the research were found to have higher values than other varieties, except for Arslanbey variety, in terms of iron content in husk (Figure 2). Li et al. [32] found that the rate of Fe in grain content of oat plants in 3 different locations of China was between 27.6-66.52 mg kg⁻¹. In another study, the Fe content in oat seeds was found to be 58.00 mg kg⁻¹ [33], and 26.7 mg kg⁻¹ [34]. The finding of Yilmaz and Koyuncu [35] was stated that Fe content of oat husk was as 26 µg g⁻¹. Yalcin [1] cited iron ratio to be variety according to year and location, it reported that it had a value between 32.6 - 123.3 mg kg⁻¹ at the Kirklareli location and 30.4 - 52.4

mg kg⁻¹ at the Karacabey location. Alemayehu et al. [26] noted that iron ratio of oat groat was 2.5-3 mg 100 g⁻¹.

The Fe content in dry matter related to cereals in previous studies was found 35 mg kg⁻¹ for wheat, 27 mg kg⁻¹ for corn, 54 mg kg⁻¹ for sorghum, 128.40 mg kg⁻¹ for barley, 199.80 mg kg⁻¹ for millet, 44.00 mg kg⁻¹ for rye, 10.6 mg kg⁻¹ for broom millet [36; 35; 30]. These results show that the iron content among cereals may vary depending on species. It is understood from the studies that the Fe content in the groat and the husk of the oat plant is higher than that of some grain plants. The human body needs Fe element too much. A person's daily need for Fe is 12 mg [38]. The daily Fe requirement of farm animals was recorded between in cattle 150-250 mg, in pig 10- 30 mg, in sheep 7-15 mg, in horse 90-100 mg [39]. Considering the daily Fe levels of humans and some farm animals, in this respect, the iron content in the oat groat and husk is of important.

**Table 3.** Mean data of oat genotypes for groat percentage, husk ratio, iron content in groat and iron content in husk

| Genotypes | Groat percentage (%) | Husk ratio (%) | Iron (Fe) content in groat (mg kg⁻¹) | Iron (Fe) content of husk (mg kg⁻¹) |
|---|---|---|---|---|
| TL38 | 69.40 bc | 30.60 bc | 22.75 e | 87.38 b |
| TL42 | 66.31 c | 33.68 a | 31.65 d | 54.06 j |
| TL137 | 68.88 bc | 32.10 ab | 34.59 c | 88.31 b |
| TL139 | 69.15 bc | 30.85 bc | 38.58 ab | 82.68 c |
| TL452 | 69.17 bc | 32.52 ab | 38.79 ab | 72.67 b |
| TL576 | 73.30 a | 26.70 d | 36.26 bc | 55.59 i |
| Fetih | 72.97 a | 27.03 d | 34.44 c | 59.42 g |
| Sari | 67.58 c | 32.42 ab | 39.44 a | 77.13 d |
| Arslanbey | 71.05 ab | 28.95 cd | 31.00 d | 90.25 a |
| Kirklar | 73.19 a | 26.89 d | 36.69 bc | 65.13 f |
| Kahraman | 73.33 a | 26.67 d | 30.35 d | 57.44 h |
| **General Means** | 70.39 | 29.85 | 34.05 | 71.82 |
| **C.V. (%)** | 2.74 | 4.94 | 4.84 | 1.34 |
| **P<0.01** | ** | ** | ** | ** |

** significant at 0.01 level, C.V. : Coefficient of Variation

In the study, it was determined that the zinc content in groat and the zinc content o of husk of the genotypes are statistically significant (p<0.01). The average zinc content in groat was 40.66 mg kg⁻¹, while the average content of zinc of husk was 25.70 mg kg⁻¹. It was noted that the highest groat zinc content was found on the TL576 genotype with 66.21 mg kg⁻¹, while the lowest one was on the TL137 genotype with 28.09 mg kg⁻¹. The highest content of zinc of husk was recorded on the TL137 genotype with 36.59 mg kg⁻¹, while the lowest content of zinc of husk was recorded in the TL576 genotype with 14.04 mg kg⁻¹ (Table 4).

It was observed that the zinc content in groat was between 28.09 and 66.21 mg kg⁻¹, and the content of zinc of husk was between 14.04 and 36.59 mg kg⁻¹. It was determined that the zinc content of the oat groat was higher than the husk, and the zinc content of the TL 38 and TL 576 lines was significantly higher than the registered varieties. Except for the TL 576 line, it was noted that the lines were superior than registered varieties in terms of zinc content in husk the exception of Arslanbey (Figure 2).
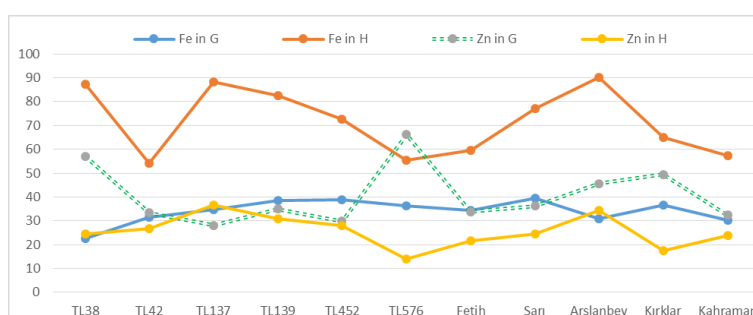


**Figure 2.** Iron content in groat, iron content of husk, zinc content in groat, zinc content of husk of oat genotypes. Fe in G; iron ratio in groat, F in H; iron ratio of husk, Zn in G; zinc ratio in groat, Zn in H; zinc ratio of husk

In previous study by Singh et al. [31] determined the content of Zn in oat seeds as 45 mg kg⁻¹. The content of Zn in oat husk was found as 12 µg g⁻¹ in researches of Yilmaz and Koyuncu [35]. Li et al. [32] were reported that different oat varieties in 3 different locations of China the amount of Zn were 18.70 - 30.50 mg kg⁻¹. Yalcin [1] cited that the zinc content of oat lines and varieties were between 17.6 - 82.7 mg kg⁻¹ for first year and 21.4 - 65.4 mg kg⁻¹ for the second year in the Karacabey location. The same researcher observed the zinc content of oat lines and varieties were between 17.4 - 45.9 mg kg⁻¹ for first year and 18.6 - 107.1 mg kg⁻¹ for second year in the Kirklareli Location [21]. It was emphasized by Alemayehu et al. [27] that the zinc content in oats ranged from 1.6 to 2.1 mg 100 g⁻¹. Ragaee et al. [30] found that the content of Zn was 74.20 mg kg⁻¹ in barley, 65.90 mg kg⁻¹ in millet and 30.60 mg kg⁻¹ in rye. In the other study conducted on barley plants, the Zn content in the seed was found to be 24.16 mg kg⁻¹ [40]. Ozcan et al. [41] stated that zinc contents

of oats were 1.5 - 3.8 mg 100 $g^{-1}$, which is in close agreement with our result. It has been noted that the amount of Zn in the human body is 2 - 4 g and the daily Zn need of a person varies between 3 and 5 mg [38].

Zinc was a vital component of a number of enzymes participating in the synthesis and degradation of proteins, carbohydrates, lipids and nucleic acids, so it was required for the accurate growth and maintenance of the human body [42]. It is seen that the content of Zn in the seed and husk of oats is enough to meet the daily Zn need of an adult.

The differences amoung the oat genotypes were found to be statistically significant (p<0.01) in terms of calcium content in the groat and calcium content of husk. As can be seen in the Table 4, it was noted that the average calcium content in the groat was 140.97 mg $kg^{-1}$ and the average calcium content of husk was 390.14 mg $kg^{-1}$. The highest calcium content in the groat was found on

the TL139 genotype with 193.10 mg $kg^{-1}$ and the lowest calcium content in groat was found on the TL576 genotype with 83.30 mg $kg^{-1}$. The highest calcium content of husk was found on the Arslanbey genotype with 442.30 mg $kg^{-1}$, and the lowest calcium content of husk was found in the TL576 genotype with 313.70 mg $kg^{-1}$.

In the research, it is determined that oat genotypes had calcium content in the seed between 83.30 and 193.10 mg kg and calcium content of husk between 313.70 and 442.30 mg $kg^{-1}$. It was observed that the calcium content in the husk of the oat grain is much higher than the grain, and the difference is still 2-3 times higher in some genotypes (Figure 3). TL139 line had a higher value than Fetih variety in terms of calcium content of groat. TL42 line showed higher value than other varieties except Fetih variety in calcium content of groat. In terms of calcium content in oat husk, TL42 line showed a higher value than other varieties, except for Arslanbey.

**Table 4.** Mean data of oat genotypes for Zinc content in groat, zinc content of husk, calcium content in groat and the calcium content of husk

| Genotypes | Zinc (Zn) content in groat (mg $kg^{-1}$) | Zinc (Zn) content of husk (mg $kg^{-1}$) | Calcium (Ca) content in groat (mg $kg^{-1}$) | Calcium (Ca) content of husk (mg $kg^{-1}$) |
|---|---|---|---|---|
| TL38 | 57.11 b | 24.50 cde | 128.50 f | 420.70 c |
| TL42 | 33.41 fg | 26.83 cd | 162.80 b | 430.10 b |
| TL137 | 28.09 h | 36.59 a | 131.70 e | 403.10 d |
| TL139 | 34.98 ef | 30.85 b | 193.10 a | 345.30 g |
| TL452 | 29.85 h | 27.96 bc | 116.50 h | 379.60 f |
| TL576 | 66.21 a | 14.04 f | 83.30 i | 313.70 h |
| Fetih | 33.88 fg | 21.76 e | 191.50 a | 348.70 g |
| Sari | 36.20 e | 24.42 cd | 144.70 d | 405.70 d |
| Arslanbey | 45.56 d | 34.53 a | 117.40 h | 442.30 a |
| Kirklar | 49.50 c | 17.51 f | 124.10 g | 417.40 c |
| Kahraman | 32.46 g | 23.79 de | 150.80 c | 385.00 e |
| General Means | 40.66 | 25.70 | 140.97 | 390.14 |
| C.V. (%) | 3.17 | 9.67 | 0.99 | 0.69 |
| P<0.01 | ** | ** | ** | ** |

** significant at 0.01 level, C.V. Coefficient of Variation.
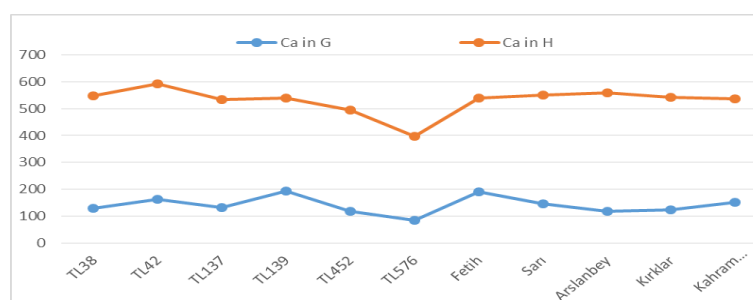


**Figure 3.** Graph of oat genotypes relative to calcium content in groat, calcium content of husk. Ca in G; calcium content in groat, Ca in H; calcium content of husk

The Ca Content in oat seeds by Singh et al. [31] was found as 796.00 mg $kg^{-1}$. Li et al. [30] were noted that the content of Ca in oats was between 480 - 600 mg $kg^{-1}$ for 3 different regions of China. Mut et al. [22] found that the calcium content for oat were between 300 and 520 mg $kg^{-1}$. Sahin [24] observed that the ratio of calcium in oats were 0.418 - 0.466% in autumn application and 0.386-0.444% in spring application. It was stated by Alemayehu et al. [27] that the calcium content in oats varies between 44 - 102.7 mg 100 $g^{-1}$. Yilmaz and Koyuncu [33] indicated that the crude protein content of oat husk was 960 µg $g^{-1}$. The Ca ratio

in previous studies was reported as 300 mg $kg^{-1}$ in wheat, 260 mg $kg^{-1}$ in corn, 250 mg kg- in sorghum, 736.20 mg $kg^{-1}$ in barley, 508.60 mg $kg^{-1}$ in millet, 348.70 mg $kg^{-1}$ in rye, and 27.30 mg $kg^{-1}$ in broomsorghum [36; 30]. These findings showed that the content of Ca of the oat plant was higher than that of some cereals. The daily Ca requirement of farm animals was found 20-30 g in cattle, 3-10 g in pigs, 2-3 g in sheep, horse 20 g [39]. The daily need of Ca element in the human body varied between 0.8 and 0.9 g [38]. Considering the amount of Ca in the nutritional values, the oat seed shell is quite good when mixed with other

cereal crops, therefore, the low oat production cost and high nutritional value will cause it to be among the plants sought today [1].

## 4. CONCLUSION

Compared to other plants cultivated in the same period as the oat plant itself, such as wheat, barley, lentils and broad beans, it is a plant to be cultivated in adverse field conditions. Knowing the nutritional values will contribute to the industrial field due to its use in human nutrion and animal feed. The highest values for agronomic traits and micronutrient contents in the study conducted out with 11 oat genotypes in Kahramanmaras province was obtained from TL137 genotype for thousand seeds weight (45.51 g) and Zn ratio (36.59 mg kg⁻¹) of husk, Kirklar for test weight (54.30 kg) value, TL38 genotype for crude protein ratio (16.55%), Kahraman variety for seed ratio (73.33%), TL42 genotype for husk ratio ( 33.68%), Sarı variety for iron ratio in seed (39.44 mg kg⁻¹), Arslanbey variety for iron ratio of husk (90.25 mg kg⁻¹) , TL576 genotype for zinc ratio in seed (66.21 mg kg⁻¹), TL139 genotype for Ca ratio in seed (193.10 mg kg⁻¹) and Arslanbey variety for calcium ratio of husk (442.30 mg kg⁻¹). It has been concluded that the oat lines used in the research can compete with the registered varieties and the researchers should be continued in the breeding programs to develop superior oat genotypes with better traits.

## REFERENCES

[1] Yalcin TG. Determination of phytic acid and mineral contents of oat breeding samples. Hacettepe University, Food Engineering Department. The Degree of Master of Science. Ankara, 2018.

[2] Yaver E, Ertas N. Composition oats, grain endustry uses and effects on human health. Journal of Food and Feed Science-Techonology, 2013; 13: 41–50.

[3] Menon R, Gonzalez T, Ferruzzi M, Jackson E, Winderl D, Watson J. Oats-from farm to fork, advances in food and nutrition research. 1st ed. Elsevier Inc. (pp. 77:1-55), 2016. https://doi.org/10.1016/bs.afnr.2015.12.001.

[4] Sari N, Imamoglu A, Yildiz O. Determination of advanced oat lines for Menemen ecological conditions. Journal of Anatolia Aegean Agricultural Research Institute, 2011; 21(1): 16-25.

[5] Decker EA, Rose DJ, Stewart D. Processing of oats and the impact of processing operations on nutrition and health benefits. British Journal of Nutrition, 2014; 112: S58–S64. https://doi.org/10.1017/S000711451400227X.

[6] Bledzki AK, Mamun AA, Volk J. Physical, chemical and surface properties of wheat husk, rye husk and soft wood and their polypropylene composites. Composites Part A: Applied Science and Manufacturing, 2010; 41: 480–488. https://doi.org/10.1016/j.compositesa. 2009.12.004

[7] Barbieri V, Lassinantti Gualtieri M, Siligardi C. Wheat husk: a renewable resource for bio-based building materials. Construction and Building Materials, 2020; 251: 118909. https://doi.org/10.1016/j.conbuildmat.2020.118909.

[8] Lehtinen P, Kaukovirta-Norja A. Oat lipids, enzymes and quality. In: Lehtinen P, Francis H, Wood Peter J. (eds). OATS: Chemistry and Technology, 2011. https://doi.org/10.1094/9781891127649.009.

[9] Makinen OE, Sozer N, Ercili-Cura D, Poutanen K. Protein from oat: Structure, processes, functionality and nutrition. Sustainable protein sources, 2017; 105-119. https://doi.org/10.1016/B978-0-12-802778-3.00006-8.

[10] Coskun G, Bahar B. Cereals and Pseudo-cereals in terms of chemical composition. Turkish Journal of Science and Health, 2020; 1(1): 52-60.

[11] Youssef MKE, Nassar AG, EL–Fishawy FA, Mostafa MA. Assessment of proximate chemical composition and nutritional status of wheat biscuits fortified with oat powder. Assiut Journal of Agricultural Sciences, 2016; 47(5): 83–94.

[12] Ma BL, Zheng Z, Pageau D, Vera C, Fregeau-Reid J, Xue A, Yan W. Nitrogen and phosphorus uptake, yield and agronomic traits of oat cultivars as affected by fertilizer N rates under diverse environments. Nutrient Cycling in Agroecosystems, 2017; 108: 245–265. https://doi.org/10.1007/s10705-017-9848-8.

[13] FAOSTAT. Food and Agriculture Organization of the United Nations. https://www.fao.org/faostat/en/#home. Accessed May 12, 2023.

[14] Peterson DM, Wesenberg DM, Burrup DE, Eriickson CA. Relationships among agronomic traits and grain composition in oat genotypes grown in different environments. Crop Science, 2005; 45(4): 1249-1255. https://doi.org/10.2135/cropsci2004.0063.

[15] Anonymous. Meteorology provincial directorate climate data, Kahramanmaraş. https://www.mgm.gov.tr/veridegerlendirme/il-ve-ilceler-istatistik.aspx?m=K.MARAS. 2017a. Accessed June 6, 2018.

[16] Anonymous. Soil analysis, KSU Agriculture Faculty Soil Laboratory Data. 2017b.

[17] SAS9.3. SAS/STAT. *SAS Institute Incorporation, Cary, NC, USA*. 2013.

[18] Sahin M, Gocmen Akcacik A, Aydogan S, Hamzaoglu S, Ceri S, Demir B. Determination of some physical properties and nutrient components in oat (*Avena sativa* spp.) grains. Journal of Bahri Dagdas Animal Research, 2017; 6(1): 23-28.

[19] Kahraman T, Avci R, Ozturk I, Tulek A. Determination of oat genotypes suitable for Thrace-Marmara region. Journal of Agricultural Sciences Research, 2012; 5 (2): 24-28. https://doi.org/10.21566/tarbitderg.359381.

[20] Dumlupinar Z. Agricultural and molecular characterization of oat lines from different gene banks. Result report, Tubitak Tovag 112 O 138 S, 85, 2015.

[21] Kahraman T, Kurt C, Seis Subası A, Ozderen T, Yildiz O, Buyukkileci C, et al. Determination of oat (*Avena sativa* L.) genotypes suitable for human

7

nutrition in the Thrace-Marmara region. Field Research Institute Journal, 2017; 26: 105−111. https://doi.org/10.21566/tarbitderg.359164.

[22] Mut Z, Erbas Kose OD, Akay H. Chemical quality properties of different oats (*Avena sativa* L.) varieties. Journal of Agricultural Sciences, 2017; 27(3): 347-356. https://doi.org/10.29133/yyutbd.290920.

[23] Erbas OD. Determination of agricultural and some quality characteristics of oat *(Avena Sativa L.)* genotypes. Bozok University Institute of Science, Field Crops Master's Thesis. Yozgat, 2012.

[24] Sahin A. Effect of sulfur doses and application time on oat grass yield and quality of oats *(Avena Sativa L.).* Yozgat Bozok University, Institute of Science, Field Crops Department. Master's Thesis. Yozgat, 2019.

[25] Sari N, Imamoglu A, Pelit S, Yildiz O, Buyukkileci C. The Determination of suitable oat (*Avena sativa* L.) Genotypes in Cost Line Aegean Region. Journal of Field Crops Central Research Institute, 2016; 25: 158-164.

[26] Topkara A. Determination of yield, yield components and quality characteristics of oat varieties and genotypes in Ordu province ecological conditions. Ordu University Institute of Science. Intermediate Master Thesis. Ordu, 2019.

[27] Alemayehu GF, Forsido SF, Tola YB, Teshager MA, Assegie AA, Amare E. Proximate, mineral and anti-nutrient compositions of oat grains (*Avena sativa*) cultivated in Ethiopia: implications for nutrition and mineral bioavailability. Heliyon, 2021; 7: e07722. https://doi.org/10.1016/j.heliyon.2021.e07722.

[28] Kendal E, Sayar MS. The stability of some spring triticale genotypes using biplot analysis. Journal of Animal and Plant Sciences, 2016; 26(3):754-765.

[29] Kendal E, Sayar MS, Tekdal S, Aktaş H, Karaman M. Assessment of the impact of ecological factors on yield and quality parameters in triticale using GGE biplot and AMMI analysis. Pakistan Journal of Botany, 2016; 48(5): 1903-1913.

[30] Ragaee S, Abdel-Aal ESM, Noaman M. Antioxidant activity and nutrient composition of selected cereals for food use. Food Chemistry, 2006; 98: 32–38. https://doi.org/10.1016/j.foodchem.2005.04.039.

[31] Bedoic R, Cosic B, Duic N. Technical potential and geographic distribution of agricultural residues, co-products and by-products in the European Union. Science of the Total Environment, 2019; 686: 568–579. https://doi.org/10.1016/j.scitotenv.2019.05.219

[32] Li H, Qiu J, Liu C, Ren C, Li Z. Milling characteristics and distribution of phytic acid, minerals, and some nutrients in oat (*Avena sativa* L.). Journal of Cereal Science, 2014; 60 (3): 549–554. https://doi.org/10.1016/j.jcs.2014.08.004.

[33] Singh R, De S, Belkheir A. *Avena sativa* (Oat), a potential neutraceutical and therapeutic agent: An overview. Critical Reviews in Food Science and Nutrition, 2013; 53(2): 126-44. https://doi.org/10.1080/10408398.2010.526725.

[34] Loskutov IG, Khlestkina EK. Wheat, barley, and oat breeding for health benefit components in grain. Plants, 2021; 10 (1): 86. https://doi.org/10.3390/plants10010086.

[35] Yilmaz O, Koyuncu O. Investigation of Mineral Matter Content of Husks Separated From Oat Varieties Cultivated in Turkey. *I*nternational Journal of Agricultural and Natural Sciences, 2021; 14(3): 210-215.

[36] Saleh ASM, Zhang Q, Chen J, Shen Q. Millet grains: Nutritional quality, processing, and potential health benefits. Comprehensive Reviews in Food Science and Food Safety, 2013; 12: 281-295. https://doi.org/10.1111/1541-4337.12012.

[37] Shahidi F, Chandrasekara A. Millet grain phenolics and their role in disease risk reduction and health promotion: A review. Journal of Functional Foods, 2013; 5: 570-581. https://doi.org/10.1016/j.jff.2013.02.004.

[38] Demirci M. Food Chemistry Book. Food Technology Association. ISBN 975-97146-2-0; 2016.

[39] Sevgican F. Ege University Faculty of Agriculture Publications. No: 524. Textbook. Bornova / İzmir, 1996.

[40] Erbas Kose OD, Mut Z. Mineral content of some local and foreign barley (*Hordeum vulgare* L.) varieties. KSU Agriculture and Nature Journal, 2019; 22 (5): 671-677. https://doi.org/10.18016/ksutarimdoga.vi.523982

[41] Ozcan M, Bagci A, Dursun N, Gezgin S, Hamurcu M, Dumlupinar Z, et al. Macro and micro element contents of several oat (*Avena sativa* L.) genotype and variety grains. Iranian Journal of Chemistry and Chemical Engineering, 2017; 36(3): 73–79. https://doi.org/10.30492/IJCCE.2017.28065.

[42] WHO. Vitamin and mineral requirements in human nutrition, second ed. World Health Organization, 2005. Retrieved from. https://apps.who.int/iris/handle/10 665/42716.

**Türk Doğa ve Fen Dergisi**
**Turkish Journal of Nature and Science**
www.dergipark.gov.tr/tdfd

# An Experimental Case Study on The Comparison of The Use of Micronized Quartz and Alumina in Brake Pads

**Hicri YAVUZ[1*]** [iD]

[1]Afyon Kocatepe University, Vocational School of Afyon, Department of Engine Vehicles and Transportation Technology, Afyon, Türkiye.
Hicri YAVUZ ORCID No: 0000-0001-8427-5164

*Corresponding author: hicriyavuz@aku.edu.tr*

**Abstract:** One of the crucial components of the brake system is the brake pads. Due to its importance in the sector, researchers have carried out many recent studies on this subject. In this study, two different brake pad samples were developed from alumina material and micronized quartz material as friction modifiers. Samples containing 12% alumina and micronized quartz were produced by hot molding method. The friction coefficient and wear rates were established in the brake pad tester in order to assess the performance of the created brake pad samples. Density, hardness, and microscopic analyses of the samples, which are other important parameters, were performed with Scanning electron microscopy. The average coefficient of friction was 0.35 in samples containing micronized quartz and 0.34 in samples containing alumina. The wear rates in both samples were obtained below the maximum desired wear rate from the brake pads. The experiments produced brake pad performance values with the desired characteristics, and it was found that micronized quartz material may be employed as an alternative to alumina in the composition of brake pads.

9

# Fren Balatalarında Mikronize Kuvars ve Alümina Kullanımının Karşılaştırılması ile İlgili Deneysel Bir Vaka Çalışması

**Öz:** Fren sisteminin en önemli bileşenlerinden biri fren balatalarıdır. Sektördeki öneminden dolayı araştırmacılar tarafından son yıllarda bu konu ile ilgili çok fazla çalışma yapılmaktadır. Yapılan bu çalışmada sürtünme düzenleyici olarak alümina malzemesi ve mikronize kuvars malzemesinden iki farklı fren balata numunesi geliştirilmiştir. %12 oranında alümina ve mikronize kuvars içeren numuneler sıcak kalıplama yöntemi ile üretilmiştir. Oluşturulan fren balatası numunelerinin performansını değerlendirmek için fren balatası test cihazında sürtünme katsayısı ve aşınma oranları belirlenmiştir. Numunelerin diğer önemli parametreleri olan yoğunluk, sertlik ve mikroskobik analizleri taramalı elektron mikroskobu ile gerçekleştirilmiştir. Mikronize kuvars içeren numunelerde ortalama sürtünme katsayısı 0.35 alümina içeren numunelerde ise 0.34 olarak elde edilmiştir. Her iki numunedeki aşınma oranları ise fren balatalarından istenilen azami aşınma oranının altında elde edilmiştir. Yapılan deneyler sonucunda fren balatalarından istenilen özelliklerde performans değerleri elde edilmiş olup, mikronize kuvars malzemesinin alümina yerine ikame olarak fren balatası içeriğinde kullanılabileceği belirlenmiştir.

## 1. INTRODUCTION

For people to continue their lives, they meet their food, drink, fuel, or energy needs by moving or transportation. They use different tools to meet these needs. Internal combustion engines working with different fuels or electric motors are used for these vehicles. The motion provided by the internal combustion engines is converted

into kinetic energy at the wheels at different torques and speeds by the driveline. While vehicles are driven by various sources for acceleration, disc or drum-type brake systems have been developed for use in vehicles such as cars, trucks, or buses for safe deceleration. The brake pads, a crucial component of the brake system, transform kinetic energy into thermal energy that radiates to the environment, allowing the vehicle to be stopped or slowed

down. The friction between the rotating disc or the brake lining pressing the drum determines how well the brake system works [1–4].

Besides the importance of moving the vehicle, stopping is also very important. Pads are important for the brake system to achieve the desired performance. Pads have a particular life due to their structure [5]. High temperatures occur due to the contact between the brake pad and the disc or drum. Under the resulting high temperature, minimum brake pad wear by transferring heat is desired [6]. One of the most crucial components of the brake system is the brake pads, which transfer the braking energy needed to slow down and stop the vehicle to the tires via a disc or drum. The brake pad wears down more quickly than the disc since it is the softer brake system component. Due to the characteristics of the components that make up the brake pad, the working environment, and environmental concerns, researchers are doing serious research. At the same time, the content and nature of the particles and the braking efficiency, should be controlled to ensure passenger safety. All these factors push scientists into a challenging and complex endeavor [7]. Although there are many options in the studies on brake pads, vehicle manufacturers should carefully select the appropriate pad material to ensure safety and optimum operation. This careful selection should also contribute to a stable coefficient of friction and less wear [8].

Brake pads, a vital component of the automobile brake system, are fixed to the steel support pieces facing the brake disc. When it is desired to reduce or stop the vehicle's speed, the pads are brought into contact with the disc with an outward force when the brake is applied. Safety and comfort in cars are of great importance for passengers and drivers. Brake pads produced from unsuitable materials do not meet the desired performance criteria. The heat generated during braking causes deterioration of the structural integrity of the components that make up the lining composite, which is called fading, and causes losses during friction. In addition, these conditions cause an increase in the wear rate and cause malfunctions. All of these elements may have a detrimental effect on the performance and longevity of brake pads. It is essential to create materials with the mechanical, tribological, thermal, and physical characteristics anticipated of brake pads. The use of locally available materials is often encouraged. In addition, they do not contain environmentally friendly asbestos-type substances harmful to health, as well as provide the desired functional properties [9,10].

Working conditions are another factor that is expected to be known or estimated in order to be able to produce brake pads at the desired criteria [2]. High temperatures occur due to the interaction of the contact surface between the lining and the disc or drum. For the brake pad to perform its duty without being worn, it must absorb the heat rapidly. Brake pad friction materials are generally developed by combining different materials to provide the desired performance and appropriate wear criteria [6]. A new composition content and production parameters in

brake pad development significantly impact performance improvement [1,11].

Because brake friction materials for vehicles fulfill complex requirements, selecting ingredients and optimizing the recipe are essential to improve the performance of the materials [12]. Brake pads, called polymeric composites, are considered a good choice in terms of cost and performance [13]. With dozens of different materials used in the brake pad, braking performance, environmentally friendly and stable friction coefficient, and high wear resistance are provided [14]. Developed countries also prohibit the use of asbestos-causing lining ingredients [15–17]. The developed brake pad content consists of the following ingredients [18]:

- Abrasives,
- Friction modifiers,
- Fillers,
- Fiber-like reinforcements,
- Phenolic resins, mainly used as binders

Materials that affect the thermal resistance, which prevents the heat generated by braking from damaging the brake pad composite, are also added to the brake pad content [19]. In addition to the materials employed, the production of composite materials using various production techniques is very effective in aspects affecting the tribological performance of the brake friction material, such as density, hardness, surface roughness, braking performance, strength, and brake pad service life [20,21]. In order to allow the driver to brake comfortably, a perfect brake pad should have a consistent coefficient of friction and low wear rate unaffected by speed, pressure, or environmental conditions [22,23]. Determining the tribological behavior of brake pads in the automotive industry is very important.[24]. In order to determine the tribological behavior of brake pads, disc wear tests are usually performed on the pin in a laboratory setting [7,25].

Two separate brake pad samples were developed for this study. The effects of micronized quartz on the brake pad content and the tribological performance of automobile brake pad samples produced from alumina material used extensively as a friction modifier were investigated comparatively.

## 2. MATERIAL AND METHOD

Table 1 gives the composition ratios by weight of the materials that make up the brake pad composites and the production method. Brake pad samples were produced in mixtures containing 12% alumina and 12% micronized quartz. AL12 code refers to brake pad sample containing alumina, and MQ12 code refers to brake pad sample containing micronized quartz. Brake pad samples were produced in three stages according to the production method specified in Table 1 [26]. In the first stage, the materials that make up the brake pad samples were weighed on a precision scale. In the second stage, they were mixed at 60 l/min for 15 minutes. In the third step,

the mixture was hot pressed under the pressing conditions given in the third step of Table 1. The lining samples taken out of the mold after hot pressing have a diameter of 25 mm and a height of approximately 11 mm.

Using the Archimedes principle, the density measuring kit calculated the densities of the brake pad sample

productions. The samples were tested in the brake pad testing apparatus under the conditions listed in Table 2 to ascertain the friction coefficient and wear rate. Using the equations in Table 2, the brake pads' friction coefficient and wear rate were computed.

**Table 1.** Brake pad sample content (% by weight) and production method

| Material / Sample | Resin | Steel fiber | Brass powder | Graphite | Barite | Cashew | Alumina | Micronize quartz |
|---|---|---|---|---|---|---|---|---|
| AL12 | 19 | 15 | 7 | 7 | 35 | 5 | 12 | - |
| MQ12 | 19 | 15 | 7 | 7 | 35 | 5 | - | 12 |
| **Production Method** | | | | | | | | |
| **Step 1** | Weighing of materials with an accuracy of 0.001 g | | | | | | | |
| **Step 2** | 60 1/min, 15 min kinetic type mixing | | | | | | | |
| **Step 3** | 25 MPa, 20 min. 150 °C hot molding | | | | | | | |

The hardness values of the brake pad samples for each sample were carried out in the Shore D durometer hardness measuring device, which is used for hardness measurement in ASTM D2240 [29] standard.

Scanning electron microscopy (SEM) microscopic analyses (LEO 1430 VP) were performed at 1000X magnification.

**Table 2.** Test method of brake pad samples and formulas used

| **Test Method and formulas** | | |
|---|---|---|
| **The friction coefficient and wear rate test conditions** | Six m/s disc speed, 1 MPa loading pressure, and 1800 min. test duration | |
| **Coefficient of friction** | $$\mu = \frac{f}{F} \text{ [27]}$$ | $\mu = Coefficient\ of\ friction$ <br> $f = Frictional\ force\ [N]$ <br> $F = Sample\ pressing\ force\ [N]$ |
| **Wear rate** | $$W_a = \frac{\Delta G}{S.M.d} \text{ [28]}$$ | $Wa = Wear\ rate\ [cm^3/Nm]$ <br> $\Delta G = Mass\ loss\ [g]$ <br> $S = Sliding\ distance\ [m]$ <br> $M = Loading\ weight\ [N]$ <br> $d = Sample\ density\ [g/cm^3]$ |

## 3. RESULTS AND DISCUSSION

Determined characteristic values of brake lining samples are given in Table 3. The density value of the brake lining sample containing micronized quartz was lower than the sample containing alumina due to the high density of the alumina material. (Alumina density: 3.92 g/cm³ [30], Quartz density: 2.65 g/cm³ [31])

The hardness of the micronized quartz sample was higher than that of alumina. The hardness values are similar to the studies in the literature [32,33]. Although the average friction coefficient is close to one another, the sample containing micronized quartz has a friction coefficient of 0.35.

**Table 3.** Characteristics of brake pad samples

| Property / Brake pad | Density (g/cm³) | Hardness (Shore D) | The average coefficient of friction (μ) | Wear rate (X10⁻⁷ cm³/Nm) |
|---|---|---|---|---|
| AL12 | 2.602 | 91.6 | 0.34 | 0.144 |
| MQ12 | 2.598 | 94.9 | 0.35 | 0.242 |

The coefficient of friction and wear rate are significant factors in determining the adequacy of the brake system when evaluating the performance of developed brake pad samples. The structure of the components that make up the brake pad, the test circumstances, and the pressure applied to the brake pad samples all affect these numbers [6]. The friction coefficient and wear rate graphs of the brake pad samples, depending on the test period, are shown in Figure 1 for the AL12 sample and Figure 2 for the MQ12 sample. In Figure 1 and Figure 2, friction

coefficient and temperature values are increasing during 100 min. slip from the first stage of the test in both brake pad samples. At the same time, the friction coefficient decreased for both samples from approximately 100 min. to 400 min. sliding time, the temperature values became more stable. After 400 min. of sliding time, the friction coefficient values of the brake pad samples showed a more stable state. When comparing the samples, the micronized quartz sample showed a slightly more unstable state than the alumina sample. The reason why

the Micronized Quartz sample is more unstable maybe because it is harder than the samples formed with alumina.

However, both samples provided the desired performance criteria for brake pad samples.
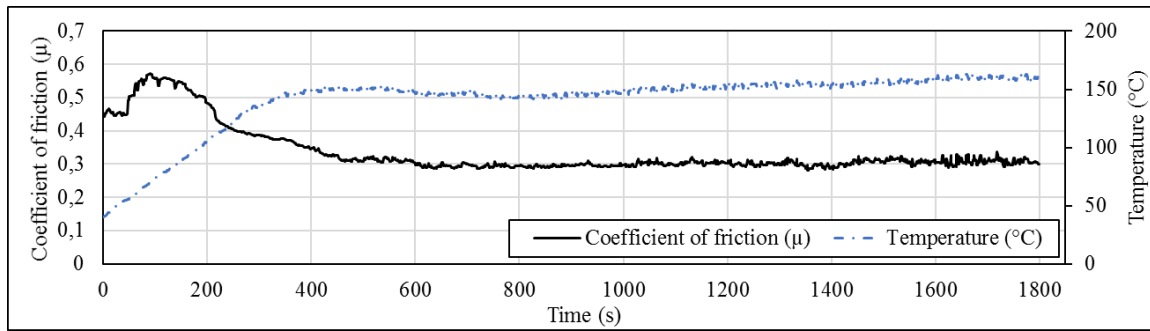


**Figure 1.** Time-dependent coefficient of friction and wear rate of AL12 brake pad sample
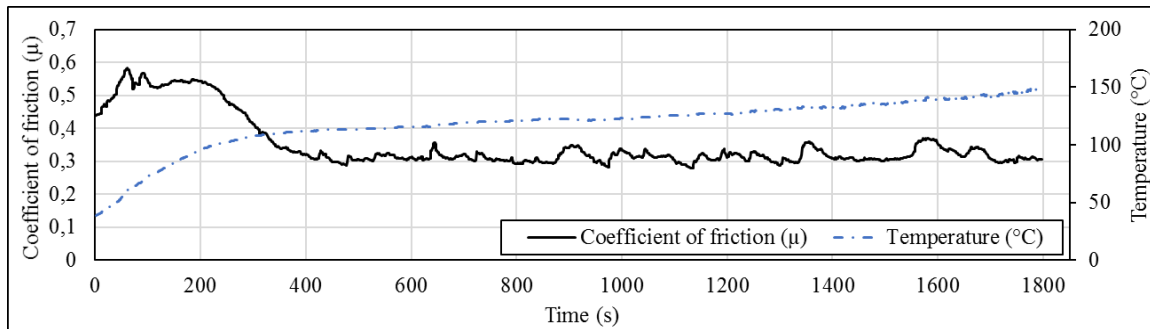


**Figure 2.** Time-dependent coefficient of friction and wear rate of MQ12 brake pad sample

The composite brake disc and brake pad wear characteristics are identical. The material of the brake disc is abrasively affected by brake pad wear [34]. Brake pad wear is a complicated phenomenon resulting from numerous interactions and friction mechanisms. As a result of plastic deformation, the temperature rise brought on by the friction between the brake pad and the disc during braking leads to wear. Mass loss of brake pad composites also happens due to the development of pits and cracks brought on by loading and vibration [8]. According to the lining standard used in the friction brakes of TS555 road vehicles, the average friction coefficient should be between 0.20-0.70 up to an operating temperature of 200 °C, and the wear rate should be $1X10^{-7}$ cm$^3$/Nm or less [27]. The produced brake pad samples' average friction coefficient and wear rate fall within these bounds.

SEM microscopic images of brake pad samples are given in Figure 3. For brake pad samples, microscopic images of worn surfaces are seen as an essential tool in evaluating surface morphology [11].
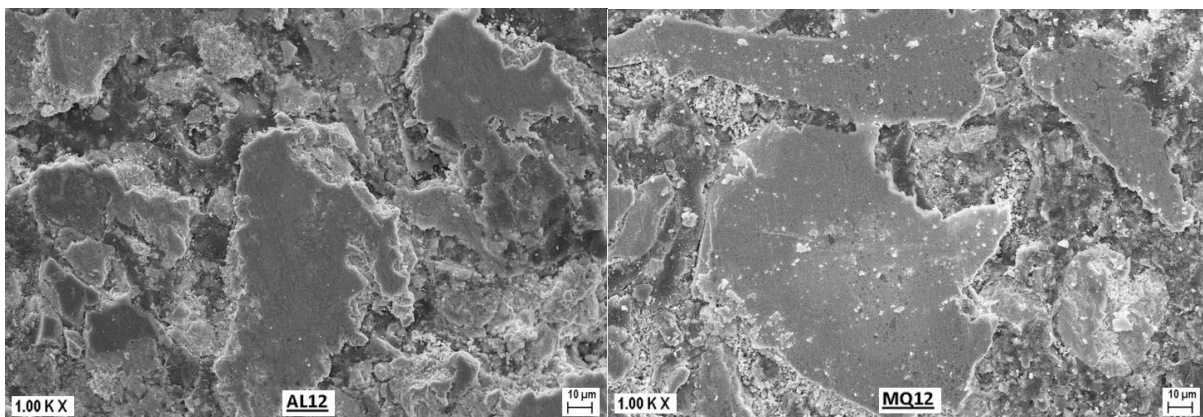


**Figure 3.** Microscope images of brake pad samples

In Figure 3, the smooth surfaces in the brake pad samples are contact plateaus. Contact plateaus consist of heat-resistant fibers, other friction modifiers, and thermally stable compounds. These plateaus are first covered with tribo film during braking, which resists high temperatures by cutting the atoms in the graphite structure. The light-colored parts on the edges of the contact surfaces are back transfer patches. Retransfer patches are less stable components that degrade during braking. Back transfer patches are caused by a hot spot on the contact surface or adhesion in the fading cycle. The contact surfaces that resist the wear movement contribute to forming a back-transfer patch by ensuring the adhesion of the wearing parts [8,23].

## 4. CONCLUSIONS

In this study, samples containing 12% alumina and 12% micronized quartz were produced as friction modifiers. The produced brake pad sample density, hardness, and tribological performance were assessed. SEM microscopic examinations were done on the worn surfaces of the brake pad samples whose tribological performance was assessed. The following results were obtained from the experiments.

- The density of the samples containing micronized quartz in brake lining samples was lower.
- The micronized quartz brake pad samples had a higher wear rate than the alumina brake pad samples. For both samples, the wear rate is at its best.
- The average friction coefficient, one of the essential properties sought for brake pads, was obtained at an optimum value of 0.34 in the sample containing alumina and 0.35 in the sample containing micronized quartz.
- The hardness of the brake pad samples was found to be 91.6 Shore D in the sample containing alumina and 94.9 Shore D in the sample containing micronized quartz, similar to the studies in the literature.
- In the SEM analysis of brake pad samples, contact surfaces, and back transfer patches, which are the light-colored parts on the edges of these surfaces, were determined.

When all the results were evaluated, it was determined that the use of micronized quartz material instead of alumina material, which is often used as a friction-regulating material in brake pads by the researchers, meets the desired performance parameters of the brake pads.

**Acknowledgement**

## REFERENCES

[1] Aras S, Tarakçıoğlu N. Experimental investigation of the effect of compression pressure on mechanical properties in glass fiber reinforced organic material-based brake pads production. International Advanced Researches and Engineering Journal 2019;03:111-115.

[2] Başoğlu G. Production of organic based composite brake lining and investigation of braking performance. Afyon Kocatepe University International Journal of Engineering Technology and Applied Sciences 2020;3:1-9.

[3] Başeğmez B. Assessment of brake discs used railway vehicles in terms of heat and material. Mühendis ve Makina 2021;62:751-767.

[4] Sivri RK, Keleş İ. Finite element thermo-mechanical analysis of heavy vehicle brake disc. Black Sea Journal of Engineering and Science 2023;6:44-52.

[5] Özel MA, Sungur C. Semi-Hot pressing with brake pad and shim components and providing control of suitable after proccess. European Journal of Science and Technology 2021;30:53-55.

[6] Gawande SH, Banait AS, Balashowry K. Study on wear analysis of substitute automotive brake pad materials. Australian Journal of Mechanical Engineering 2023;21:144-153.

[7] Hatam A, Khalkhali A. Simulation and sensitivity analysis of wear on the automotive brake pad. Simul Model Pract Theory 2018;84:106-123.

[8] Kanagaraj M, Babu S, Jegan Mohan SR, Christy T V. The evaluation of friction and wear performances of commercial automotive brake friction polymer composites. Industrial Lubrication and Tribology 2023;75(3):299-304.

[9] Sekunowo O, Durowaye S, Lawal G. Physical and mechanical characterisation of asbestos-free particulate ceramic matrix composites. Eskişehir Technical University Journal of Science and Technology A- Applied Sciences and Engineering 2020;21:562-574.

[10] Ünal A, Akkuş N, Kandil ST. Finite element method approach against to brake fading problem in railway vehicle brake friction element design. Demiryolu Mühendisliği 2022;15:134-144.

[11] Öktem H, Akıncıoğlu S, Uygur İ, Akıncıoğlu G. A novel study of hybrid brake pad composites: new formulation, tribological behaviour and characterisation of microstructure. Plastics, Rubber and Composites 2021;50:249-261.

[12] Oral B, Akkoyun Ş. Processing and characterization of sepiolite clay containing composites for organic brake pad application. European Journal of Science and Technology 2020;Special Issue:89-94.

[13] Marin E, Daimon E, Boschetto F, Rondinella A, Inada K, Zhu W, et al. Diagnostic spectroscopic tools for worn brake pad materials: A case study. Wear 2019;432-433.

[14] Akıncıoğlu G, Akıncıoğlu S, Uygur İ, Öktem H. Investigation of the effect of boron oxide on the friction behavior of brake pads as an alternative additive. Journal of Boron 2019;4:1-6.

[15] Karthikeyan SS, Balakrishnan E, Meganathan S, Balachander M, Ponshanmugakumar A. Elemental anlysis of brake pad using natural fibres. Mater Today Proc 2019;16:1067-1074.

[16] Pujari S, Srikiran S. Experimental investigations on wear properties of Palm kernel reinforced composites for brake pad applications. Defence Technology 2019;15:295-299.

[17] Bala KC, Lawal SS, Ademoh NA, Abdulrahman AS, Adedıpe O. Effects of nigerian plant gum binder in the optimized multi-response performance of cashew nut shells based composites for automobile brake pads. The Eurasia Proceedings of Science, Technology, Engineering & Mathematics 2021;12:17-27.

13

[18] Lagel MC, Hai L, Pizzi A, Basso MC, Delmotte L, Abdalla S, et al. Automotive brake pads made with a bioresin matrix. Ind Crops Prod 2016;85:372-381.

[19] Sugözü İ, Öner C, Mutlu İ, Sugözü B. Production of boric acid added brake friction composite and the effect of heat treatment on braking characterization. Industrial Lubrication and Tribology 2022;74:1132-1139.

[20] Yılmaz AC. Effects of fly ash introduction on friction and wear characteristics of brake pads. International Journal of Automotive Engineering and Technologies 2022;11:96-103.

[21] Hamamcı B, Sali M. The effect of different sintering temperature and time on tribological and mechanical properties in non asbestos brake pad manufacturing. Journal of the Institute of Science and Technology 2020;10:520-531.

[22] Justin Antonyraj I, Vijay R, Sathyamoorthy G, Lenin Singaravelu D. Influence of graphite purity concentrations on the tribological performance of non-asbestos organic copper-free brake pads. Industrial Lubrication and Tribology 2023;75:9-16.

[23] Saikrishnan G, Jayakumari LS, Vijay R. Effect of graphitization percentage on fade and recovery performance of copper-free non-asbestos organic brake pads. Industrial Lubrication and Tribology 2022;74:901-909.

[24] Öktem H, Uygur I, Çevik M. Design, construction and performance of a novel brake pad friction tester. Measurement (Lond) 2018;115:299-305.

[25] Kchaou M, Kus R, Singaravelu DL, Haran SM. Design, characterization, and performance analysis of Miscanthus fiber reinforced composite for brake application. Journal of Engineering Research (Kuwait) 2021;9:222-234.

[26] Yavuz H, Bayrakceken H. Friction and wear characteristics of brake friction materials obtained from fiber and huntite blends. Industrial Lubrication and Tribology 2022;74:844-52.

[27] TS 555, Road vehicles - brake linings and pads for friction type brakes 2019.

[28] Al-Sarraf AHRM. Study on adhesion wear damage done on the hybrid composite Novolac under the experimental variables. Energy Procedia, 2019;157:644-654.

[29] ASTM D2240-15, Standard test method for rubber property-durometer hardness, 2021.

[30] Anonymous [Internet]. 2023 [Cited 2023 Jun 16]. Available from: http://www.aluminyumoksit.com/aluminyum_oksit_ozellikleri

[31] Anonymous [Internet]. 2023 [Cited 2023 Jun 16]. Available from: https://www.mta.gov.tr/v3.0/bilgi-merkezi/kuvars

[32] Yavuz H. Effect of limestone usage on tribological properties in copper and asbestos-free brake friction materials. Industrial Lubrication and Tribology 2023;75:238-245.

[33] Yavuz H, Bayrakçeken H. Investigation of friction and wear behavior of composite brake pads produced with huntite mineral. International Journal of Automotive Science And Technology 2022;6:9-16.

[34] Zhang M, Shi H, Ding S, Ma L. Influence of braking speed on the wear property and simulation analysis of high-speed railway braking materials at low temperature. Industrial Lubrication and Tribology 2023;75(4):387-397.

# Effect of Longer Waiting Time During OCP and Pre-Applied Cleaning Potential In Corrosion Analysis of Zinc Metal

**Salih CİHANGİR**[*] ID

[1] Munzur University, Rare Earth Elements Application and Research Centre, Tunceli, Türkiye
[2] Munzur University, Department of Chemistry and Chemical Processes, Tunceli Vocational School, Tunceli, Türkiye
Salih CİHANGİR ORCID No: 0000-0001-5989-5230

*Corresponding author: salihcihangir@munzur.edu.tr*

**Abstract:** Tafel analysis is a widely accepted electrochemical technique for corrosion studies. A general literature search for one of the electronegative metals, zinc, revealed serious deviations in corrosion results. In order to understand the reasons behind these deviations, zinc metal was investigated at macro and micro levels during and after the Tafel corrosion analysis. In-situ macro surface investigation during the open circuit potential period and Tafel analysis were performed, and it was found that the zinc surface undergoes proceeding corrosion attack following the immersion in 3.5 wt.% NaCl solution. In-situ macro surface analysis exhibited that the pre-oxidation of the surface proceeds as nonuniform at local regions. SEM-EDS and XRD analysis proved that the particular crystal planes of the zinc form ZnO with increasing immersion time. A linear sweep voltammetry (LSV) technique was applied to detect the oxygen removal and starting hydrogen evolution potentials. Three identical Tafel experiments were performed on samples without any treatment, and another three consecutive Tafel experiments were performed on the samples which applied pre-reduction potential. Obtained results revealed that in-situ pre-applied reduction potential just before the Tafel analysis cleaned the surface and allowed uniform oxide formation, resulting in the lowest standard deviation of the calculated Tafel elements.

# Çinko Metalinin Korozyon Analizinde OCP Sırasında Uzun Bekleme Süresinin ve Önceden Uygulanan Temizleme Potansiyelinin Etkisi

**Öz:** Tafel analizi korozyon çalışmaları için yaygın olarak kabul edilen bir elektrokimyasal tekniktir. Elektronegatif metallerden biri olan çinko için genel bir literatür araştırması sonucu korozyon parametrelerinde ciddi sapmalar olduğu gözlemlenmiştir. Bu sapmaların arkasındaki nedenleri anlamak için Tafel korozyon analizi sırasında ve sonrasında çinko metali makro ve mikro seviyelerde incelenmiştir. Açık devre potansiyel süresi boyunca yerinde makro yüzey araştırması ve Tafel analizi yapılmış ve çinko yüzeyinin ağırlıkça %3.5 NaCl çözeltisine daldırıldıktan sonra devam eden korozyon ataklarına uğradığı tespit edilmiştir. Yerinde makro yüzey analizi, yüzeyin ön oksidasyonunun yerel bölgelerde tekdüze olmayan bir şekilde ilerlediğini göstermiştir. SEM-EDS ve XRD analizi, çinkonun belirli kristal düzlemlerinin artan daldırma süresi ile ZnO oluşturduğunu göstermiştir. Oksijen giderimi ve hidrojen oluşum potansiyellerini tespit etmek için lineer tarama voltametresi (LSV) tekniği uygulanmıştır. Herhangi bir işlem uygulanmadan numuneler üzerinde üç özdeş Tafel deneyi yapılmış ve ön indirgeme potansiyeli uygulan numuneler üzerinde ardışık üç Tafel deneyi daha yapıldı. Elde edilen sonuçlar Tafel analizinin yüzeyi temizlemesinden hemen önce yerinde önceden uygulanan numunelerde indirgeme potansiyeli ile homojen oksit oluşumuna sağlanmış ve hesaplanan Tafel elementlerinin oldukça düşük standart sapma ile tekrar edilebilir olduğu bulunmuştur.

# 1. INTRODUCTION

Zinc (Zn) is one of the most attractive materials in the literature. Zn alone was mentioned in the titles of approximately 4500 papers in 2022 and over 1300 papers in just the first quarter of 2023. While Zn is used in medical research for its effect on organisms [1], energy research for long-life metal batteries [2], and solar perovskite cells [3], micro-electronics research for semiconductors [4], Zn is also commonly used for anticorrosive surface preparation as standalone or in alloy structures [5-8]. Regardless of the main research focus of Zn-related studies, potentiodynamic corrosion investigations are widely employed. In the performed literature search, it was found a serious fluctuation of obtained corrosion parameters for especially zinc metal. For example, corrosion current densities in various Tafel studies (one of the most critical parameters in corrosion analysis) are reported as low as a few milliamperes per square to a few thousand milliamperes per centimeter square in various studies for Zn surfaces tested in 3.5 wt.% NaCl solution at 25°C is presented in Table 1.

**Table 1.** Obtained corrosion current densities of Zn metal in various studies.

| The Method of Obtaining Zinc Metal Used for Corrosion Analysis | $J_{corr}$/ μA cm$^{-2}$ |
|---|---|
| Electrodeposition [9] | 10.60 |
| Electrodeposition [10] | 89.98 |
| Pure Zn Sheet [11] | 266.5 |
| Pure Zn Sheet [12] | 115 |
| Electrodeposition [13] | 11.23 |
| Electrodeposition [14] | 54.4 |
| Electrodeposition [15] | 28 |
| Pure Zn Sheet [16] | ~ 60 |
| Pure Zn Sheet [17] | 8442 |
| Electrodeposition [18] | 42 |
| Electrodeposition [19] | 8.91 |
| Electrodeposition [20] | 270 |
| Electrodeposition (three different potentials) [21] | 181.85 - 401.89 |
| Electrodeposition (three different temperatures) [22] | 8.94 - 182 |

It is a rather interesting outcome for a standardized corrosion measurement technique with quite fluctuated results. In fact, in corrosion measurements, the type of the surface phase also plays a critical role during the passivation in the anodic scan. However, there is an obvious pinpoint to explore for a better understanding and correct application of corrosion measurement. The reason behind this claim is the applied cleaning procedures of the surfaces before performing the corrosion experiment. In the literature, before corrosion, samples are polished with sandpapers by starting from 400 grids up to 3000- 5000 grids to get a finer polished surface. While it is practically impossible to reach two-dimensional (2D) flatness at the close or sub-micron level, the main purpose here is to assume the existence of a surface as possible as 2D because mathematical models developed for electrochemical processes are based on 2D space. In one aspect, if the surface energetics and the roughness of the metal count into account, it may likely be possible that corrosion attack only interacts outer layer (not with the sub or close micron holes) of the rough surfaces. While no direct study is encountered to support this claim, it is declared that there are two states called Cassie-Baxter and Wenzel for the surfaces subject to liquid contact [23]. The Cassie-Baxter state for rough surfaces is observed for most high-surface tension liquids, such as salty water (73 mN m$^{-1}$ [24]). The Cassie-Baxter state supports that dry spaces are air-filled on rough surfaces in relatively higher surface tension liquids [25]. However, the dry locations in holes of rough surfaces do not tend to form when using low surface tension liquids, such as hexane (0.013 mN m$^{-1}$ [26]). Therefore, it is undoubtedly expected to get more reliable results from well-polished surfaces. As discussed in the zinc case, reliable results are not always the case for even the corrosion tests of the same sample. In potentiodynamic scan (Tafel) analysis, the 15% deviation is declared as good reliability of the setup by leading potentiostat manufacturers because the contamination of the surface and the air-formed oxide, or even dissolved oxygen in the solution are expected to deviate the outcome. Moreover, the possibility of three-dimensional (3D) interaction of the corrosive solution with the surface is always in question, especially in insufficient polishing cases. In order to eliminate as possible as inflictive parameters on Tafel results, researchers mentioned applying pre-cleaning potential vs. reference or open circuit potential of the sample prior to the Tafel scan [27, 28]. Although sample preparation and cleaning processes were discussed, another important; unfortunately not as much considered parameter, the scan rate, is rather critical in corrosion experiments. While the most applied scan rate in the literature for Tafel corrosion experiments is between 0.1 mV s$^{-1}$ and 1 mV s$^{-1}$, ASTM G5 (Standard Reference Test Method for Making Potentiodynamic Anodic Polarization Measurements) strongly recommends using 0.1667 mV s$^{-1}$ as it allows sufficient time to protect the stable-state of the ongoing reactions still minimizing the capacitive current contribution [29]. Faster scan rate may be useful in particular cases, such as rather thin samples (less than a few microns), rapid dissolution and accumulation of the corroded species on the surface, or fast dealloying of the investigated alloy in question, to prevent the rapid degradation. In fact, the Tafel technique is based on the potential scan as applied in cyclic voltammetry (CV) and linear sweep voltammetry techniques (LSV), and it is known that higher scan rates always tend to decrease diffusion layer size and reveal higher current outputs [30, 31].

This study aims to investigate the effect of a long waiting time to reach the steady state condition (OCP) condition and applied pre-oxidation potential on corrosion parameters of Zn metal. In this approach, it will be observable if there are possible deviations in the Tafel parameters. Additionally, surfaces will also be examined at various stages for further understanding. Consequently, the study will be useful to the researchers for their Tafel corrosion experiments.

16

## 2. MATERIAL AND METHOD

All the chemicals were used as received. 3.5% wt. NaCl solution was prepared by a simple mixture of double-distilled water and NaCl salt (MERC). Employed potentiodynamic and potentiostatic experiments were carried out at room temperature with a three-electrode electrochemical workstation (Biologic, SP240) potentiostat. A pure zinc sheet (%99.9 pure, Alfa Aesar) was a working electrode. Standard Ag/AgCl (3.5M KCl, Gamry) glass frit-tip electrode was a reference electrode. The counter electrode was Ruthenium/Iridium coated Ti (40 cm$^2$ mesh electrode). A 3D-printed jacketed corrosion cell was used to standardize the Tafel experiments. Figure 1. Shows the photograph of the employed cell system in corrosion experiments. Before the corrosion experiment, samples were cleaned with 3000-4000 and 5000 grids polishing pads, washed with alcohol, and cleaned in ultrasound cleaner at 40 Hz for 2 minutes. The morphology and chemical composition of the deposited films were analyzed by scanning electron microscope (HITACHI SU3500, SEM) equipped with electron dispersive spectroscopy (EDS, Oxford Aztech) for elemental analysis. Energy dispersive X-ray (EDX, Oxford Inca) was used to analyze the crystal planes. XRD analysis was carried out using RIGAKU Miniflex 600 equipped with Cu Kα (λ = 1.788965 Å) radiation operated at 40 kV and 30 mA in 0,02° step size at 10-90°. In corrosion experiments, the Zn sheet served as a working electrode; Ag/AgCl (3.5 M KCl) electrode was used as the reference electrode; 25 cm$^2$ Ruthenium/Iridium coated Ti was used as a counter electrode. Stable open circuit potential (OCP) was observed before starting the Tafel analysis. For Tafel corrosion tests, a potentiodynamic voltammetric scan from -0.25 V$_{OCP}$ to 0.25 V$_{OCP}$ was performed at 0.166 mV s$^{-1}$ scan rate.
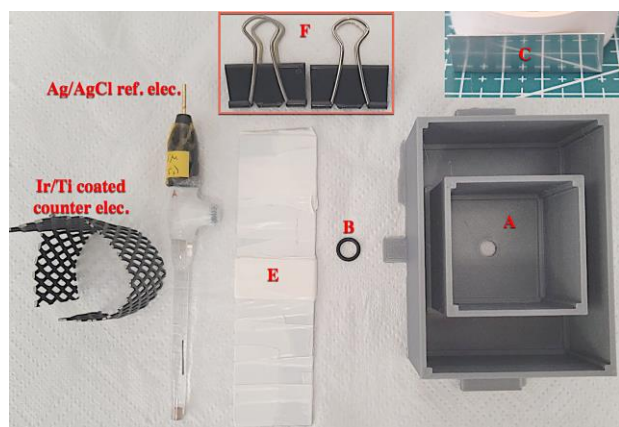


**Figure 1.** A (3D printed cell, PETG) is the topmost part, B (O-ring) is placed under the hole of A, and C (polished Zn substrate) is placed under B. Then, 1.5 mm thick, white electric tape-insulated SS-316 support (labeled as E) is placed under C. Binder clips (labeled as F) apply adequate pressure to support (E) and two side paddles of cell A. This way, the O-ring (B) and the main cell (A) are ready for a watertight operation. Reference and counter electrodes are placed inside the square corrosion chamber (A).

During corrosion experiments, a computer-controlled USB microscope was used for in situ observation of surface change to distinguish the macro surface changes depending on the applied potential. The images of the surfaces before the applied potential states and after the

applied potential states were taken with a high-resolution material microscope equipped with a SONY-IMX485 camera and Mitutoyo optic lenses.

## 3. RESULTS AND DISCUSSION

If Tafel calculation is examined from obtained logarithmic current vs. potential graph, slopes for cathodic and anodic regions start from close points of the E$_{corr}$, as shown in Figure 2. As it is known, the sample does not corrode at the cathodic region in which hydrogen evolution reaction (HER) at the very negative potentials of starting cathodic slope takes place, but also Zn surface may reduce the oxygen by $O_2 + H_2O + 2e^- \rightarrow HO_2^- + OH^-$ in saline media [32]. At close points of the E$_{corr}$ sample may initiate a weak nano/micro passivation region (usually rapidly breaks down) just before the anodic scan.
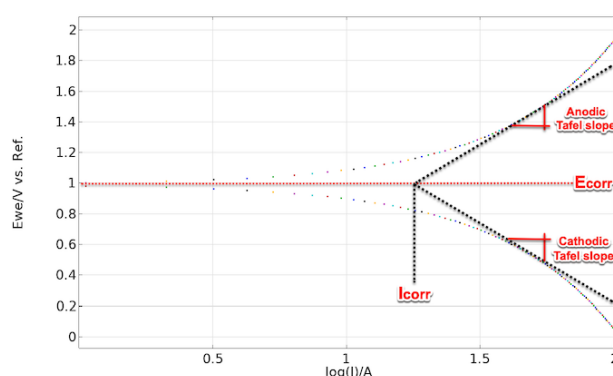


**Figure 2.** Anodic and cathodic lines are shown in a standard Tafel graph.

As mentioned, the mathematical models produced for initially heterogeneous electrochemical-based reactions (homogenous chemical redox transformation reactions may also occur) are usually based on 2D space. In order to properly fit the 2D mathematical approximation, it is important to evaluate the data that the surface does not significantly deviate from its initial geometrical state (tens of microns deep and wide cracking/pitting does not yet occur). Therefore, Tafel analysis generally uses the anodic and cathodic slopes of the region close to the E$_{corr}$ value because the samples may undergo severe corrosion attack at far potential values of E$_{corr}$, especially in the anodic region. At more positive values from the E$_{corr}$ at the anodic region, micro-cracks and holes are expected to occur for most surfaces. In this case, the surface moves away from its two-dimensional form, to which the mathematical model can be applied.

### 3.1 Investigation of Repetitive Open Circuit Potential Scan

OCP determination is applied for both Tafel and EIS corrosion studies, and various approaches are employed in different studies for stable OCP determination. In some studies, less than 20 mV deviation in 30 minutes is accepted as a sign of equilibrium before starting the corrosion analysis [33], and in a typical application, 30 minutes waiting time is declared as stable OCP deviation, usually without quantitative support of OCP deviation as a function of time [34-36]. Some groups also follow an

hour waiting time rule [37-39] because ASTM (American Society for Testing and Materials) states that an hour immersion time is required to reach the equilibrium state with an expected 10 mV h$^{-1}$ or lower deviation [40]. In the former approach, the 20 mV s$^{-1}$ deviation is a slightly higher value to accept as an equilibrium point or stable OCP because it corresponds to 40 mV h$^{-1}$. Still, the latter approach may also be detrimental to thin, less corrosion-resistant materials because chloride will continuously attack the surface once the sample is immersed in a corrosion solution. Then, the surface phase is eventually changed and prevents proper Tafel analysis. It is known that the reactions on the electrode surface take forever to reach a perfect equilibrium of infinite steady condition, but the point that these ongoing reactions proceed quite slowly and in near balance is accepted as equilibrium potential.

In order to overcome these issues, new-generation potentiostat devices provide an option for time-dependent potential change. In this option, even determined time is 2h for OCP, a limit function of time-dependent potential change (mV s$^{-1}$) is applied. If a limit function, for example, <0.1mV s$^{-1}$, the deviation is fulfilled before the 2h time condition, the Tafel scan starts. This way, good equilibrium (<10 mV h$^{-1}$) can be obtained, with unnecessary waiting time, and possible or further surface damage is prevented. In this study, three identical well-polished surfaces were prepared for OCP determination. The reference surface image of the prepared samples is shown in Figure 3. Then, samples were placed in the corrosion cell at room temperature for over 25 minutes until the observation of negligible deviation at OCP. This experiment was performed with two different approaches. The first approach was time-dependent, as mostly applied in the literature in which the sample was kept for a prolonged time (generally over 1000 s) to get stable OCP. The second approach was kinetic-based, as suggested by leading potentiostat manufacturers and in some literature studies. In the kinetic dependence, having <10 mV s$^{-1}$ in the OCP measurement is strongly suggested.
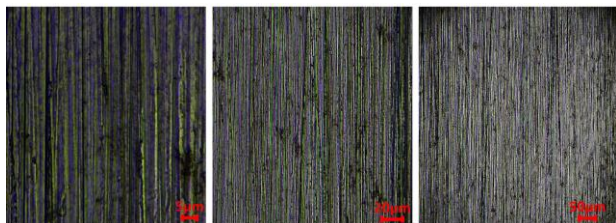


**Figure 3.** Before corrosion tests, the optical images of polished samples (presented in Figure 1. C) were taken. Scratches are expected to occur after polishing and were detected under a micron size.

In the first experiment, samples were observed for about 1800 s to reach a stable OCP value. Obtained OCP graphics are presented in Figure 4. In each performed OCP experiment, especially the last 300 s were more focused, and the deviation in the last 300 s was specifically sought for 10 mV h$^{-1}$ or less.
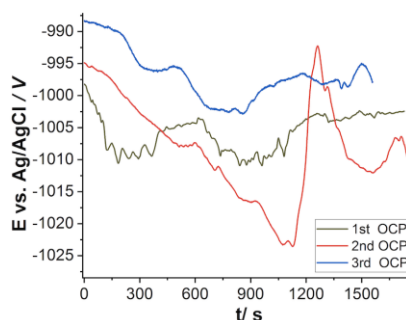


**Figure 4.** Three identical well-polished surfaces are placed in the corrosion cell and left for over 25 minutes until the observation of stable OCP behavior.

In the 1$^{st}$ OCP experiment, OCP was detected as -1002 mV$_{Ag/AgCl}$, and the deviation in the last 300 s was calculated as 6 mV h$^{-1}$. In the 2$^{nd}$ OCP experiment, OCP was detected as -1009 mV$_{Ag/AgCl}$, and the deviation in the last 300 s was calculated as 11 mV h$^{-1}$. In the 3$^{rd}$ OCP experiment, OCP was detected as -998mV$_{Ag/AgCl}$, and the deviation in the last 300 s was calculated as 1.2 mV h$^{-1}$. During the OCP experiments, a USB microscope camera system was set to observe macro surface changes, such as color alterations, bubble formations, etc. It was found interesting that the surface is expected to form ZnO with increasing immersion time during open circuit potential, as shown in Figure 5. because it is already reported in a comprehensive study that Zn initially tends to form ZnO at the early time of immersion along with the expected formation of Zn(OH)$_2$ for a prolonged time (over >10 hours) [32]. When obtained images at minutes 6 and 12 are compared, a clear color change is seen, and this color difference becomes more apparent at longer times, with a predominance at the edges. Initial surface corrosion products are formed following the immersion without any applied potential. In fact, formed oxide and hydroxide corrosion products creates a surface film resistant to further zinc corrosion, and thus, it is a protective result of the metal in corrosion media [32]. SEM-EDS and XRD carried out morphological and crystal plane investigations for the initial state and after the OCP state of the surfaces.

18
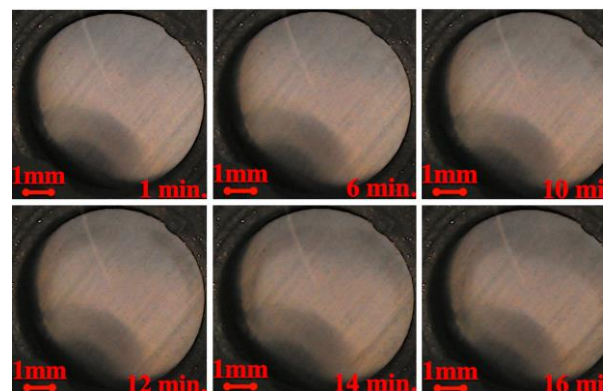


**Figure 5.** Macro surface images taken at various stages of the OCP period (as exhibited in Figure 4.) are presented.

In the SEM-EDS analysis, clean samples were first investigated. Then the sample employed OCP determination experiments for 1500 s and then examined with the SEM-EDS technique, as shown in Figure 6. When the pure Zn surface was investigated, it can be seen that the air-formed oxygen was equally distributed. EDS

analysis revealed 2.2% oxygen content. However, in the case of OCP-employed Zn surface, local blemishes were observed, oxygens were accumulated locally on the surface, and EDS analysis revealed a three-fold increase in oxygen content. An increase in oxygen content is expected due to the formation of ZnO and $Zn(OH)_2$. In the EDS analysis of OCP employed Zn, the right part of the sample, which, out of local blemished spot, more oxygen was detected.
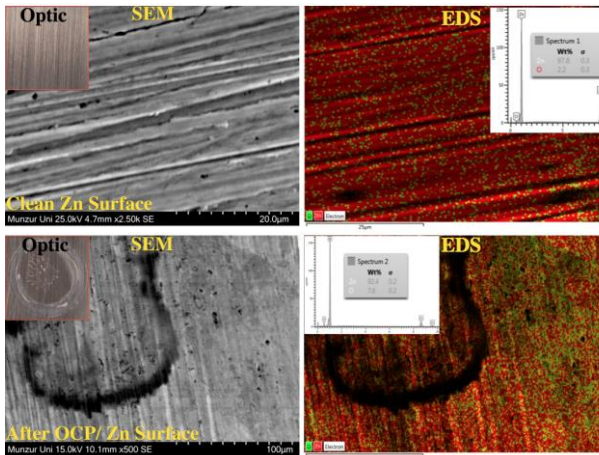


**Figure 6.** The electrochemically non-treated clean polished surface and the surface after the 1500 s OCP stage are investigated with SEM-EDS analysis.

In order to collect more data for the phenomenon of the initial formation of ZnO, XRD analysis was performed, as presented in Figure 7. The XRD data for pure ZnO powder was also presented in the XRD data graph. It is found that while all the peak intensities of the Zn (COD ID:9008522) decreased after the OCP stage, abrupt decreases in the intensity of (002) and (004) crystal planes were observed. Indeed, crystal planes analyzed after the OCP state became similar to that of (101) and (202) ZnO crystal planes (COD ID:2300112). In other words, the behavior at around 36° and 77° for OCP employed Zn started to resemble the (101) and (202) crystal planes of ZnO.
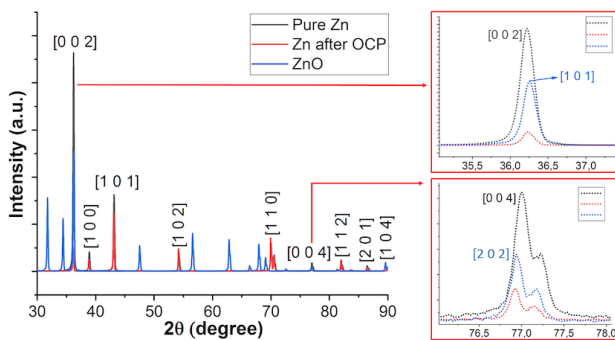


**Figure 7.** XRD analysis of Zn without treatment, after the OCP stage, and ZnO powder are presented.

When collected data in the optic microscope, SEM, EDS-mapping, and XRD are evaluated, it can be seen that the surface of the Zn starts to oxidize following the immersion and increases with immersion time. It was observed that the oxidation of the employed sample specifically preferred to occur in (004) and (101) crystal planes which are the most depressed crystal planes after OCP.

Following the OCP investigation, three identical Tafel experiments were performed on identical Zn surfaces. The Tafel polarization data with OCP graphs are presented in Figure 8. In the OCP analysis part, the potentiostat was adjusted to seek <10 mV h$^{-1}$.
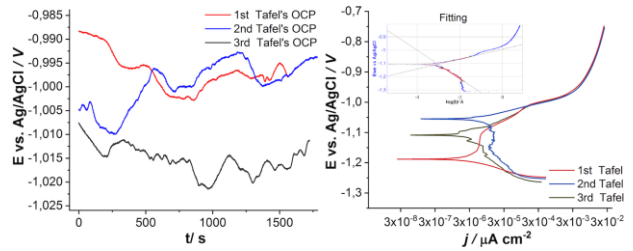


**Figure 8.** Three identical cleaned polished Zn sheets were observed for 1500 s in the OCP stage, and then the Tafel measurements were performed.

Biologic's advanced Tafel corrosion fit analysis program was used to obtain fitting parameters. Table 2 shows the obtained fitting parameters with mean and standard deviation values. Obtained $E_{corr}$ and $I_{corr}$ values match literature but deviate from each other. Normally, OCP and $E_{corr}$ values are expected to be as possible as a match, but the 10% difference is still within the acceptable limit. The reason for the 10% deviation in $E_{corr}$ values is explained in the OCP macro surface investigation section, given in Figure 5, in which the 3.5 wt.% NaCl medium caused changes on the surface with increasing immersion time before the actual Tafel scan took place.

**Table 2.** Tafel elements and the OCP data for performed experiments in Figure 8 are presented with mean and standard deviation values.

| Samples | OCP/ mV | $E_{corr}$/ mV | $J_{corr}$/ μA cm$^{-2}$ | $\beta a$/ mV | $\beta c$/ mV |
|---|---|---|---|---|---|
| 1st sample | -998 | -1189 | 2.667 | 164.7 | 345 |
| 2nd sample | -994 | -1051 | 5.509 | 28.9 | 111 |
| 3rd sample | -1011 | -1101 | 2.979 | 49 | 162 |
| Mean | -1001 | -1114 | 3.72 | 81 | 206 |
| Standard Dev. | 8.89 | 68.87 | 1.56 | 73.43 | 123.05 |

When Tafel polarization curves are examined, it can be seen that the cathodic curves deviate more than the anodic curves. Following the immersion and at the end of the cathodic part (close points to starting anodic region), the reaction (1) take place, as observed in the OCP stages and examined in XRD analysis. In other words, Zn already starts to oxidize with increasing immersion time.

$$Zn \rightarrow Zn^{2+} + 2e^- \qquad (1)$$

In the Tafel analysis of the samples, before -1.2 $V_{AgCl}$, -1.05 $V_{AgCl}$, and -1.15 $V_{AgCl}$ for the 1st, 2nd and, 3rd Tafel samples, respectively, hydrogen evolution given in reaction (2) takes place.

$$2H_2O + 2e^- \rightarrow 2OH^- + H_2 \qquad (2)$$
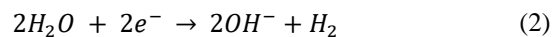
While potential is scanning to more positive values in the cathodic region, oxygen consumption reactions (3) and (4) occur.

$$O_2 + H_2O + 2e^- \rightarrow HO_2^- + OH^- \qquad (3)$$

$$HO_2^- + H_2O + 2e^- \rightarrow 3OH^- \qquad (4)$$
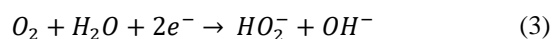
If the surface is already oxidized, as observed in OCP experiments, and thus, the deviation at the cathodic region is expected to occur. In the final experiment, the surface of each sample is planned to be applied to a pre-potential for in-situ cleaning, and the OCP waiting times are kept under 600 s. In macro surface recorded OCP experiments, as discussed in Figure 5 and Figure 6 sections, the Zn surfaces were found to change at around 500 s. Moreover, in the OCP stage, the potentials at 500 s and 1500 s, given in Figure 8, were analyzed, and 1 mV difference for 1st Tafel sample (500 s: -997 mV and 1500 s: 997 mV), 3 mV difference for 2nd Tafel sample (500 s: -997 mV and 1500 s: 994 mV), and 2 mV difference for the 3rd Tafel sample (500 s: -1013 mV and 1500 s: 1011 mV) were detected. In other words, the potential values at 500 s, in which macro surface change does not evolve, were very close to the final OCP values at 1500 s. If the big picture is this, applied pre-potential along with shorter waiting time at the OCP stage may bring much more reliable results in Tafel corrosion tests.

In order to determine the correct potential which does not vigorously decompose the $H_2O$ and damage the solution dynamics, a linear sweep voltammetry (LSV) experiment was performed at 0.2 mV s$^{-1}$ scan rate after the OCP stage, as shown in Figure 9. Scan rate chosen as close as Tafel scan rate of 0.166 mV s$^{-1}$. Before the LSV scan, the OCP of the sample was determined, and then the linear voltammetry scan was started from 0 V$_{OCP}$ to -500 mV$_{OCP}$. OCP of the samples was determined as -1034 mV, similar to those found in the Tafel experiments. The conspicuous thing is that the OCP value at 500 s was -1024 mV, which was acceptable to start the Tafel scan rather than waiting for an extra 1000 s to get -1034 mV. OCP and LSV curves of the Zn metal, along with macro surface images, are presented in Figure 9. The emerged peak at -300 mV$_{OCP}$ (at -1.33 V) in LSV occurs mostly in reactions (3) and (4). However, the observed torsion after -1.4 V$_{OCP}$ (more negative potentials) shows the starting of hydrogen evolution given in reaction (2).
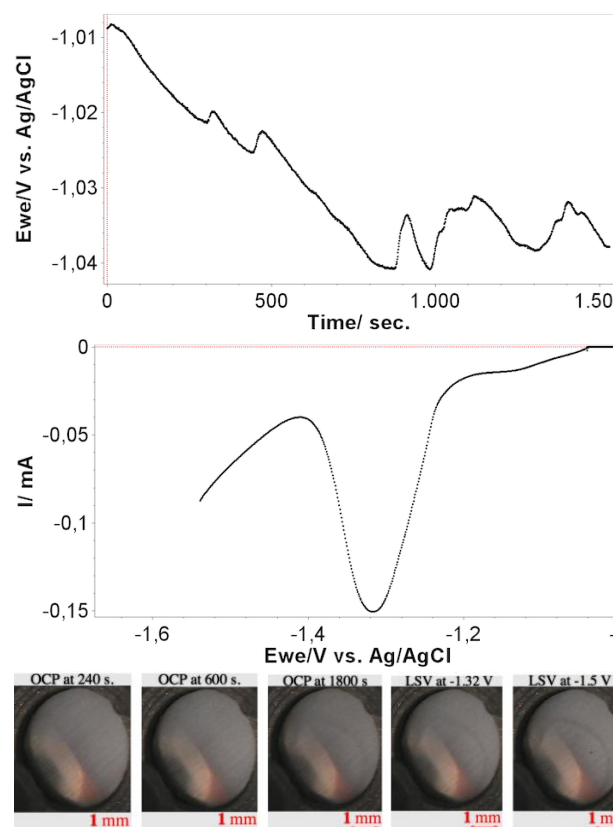


**Figure 9.** OCP and LSV graphs for the Zn working electrode are presented. The red line represents the zero-time baseline for OCP and the zero potential baselines for LSV.

If the macro surface images are investigated, it can be seen that the OCP image gets much darker through the end of the OCP (at 1800 seconds), forming shades on the surface. The observed darkness of the surface at the end of OCP started to disappear and became indistinct at -1.32 V of LSV, from which the peak emerged. Then, small hydrogen gas bubbles occurred at -1.5 V of the LSV scan.

In the next experiment, the sample was decided to be kept at OCP for 500 s because both performed experiments given Figure 5 and Figure 9 showed that longer waiting time causes oxide products that are not easy to dissolve. Moreover, 500 s and 1800 s of OCP have only a 1% difference. Following the OCP stage, samples are aimed to be applied a -600 mV potential difference (vs. V$_{OCP}$) to remove any air-formed oxide or reducible impurities. Then, after another 500 s OCP stage, the Tafel test was employed. In this way, it is aimed to obtain a more reliable and repeatable corrosion testing procedure. Pre-applied potential-based Tafel analysis is presented in Figure 10 with relevant macro surface images at the end of each stage.
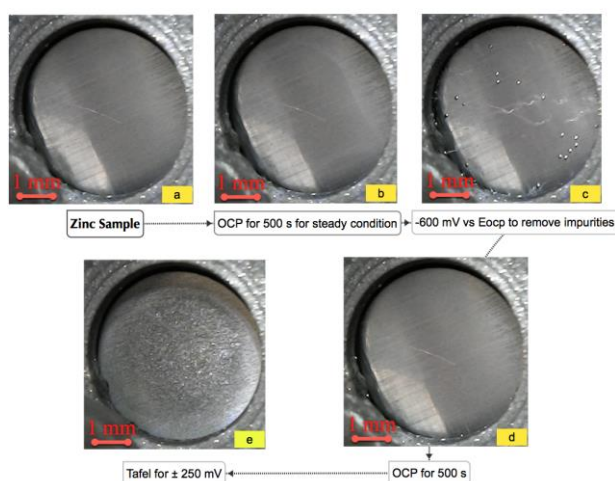
**Figure 10.** a represents the polished zinc surface in the corrosion solution, b represents the 500 s OCP stage, c represents the -600 mV vs. EOCP potential, d represents the OCP stage before Tafel, and e represents the surface in the corrosion solution following the Tafel.

One of the interesting findings in pre-applied potential-based Tafel analysis was observed in the OCP stage shown in Figure 10d. There was no locally formed blemished area with 500 s OCP stage, as it was observed in the OCP stage for 1800 s in Figure 9. The surface was quite uniform, and any possible impurities were removed during the applied -600 mV potential, given in Figure 10c. A clear white blemishing shade, normally, appeared in Figure 10b., was disappeared in Figure 10c. It was, in fact, an expected result because applied reduction potential removed the formed oxide layer along with any other impurities during hydrogen evolution. Moreover, nearly a perfectly uniform surface behavior at OCP before Tafel in Figure 10d emerged as a great improvement. If pre-applied potential-based Tafel analysis and Tafel analysis without pre-applied reduction potential are compared, it can be said that no other surface cleaning procedure, such as polishing, ultrasound cleaning, or alcohol cleaning, is effective as the in-situ surface cleaning procedure. In order to understand the effect of in-situ surface cleaning on the Tafel analysis, three repetitive experiments were performed in the given order in Figure 10, and it is presented in Figure 11.
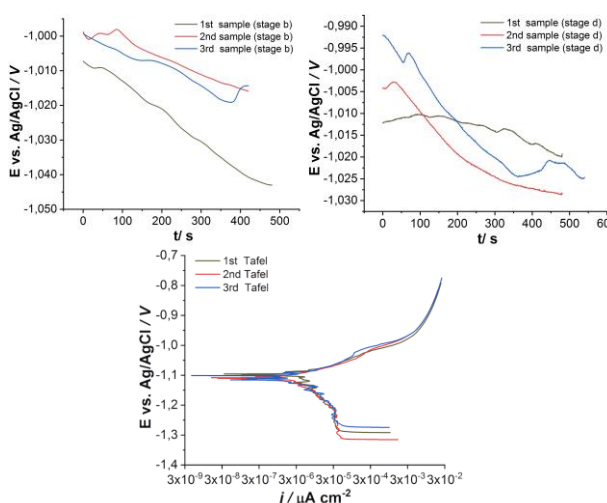


**Figure 11.** Three repetitive experiments at stage b and stage d for OCP, given in Figure 10, are presented with repetitive Tafel polarization curves.

Obtained curves are rather consistent when compared with the direct Tafel analysis in Figure 8. The calculated mean and standard deviation analysis in Table 2 shows a significant match between repetitive experiments.

**Table 3.** Tafel fitting elements for each sample are presented for performed repetitive experiments given in Figure 11.

| Samples | OCP/ mV | $E_{corr}$/ mV | $J_{corr}$/ μA cm$^{-2}$ | βa/ mV | βc/ mV |
|---|---|---|---|---|---|
| 1 st Tafel | -1027 | -1106 | 1.94 | 37.2 | 84 |
| 2 nd Tafel | -1025 | -1105 | 2.32 | 35.6 | 99 |
| 3 rd Tafel | -1020 | -1107 | 2.77 | 47 | 103 |
| Mean | -1024 | -1106 | 2.34 | 39.93 | 95.33 |
| Standard Dev. | 3.60 | 1 | 0.41 | 6.17 | 10.01 |

If each component of the pre-applied potential-based Tafel analysis given in Table 2 and the direct Tafel analysis given in Table 1 are compared, a slight deviation in each parameter is seen as contrary to Table 1. However, two of the most important kinetic parameters, $βa$, and $βc$, are consistent because providing similar results in $βa$ and $βc$ is normally difficult compared to the Ecorr and Jcorr values. Almost every experiment revealed identical results. As mentioned, the obtained consistent results likely emerge from equalizing the starting conditions of each surface in in-situ via applied moderate reduction potential. This way, a uniform oxidation process at the relaxed OCP state while reaching the steady state condition and during the potentiodynamic scan is provided.

## 4. CONCLUSIONS

The study questioned the deviation for Tafel corrosion analysis results of Zinc metal in various reports. Also, rarely applied in-situ surface cleaning potential before Tafel analysis was investigated in detail. This study has shown that pre-applied surface cleaning reduction potential before Tafel can improve the consistency and repeatability of the experiments. Macro surface investigation and EDS/XRD analysis prove that surface oxidation is initiated upon immersion and increases in time, and the oxidation of the surface does not proceed at the same rate through the surface. This non-uniform behavior is likely the result of surface impurities, such as air oxidation of the surface and other pre-existed impurities. However, after determining the correct cleaning potential via LSV and applying the determined potential prior to Tafel to clean the surface revealed remarkable results in terms of repeatability and consistency of the Tafel parameters. A few general trends can be written if the performed study is translated to other metals investigated for Tafel analysis.

- As the corrosion medium starts to change the surface with increasing immersion time, the optimum OCP period can be decided after a few consecutive OCP experiments, and the optimum time can be chosen as the shortest time, which is the closest time to the long OCP analysis.

21

- Prior to Tafel analysis, LSV analysis following the OCP analysis can be performed to detect the oxide removal potential and starting potential for hydrogen evolution.

- The sample can be applied in-situ reduction potential to remove the oxide layer and other uncounted impurities to obtain a standardized surface before Tafel analysis.

**Acknowledgement**

**REFERENCES**

[1] L.H. Jørgensen, M.D. Sørensen, M.M. Lauridsen, L. Rasmussen, R.M. Alfiler, V.N. Iversen, O.B. Schaffalitzky de Muckadell, Albumin-corrected Zn and available free Zn-binding capacity as indicators of Zn status–potential for clinical implementation, Scandinavian Journal of Clinical and Laboratory Investigation. 2022;82(4):261-266.

[2] Z. Huang, Z. Li, Y. Wang, J. Cong, X. Wu, X. Song, Y. Ma, H. Xiang, Y. Huang, Regulating Zn (002) Deposition toward Long Cycle Life for Zn Metal Batteries, ACS Energy Letters. 2022;8(1):372-380.

[3] M. Badrooj, F. Jamali-Sheini, N. Torabi, Zn-doped Pb/Sn hybrid perovskite solar cells: Towards high photovoltaic performance, Solar Energy. 2022;236:63-74.

[4] X. Xie, J. Zhao, O. Lin, Z. Yin, X. Li, Y. Zhang, A. Tang, Narrow-Bandwidth Blue-Emitting Ag–Ga–Zn–S Semiconductor Nanocrystals for Quantum-Dot Light-Emitting Diodes, The Journal of Physical Chemistry Letters. 2022;13:11857-11863.

[5] H. Jia, M. Wang, S. Luo, The corrosion behaviour of a novel Mg–Zn–Zr–Y–Cu alloy, Materials Science and Technology. 2023:1-8.

[6] W. Wu, G. Sun, Q. Wang, S. Lin, Preparation, Wear Resistance, and Corrosion Performance of Arc-Sprayed Zn, Al, and Zn-Al Coatings on Carbon Steel Substrates, Journal of Materials Engineering and Performance. 2023:1-14.

[7] S. Huang, W. Wu, G. Han, L. Wang, X. Mei, L. Qiao, Y. Yan, Revealing the corrosion product films of ion-implanted biodegradable Zn–Cu alloys, Corrosion Science. 2023;210:110814.

[8] R.E. Hammam, S.A. Abdel-Gawad, M.E. Moussa, M. Shoeib, S. El-Hadad, Study of Microstructure and Corrosion Behavior of Cast Zn–Al–Mg Alloys, International Journal of Metalcasting. 2023:1-14.

[9] K. Baldwin, C. Smith, Advances in replacements for cadmium plating in aerospace applications, Transactions of the IMF. 1996;74(6):202-209.

[10] A. El Fazazi, M. Ouakki, M. Cherkaoui, Electrochemical Deposition and Spectroscopy Investigation of Zn Coatings on Steel, Journal of Bio-and Tribo-Corrosion. 2021;7:1-22.

[11] L. Hao, G. Lv, Y. Zhou, K. Zhu, M. Dong, Y. Liu, D. Yu, High performance anti-corrosion coatings of poly (vinyl butyral) composites with poly n-(vinyl) pyrrole and carbon black nanoparticles, Materials. 2018;11(11):2307.

[12] H.M. Abd El-Lateef, E.-S. Abdel-Rahman, H.S. Mohran, Role of Ni content in improvement of corrosion resistance of Zn–Ni alloy in 3.5% NaCl solution. Part I: Polarization and impedance studies, Transactions of Nonferrous Metals Society of China. 2015;25(8):2807-2816.

[13] K. Vathsala, T.V. Venkatesha, Zn–ZrO2 nanocomposite coatings: elecrodeposition and evaluation of corrosion resistance, Applied Surface Science. 2011;257(21):8929-8936.

[14] M.M.K. Azar, H.S. Gugtapeh, M. Rezaei, Evaluation of corrosion protection performance of electroplated zinc and zinc-graphene oxide nanocomposite coatings in air saturated 3.5 wt.% NaCl solution, Colloids and Surfaces A: Physicochemical and Engineering Aspects. 2020;601:125051.

[15] S. Ganesan, G. Prabhu, B.N. Popov, Electrodeposition and characterization of Zn-Mn coatings for corrosion protection, Surface and Coatings Technology. 2014;238:143-151.

[16] J. Wang, Y. Qi, X. Zhao, Z. Zhang, Electrochemical investigation of corrosion behavior of epoxy modified silicate zinc-rich coatings in 3.5% NaCl solution, Coatings. 2020;10(5):444.

[17] M. Sudha, S. Surendhiran, V. Gowthambabu, A. Balamurugan, R. Anandarasu, Y.A. Syed Khadar, D. Vasudevan, Enhancement of Corrosive-Resistant Behavior of Zn and Mg Metal Plates Using Biosynthesized Nickel Oxide Nanoparticles, Journal of Bio- and Tribo-Corrosion. 2021;7(2):60.

[18] S. Ranganatha, T. Venkatesha, Fabrication and electrochemical characterization of Zn–halloysite nanotubes composite coatings, RSC Advances. 2014;4(59):31230-31238.

[19] A. Yavuz, P. Yilmaz Erdogan, H. Zengin, G. Zengin, Electrodeposition and Characterisation of Zn-Co Alloys from Ionic Liquids on Copper, Journal of Electronic Materials. 2022;51(9):5253-5261.

[20] F. Azizi, A. Kahoul, Electrodeposition and corrosion behaviour of Zn–Co coating produced from a sulphate bath, Transactions of the IMF. 2016;94(1):43-48.

[21] R. Kumar Swain, P. Upadhyay, A. Nag, A. Banerjee, A.N. Bhagat, A. Basu, A. Mallik, Electro-galvanization of zinc and zinc-nickel onto mild steel for improved corrosion resistance, Materials Today: Proceedings. 2022;62:6257-6264.

[22] K. Sai Jyotheender, M.K. Punith Kumar, C. Srivastava, Low temperature electrogalvanization: Texture and corrosion behavior, Applied Surface Science. 2021;559:149953.

[23] B.M.L. Koch, A. Amirfazli, J.A.W. Elliott, Wetting of Rough Surfaces by a Low Surface Tension Liquid, The Journal of Physical Chemistry C. 2014;118(41):23777-23782.

[24] V. Vinš, J. Hykl, J. Hrubý, Surface tension of seawater at low temperatures including supercooled region down to–25 C, Marine Chemistry. 2019;213:13-23.

[25] S.K. Behera, A. Kumar P, N. Dogra, M. Nosonovsky, P. Rohatgi, Effect of Microstructure on Contact Angle and Corrosion of Ductile Iron: Iron–Graphite Composite, Langmuir. 2019;35(49):16120-16129.

[26] B. Grigoryev, B. Nemzer, D. Kurumov, J. Sengers, Surface tension of normal pentane, hexane, heptane, and octane, International journal of thermophysics. 1992;13:453-464.

[27] H. Luo, H. Su, C. Dong, X. Li, Passivation and electrochemical behavior of 316L stainless steel in chlorinated simulated concrete pore solution, Applied Surface Science. 2017;400:38-48.

[28] Li, O.J. Swanson, G.S. Frankel, A.Y. Gerard, P. Lu, J.E. Saal, J.R. Scully, Localized corrosion behavior of a single-phase non-equimolar high entropy alloy, Electrochimica Acta. 2019;306:71-84.

[29] N. Elgrishi, K.J. Rountree, B.D. McCarthy, E.S. Rountree, T.T. Eisenhart, J.L. Dempsey, A Practical Beginner's Guide to Cyclic Voltammetry, Journal of Chemical Education. 2018;95(2):197-206.

[30] A.J. Bard, L.R. Faulkner, Fundamentals and applications, Electrochemical methods. 2001;2(482):580-632.

[31] J.-M. Savéant, Elements of molecular and biomolecular electrochemistry: an electrochemical approach to electron transfer chemistry, John Wiley & Sons2006.

[32] Y. Meng, L. Liu, D. Zhang, C. Dong, Y. Yan, A.A. Volinsky, L.-N. Wang, Initial formation of corrosion products on pure zinc in saline solution, Bioactive materials. 2019;4:87-96.

[33] Y.F. Cherneikina, Ruzil; Kulyasova, Olga; Mingo, Beatriz; Mukaeva, Veta; Parfenov, Evgeny; Yerokhin, Aleksey, Microstructure effects on corrosion behaviour of Mg-1Ca alloy in Ringer's solution, Mendeley_Data 2019;http://dx.doi.org/10.17632/ccrp8sc3sj.1

[34] J.D. Brassard, D.K. Sarkar, J. Perron, A. Audibert-Hayet, D. Melot, Nano-micro structured superhydrophobic zinc coating on steel for prevention of corrosion and ice adhesion, Journal of Colloid and Interface Science. 2014;447(1095-7103 (Electronic)):240-247.

[35] C. Xiang, Z.M. Zhang, H.M. Fu, E.H. Han, H.F. Zhang, J.Q. Wang, Microstructure and corrosion behavior of AlCoCrFeNiSi0.1 high-entropy alloy, Intermetallics. 2019;114:106599.

[36] H. Luo, Z. Li, A.M. Mingers, D. Raabe, Corrosion behavior of an equiatomic CoCrFeMnNi high-entropy alloy compared with 304 stainless steel in sulfuric acid solution, Corrosion Science. 2018;134:131-139.

[37] Z.B. Wang, H.X. Hu, Y.G. Zheng, Synergistic effects of fluoride and chloride on general corrosion behavior of AISI 316 stainless steel and pure titanium in H2SO4 solutions, Corrosion Science. 2018;130:203-217.

[38] Q. Ye, K. Feng, Z. Li, F. Lu, R. Li, J. Huang, Y. Wu, Microstructure and corrosion properties of CrMnFeCoNi high entropy alloy coating, Applied Surface Science. 2017;396:1420-1426.

[39] Z. Cui, L. Wang, H. Ni, W. Hao, C. Man, S. Chen, X. Wang, Z. Liu, X. Li, Influence of temperature on the electrochemical and passivation behavior of 2507 super duplex stainless steel in simulated desulfurized flue gas condensates, Corrosion Science. 2017;118:31-48.

[40] A. International, ASTM G59-97, Standard Test Method for Conducting Potentiodynamic Polarization Resistance Measurements, ASTM West Conshohocken, PA, 2014.

**Türk Doğa ve Fen Dergisi**
**Turkish Journal of Nature and Science**

BİNGÖL
ÜNİVERSİTESİ

# Effects of Silica Aerogel Produced From Boron Wastes To Compressive Strength And Thermal Performance Of Environmentally Friendly Bricks

**Arzu ÇAĞLAR[1*]** iD

[1] Kırsehir Ahi Evran University, Engineering-Architecture Faculty, Architecture Department, Kırsehir, Türkiye
Arzu ÇAĞLAR ORCID No: 0000-0003-3928-8059

*Corresponding author: arzu.caglar@ahievran.edu.tr*

**Abstract:** In this study, the aim is to inspect the effects of silica aerogel produced from boron waster to compressive strength and thermal performance of bricks. Firstly, silica aerogel was produced by using boron waste obtained from Türkiye/Eskişehir/Kırka region. After, silica aerogel produced was mixed into the brick in different proportions (%0 (REF), %15 (AB1), %25 (AB2), %35 (AB3), %45 (AB4)), and was baked in 900 °C and 1000 °C to create mixed brick samples. Finally, samples produced was experimented with compressive strength and thermal conductivity coefficient and SEM (Scanning Electron Microscopy) images were taken. As a result, the increase of aerogel amount caused decrease in compressive strength and thermal conductivity coefficient values in both temperatures. It was observed that amorphous structure increased with the increase of silica aerogel and partial holes and cracks emerged in SEM images. Additionally, when compressive strength was used as basis, it was determined that AB1 sample could be used as load bearing material, while AB2, AB3 and AB4 samples could be used as coating or back filling material in traditional structures. Use of wastes which contain silica such as boron waste in aerogel production is thought to be an appropriate solution for waste disposal.

# Bor Atıklarından Üretilen Silika Aerojelin Çevre Dostu Tuğlaların Basınç Dayanımına ve Isıl Performansına Etkileri

**Öz:** Bu çalışmada, bor atıklarından üretilen silika aerojelin tuğlanın basınç dayanımı ve ısıl performansına etkisinin incelenmesi amaçlanmıştır. Çalışma üç aşamada gerçekleştirilmiştir. İlk aşamada Türkiye/Eskişehir/Kırka bölgesinden temin edilen bor atığı kullanılarak silika aerojel üretimi yapılmıştır. İkinci aşamada, üretilen silika aerojel hacimce farklı oranlarda (%0 (REF), %15 (AB1), %25 (AB2), %35 (AB3), %45 (AB4)) tuğla bünyesine ikame edilmiş, 900 oC ve 1000 oC pişirilerek katkılı tuğla numuneleri üretilmiştir. Üçüncü ve son aşamada ise, üretilen numunelere basınç dayanımı ve ısı iletim katsayısı tayini deneyleri uygulanmıştır. Ayrıca numunelerin içyapısının incelenmesi amacıyla SEM görüntüleri alınmıştır. Sonuç olarak; her iki sıcaklıkta da aerojel miktarının artması ile basınç dayanımı ve ısı iletim katsayısı değerinde azalma meydana gelmiştir. SEM görüntülerinde silika aerojel miktarının artmasıyla amorf yapının arttığı ve yer yer boşluklar ve çatlaklar oluştuğu görülmüştür. Ayrıca basınç dayanımı baz alındığında; üretilen numunelerden AB1 numunesi taşıyıcı olarak kullanılabileceği, AB2, AB3 ve AB4 numunelerinin ise kaplama veya geleneksel yapılarda duvar dolgu malzemesi olarak kullanılabileceği tespit edilmiştir. Bor atığı gibi silis içeren atıkların aerojel üretiminde kullanılmaları atıkların bertaraf edilmesi için uygun bir çözüm yolu olacağı düşünülmektedir.

## 1. INTRODUCTION

Energy crisis, which encourage development of new materials aiming to establish thermal comfort for users and energy efficiency of buildings have been occurring more frequently around the world [1]. Energy demand has been increasing for the last thirty years with industrial improvement and increase of population [2]. The construction industry has been using 42% of the total consumed energy and 50% of the natural resources from earth [3].

A large part of the structures built in the construction sector consists of buildings. Energy consumption in

buildings has increased massively in the last ten years due to population growth, necessary interior quality, increase in time spent inside and demand for building functions etc. [4]. While buildings with building envelopes that have less thermal conduction achieve up to 80% energy saving and provide better living and working conditions to inhabitants and users [5]. Additionally, it could be beneficial to extend thermal comfort periods with-out relying on heating and cooling systems, especially during the period between seasons [6].

It has been stated in the literature that depending on the country, approximately 20%-40% of the total energy consumption and globally one in three of greenhouse gas emission consists of buildings [7]. Heat loss in the buildings generally occur through exterior walls, ceiling, floor, windows and air leak [8]. It is also known that building envelope is an important cause of energy loss in constructed area [9]. Generally, the biggest thermal losses related to buildings occur as heat conduction through opaque building envelope [10]. Since materials used in most building constructions have low isolation levels and high heat losses, decreasing energy consumption of buildings is one of the most important requirements [11]. The heat loss through exterior walls are generally recognized as between 10% and 45% [12]. The best way of ensuring energy saving is applying heat insulation to building or using materials with heat insulation features during construction. Brick is one of the construction materials consisting building envelope. Bricks are universal construction materials which have emerged independently in various cultures, evolved through ages and continued its existence through centuries. It is still widely popular around the globe and symbolizes characteristic atmosphere of many different places [9]. Increase of standards such as fire safety, sustainability, heat insulation features etc. has limited the use of traditional bricks as a construction component carrying weight. Today, bricks are used mostly as coating because of their aesthetic look, ease of use and low maintenance surfaces. But if their heat insulation properties improves, bricks will have the potential to be-come desired structural materials once again.

Bricks have been objected to improvement by mixing with various organic (rice husk ash, rice hull etc.) or industrial wastes (silica fume, fly ash, boron waste etc) [13-18, 79-81]. Recently, use of aerogel instead of these wastes gained popularity. The word aerogel consists of two words, air and gel, and contains of nanoparticles that are located in a three-dimensional network with a high porosity (containing 99-95% of the empty volume) [82]. Aerogel was discovered in 1931 [19-22]. Aerogel, which is produced by removing fluids from gels, is a dry gel with high porosity (more than 90%) [23] and less heat conductivity than air [19, 23, 24]. It has a transparent, highly porous, ultra lightweight, low density (bulk density 3-20 kg/m$^3$) and wide exterior surface area. Porous compound of nano material makes it hard for heat to pass through structure [19, 78].

It decreases high energy demand compared to other materials with same width because of its low heat conduction [26]: It is widely used in aerogels [27], spare

parts catalyzator support [28, 29], heat insulation [23], nanoparticle filtration from air [30-33], medicine delivery [34] and aviation industries [35].

The most used type of aerogels, which have different types, is silica aerogels [36]. Silica aerogel, which is a nano structured material is a unique construction material with high porosity, ultra-low density and highly cross-bound three dimensional webs, and consists of silica [37-38]. Silica aerogel consists of amorphous silica structure with air more than 90% and is considered as the most lightweight solid material of the world. Its porous structure enables it to breathe with the clean air passing through [5]. It also has the lowest thermal conduction (0.015 W m-1K-1) among all solid insulation materials on the world [39-40].

Research on silica aerogel, which has lower heat conduction [23-41] when compared to other materials produced through complicated and expensive procedures [23-41], has proved that it has higher potential for thermal and acoustic insulation. Adding silica aerogel into construction materials can decrease their thermal conductivity or k-value significantly and result in thermal performance which was not previously possible [5].

It was observed that aerogels are used intensely in cement [43-45], mortar [1, 46], coating [36,39,42,47-49,50,51], concrete [41,52-56], self-conpacting concrete [57] and light concrete production. But it was determined that aerogel is not used in brick production frequently. Based on this gap, silica aerogel was produced using boron wastes taken from Eskişehir /Kırka region for this study with the aim of mixing silica aerogel product into brick in different percentages and inspect compressive strength and thermal performance. SEM images were used to confirm compressive strength rest results and thermal properties.

## 2. MATERIAL AND METHOD

### 2.1. Material

Clay: Clay, which is the main raw material used in the production of brick building material and used in the study, was obtained from Taşköprü district of Kastamonu province. The mineralogy of the clay used is presented in Table 1.

It was observed that there is mostly element silicium (Si) found in blend brick clay examined in Kastamonu University Central Research Laboratory Implementation and Research Center. There were aliminium (Al) calcium (Ca), oxygen (O), iron (Fe) and magnesium (Mg) elements found in clay as well. Raw clay material was grounded in rotary squeezer into a 1mm undersize material before entering production. All additives were subjected to same procedures.

25

**Table 1.** Clay mineralogy

| Element | O | Mg | Al | Si | Nb | K | Ca | Fe | Others |
|---|---|---|---|---|---|---|---|---|---|
| Weight % | 22,53 | 1. 98 | 8. 74 | 42.12 | 5. 38 | 0. 94 | 15,41 | 6,83 | 36,07 |

**Table 2.** Chemical properties of boron waste

| Compound | $B_2O_3$ | CaO | MgO | SiO2 | Na2O | Al2O3 | Fe2O3 | K2O | Ignition Loss |
|---|---|---|---|---|---|---|---|---|---|
| Boron Waste, % | 25.5 | 10.20 | 14.28 | 13.60 | 5. 66 | 0. 98 | 0. 41 | 0. 78 | 28. 59 |

**Table 3.** Chemical Analysis of Seyitömer Fly Ash

| Compound | $SiO_2$ | CaO | MgO | $Fe_2O_3$ | $Al_2O_3$ | $Na_2O$ | $K_2O$ | $SO_3$ | $Na_2O$ (eq) | Free CaO |
|---|---|---|---|---|---|---|---|---|---|---|
| % | 52.23 | 7. 85 | 5. 92 | 9. 10 | 19.03 | 0. 92 | 1. 98 | 2. 52 | 2. 02 | 0. 27 |

Boron Waste: The boron waste used in the study is chemical properties are provided in Table 2. It was observed that it consists of 25.5% boron and silica 13,60 % after examination of the Table 2.

Fly Ash: Fly ash which was used in the study anc chemical compounds of which are provided on Table 3 was obtained from Seyitömer Thermal Power Plant. Type F fly ash with 0,88 $g/cm^3$ bulk density, 1,58 $g/cm^3$ specific weight, 0,115 $m^2$ /g specific surface area and 8,3 pH was used in the experiments.

Mixture water: Kastamonu province city water was used as the mixture water in sample production.

## 2.1. Medhod

### 2.1.1. Aerogel production from boron wastes

Sol-gel method was used in production of silica aerogel from boron waste (Figure 1). Production was carried out in three stages: preparation, aging and drying.
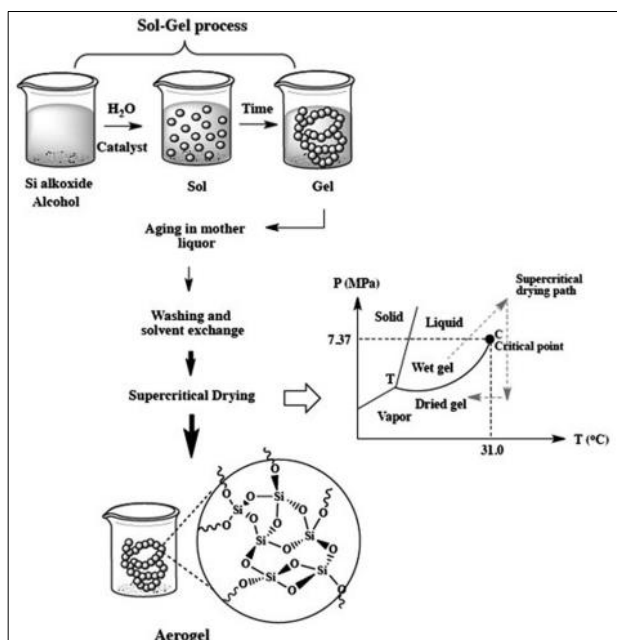


**Figure 1.** Schematic image of the sol-gel process which was used to prepare aerogels [77].

## Preparation of the gel

250 ml distilled water, 15 g KOH and 40 gr borax slime was put in 500 ml beaker. Mixed for 4 hour in mixing device with heater, with settings 150 °C, 5 cycles/mins.

After mixing, it was filtered using filter paper. Mixture that passed through filter paper was used in borosilicate aerogel.

## Aging the gel

pH value of the mixture that passed through the filter paper was determined. Since the solution was acidic, a mixture of 10 g NaOH and 250 ml distilled water was added slowly and mixed with a stick (Figure 2a) Solution was gelled when it became neutralized (pH:7) (Figure 2b) Mixture was closed with a plastic wrap for the aging process and waited for 4 weeks.

After 2 weeks, in order to rid of salt inside the gel, gel was washed with hot distilled water. Water on the gel was taken with a syringe and mixed again after adding hot dis-tilled water. After waiting for the gel to collapse after mixing, and water on the surface was taken once again. This process was repeated 3 times. Afterwards, beaker was wrapped with wrap once again and waited in 60 $^0$C drying oven for 24 hours. Gel phase filtered once again and mixed with 20% ethanol and 80% distilled water solution. Beaker was re-wrapped with wrap and waited in 60 $^0$C drying oven for 24 hours. This process was repeated two times. Afterwards, 100% ethanol was added and waited in 60 $^0$C drying oven for 24 hours. In order to get the desired chemical mixture of gel, after carrying out a filtering process, 70% Ethanol/TEOS was added and the mixture waited in 60 $^0$C drying oven for 24 hours. After filtering, it was kept inside 100& n-heptane for 24 hours.
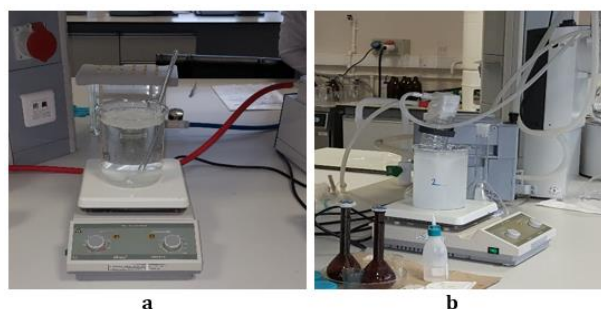
**Figure 2.** a: Before gelling, b: After gelling

**Drying the gel**

After filtering the solution, gel was closed and kept in room temperature for 24 hours. Afterwards it was subjected to drying process in 90 °C for 4 hours and 125 °C for 24 hours. Silica aerogel powder produces after the drying process was packaged using leak proof packs and stored to be used in brick production.

**2.2.2 Production of aerogel mixed brick**

Clay material which was obtained through quartation method was grounded in rotary squeezer into a 1mm undersize material before entering production. Fly ash, which was to be used as additive in experiment was also subjected to the same procedures. Fly ash was added into brick to increase its compressive strength [60]. Formula of the mixture is shown in Table 4. Mixing water was added in 20% of the total weight of the materials in samples to each mixtures. Within the scope of the experiment, a total of 12 samples, 6 for each experiment, were produced.

**Table 4.** Mixture formula

|        | Aerojel (%) | Fly Ash (%) | Clay (%) | Mixed Water (%) |
|--------|-------------|-------------|----------|-----------------|
| REF    | ---         | ---         | 100      | 20              |
| AB1    | 15          | 5           | 80       | 20              |
| AB2    | 25          | 5           | 70       | 20              |
| AB3    | 35          | 5           | 60       | 20              |
| AB4    | 45          | 5           | 50       | 20              |

During sample production, first, aerogel, fly ash and clay, which are dry materials, were mixed with a mixer with 200 rpm speed for 5 minutes. Then the bonding substance water was added and mixed for 10 minutes. After the mixing process, the mixture was pressed with 50 MPa pressure and 40 x 40 x 160 mm samples were produces. Samples waited 24 hours to easily detach from the mold. Afterwards, the samples were dried in drying oven with 105 °C for 24 hours. Dried samples, which are given in Figure 3 were baked progressively in electric oven which had 3°C/s heating feature with 900 °C and 1000 °C. In case of deviations, the six samples were produced for each series. The samples produced were experimented with compressive strength and solid thermal conductivity coefficient experiments.



**Figure 3.** Silica aerogel mixed brick samples

**2.2.3 Experiments on samples**

The compressive strength values of the aerogel mixed brick products were calculated in accordance with TS EN 771-1, (2012) [61] standard. Thermal conduction device was used to determine the heat conduction constant. Probes of the conduction device were contacted with sample surface, heat conduction value of which were to be determined, and constant was determined by measuring heat change of the material depending on the energy given. SEM images were taken to inspect internal structures of the samples.

## 3. RESULTS AND DISCUSSIONS

### 3.1 Compressive Strength

Compressive strength, which is the basis of all structural materials, is the best measurement method to determine the suitability of the material [60].

A material needs to have high compressive strength to be used in a structure. That is why one of the main aims of the studies is to improve compressive strength of the structural materials such as cement [62, 66], concrete [63], mortar, coating, brick [60] etc.

Aerogel is a material with low mechanic properties and high thermal conduction [64]. That is why, aerogel is used in heat insulation generally. In many studies, aerogel is reported to lower the compressive strength [65, 66, 42]. In this study, fly ash has been mixed in order to increase compressive strength.

Compressive strength values of aerogel mixed brick samples are displayed in Figure 4. It was observed that compressive strengths of samples change between 6,8-14,2 MPa in image. It was observed that in both temperatures the highest compressive strength be-longed to reference sample, and lowest compressive strength belonged to AB4 sample. According to TS EN 771-1, (2012), the average compressive strength value is 10 MPa. In this case, among silica aerogel mixed brick samples that baked in both temperatures, AB1 value was above average, and AB2, AB3 and AB4 values were below average. AB1 can be used in residence buildings and restoration works as holder brick, AB2, AB3 and AB4 can be used for coating and decoration purposes. Also, AB2, AB3 and AB4 samples can be used as filling material in traditional residence construction.

In this study, it was determined that compressive strength lowers with the increase of silica aerogel amount. In other words, changing natural aggregates with aerogel caused lower compressive strength. According to this, fragile nature and low resistance of aerogel aggregates as well as their low compound effects result in low mechanic resistance in construction material mixtures with aerogel materials. They effect mechanical properties of AB samples negatively because of their fragile structure as well.
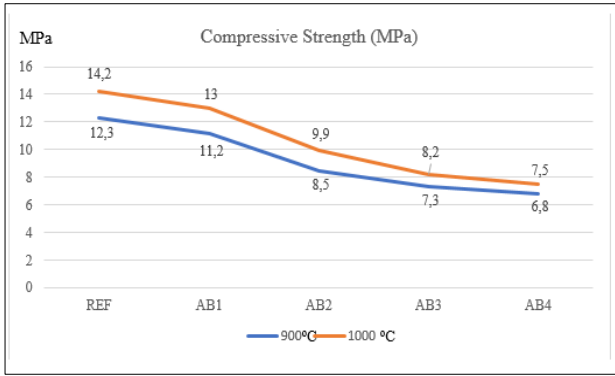
**Figure 4.** Compressive strength of samples



**Figure 5.** Heat conduction coefficient appointment of samples

Moreover, in Table 5, the ratios of decreasing compressive strength values as a result of aerogel substitution are given. It is seen that the highest decrease rate at 900 and 1000 ºC belongs to the AB4 sample with 47.18% and 44.71%, respectively. It is thought that the reason for this is that the aerogel additive creates a void in the brick sample. Studies on compressive strength of silica aerogel support our study [41, 45, 55-56].

**Table 5.** Value of Compressive strength and reduction rate

|  | 900 ºC | | 1000 ºC | |
| --- | --- | --- | --- | --- |
|  | Compressive Strength (MPa) | Reduction Rate (%) | Compressive Strength (MPa) | Reduction Rate (%) |
| REF | 14,2 | --- | 12,3 | --- |
| AB1 | 13,0 | 8,45 | 11,2 | 8,94 |
| AB2 | 9,9 | 30,28 | 8,5 | 30,90 |
| AB3 | 8,2 | 42,25 | 7,3 | 40,65 |
| AB4 | 7,5 | 47,18 | 6,8 | 44,71 |

## 3.2 Determination of Heat Conduction Coefficient

Aerogel is a porous material with low thermal conductivity because of its small pores. Thermal conductivity of aerogel mixed brick samples in different temperatures are displayed in Figure 5. It was determined that thermal conductivity coefficient of samples change between 0,52 and 1,7 W/mK. It was observed that thermal conductivity improved with increase of baking temperature. Among all samples, AT4 sample with baking temperature of 1000 ºC (0,52 w/mK) had the lowest, reference sample with baking temperature of 900 °C (1,07 W/mK) had the highest heat conduction coefficient. Additionally, higher aerogel in mixtures resulted in lower thermal conductivity. In other words, significant amount of air holes in aerogel pores isolate heat and result lower thermal conductivity in samples. Other studies in literature support data we acquired during our study. Silica aerogel addition was observed to improve thermal conductivity property of structural materials such as concrete, cement, coating etc. as well as brick [6,41,42,45,51,52, 56, 68-72].
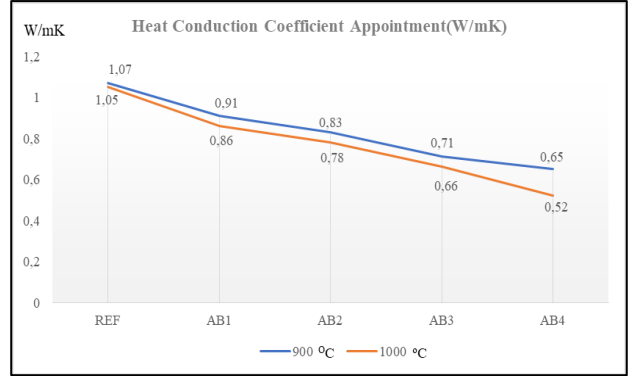
The decrease in the heat conductivity coefficients of the airgel-added brick samples at 900 and 1000 ºC is given in Table 6. The lowest heat transfer coefficient reduction rate was obtained from the AB4 sample at both temperatures. The reason for this is thought to be that the airgel creates a void in the brick, as in the compressive strength. These voids keep the heat within the brick.

**Table 6.** Heat conduction coefficient of samples and reduction rate

|  | 900 ºC | | 1000 ºC | |
| --- | --- | --- | --- | --- |
|  | Heat Conduction Coefficient (W/mK) | Reducttion Rate (%) | Heat Conduction Coefficient (W/mK) | Reducttion Rate (%) |
| REF | 1,07 | --- | 1,05 | --- |
| AB1 | 0,91 | 14,95 | 0,86 | 18,09 |
| AB2 | 0,83 | 22,42 | 0,78 | 25,71 |
| AB3 | 0,71 | 33,64 | 0,66 | 37,14 |
| AB4 | 0,65 | 39,25 | 0,52 | 50,47 |

## 3.3 SEM Images

Reference and SEM images of silica aerogel mixed brick samples are displayed in Figure 6. It was observed in Figure 6a belonging to reference sample that the amount of crystal structure was higher. This means that sample have high compressive strength. It is a proof that compressive strength test results of reference sample supports SEM images. SEM images of AB1 sample are displayed in Figure 6b. In image, reference sample with crystal structure had partially turned into amorphous structure with silica aerogel mixture. Amount of amorphous structure had increased in Figure 6c displaying SEM image of AB2 and became irregular. Fragile nature of amorphous structure and aerogel [41] lowered compressive strength of the sample. Decrease in compressive strength experiment values of AB2 sample supports SEM images. In Figure 6d (AB3), crystal structure had de-creased significantly and amorphous structure increased. Additionally, partial globule and cavitied structures were observed. In some areas, cracks were observed. In Image 6e (AB4) which had the highest amount of silica aerogel almost all crystal structures were gone and amount of amorphous and cavitied structure were increased. Water/air can be transferred or thicken with these cavities and thermal insulation and mechanical performance of brick can be affected. The fact that AB4 samples, which have the highest amount of silica aerogel have the lowest compressive strength and lowest heat conduction coefficient proves this fact. With the increase

of aerogel, which is a fragile material, surface cracks were increased as well.

Literature studies proved that aerogel makes construction materials more fragile [41-42, 73-76]. Research results prove that aerogel is a highly fragile material, it can be crushed easily and have cracks on its surface. It was also stated that cavitied structure de-crease compressive strength of brick and improved thermal properties.
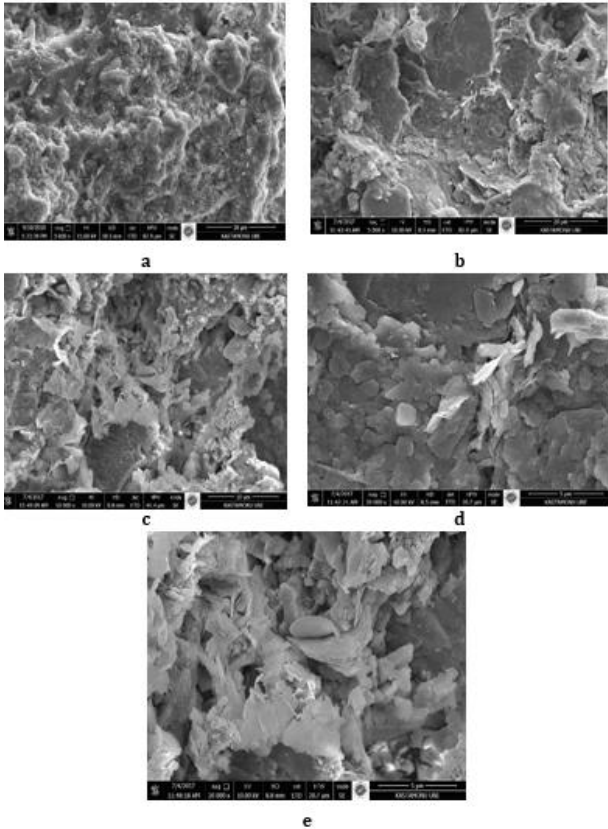


**Figure 6.** a: Reference sample, b: AB1 sample c: AB2 sample, d: AB3 sample, e: AB4 sample aerogel mixed brick samples

## 4. CONCLUSION

Energy crisis, In this study, aerogel was produced using boron waste and produced aerogel was mixed into prick in different ratios as additional material. According to the data obtained from experiments;

- Compressive strength decreased with the increasing amount of aerogel.
- AB1 sample had the highest compressive strength in both temperatures among mixed samples.
- Heat conduction coefficient value decreased with the increasing amount of aerogel. Lowest heat conduction coefficient belonged to AB4 sample with 0,52 W/mK.
- It was observed that with the increasing amount of aerogel, the crystal structure of the samples turned into amorphous structure and AB3 and AB4 samples developed gaps and cavities in SEM images of samples.
- Use of boron waste in aerogel production is an appropriate solution to dispose of wastes in environment. With boron waste, all wastes with

silica must be encouraged to be used during aerogel production.
- Studies in the future should not focus on academy, on the contrary, their aim should be determination of the properties of aerogel and application.

## REFERENCES

[1] Becker PFB, Effting C, Schackow A. Lightweight thermal insulating coating mortars with aerogel, EPS, and vermiculite for energy conservation in buildings. Cem. Conc. Comp. 2022; 125(2022): 104283.

[2] Calisesi M. Aerogel Incorporated Plasters and Mortars, The Case Study of Precast Panels; Degree Course: Build. Eng. and Arch.; University of Bologna: Bologna, Italy, 2017.

[3] Stephan A, Athanassi A. Towards a more circular construction sector: Estimating and spatialising current and future non-structural material replacement flows to maintain urban building stocks. Res., Conser. & Recy., 2018; 119: 248–262.

[4] Cao VD, Pilehvar S, Salas-Bringas C, Szczotok AM, Rodriguez JF, Carmona M, Al-Manasir N, Kjoniksen AL. Microencapsulated phase change materials for enhancing the thermal performance of Portland cement concrete and geopolymer concrete for passive building applications. Ener. Conv. and Man. 2017; 133: 56e66.

[5] Lu Y, Liu Z, Li X, Yin XJ, Utomo HD. Development of water-based thermal insulation paints using silica aerogel made from incineration bottom ash. Energy & Build. 2022; 259, (2022): 111866.

[6] Buratti C, Moretti E, Belloni E, Agosti F. Development of Innovative Aerogel Based Plasters: Preliminary Thermal and Acoustic Performance Evaluation. Sustainability; 2014(6): 5839-5852.

[7] Berardi U, Akos L. Thermal bridges of metal fasteners for aerogel-enhanced blankets. Ener. & Build. 2019; 185 (2019): 307-315.

[8] Elshazli MT, Mudaqiq M, Xing T, Ibrahim A, Engin BJS, Yuand J. Experimental study of using Aerogel insulation for residential buildings. Adv. in Build. Ener. Res. 2022; 16(5): 569-588.

[9] Ganobjaka M, Brunner S, Wernery J. Aerogel materials for heritage buildings: Materials, properties and case studies. J. Cult. Her. 2020; 42(2020): 81–98.

[10] Lucchi E, Becherini F, Tuccio, MCD, Troi A, Frick J, Roberti F, Hermann C, Fairnington I, Mezzasalma G, Pockele L, Bernardi, A. Thermal performance evaluation and comfort assessment of advanced aerogel as blown-in insulation for historic buildings. Build. Env. 2017; 122 (2017): 258-268.

[11] Aste N, Leonforte F, Manfren M, Mazzon M. Thermal inertia and energy efficiency - parametric simulation assessment on a calibrated case study, App. Ener. 2015; 145 (2015): 111–123.

[12] Walker R, Pavia S. Thermal Performance of a selection of insulation materials suitable for historic buildings. Build. Env. 2015; 94(2015): 155e165.

29

[13] Fernando S, Gunasekara C, Law DW, Nasvic MCM, Setunge S, Dissanayake R. Engineering properties of waste-based alkali activated concrete brick containing low calcium fly ash and rice husk ash: A comparison with traditional Portland cement concrete brick. J. Build. Eng. 2022; 46 (2022): 103810.

[14] Mahdi SN, Dushyanth V, Babu R, Hossiney N, Abdullah MMAB. Strength and durability properties of geopolymer paver blocks made with fly ash and brick kiln rice husk ash. Case Stud. Const. Mat. 2022; 16(2022): e00800.

[15] Soharu A, Naveen BP, Sil A. Fly ash bricks development using concrete waste debris and self-healing bacteria. J. Mat. Cyc. Waste Manag. 2022, 35(2022): 1-12.

[16] Debnatha, NK, Boga S, Singha A, Majhi MR, Singh VK. Fabrication of low to high duty fireclay refractory bricks from lignite fly ash. Ceram. Int. Avai. 2022, 48(9): 12152-12160.

[17] Suganya STD, Krishnaraj L, Nakkeeran G. Evaluation of failure mode analysis and strength behavior of fly ash brick masonry prisms, Sust. Const. Mat. 2022; 107–121.

[18] Araf T, Islam MS, Shipon MFA. Suitability of waste slag as partial replacement of fine aggregate in making sustainable brick. Prooceding of 3rd International conference on Research and Innovation in Civil Engineering, Prague. (2022). ISBN: 978-984—35-1935-1.

[19] Abu-Jdayil B, Mourad AH, Hittini W, Hassan M, Hameedi S. Traditional, state of the art and renewable thermal building insulation materials: An overview. Const. and Build. Mat., 2019; 214: 709–735.

[20] Fricke J. Tillotson, T. Aerogels: Production, characterization, and applications. Thin Sol. Films. 1997; 297(1–2): 212–223.

[21] Mahadik DB, Lee YK, Chavan NK, Mahadik SA, Park HH. Monolithic and shrinkage free hydrophobic silica aerogels via new rapid supercritical extraction process. J. Sup. Fluids, 2016; 107: 84–91.

[22] Joo P, Yao Y, Teo N, Jana SC. Modular aerogel brick fabrication via 3D-printed molds. Additive Manufacturing, 2021; 46(2021): 102059.

[23] Baetens R, Jelle BP, Gustavsen A. Aerogel insulation for building applications: a state-of-the-art review. Ene. Build.. 2011; 43(4): 761e769.

[24] Jelle BP. Traditional, state-of-the-art and future thermal building insulation materials and solutions – Properties, requirements and possibilities. In Ener. Build., 2011; 43 (10): 2549-2563.

[25] Berardi U. Aerogel-enhanced systems for building energy retrofits: Insights from a case study, Ene. Build. 2018; 159(2018): 370-381.

[26] Ibrahim M, Biwole PH, Wurtz E, Achard, P. A study on the thermal performance of exterior walls covered with a recently patented silica-aerogel-based insulating coating. Building Environment, 2014; 81 (2014): 112-122.

[27] Riffat SB, Qiu G. A review of state-of-the-art aerogel applications in buildings. Int. J. of Low - Carbon Tech., 2013; 8 (2013): 1–6.

[28] Guilminot E, Fischer F, Chatenet M, Rigacci A, Berthon-Fabry S, Achard P, Chainet, E. Use of cellulose-based carbon aerogels as catalyst support for PEM fuel cell electrodes: electrochemical characterization. J. of Pow. Sour., 2007; 166(2007): 104–111.

[29] Rotter H, Landau MV, Carrera M, Goldfarb D, Herskowitz M. High surface area chromia aerogel efficient catalyst and catalyst support for ethylacetate combustion. App. Catal. B: Envir. 2004; 47 (2004): 111–126 (4).

[30] Kim SJ, Chase G, Jana SC. Polymer aerogels for efficient removal of airborne nanoparticles. Sep. Purif. Tech. 2015; 156 (2015): 803–808.

[31] Kim SJ, Chase G, Jana SC. The role of mesopores in achieving high efficiency airborne nanoparticle filtration using aerogel monoliths. Separation and Purification Technology, 2016: 166 (2016); 48–54.

[32] Kim SJ, Raut P, Chase G, Jana SC. Electrostatically active polymer hybrid aerogels for airborne nanoparticle filtration, ACS App. Mat. & Inter.. 2017; 9 (2017): 6401–6410.

[33] Zhai C, Jana SC. Tuning porous networks in polyimide aerogels for airborne nanoparticle filtration, ACS App. Mat. & Inter. 2017; 9 (2017): 30074–30082.

[34] García-Gonzalez CA, Alnaief M, Smirnova I. Polysaccharide-based aerogelspromising biodegradable carriers for drug delivery systems. Carboh. Poly. 2011; 86 (2011): 1425–1438.

[35] Randall JP, Meador MAP, Jana SC. Tailoring mechanical properties of aerogels for aerospace applications. ACS App. Mat. & Inter. 2011; 3(2011): 613–626.

[36] Stahl T, Wakili KG, Heiduk E. Stability Relevant Properties of an SiO2 Aerogel-Based Rendering and Its Application on Buildings. Sustain. 2021; 13: 10035.

[37] Stojanovic A, Zhao S, Angelica E, Malfait WJ, Koebel MM. Three routes to superinsulating silica aerogel powder. J. Sol-Gel Sci. and Tech. 2021; 90, 57–66.

[38] Ng S, Jelle BP, Stæhli T. Calcined clays as binder for thermal insulating and structural aerogel incorporated mortar. Cem. Conc. Comp. 2016; 72(2016): 213–221.

[39] Curto DD, Cinieri V. Aerogel-Based plasters and energy efficiency of historic buildings. Literature Review and Guidelines for Manufacturing Specimens Destined for Thermal Tests. Sustain. 2020; 12, 9457.

[40] Koebel M, Rigacci A, Achard P. Aerogel-based thermal superinsulation: an overview. J. Sol-Gel Sci. and Tech. 63(2012), 315e339.

[41] Gao T, Jelle BP, Gustavsen A, Jacobsen S. Aerogel - incorporated concrete: an experimental study. Const. and Build. Mat. 2014; 52(2014): 130–136.

[42] Westgate P. Paine K, Ball RJ. Physical and mechanical properties of plasters incorporating aerogel granules and polypropylene monofilament

fibres. Const. and Build. Mat., 2018; 158(2018): 472–480.

[43] Peter AEK, Balasubramanian M, Jayakumar AA, Mukilan P, Aishwarya S. A Partial Replacement of Cement Using Extract Powder Form of Silica Aerogel. Sustain. Const. Mat. 2022; Conference paper, 61–73.

[44] Shah SN, Mo KH, Yap SP, Radwan MKH. Effect of micro-sized silica aerogel on the properties of lightweight cement composite. Const. and Build. Mat., 2021; 290 (2021), 123229.

[45] Rostami J, Khandel O, Sedighardekani R, Sahneh AR, Ghahari SA. Enhanced workability, durability, and thermal properties of cement based composites with aerogel and paraffin coated recycled aggregates. J. Clean. Prod. 2021; 297 (2021), 126518.

[46] Karim AN, Pär J, Angela SK. Knowledge gaps regarding the hygrothermal and long-term performance of aerogel-based coating mortars, Const. Build. Mat. 2022; 314, Part A, 125602: 1-19.

[47] Maia J, Pedroso M, Ramos NMM, Pereira PF, Flores-Colen I, Glória Gomes M, Silva L. Hygrothermal Performance Of A New Thermal Aerogel-Based Render Under Distinct Climatic Conditions. Ener. & Build. 2021; 243(2021), 111001; 1-18.

[48] Karim AN. Aerogel-Based Plasters For Renovation Of Buildings İn Sweden. Thesıs For The Degree Of Lıcentıate Of Engıneerıng, Chalmers Teknoloji Üniversitesi, Gothenburg, Sweden. 2021.

[49] Sebdani ZM, Stefan HB, Kirill S, Wim H, Malfait J. A Review On Silica Aerogel-Based Materials For Acoustic Applications. Journal of Non-Crystalline Solids. 2021; 562 (2021) 120770: 1-15.

[50] Berardi U. Aerogel-enhanced systems for building energy retrofits: insights from a case study. Ener. and Build.. 2018; 159, (2018): 370-381.

[51] Fantucci S, Fenoglio E, Grosso G, Serra V, Perino M, Marino V, Dutto M. Development of an aerogel-based thermal coating for the energy retrofit and the prevention of condensation risk in existing buildings. Sci. and Tech. for the Built Env. 2019; 25 (9): 1178–1186.

[52] Ng, S., Jelle BP, Sandberg LIC, Gao T, Wallevik OH. Experimental investigations of aerogel-incorporated ultra-high performance concrete. Const. and Build. Mat.. 2015; 77 (2015): 307–316.

[53] Welsch T, Held MS, Milow B. High performance aerogel concrete. Proc. 12th Conference on Advanced Building Skins, Bern 2017, 591-9.

[54] Tsioulou Q, Ayegbusi J, Lampropoulos A. Experimental investigation on thermal conductivity and mechanical properties of a novel Aerogel concrete. High Tech Concrete: Where Technology and Engineering Meet, 2017: 125-131.

[55] Welsch T, Held MS, Milow B. High performance aerogel concrete. Proc. 12th Conference on Advanced Building Skins, Bern 2017, 591-599.

[56] Wang L, Liu P, Jing Q, Liu Y, Wanga W, Zhanga Y, Li Z. Strength properties and thermal conductivity of concrete with the addition of expanded perlite filled

with aerogel. Const. and Build. Mat. 2018; 188(2018): 447-457.

[57] Adhikarya SK., Rudžionis Z, Tučkutė S. Characterization of novel lightweight self-compacting cement composites with incorporated expanded glass, aerogel, zeolite and fly ash. Case Stud. in Const. Mat. 2022; 16(2022), e00879:1-11.

[58] Çağlar H, Çağlar A Research of Physical and Mechanical Properties of Blended Bricks with Fly Ash Based, Blast Furnace Slag Addition. Int. J. Res. –Granth.. 2019; 7(1): 126-136.

[59] Çağlar A, Korkmaz SZ, Demirel B, Çağlar H. Use Of Boron Wastes As An Additive in Blend Bricks. Research & Reviews In Architecture, Plannıng And Design Gece Kitaplığı, 5-14, 2019.

[60] Kumar A, Kumar R, Das V, Jhatial AA, Ali TH. Assessing the structural efficiency and durability of burnt clay bricks incorporating fly ash and silica fume as additives. Const. and Build. Mat. 2021; 310(2021), 125233: 1-17.

[61] TS EN 772-1, (2012). Masonry units - Test methods - Part 1: Determination of compressive strength, Turkish Standards, Ankara.

[62] Bahari A, Sadeghi-Nik A, Shaikh FUA, Sadeghi-Nik A, Prada EC, Mirshafiei E, Roodbar M. Experimental studies on rheological, mechanical, and microstructure properties of self-compacting concrete containing perovskite nanomaterial”, Struct. Conc. (2021A) suco.202000548.

[63] Bahari A, Sadeghi-Nik A, Cerro-Prada E, Roodbari M, Zhuge Y. One-step random-walk process of nanoparticles in cement-based materials”, J. of Cent. South Uni. 2021B; 28 (6) (2021B): 1679–1691.

[64] Adhikary SK, Rudžionis Z, Tučkutė Z, Ashish DK. Efects of carbon nanotubes on expanded glass and silica aerogel based lightweight concrete. Sci. Rep.. 2021; 11(2104): 1-11.

[65] Adhikary SK, Rudžionis Z, Vaičiukynienė D. Development of flowable ultra - lightweight concrete using expanded glass aggregate, silica aerogel, and prefabricated plastic bubbles. J. Build. Eng. 2020; 31, 101399: 1-20.

[66] Shah SN, Mo KH, Yap SP, Radwan MKH. Effect of micro-sized silica aerogel on the properties of lightweight cement composite. Construction and Building Materials. 2021; 290(2021), 123229, 1-15.

[67] Jia G, Li Z, Liu P, Jing Q. Applications of aerogel in cement-based thermal insulation materials: an overview. Mag. of Conc. Res. 2018; 70(16): 822-837.

[68] Li P, Wu H, Liu Y, Yang J, Fang Z, Lin B. Preparation and optimization of ultra-light and thermal insulative aerogel foam concrete. Const. and Build. Mat. 2019; 205(2019): 529-542.

[69] Zhang H, Yang J, Wu H, Fu P, Liu Y, Yang W. Dynamic thermal performance of ultra-light and thermal-insulative aerogelfoamed concrete for building energy efficiency. Solar Ener. 2020; 204(2020), 569-576.

[70] Kim S, Seo J, Cha J, Kim S. Chemical retreating for gel - typed aerogel and insulation performance of cement containing aerogel. Const. and Build. Mat. 2013, 40 (2013), 501 505.

[71] Shafi S, Tian J, Navik R, Gai Y, Ding X, Zhao Y. Fume silica improves the insulating and mechanical performance of silica aerogel/glass fiber composite. J. of Sup. Fluids, 2019; 148: 9–15.

[72] Júlio MF, Soares A, Ilharco LM, Colen IF, Brito J. Aerogel-based renders with lightweight aggregates: Correlation betweenmolecular/pore structure and performance. Const. and Build. Mat. 2016; 124(2016): 485-495.

[73] Bostancı L, Sola ÖÇ. Mechanical Properties and Thermal Conductivity of Aerogel-Incorporated Alkali-Activated Slag Mortars. Adv. in Civ. Eng. 2018; Article ID 4156248: 1-9.

[74] Zhu P, Brunner S, Zhao S, Griffa M, Leemann A, Toropovs N, Malekos A, Koebel MM, Lura, P. Study of physical properties and microstructure of aerogel-cement mortars for improving the fire safety of high-performance concrete linings in tunnels. Cem. and Conc. Comp. 2019; (104), 103414: 1-14.

[75] Zhang H, Yang J, Wu H, Fu P, Liu Y, Yang W. Dynamic thermal performance of ultra-light and thermal-insulative aerogelfoamed concrete for building energy efficiency. Solar Ene.. 2020; 204(2020): 569-576.

[76] Lu X, Wang P, Buttner D, Heinemann U, Nilsson O, Kuhn J, Fricke J. Thermal transport in opacified monolithic silica aerogels, High Temp.-High Pres. 1991, 23 (4), 431-436.

[77] Alyne Lamy-Mendes A, Pontinha ADR, Alves P, Santos P, Durães L. Progress in silica aerogel-containing materials for buildings thermal insulation", Construction and Building Materials. 2021; 286(2021), 122815: 1-13.

[78] Aldakshe A., Çağlar H, Çağlar A, Avan A. The Investigation of Use as Aggregate in Lightweight Concrete Production of Boron Wastes, Civil Engineering Journal, 2020; 6(7): 1328-1335.

[79] Çimen S, Çağlar H, Çağlar A, Can Ö. Effect of Boron Wastes on the Engineering Properties of Perlite Based Brick. Turkish J. of Nat. Sci. 2020; 9(2): 50-56.

[80] Çağlar H, Çağlar A, Korkmaz SZ, Demirel B, Bayraktar O.Y. Comparison Of The Physical And Mechanical Properties Of Manually Manufactured And Factory Production Blended Bricks Used In Build Of Traditional Kastamonu Houses. Fırat Univ. J. Eng. Sci. 2018; 30(2), 39-48.

[81] Çağlar H. Investigation of the Effect of Fly Ash and Boron Waste Additive on Brick Structure Material. Turkish Journal of Nature and Science; 2021; 10(1): 137-143.

[82] Massoudinejad M, Hashempour Y, Mohammadi H. Evaluation of Carbon Aerogel Manufacturing Process in Order to Desalination of Saline and Brackish Water in Laboratory Scale, Civil Engineering Journal. 2018; 4(1): 212-220.

[83] Kwan I, Mapstone J. Visibility aids for pedestrians and cyclists: a systematic review of randomised controlled trials. Accid Anal Prev. 2004;36(3):305-12.

[84] Carlson BM. Human embryology and developmental biology. 4th ed. St. Louis: Mosby; 2009.

[85] Nørvåg K. Space-efficient support for temporal text indexing in a document archive context. 7th European Conference, ECDL 2003. Berlin: Springer; 2003. p. 511-22.

[86] Hasund IK. The discourse markers like in English and liksom in Norwegian teenage language : A corpus-based, cross-linguistic study [dissertation]. Bergen: University of Bergen; 2003.

[87] Kapperud G. Utbruddsveil [Internet]. I Folkehelseins; 2016 [cited 2016 Jun 30]. Available from:
https://www.fhi.no/nettpub/utbruddsveilederen/

32

**Türk Doğa ve Fen Dergisi**
**Turkish Journal of Nature and Science**
www.dergipark.gov.tr/tdfd

# Determination of Some Quality Parameters of Filtered Blossom Honey Obtained from Bingöl and Its Districts

## Buket ARICI[1*] ID, İsa GÖKÇE[2] ID

[1] Bingöl University, Central Laboratory Application and Research Center, Bingöl, Türkiye
[2] Tokat Gaziosmanpaşa University, Pharmacy Faculty, Department of Biochemistry, Bingöl, Türkiye
Buket ARICI ORCID No: 0000-0003-2570-0524
İsa GÖKÇE ORCID No: 0000-0002-5023-9947

*Corresponding author: barici@bingol.edu.tr*

**Keywords**
Bingöl,
Moisture,
Free acidity,
Electrical
conductivity,
pH,
Color

**Abstract:** The most well-known bee products are honey, pollen and propolis. The most consumed bee product is honey among these. It is of great importance to investigate and follow the physicochemical properties of honey in terms of food safety. Therefore, it was aimed to determine some quality parameters for filtered blossom honey harvested from the center and 7 districts of Bingöl Province in 2021. The moisture, free acidity, electrical conductivity, pH and color parameters of the supplied filtered blossom honey samples were investigated. The average values of 22 honey samples collected from the center and districts of Bingöl were determined as; humidity $15.43\pm0.06$, free acidity $14.584\pm0.427$ meq kg$^{-1}$, electrical conductivity $0.228\pm0.001$ (mS cm$^{-1}$), pH $3.48\pm0.015$ and color parameters L*, a*, b* values $58.404\pm0.275$, $3.906\pm0.033$, $38.552$, respectively. According to these results, it was observed that the investigated filtered blossom honeys were within the limit values specified in the Turkish Food Codex Honey Communiqué.

# Bingöl ve İlçelerinden Elde Edilen Süzme Çiçek Ballarının Bazı Kalite Parametrelerinin Belirlenmesi

**Anahtar Kelimeler**
Bingöl,
Nem,
Serbest
asitlik,
Elektriksel
iletkenlik,
pH,
Renk

**Öz:** Arıcılık ürünleri arasında en bilinen arı ürünleri bal, polen ve propolistir. Bunlar arasında en fazla tüketilen arı ürünü ise baldır. Gıda güvenliği açısından balda fizikokimyasal özelliklerin incelenmesi ve takip edilmesi büyük önem taşımaktadır. Bu bağlamda, Bingöl İli merkez ve 7 ilçesinden 2021 yılında hasat edilen süzme çiçek balları için bazı kalite parametrelerinin belirlenmesi amaçlanmıştır. Temin edilen süzme çiçek bal örneklerinin nem, serbest asitlik, elektriksel iletkenlik, pH ve renk parametreleri incelenmiştir. Bingöl merkez ve ilçelerinden toplanan 22 adet bal örneğinin ortalama değerleri; nem $15.43\pm0.06$, serbest asitlik $14.584\pm0.427$ meq kg$^{-1}$, elektriksel iletkenlik $0.228\pm0.001$ (mS cm$^{-1}$), pH $3.48\pm0.015$ ve renk parametreleri L*, a*, b* değerleri sırasıyla $58.404\pm0.275$, $3.906\pm0.033$, $38.552\pm0.217$ olarak belirlenmiştir. Bu sonuçlara göre incelenen süzme çiçek ballarının Türk Gıda Kodeksi Bal Tebliği'nde belirtilen sınır değerler içerisinde olduğu görülmüştür.

## 1. INTRODUCTION

In addition to honey, honeybees (*Apis mellifera* L.) can also produce beeswax, royal jelly, bee pollen, propolis, and bee bread. Even while ancient civilizations have been aware of the medical benefits of these substances for thousands of years, they are mostly employed as dietary supplements or health products today. However, these natural products are great sources of macro- and micronutrients known as bioactive compounds, which work synergistically to provide these by products

numerous biological actions, such as, for example, antibacterial, antioxidant, and anti-inflammatory qualities [1-3].

In the Turkish Food Codex (TGK) Honey Communique No. 2020/7, honey is defined as "plant nectars, the secretions of living parts of plants or the secretions of plant-sucking insects living on the living parts of plants, after being collected by the honey bee, combine with their own specific substances, reducing the water content, matured by storing in honeycomb and a natural

product that can be crystallized according to its nature [4].

Bingöl province, which is located in the Iran-Turan flora region, is a very suitable region for beekeeping activities with its rich flora, differences in flowering times, clean nature and climatic conditions. According to Türkiye Statistical Institute (TURKSTAT) 2022 data, Bingöl has 1033 beekeeping enterprises, 2043 old-style beehives and 158.966 new-type beehives, in total 161.009 beehives. In 2022, 1.488.937 tons of honey was produced from 161.009 beehives. Bingöl province ranks 20th in Türkiye's honey ranking [5].

In the present study, moisture, free acidity, electrical conductivity, pH and color parameters were determined in strained blossom honey samples. Humidity is a parameter that affects the color, taste, aroma, solubility and specific gravity of honey, as well as its physical properties such as viscosity, crystallization, and the shelf life of honey [6]. The high moisture content in honey allows for crystallization and the development of osmotolerant (resistant to high sugar concentration) yeasts. When osmotolerant yeasts use the sugar in the environment, ethyl alcohol and carbon dioxide are released, which causes the honey to ferment. Alcohol formed as a result of fermentation transforms into acetic acid and water in the presence of oxygen and creates a sour taste in honey [7]. According to the Turkish Food Codex Honey Communiqué (2020/7) and the European Union Honey Directive, the moisture content of honey should not be more than 20% in blossom honey, secretory honey, blossom and secretory honey mixtures, 23% in puree (Calluna vulgaris), heather (Erica spp), and bakery honeys and 25% in heather based bakery honeys. The electrical conductivity of honey is a method used both to determine the botanical origin of honey and to distinguish between floral and secretory honeys. The electrical conductivity of secretory honey is higher than blossom honey [8,9]. The electrical conductivity value varies in proportion to the mineral content of honey [10].

One of the quality parameters of honey is free acidity. Free acidity creates the aroma of honey and increases the antioxidant activity of honey. It also gives information about the origin of honey. Acetic acid, butyric acid, formic acid, gluconic acid, lactic acid, malic acid, citric acid, succinic acid and oxalic acid are the acids found in honey [11]. According to the Turkish Food Codex Honey Communiqué (2020/7), the free acidity value in honey should not be more than 50 meq kg$^{-1}$ in blossom honey, secretory honey, blossom honey and secretory honey mixture and 80 meq kg$^{-1}$ in bakery honey.

The pH value affects the enzymatic activity, microorganism growth, shelf life, stability and texture of honey [12]. The pH value of honey is determined by the amount of mineral substances and organic acids in its content. The pH values of honeys rich in mineral substances are mostly high [13]. There is no regulation in the Turkish Food Codex Honey Communiqué on the pH value of honey.

In addition to taste and aroma, color which is one of the quality standards of honey, it is a parameter used to determine the origin of honey [14]. According to clause 5/d of the Turkish Food Codex Honey Communiqué (2020/7), there is the phrase "The color of honey can vary from water white to dark amber".

With this study, the determination of the quality parameters of the honey obtained from the center and districts of Bingöl and its compliance with the standard were investigated. For this purpose, moisture, free acidity, pH, electrical conductivity and color parameters of 22 filtered blossom honey samples produced in the center and seven districts of Bingöl in 2021 were determined and their compliance with the standard was investigated.

## 2. MATERIAL AND METHOD

Bingöl, which is located in the Upper Euphrates section of the Eastern Anatolia Region, is at an altitude of 1151 m from the sea, and is located between 41°-20' and 39°-56' east longitudes and 39°-31' and 36°-28' north latitudes. Bingöl province has 7 districts in total, namely Yedisu, Genç, Karlıova, Yayladere, Solhan, Kiğı and Adaklı. In 2021, 22 honey samples were obtained from 8 different regions of Bingöl province. After the honey samples were coded, they were stored in glass jars at room temperature, dry, out of direct light, until analysis. Honey samples were homogenized before each analysis.

### 2.1. Determination of the Moisture

Abbe type refractometer was used for moisture analysis of honey samples. This method, which uses the refractive index, was proposed by Bogdanov [15]. Firstly, 1 g of the honey samples, which were mixed thoroughly with the help of glass baguette and became homogeneous, was weighed. The weighed honey samples were evenly spread on the prism section of the refractometer and the moisture content of the honey was measured by the ruler on the lens part. The measurements were repeated three times for each honey.

### 2.2. Determination of the Electrical Conductivity

For the measurement of the conductivity of the honey samples, taking into account the moisture value of each honey, honey containing 20 g of dry matter was weighed into 50 mL falcon tubes and dissolved in some ultrapure water. Each of the dissolved honeys was taken into 100 mL balloon joe and the solution volume was completed to 100 mL with ultrapure water. The ambient temperature was set to 20 °C and the solutions were transferred to 40 mL beakers. The measurement of the solutions was recorded with the Consort Brand C3010 model conductor, which was calibrated [15].

### 2.3. Determination of the pH

After calibration of Thermo Scientific brand ORION 3 STAR model pH meter with buffer solutions (pH:4.01, pH:7.00 and pH:10.01), the electrode of the pH meter

was immersed in honey samples dissolved in ultrapure water and the pH values of the samples were read [15].

## 2.4. Determination of the Free Acidity

10 g of honey from each honey sample was weighed in 250 mL beakers and thoroughly dissolved with 75 mL ultrapure water using a magnetic stirrer. 5 drops of phenolphthalein were added to the dissolved honey samples and while the electrode of the pH meter remained in the solution and stirring with the magnetic stirrer, the samples were titrated within 60 seconds with 0.05 N NaOH solution poured in a controlled manner from the burette until the color change turned pink (pH=8.3). The amount of solution used in the titration was recorded and calculations were made with the help of the following equation [15].

$$SA = \frac{50.a}{m} \qquad (1)$$

In the equation, SA is the amount of free acidity (meq kg-1), $\alpha$ is the amount of used NaOH solution (mL), and m is the amount of measured honey sample (g).

## 2.5. Determination of the Color

Before the analysis process, honey samples were kept in a water bath set at 50°C for 30 minutes [16]. Honey samples taken from the water bath were mixed for 3 minutes until homogeneity was achieved. Honey samples taken from the water bath were mixed for 3 minutes until provided homogeneity. Then, the samples were taken into 4 mL spectrophotometer cuvettes for color analysis and measured in a Konica Minolta, CR-5 model colorimeter device. Thus, L*, a* and b* color parameters of honey samples were determined. Then, Hue angle (h°) was calculated by using a* and b* parameters in Equation 2.

$$h° = tan^{-1}\left(b*/a*\right) \qquad (2)$$

L, darkness/lightness (0: darkness; 100: lightness); a (-a, greenness; +a, redness); and b (-b, blueness; +b, yellowness) values are defined. Experiments were repeated three times and the results were averaged.

## 3. RESULTS AND DISCUSSION

In the present study, quality standards were determined by investigating the moisture, electrical conductivity, free acidity, pH and color parameters of 22 filtered blossom honey harvested in 2021 from the center and seven districts of Bingöl province. The experimental results of humidity are presented in Table 1 and Figure 1. The maximum relative standard deviation of the humidity parameter was determined as 1.61%. As can be seen from Table 1 and Figure 1, coded as A2 and KA2 honey samples have the lowest moisture content with a value of 14.00%, while the coded as LAV honey sample has the highest moisture content with a value of 16.93%. There is 21% difference between the lowest and highest humidity levels. Since the maximum amount of moisture

that can be found in blossom honeys is 20% according to the Turkish Food Codex Honey Communiqué (2020/7), it has been observed that investigated all honey samples comply with this Communiqué.
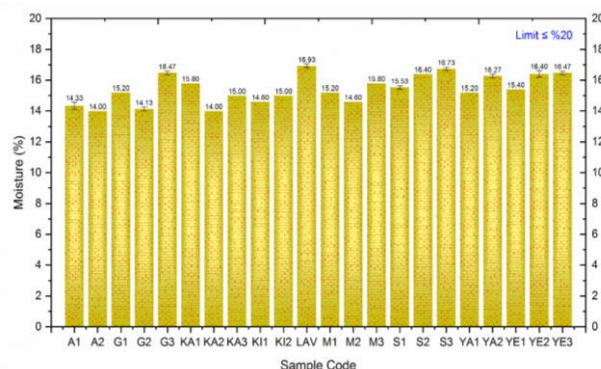


**Figure 1.** The graph for moisture results of the investigated honey samples

**Table 1**. The moisture, electrical conductivity, pH and free acidity results of the investigated honey samples

| Sample Code | Moisture (%) | Electrical Conductivity (mS cm-1) | pH | Free Acidity (meq kg-1) |
|---|---|---|---|---|
| A1 | 14.33±0.23 | 0.178± 0.001 | 3.43±0.009 | 12.161±0.286 |
| A2 | 14.00±0.00 | 0.495± 0.003 | 4.17±0.029 | 20.825±0.767 |
| G1 | 15.20±0.00 | 0.195± 0.001 | 3.38±0.016 | 14.326±0.766 |
| G2 | 14.13±0.12 | 0.162± 0.001 | 3.43±0.056 | 11.163±1.041 |
| G3 | 16.47±0.12 | 0.216± 0.001 | 3.27±0.012 | 16.491±0.500 |
| KA1 | 15.80±0.00 | 0.137± 0.001 | 3.43±0.009 | 7.496±0.499 |
| KA2 | 14.00±0.00 | 0.385± 0.002 | 3.61±0.009 | 22.322±0.283 |
| KA3 | 15.00±0.00 | 0.249± 0.001 | 3.29±0.005 | 17.157±0.287 |
| KI1 | 14.60±0.00 | 0.226± 0.001 | 3.34±0.009 | 16.991±0.004 |
| KI2 | 15.00±0.00 | 0.267± 0.001 | 3.58±0.019 | 14.658±0.288 |
| LAV | 16.93±0.12 | 0.199± 0.001 | 3.29±0.025 | 14.493±0.499 |
| M1 | 15.20±0.00 | 0.263± 0.002 | 3.39±0.012 | 18.323±0.580 |
| M2 | 14.60±0.00 | 0.196± 0.001 | 3.26±0.009 | 14.659±0.288 |
| M3 | 15.80±0.00 | 0.329± 0.004 | 3.57±0.005 | 19.324±0.285 |
| S1 | 15.53±0.12 | 0.165± 0.001 | 3.38±0.008 | 11.328±0.287 |
| S2 | 16.40±0.00 | 0.196± 0.001 | 3.43±0.012 | 14.159±0.288 |
| S3 | 16.73±0.12 | 0.184± 0.001 | 3.31±0.012 | 13.658±0.287 |
| YA1 | 15.20±0.00 | 0.175± 0.001 | 3.39±0.008 | 12.328±0.287 |
| YA2 | 16.27±0.12 | 0.188± 0.001 | 3.69±0.005 | 10.495±0.501 |
| YE1 | 15.40±0.00 | 0.222± 0.001 | 3.57±0.009 | 13.164±0.290 |
| YE2 | 16.40±0.20 | 0.216± 0.001 | 3.44±0.016 | 13.327±0.574 |
| YE3 | 16.47±0.12 | 0.180± 0.001 | 3.42±0.024 | 11.995±0.499 |

Zaitoun et al. [17] found the highest moisture value of 16.78% in their study on Jordan honey, and Sopade et al. [18] found the highest moisture value of 18% in their study on Australian honey, while the lowest moisture value was found to be 15.8%. Escriche et al. [19] found

the moisture value was the lowest 16.63% and the highest 23.3% in Mozambique honey; Çiftçi [20] found the moisture content in the range of 15.48-17.63%; Kalafat Kul [21] reported that the humidity values are in the range of 15.6%-20.3%. In previous studies, moisture values for blossom honey in Bingöl province were determined as 15.70% [22], 15.39% [23], and 15.43% [24]. Considering the results of these studies, it is seen that there is a general agreement between the moisture content of the honey samples in the present study and the studies in the literature.

Another investigated quality parameter is the electrical conductivity of honey. The experimental results of this parameter are presented comparatively in Table 1 and Figure 2. It was determined that the relative standard deviation in the electrical conductivity results of the investigated honey samples was between 0.37% and 1.22%. The average electrical conductivity of the investigated 22 filtered blossom honeys was determined as 0.228 mS cm$^{-1}$. Among the honey samples, it was determined that the coded as A2 sample had the highest electrical conductivity with value of 0.495 mS cm$^{-1}$ and the coded as KA1 sample had the lowest electrical conductivity with value of 0.137 mS cm$^{-1}$. There is a 261% difference between the lowest and highest electrical conductivity values. Since the electrical conductivity of blossom honey is reported to be maximum 0.8 mS cm$^{-1}$ according to the Turkish Food Codex Honey Communiqué, it has been observed that all the studied honey samples are in compliance with this Communiqué.
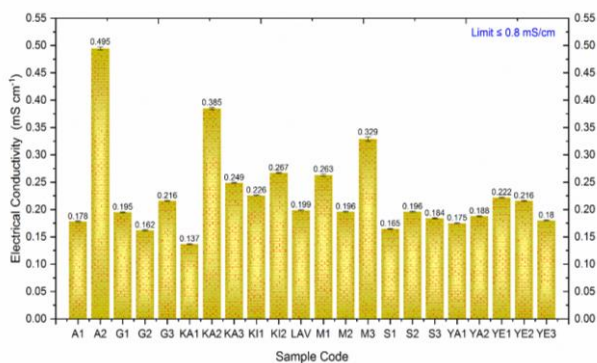


**Figure 2.** The graph for electrical conductivity results of the investigated honey samples

It has been reported that the electrical conductivity value for 46 secretion and nectar honeys obtained from different regions of Madrid, the capital of Spain, is between 0.119 -1.515 mS cm$^{-1}$[25]. Again, in a study on monofloral honeys in Spain, it was reported that the electrical conductivity values for honeys ranged from 0.30-0.99 mS cm$^{-1}$[26]. In 50 honey samples produced and offered for sale in Türkiye, the electrical conductivity value was 0.14-0.95 mS cm$^{-1}$[27]; In the study conducted on blossom honey obtained from Eastern Anatolia and Eastern Black Sea regions, the electrical conductivity values were recorded to be between 0.18 mS cm$^{-1}$ and 0.47 mS cm$^{-1}$[28]. In the study on the physicochemical properties of different honeys, the electrical conductivity values for blossom

honeys were found to be in the range of 0.11-0.89 mS cm$^{-1}$[29]. Simsek et al. [22] found the electrical conductivity values of 2 different honey samples belonging to the province of Bingöl as 0.19 mS cm$^{-1}$ and 0.35 mS cm$^{-1}$. Since the electrical conductivity values of the investigated blossom honeys in the present study vary in the range of 0.137 to 0.495 mS cm$^{-1}$, it can be said that the electrical conductivity of these honey samples is generally compatible with the electrical conductivity of other honeys in the literature.

Free acidity, which is related to the aroma and antioxidant activity of honey, is another investigated parameter. The experimental results of this parameter are presented in Table 1 and Figure 3, and the maximum relative standard deviation of this parameter was determined as 9.33%. It was determined that the average free acidity value of the investigated honey samples was 14.584 meq kg$^{-1}$. It was observed that the free acidity values of the coded as A2 and KA2 samples were the highest, while the coded as KA1 sample had the lowest free acidity values. The highest free acid value was determined to be approximately 3 times greater than the lowest. When Table 1 and Figure 3 are examined, it is obvious that all studied honey samples are in compliance with the Turkish Food Codex Honey Communiqué (2020/7).
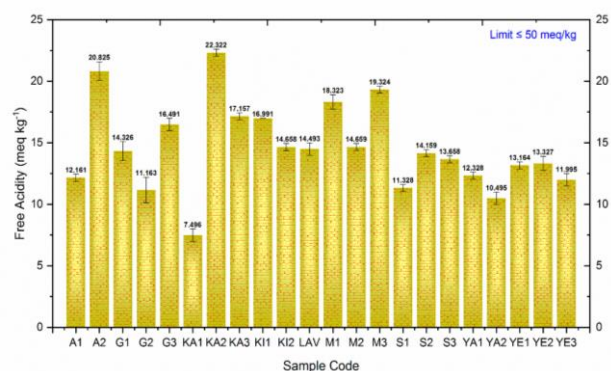


**Figure 3.** The graph for free acidity results of the investigated honey samples

In the study conducted in Eastern and Southeastern Anatolia, the average free acidity value of honey samples was 22.3 meq kg$^{-1}$[30], the average free acidity value in the honey obtained in Argentina was 20.6 meq kg$^{-1}$[31], the acidity value of highland honey in a study conducted in Hatay region was 32.3 meq kg$^{-1}$[32], the acidity value in sunflower honey from Tekirdağ region was 30.75 meq kg-1[33] and in a study conducted on Brazilian honeys, free acidity values have been reported to vary between 24.66-59.66 meq kg$^{-1}$ [34]. In studies conducted in Madrid, the free acidity value of blossom and secretory honeys was between 13.1-51.2 meq kg$^{-1}$[25] and in a study conducted in Tunisia with honeys of different origins, the free acidity values were reported between 8.15 meq kg$^{-1}$ and 27.77 meq kg$^{-1}$[35]. Ünal and Küplülü [36] reported the free acidity values were 8.23-33.21 meq kg$^{-1}$ for some honey samples, Finola et al. [31] obtained the average free acidity value as 2.6 meq kg$^{-1}$ for some Argentina honeys. Aydın et al. [37] was reported that the acidity level was between 6-24 meq kg$^{-1}$

for filtered honey offered for consumption in Kars province. Yaşar and Söğütlü [38] determined the average free acidity was determined as 10.675 meq kg$^{-1}$ for 8 blossom honeys in Bingöl and its districts. It has been observed that there is a parallelism between the free acidity values of the honey samples in the present study and those in the literature.

The pH indicator, which generally varies according to the minerals and organic acids in honey, is another determined parameter. The experimental results of the pH parameter are presented in Table 1 and Figure 4. The maximum relative standard deviation of this parameter was determined as 1.63%. While the average pH values of 22 investigated blossom honeys were determined as 3.48, it was observed that the pH value of the coded as A2 sample was the highest (4.17) and the pH value of the coded as M2 sample was the lowest (3.26). It was determined that there was difference of approximately 28% between the lowest and highest pH values.
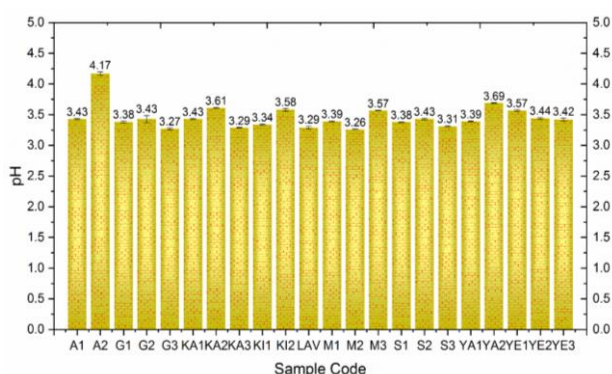


**Figure 4.** The graph for pH results of the investigated honey samples

pH values in the studies has been reported as; the average pH value is 3.8 in honeys in the Eastern and Southeastern Anatolia regions [30], 3.33-6.30 for Pakistan honey [39], 3.62-5.46 for Indian honeys [16], 3.65 for Brazilian honey [40]. It has been reported that the pH value is in the range of 3.63-5.01 [25] for honeys from Madrid, and in the range of 3.7-4.5 [41] for highland honey from the Ordu region. The pH values of blossom honey produced in Argentina are between 3.00 and 3.88 [42] and pH values were found to be in the range of 3.37−3.89 for Hatay region of blossom honey, [43]. The average pH value for 200 honey samples from Türkiye was reported as 3.30 [44] and the average pH value for 7 honey samples in Bingöl was reported as 2.81 [24]. When the literature studies are examined, the pH values for the honey samples of the present study are similar to those in the literature.

The last parameter that determines honey quality in the present study is color. The color of honey can be affected by the vitamins it contains, the total ash amount, the plant flora from which the nectar is taken, the application of heat treatment, the storage period, the harvest method, and the amount of phenolic substances [45]. L*, a*, b* and h° parameters were obtained to determine the colors of the investigated honey samples in the present study. Experimental results of these parameters are presented in Table 2 and Figure 5.

**Table 2.** L*, a*, b* and h° values for the investigated honey samples

| Sample Code | L* | a* | b* | h° |
|---|---|---|---|---|
| A1 | 60.02±0.32 | 3.27±0.01 | 36.57±0.14 | 84.89±0.002 |
| A2 | 63.96±0.15 | 10.90±0.03 | 61.94±0.09 | 80.02±0.001 |
| G1 | 75.58±0.21 | 3.01±0.03 | 44.21±0.09 | 86.11±0.009 |
| G2 | 66.94±0.18 | 1.92±0.02 | 31.21±0.03 | 86.49±0.010 |
| G3 | 78.76±0.26 | 2.69±0.03 | 46.50±0.23 | 86.69±0.011 |
| KA1 | 37.99±0.17 | 0.63±0.03 | 15.55±0.17 | 87.67±0.149 |
| KA2 | 35.24±0.06 | 8.27±0.05 | 41.14±0.06 | 78.63±0.003 |
| KA3 | 46.14±0.24 | 5.76±0.02 | 42.94±0.39 | 82.35±0.008 |
| KI1 | 28.85±0.15 | 4.56±0.07 | 29.58±0.05 | 81.24±0.021 |
| KI2 | 32.95±0.13 | 2.49±0.05 | 27.55±0.08 | 84.84±0.029 |
| LAV | 70.14±0.03 | 4.08±0.01 | 37.86±0.02 | 83.85±0.001 |
| M1 | 65.46±0.12 | 7.10±0.03 | 58.08±0.37 | 83.03±0.004 |
| M2 | 63.58±0.71 | 2.93±0.02 | 37.75±0.31 | 85.56±0.008 |
| M3 | 59.00±1.02 | 9.58±0.19 | 54.54±1.46 | 80.04±0.089 |
| S1 | 48.84±0.40 | 0.19±0.02 | 21.33±0.01 | 89.50±0.599 |
| S2 | 61.45±0.08 | 1.50±0.02 | 34.95±0.22 | 87.54±0.013 |
| S3 | 69.69±0.11 | 2.57±0.01 | 39.88±0.06 | 86.32±0.001 |
| YA1 | 52.54±0.23 | 3.04±0.01 | 31.80±0.20 | 84.55±0.003 |
| YA2 | 74.58±0.11 | 1.64±0.02 | 37.08±0.03 | 87.46±0.008 |
| YE1 | 54.46±0.27 | 3.93±0.06 | 37.18±0.12 | 83.97±0.018 |
| YE2 | 65.64±0.93 | 3.00±0.03 | 38.93±0.56 | 85.59±0.027 |
| YE3 | 73.07±0.17 | 2.88±0.02 | 41.55±0.12 | 86.04±0.004 |

Evaluation of the obtained results of L*, a*, b* and h° parameters can be done with the help of Figure 6. The maximum relative standard deviations of L*, a*, b* and h° parameters were determined as 1.74%, 8.18%, 2.67% and 0.67%, respectively. As seen in Table 2 and Figure 5, L*, a*, b* and h° values vary between 78.76-28.85, 10.90-0.19, 61.94-15.55 and 89.50-78.63, respectively. The sample coded as G3 has the highest L* value, sample coded as A2 has a* and b* values, the sample coded as KI1 has the lowest L* value, sample coded as S1 has a* value and sample coded as KA1 has b* value. When the L*, a*, b* and h° values are examined by considering Figure 6, it can be said that the studied honey samples have generally extra light amber color.
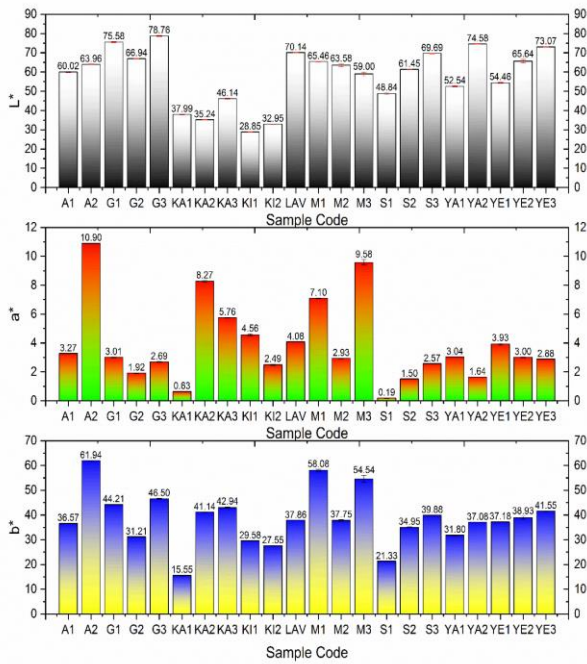
**Figure 5.** The graph for L*, a* and b* results of the investigated honey samples
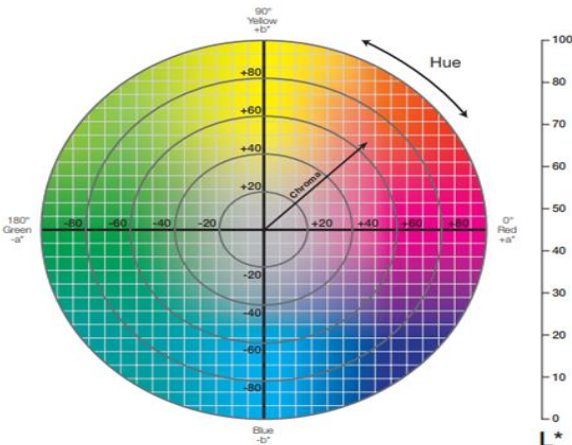


**Figure 6.** Color space notations [46]

In the study on Aegean Region honeys, the color values were found as L* 7.03-39.26; a* 1.23-13.32 and b* 2.34-17.27 [47]; in the color analysis for 80 honeys obtained from different regions in Brazil, it was determined that the L* value was between 43.02-81.21, a* value was between 2.91-63.40, and b* value was between 25.44-43.47 [48]. For the Mediterranean, Aegean, Southeastern Anatolia and Central Anatolia regions of Türkiye, it was reported that the L* values of the honey samples were between 24.56-41.21, a* values were between 0.11-1.00 and b* values were between 0.87-9.84 [49]. In another study, it was determined that the L* value was between as 19.75-28.00, a* value was between as -0.56 and 0.07 and b* value was between as 0.45-2.85 for blossom honey obtained from various regions of Türkiye [50]. When the studies in the literature are examined, the honey samples in the study present in terms of L* and b* parameters are generally similar to the honey samples from Brazil and the honey samples from the Aegean region in terms of a* parameter.

# 4. CONCLUSION

The moisture, electrical conductivity, free acidity, pH and color parameters of filtered blossom honey collected from the center and seven districts of Bingöl province were determined and their quality was revealed. While the humidity parameter was observed in the lowest samples coded as A2 and KA2, the highest sample coded as LAV, the highest electrical conductivity was observed in the A2 coded sample and the lowest KA1 coded sample. The highest free acidity value was observed in the A2 and KA2 coded samples, the lowest in the KA1 coded sample, while the highest pH value was observed in the A2 coded sample and the lowest in the M2 coded sample. When the L*, a*, b* and h° parameters of the investigated honey samples are taken into consideration, it was determined that they generally have an extra light amber color.

According to the analyzed parameters, 22 honey samples collected from the center and districts of Bingöl were found to be in compliance with the Turkish Food Codex Honey Communiqué (2020/7). There is no standard set in pH analysis, but the results found are in line with previous studies. Honey is extremely important because it is a healthy food and contributes to the country's economy. Therefore, in order to produce quality honey that supports the country's economy, the determined standards should not be ignored. In order to increase the quality and production capacity of Bingöl honey, whose place and recognition in the international market are increasing day by day, it is necessary to increase the awareness of producers and consumers in line with the findings of such studies.

# REFERENCES

[1] Ayna A, Tunc A, Özbolat SN, Bengü AŞ, Aykutoğlu G, Canli D, et al. Anticancer, and antioxidant activities of royal jelly on HT-29 colon cancer cells and melissopalynological analysis. Turkish Journal of Botany. 2021;45(8), 809-19.

[2] Bengü AŞ, Ayna A, Özbolat S, Tunc A, Aykutoğlu G, Çiftci M, et al. Content and antimicrobial activities of bingol royal jelly. Türk Tarım ve Doğa Bilimleri Dergisi. 2020;7(2), 480-6.

[3] Ayna A, Darendelioğlu E. Evaluation of the biological activities of royal jelly on prostate and breast cancer cells. Türk Doğa ve Fen Dergisi. 2022;11(3), 166-70.

[4] Anonim, 2020. Türk Gıda Kodeksi Bal Tebliği, Tarım ve Orman Bakanlığı, Ankara, 2020/7.

[5] TÜİK [Internet]. Türkiye İstatistik Kurumu; 2023 [cited 2023 Jun 23]. Available from: https://www.tuik.gov.tr/

38

[6] Mutlu C, Erbaş M, Tontul SA. Bal ve diğer arı ürünlerinin bazı özellikleri ve insan sağlığı üzerine etkileri. Akademik Gıda. 2017;15(1);75-83.

[7] Snowdon JA, Cliver DO. Microorganisms in honey.Int JFood Microbiol.1996; 31(1-3): 1-26.

[8] Marghitaş LA, Dezmirean D, Popescu O, Maghear O, Moise A, Bobiş O. Correlation between ash content and electrical conductivity in honeydew honey from Romania. In1st World Honeydew Honey Symposium, Tzarevo, Bulgaria 2008 (Vol. 30).

[9] Bogdanov S, Vit P, Kilchenmann V. Sugar profiles and conductivity of stingless bee honeys from Venezuela. Apidologie. 1996;27(6):445-50.

[10] Andrade P, Ferreres F, Gil MI, Tomás-Barberán FA. Determination of phenolic compounds in honeys with different floral origin by capillary zone electrophoresis. Food Chem. 1997;60(1):79-84.

[11] Ötleş S. Bal ve bal teknolojisi (kimyası ve analizleri) Alaşehir Meslek Yüksekokulu Yayınları. Manisa, Yayın. 1995(2).

[12] Gomes S, Dias LG, Moreira LL, Rodrigues P, Estevinho L. Physicochemical, microbiological and antimicrobial properties of commercial honeys from Portugal. Food ChemToxicol. 2010;48(2):544-8.

[13] Lawless HT, Horne J, Giasi P. Astringency of organic acids is related to pH. ChemSenses. 1996;21(4):397-403.

[14] González-Miret ML, Ayala F, Terrab A, Echávarri JF, Negueruela AI, Heredia FJ. Simplified method for calculating colour of honey by application of the characteristic vector method. Food Res Int. 2007;40(8):1080-6.

[15] Bogdanov S, Martin P, Lullmann C. Harmonised methods of the international honey commission. Swiss Bee Research Centre, FAM, Liebefeld. 2002;5:1-62.

[16] Anupama D, Bhat KK, Sapna VK. Sensory and physico-chemical properties of commercial samples of honey. Food Res Int. 2003;36(2):183-91.

[17] Zaitoun S, Ghzawi AA, Al-Malah KI, Abu-Jdayil B. Rheological properties of selected light colored Jordanian honey. Int J Food Proper. 2001;4(1):139-48.

[18] Sopade PA, Halley P, Bhandari B, D'arcy B, Doebler C, Caffin N. Application of the Williams–Landel–Ferry model to the viscosity–temperature relationship of Australian honeys. J Food Eng. 2003;56(1):67-75.

[19] Escriche I, Tanleque-Alberto F, Visquert M, Oroian M. Physicochemical and rheological characterization of honey from Mozambique. LWT-Food Sci Technol. 2017;86:108-15.

[20] Çiftçi M, Parlat SS. Konya Bölgesindeki arketlerde satılan farklı ticari çiçek ballarının bazı kimyasal özelliklerinin Türk Gıda Kodeksi-Bal Tebliğine uygunluğunun Araştırılması. Selcuk J Agr Food Sci. 2018;32(1):38-42.

[21] Kalafat Kul M. Gümüşhane yöresi çiçek ballarının kalite özellikleri ve antioksidan aktiviteleri [dissertation]. Gümüşhane: Gümüşhane University; 2020.

[22] Simsek A, Bilsel M, Goren AC. 13C/12C pattern of honey from Turkey and determination of adulteration in commercially available honey samples using EA-IRMS. Food Chem. 2012;130(4):1115-21.

[23] Bengü AŞ, Kutlu MA. Bingöl'de üretilen ballarda bazi kalite kriterlerinin belirlenmesi. Türk Doğa ve Fen Derg. 2018;7(1):7-10.

[24] Yılmaz AT, Yaşar S. Chemical investigations on honey produced in Bingol and surroundings. Uludağ Arıcılık Derg. 2020;20(1):72-80.

[25] Soria AC, González M, De Lorenzo C, Martınez-Castro I, Sanz J. Characterization of artisanal honeys from Madrid (Central Spain) on the basis of their melissopalynological, physicochemical and volatile composition data. Food Chem. 2004;85(1):121-30.

[26] Manzanares AB, García ZH, Galdón BR, Rodríguez ER, Romero CD. Physicochemical characteristics of minor monofloral honeys from Tenerife, Spain. LWT-Food SciTechnol. 2014;55(2):572-8.

[27] Çetin K, Alkın E, Uçurum HÖ. Piyasada satılan çiçek ballarının kalite kriterlerinin belirlenmesi. Gıda ve Yem Bilimi-Teknolojisi Derg. 2011;11:49-56.

[28] Batu A, Küçük E, Çimen M. Doğu Anadolu ve Doğu Karadeniz Bölgeleri çiçek ballarının fizikokimyasal ve biyokimyasal değerlerinin belirlenmesi. Gıda Teknolojileri Elektronik Derg. 2013;8(1):52-62.

[29] Yıldız İ. Çam, pamuk, yayla ve ayçiçeği ballarinin fizikokimyasal özelliklerinin belirlenmesi. Uludağ Arıcılık Derg. 2016;16(1):12-9.

[30] Yılmaz H, Küfrevioğlu İ. Composition of honeys collected from eastern and south-eastern anatolia and effect of storage on hydroxymethylfurfural content and diastase activity. Turk J Agr For. 2001;25(5):347-9.

[31] Finola MS, Lasagno MC, Marioli JM. Microbiological and chemical characterization of honeys from central Argentina. Food Chem. 2007;100(4):1649-53.

[32] Şahinler N, Şahinler S, Gül A. Hatay yöresi ballarının bileşimi ve biyokimyasal analizi. MKÜ Ziraat Fak Derg. 2001;6:93-108.

[33] Yardibi MF. Tekirdağ yöresinde üretilen ayçiçeği ballarının bazı kimyasal özelliklerinin belirlenmesi [dissertation]. Tekirdağ: Namık Kemal University;2008.

[34] Silva TM, Dos Santos FP, Evangelista-Rodrigues A, Da Silva EM, Da Silva GS, De Novais JS, et al. Phenolic compounds, melissopalynological, physicochemical analysis and antioxidant activity of jandaíra (Melipona subnitida) honey. J Food ComposAnal. 2013;29(1):10-8.

[35] Boussaid A, Chouaibi M, Rezig L, Missaoui R, Donsì F, Ferrari G, Hamdi S. Physicochemical, rheological, and thermal properties of six types of honey from various floral origins in Tunisia. Int J Food Proper. 2015;18(12):2624-37.

39

[36] Cenk ÜN, Küplülü Ö. Chemical quality of strained honey consumed in Ankara. Ankara Üniv Vet Fak Derg. 2006;53(1):1-4.

[37] Aydın BD, Sezer Ç, Oral NB. Kars' ta satışa sunulan süzme balların kalite niteliklerinin araştırılması. Kafkas Ünv Vet Fak Derg. 2008;14(1):89-94.

[38] Yaşar S, Söğütlü İ. Investigation of Acidity, Diastase Number, HMF, Insoluble Dry Matter and Ash Percentage Values of Some Honey Samples Produced in Bingöl and Districts. Van Vet J. 2020;31(1):42-5.

[39] Kamal A, Raza S, Rashid N, Hameed T, Gilani M, Qureshi MA, et al. Comparative study of honey collected from different flora of Pakistan. Online JB Sci. 2002;2:626-7.

[40] Da C Azeredo L, Azeredo MA, De Souza SR, Dutra VM. Protein contents and physicochemical properties in honey samples of Apis mellifera of different floral origins. Food Chem. 2003;80(2):249-54.

[41] Günbey VS, Günbey B, Güney F, Yılmaz Ö. Ordu ili bal üreticilerinden elde edilen balların biyokimyasal yapısının incelenmesi. Arıcılık Araştırma Derg. 2010;2(4):20-3.

[42] Acquarone C, Buera P, Elizalde B. Pattern of pH and electrical conductivity upon honey dilution as a complementary tool for discriminating geographical origin of honeys. Food Chem. 2007;101(2):695-703.

[43] Yücel Y, Sultanoglu P. Characterization of honeys from Hatay Region by their physicochemical properties combined with chemometrics. Food Biosci. 2013;1:16-25.

[44] Gül A. Türkiye'de üretilen bazı balların yapısal özelliklerinin gıda güvenliği bakımından araştırılması [dissertation]. Hatay: Mustafa Kemal Üniversitesi University; 2008.

[45] Sorkun K, Yılmaz B, Özkırım A, Özkök A, Gençay Ö, Bölükbaşı DN. Yaşam için arılar. Türkiye Arı Yetiştiricileri Merkez Birliği Yayın. 2012(5).

[46] URL-1 [Internet]. 2023 [cited 2023 Jun 23]. Available from:https://leventkirca.com.tr/hue-acisi-nedir-excelde-hue-acisi-nasil-hesaplanir

[47] Kaplan HB. Ege Bölgesi Ballarının Kimyasal Özellikleri [dissertation]. Denizli: Pamukkale University; 2014.

[48] Ribeiro RD, Mársico ET, Da Silva Carneiro C, Monteiro ML, Júnior CA, Mano S, et al. Classification of Brazilian honeys by physical and chemical analytical methods and low field nuclear magnetic resonance (LF 1H NMR). LWT-Food Sci Technol. 2014;55(1):90-5.

[49] Ölmez Ç. Türkiye'de üretilen farklı çiçek ve salgı bal çeşitlerinin bazı kalitatif ve besinsel özellikleri [dissertation]. Konya: Selçuk University; 2009.

[50] Durmaz NE. Çiçek Ballarının Fenolik Bileşik ve Aroma Bileşenleri Üzerine Araştırma [dissertation]. Ankara: Ankara University; 2020.

Türk Doğa ve Fen Dergisi
**Turkish Journal of Nature and Science**

www.dergipark.gov.tr/tdfd

# Evaluation of Glucose, AST, ALT, Urea and Albumin Parameters in Children with Rotavirus Diagnosis

**Veysel TAHİROĞLU[1*]** iD **, Cihat ÖZTÜRK[2]** iD

[1]Şırnak University, Faculty of Health Sciences, Department of Nursing, Şırnak, Türkiye
[2] Kırşehir Ahi Evran University, Faculty of Medicine, Department of Medical Microbiology, Kırşehir, Türkiye
Veysel TAHİROĞLU ORCID No: 0000-0003-3516-5561
Cihat ÖZTÜRK ORCID No: 0000-0003-2868-2317

*Corresponding author: veysel.tahiroglu@sirnak.edu.tr*

**Abstract:** This study aims to evaluate glucose, AST, ALT, urea and albumin parameters in patients diagnosed with rotavirus. Children who applied to Şırnak State Hospital Pediatrics Polyclinics (6 months to 18 years of age), whose fecal samples were sent to the laboratory by the pediatrician considering the diagnosis of rotavirus, and whose microbiological examinations were confirmed by immunochromatographic methods (6 months to 18 years), were included in the study by scanning the system. When the mean ages of glucose, ALT, AST, urea, and albumin data of the rotavirus negative group were evaluated, they were found to be 1.82±2.66, 1.77±2.72, 1.76±2.72, 1.69±2.68, 1.87±2.88, respectively. and in rotavirus positives, respectively; It was found to be 1.16±1.35, 1.09±1.31, 1.09±1.31, 1.10±1.32, 1.11±1.30. While the median values of glucose, AST, ALT, urea and albumin in rotavirus negatives were 84 mg/dl, 36 U/L, 19 U/L, 14 mg/dL, 3.79 g/dL, respectively, the median values in rotavirus positives were 75 mg, respectively. /dL, 45 U/L, 26 U/L, 18 mg/dL, 3.98 g/dL were detected. All parameters were statistically significant (p<0.01). We think that laboratory parameters (glucose, AST, ALT, urea and albumin) in gastroenteritis due to rotavirus should definitely be evaluated in determining the prognosis of patients with rotavirus diagnosis.

41

# *Rotavirüs* Tanılı Çocuklarda Glukoz, AST, ALT, Üre ve Albümin Parametrelerin Değerlendirilmesi

**Anahtar Kelimeler**
Rotavirüs,
Glukoz,
AST,
ALT,
Üre,
Albümin

**Öz:** Bu çalışma rotavirüs tanılı hastalarda glukoz, AST, ALT, üre ve albümin parametrelerinin değerlendirilmesini amaçlamaktadır. Şırnak Devlet Hastanesi Çocuk Hastalıkları Polikliniklerine başvuran çocuklardan, pediatrist tarafından rotavirüs tanısı düşünülerek laboratuvara fekal örnekleri gönderilen ve mikrobiyolojik tetkikleri immünokromatografik yöntemler ile Rotavirüs tanısı doğrulanmış (6 aylık-18 yaş arası) çocuklar sistemden taranarak çalışmaya dahil edildi. Rotavirüs negatif grubun glukoz, ALT, AST, üre, albumin verilerinin ortalama yaşları değerlendirildiğinde sırasıyla 1.82±2.66, 1.77±2.72, 1,76±2,72, 1,69±2,68, 1,87±2,88 yaş ortalamasına, rotavirüs pozitiflerde ise sırasıyla; 1.16±1.35, 1.09±1.31, 1.09±1.31, 1.10±1.32, 1,11±1,30 olduğu tespit edildi. Glukoz, AST, ALT, üre ve albüminin rotavirüs negatiflerde medyan değerleri sırasıyla 84 mg/dl, 36 U/L, 19 U/L, 14 mg/dL, 3,79 g/dL iken, rotavirüs pozitiflerde ise medyan değerleri sırasıyla 75 mg/dL, 45 U/L, 26 U/L, 18 mg/dL, 3,98 g/dL tespit edildi. Tüm parametreler istatistiksel olarak anlamlı bulundu (p<0.01). Rotaviruse bağlı gastroenteritlerde laboratuvar parametrelerinden (glukoz, AST, ALT, üre ve albüminin) rotavirüs tanılı hastaların prognozunun tespitinde mutlaka değerlendirilmesi gerektiğini düşünmekteyiz.

## 1. INTRODUCTION

Rotavirus has been reported as the most important cause of mortality and morbidity related to acute gastroenteritis in children worldwide [1]. Rotaviruses have 11 segments and non-enveloped double-stranded RNA (dsRNA). dsRNA segments encode 12 viral proteins, six of which are structural viral proteins (SVP1, SVP2, SVP3, SVP4, SVP6, SVP7) and six nonstructural viral proteins (NSVP1, NSVP2, NSVP3, NSVP4, NSVP5, NSVP6) [5]. Rotavirus infection is a major cause of acute

gastroenteritis in children under 5 years of age, mostly in the first 2 years of life. While infection is usually asymptomatic or mild depending on the presence of maternal antibodies, it can cause death in infants aged 3-24 months as a result of rapid dehydration due to severe diarrhea, malaise, fever and vomiting [2, 3, 4]. Globally, 114 million cases of rotavirus infection were reported in children under 5 years of age in 2003, while an estimated more than 200,000 cases of rotavirus diagnosis were associated with death in 2013 [5]. It has been reported that with diarrhea caused by rotavirus in children under the age of 5 in the USA, seventy thousand cases are admitted to home care, two hundred thousand cases are admitted to the emergency departments, and an average of four hundred thousand patients are hospitalized each year, resulting in death in an average of 60 cases per year [6]. In studies conducted in our country, it has been reported that rotavirus causes 15-40% of diarrhea in children under the age of 5 [7]. Rotavirus is the most important pathogen causing gastroenteritis in children in Turkey as in the world [8]. Studies reporting the results of laboratory markers in the clinical management of patients are limited. In this study, it is aimed to retrospectively evaluate the relationship between various biochemical parameters (glucose, aspartate aminotransferase (AST), alanine aminotransferase (ALT), urea and albumin) in rotavirus-positive patients with gastroenteritis symptoms in the years 2020-2022.

## 2. MATERIAL AND METHOD

The study was approved by Şırnak University Ethics Committee (decision no: 2023/56246-1, date: 06.01.2023). Children (6 months-18 years old) who applied to Şırnak State Hospital Pediatrics Outpatient Clinic between 2020-2022, whose stool samples were sent to the laboratory on suspicion of rotavirus diagnosis and whose microbiological examinations were performed, were included in the study. Age, gender, detection of rotavirus and biochemical parameters of the patients were evaluated retrospectively. Each biochemical parameter (Glucose, AST, ALT, Urea, Albumin) was evaluated according to gender, and rotavirus positive patients were statistically compared with rotavirus negative patients.

### 2.1. Statistical Analysis

Statistical analysis of the data was performed using the SPSS 25.0 package program. Data were expressed as median [min-max value], qualitative data as percentage and non-normally distributed data as Median (IQR, Inter QuntifierRatio, 25%-75%). In data analysis, the distribution of continuous variables was determined by Kolmogorov-Smirnov and Shapiro-Wilk normality tests. Since the data were not normally distributed, the Mann-Whitney U test was used to determine the relationship between the paired groups. Frequency distributions, number, median, minimum and maximum values were given in descriptive statistics. A p value of <0.05 was considered significant.

## 3. RESULTS

Gender distribution and mean age by groups are given in Table 1. According to the table, when the sex distribution of glucose, ALT, AST, Urea and Albumin data in rotavirus negatives is examined, 56.4%, 57.1, 59.6, 56.6 and 60.5 percent of them were males, respectively; It was determined that 43.6, 42.9, 43.1, 43.4, 39.5 were girls. On the other hand, when the sex distribution of the glucose, ALT, AST, Urea and Albumin data of the rotavirus positive patients was examined, it was determined that 61.3, 62.8, 62.8, 63.1, 60.4 were boys, 38.7, 37.2, 37.2, 36.9, 39.6 were girls, respectively. When the mean ages of rotavirus negative glucose, ALT, AST, urea, and albumin data are evaluated according to the table, 1.82±2.66, 1.77±2.72, 1.76±2.72, 1.69±2.68, 1.87±2.88 years, respectively. average, in rotavirus positive, respectively; It was found to be 1.16±1.35, 1.09±1.31, 1.09±1.31, 1.10±1.32, 1.11±1.30. The evaluation of glucose, AST, ALT, urea and albumin parameters are given in Table 2. Accordingly, the median value of glucose was 84 mg/dL in rotavirus negatives, and 75 mg/dL in rotavirus positives, and it was found to be statistically significant (p<0.01). While the median value was 36 U/L in AST rotavirus negatives, the median value was 45 U/L in rotavirus positives, which was statistically significant (p<0.01). While the median value was 19 U/L in ALT rotavirus negatives and 26 U/L in rotavirus positives, it was found to be statistically significant (p<0.01). It was revealed that the median value of urea was 14 mg/dL in rotavirus negatives, and 18 mg/dL in rotavirus positives, which was statistically significant (p<0.01). The median value of the urea negative group was 3.79 g/dL, and the median value of the positive group was 3.98 g/dL, and it was statistically significant (p<0.01).

42

**Table 1.** Gender Distribution and Average Age of the Parameters by Groups

| Parameters | Rotavirus negative | | | Rotavirus positive | | | Total |
|---|---|---|---|---|---|---|---|
| | Gender | | Age | Gender | | Age | |
| | Male n(%) | Female n(%) | Mean ±SD | Male n (%) | Female n (%) | Mean ±SD | |
| Glucose | 181(56,4) | 140(43,6) | 1,82±2,66 | 46 (61,3) | 29 (38,7) | 1,16±1,35 | 396 |
| AST | 224(57,1) | 168(42,9) | 1,77±2,72 | 54 (62,8) | 32 (37,2) | 1,09±1,31 | 478 |
| ALT | 219(56,9) | 166(43,1) | 1,76±2,72 | 54 (62,8) | 32 (37,2) | 1,09±1,31 | 471 |
| Urea | 194(56,6) | 149(43,4,) | 1,69±2,68 | 53 (63,1) | 31 (36,9) | 1,10±1,32 | 427 |
| Albumin | 193(60,5) | 126(39,5) | 1,87±2,88 | 65 (60,4) | 43 (39,6) | 1,11±1,30 | 427 |

**Table 2.** Glucose, AST, ALT, Urea and Albumin parameters in groups

| Parameters | Rotavirüs | N | Median | Min-Max | IQR | P value |
|---|---|---|---|---|---|---|
| Glucose (mg/dL) | Negative | 321 | 84 | 54-115 | 17 | <0.01 |
| | Positive | 75 | 75 | 42-105 | 17 | |
| AST(U/L) | Negative | 392 | 36 | 11-69 | 16 | <0.01 |
| | Positive | 86 | 45 | 24-70 | 15 | |
| ALT (U/L) | Negative | 385 | 19 | 6-44 | 12 | <0.01 |
| | Positive | 86 | 26 | 10-59 | 17 | |
| Urea (mg/dL) | Negative | 343 | 14 | 2-33 | 13 | <0.01 |
| | Positive | 84 | 18 | 2-54 | 17 | |
| Albumin (g/dL) | Negative | 208 | 3,79 | 3-4 | 1 | <0.01 |
| | Positive | 66 | 3,98 | 3-5 | 1 | |

## 4. DISCUSSION AND CONCLUSION

In our study, we aimed to evaluate the glucose, AST, ALT, urea and albumin of rotavirus positive patients diagnosed with immunochromatographic methods in the microbiology laboratory and registered in the automation system. Rotavirus infection creates a serious financial burden on the economy every year, especially in developing countries. Although the hospitalization rates differ according to the countries, the average cost of rotavirus-infected patients to the country every year; It is estimated to be 7 million New Zealand dollars in New Zealand, 890 million dollars in the USA, 27 million dollars in Italy and 40-70 million dollars in India [9-12]. For Turkey, this rate covers the whole country for children under the age of 5; A comprehensive cost analysis cannot be performed because there are no reliable records regarding outpatient admission, rotavirus positivity, and hospitalization [13]. 70% of rotavirus diarrhea in Turkey is seen in children under the age of two [14]. In our study, we found that those diagnosed with rotavirus were under the age of two. It is known that adequate fluids containing physiological concentrations of glucose and electrolytes should be provided to compensate for gastrointestinal losses and to meet maintenance needs [15]. Karsligil et al. In a study on rotavirus gastroenteritis and its effect on lactose intolerance in children aged 0-6 years, they reported that patients with low glucose were also diagnosed with rotavirus [16]. In our study, we found that the positive group had a lower glucose level than the negative group and it was statistically significant. A 2-fold increase in liver enzymes is observed in approximately 2/3 of the patients hospitalized with the diagnosis of rotavirus [17]. Işık et al. reported that AST and ALT were higher in patients diagnosed with rotavirus compared to the negative group [18]. In our study, we found that both AST and ALT were higher in positive patients compared to the literature, and we found it statistically significant. The reason for this may have varied depending on the electrolyte abnormality or the severity of the infection. Çubuk et al. reported that no significant difference was found between CRP, hematological and biochemical parameters in their study [19]. Qadori et al. in a study evaluating sodium, potassium, urea, creatinine and glucose in gastroenteritis, stated that they did not detect major electrolyte disturbances other than hypoglycemia in gastroenteritis [20]. Asena et al. In a study evaluating laboratory parameters, it was found that no difference was found between the control group and the group positive for Rotavirus, hemoglobin, platelets, eosinophils, basophils, glucose, creatinine, total protein, albumin, sodium, potassium, calcium, chlorine, and CRP, but it was higher in the white blood cell and neutrophil control group. While they were found to be higher in lymphocyte, urea, AST and ALT positive groups, they were found to be slightly higher, but they reported that they could not find it statistically significant [21]. In our study, we found that both urea and albumin positive groups were higher and statistically significant compared to the negative group.

Rotavirus gastroenteritis is an important health problem that is common in Turkey as well as in almost every country in the world, causing hospitalizations and morbidity. Considering the results of the study, it is thought that laboratory parameters (glucose, AST, ALT, urea and albumin) in gastroenteritis due to rotavirus should definitely be evaluated in determining the prognosis of patients with rotavirus, and detailed analyzes should be performed in larger populations, since there are few studies on the subject in our country.

**Limitations of the Research**

The main limitation of the study is that it is a retrospective study. However, the fact that the vaccination status of the patients was not recorded is an important limitation.

**REFERENCES**

[1] Lundgren O, Svensson L. Pathogenesis of rotavirus diarrhea. Microbes Infect. 2001;3(13):1145-1156.

[2] Crawford SE, Ramani S, Tate JE, Parashar UD, Svensson L, Hagbom M, et al. Rotavirus infection. Nat Rev Dis Primers. 2017; 3:17083.

[3] Marchetti F, Lamiani G, Bona M, Amerighi C, Ruffato B, Conforti G. Developing communication tools on rotavirus vaccination to support family paediatricians in Italy. Vaccine. 2022;40(49):7108-7114.

[4] World Health Organization, The treatment of diarrhoea: a manual for physicians and other senior health workers. 2005.

[5] Florez ID, Niño-Serna LF, Beltrán-Arroyave CP. Acute Infectious Diarrhea and Gastroenteritis in Children. Curr Infect Dis Rep. 2020;22(2):4

[6] Available from: https://www.cdc.gov/rotavirus/surveillance.html (Access Date: 20.05.2023).

[7] Kurugöl Z. Rotavirus aşıları Derleme. Türk Pediatri Arşivi. 2007; 42(11): 36-42.

[8] Tapisiz A, Bedir Demirdag T, Cura Yayla BC, et al. Rotavirus infections in children in Turkey: A systematic review. Rev Med Virol. 2019;29(1):e2020.

[9] Milne RJ, Grimwood K. Budget impact and cost-effectiveness of including a pentavalent rotavirus vaccine in the New Zealand childhood immunization schedule. Value Health. 2009;12(6):888-898.

[10] Giammanco MD, Coniglio MA, Pignato S, Giammanco G. An economic analysis of rotavirus vaccination in Italy. Vaccine. 2009;27(29):3904-3911.

[11] Widdowson MA, Meltzer MI, Zhang X, Bresee JS, Parashar UD, Glass RI. Cost-effectiveness and potential impact of rotavirus vaccination in the United States. Pediatrics. 2007;119(4):684-697.

[12] Tate JE, Chitambar S, Esposito DH, Sarkar R, Gladstone B, Ramani S, et al. Disease and economic burden of rotavirus diarrhoea in India. Vaccine. 2009;27(5):18-24.

[13] Sancar M, Dalgış N, Haşim Ö, Pullu M. Bir Eğitim ve Araştırma Hastanesindeki rotavirüslü çocuklarda yatış maliyeti. Çocuk Enfeksiyon Dergisi. 2011; 5(1): 7- 11.

[14] Ceyhan M, Alhan E, Salman N, Kurugol Z, Yildirim I, Celik U, et al. Multicenter prospective study on the burden of rotavirus gastroenteritis in Turkey, 2005-2006: a hospital-based study. J Infect Dis. 2009;200 (1): 234-238.

[15] Leung AK, Hon KL. Paediatrics: how to manage viral gastroenteritis. Drugs Context. 2021; 10:2020-11-17.

[16] Karslıgil T, Kılıç İH, Balcı İ. 0-6 yaş çocuklarda rotavirus gastroenteritleri ve bunun laktoz intoleransı üzerine etkisi. Türk Mikrobiyol Cem Derg 2003; 33: 137-142.

[17] Kovacs A, Chan L, Hotrakitya C, Overturf G, Portnoy B. Serum transaminase elevations in infants with rotavirus gastroenteritis. J Pediatr Gastroenterol Nutr. 1986;5(6):873-877

[18] Işık I, Tokgöz Y, Erdur B, Arslan N. Aminotransferase elevations in rotavirus positive and negative acute gastroenteritis and its relation with disease severity. Minerva Pediatr. 2017;69(1):36-41.

[19] Çubuk E, Aktar F, Yılmaz K, Sabaz M, Solmaz M, Asena M, Devecioğlu M. 2011-2015 Yılları Arasında Üniversitemiz Çocuk Polikliniklerine ishal Şikâyeti Ile Başvuran ve Adenovirüs ve/veya Rotavirüs Pozitifliği Saptanan Hastaların Retrospektif Değerlendirilmesi. Van Tıp Dergisi. 2018; 25(3): 374- 380.

[20] Qadori M, Flem E, Bekkevold T, et al. Hypoglycaemia was common in acute gastroenteritis in a prospective hospital-based study, but electrolyte imbalances were not. Acta Paediatr. 2018;107(8):1455-1460.

[21] Asena M., Canan A., Öztürk Ü., Aydın Öztürk P., Pirinççioğlu A. G. Gastroenterit Nedeniyle Yatırılan Pediatrik Hastaların Rotavirüs/Adenovirüs Açısından Değerlendirilmesi. Dicle Tıp Dergisi. 2019; 46(4): 799-806.

**BİNGÖL ÜNİVERSİTESİ**

**Türk Doğa ve Fen Dergisi**
**Turkish Journal of Nature and Science**
www.dergipark.gov.tr/tdfd

# Transfer Learning for Detection of Casting Defects Model In Scope of Industrial 4.0

**Hayriye TANYILDIZ[1]** , **Canan BATUR ŞAHİN[1*]**

[1] Faculty of Engineering and Natural Sciences, Malatya Turgut Ozal University, Malatya 44210, Türkiye
Hayriye TANYILDIZ ORCID No: 0000-0002-6300-9016
Canan BATUR ŞAHİN ORCID No: 0000-0002-2131-6368

*Corresponding author: canan.batur@ozal.edu.tr*

**Abstract:** Casting is a major manufacturing process in various industries, and the elimination of its flaws is of great importance. Traditional casting flaw detection processes are usually performed manually, which is both time-consuming and prone to human errors. In this paper, we will validate whether the bottleneck of "manual inspection" can be eliminated by automating the inspection process of casting products in the manufacturing process using transfer learning. The motivation is to enhance the accuracy and efficiency values in manual examination processes. The need to reduce production errors and increase overall production efficiency are key goals of Industry 4.0. This paper could represent a significant step towards achieving these goals and aims to automate casting defect detection using deep learning and transfer learning, thereby eliminating the time-consuming and error-prone nature of the manual inspection. Using deep learning architectures and transfer learning techniques, we divide casting images into two separate classes, achieving a level of accuracy never before achieved in this process. The innovative aspect is that it's among the first to apply transfer learning and deep learning techniques to casting defect detection. This presents a great potential for automating defect detection in casting and increasing overall production efficiency. Furthermore, this paper demonstrates how these technologies could be used to improve production processes more broadly in line with the goals of Industry 4.0.

The benefits of this approach include the ability to automate manual inspection processes, thereby speeding up the production process, increasing accuracy, and reducing human errors. This is proposed as a more efficient way of controlling the quality of end products under Industry 4.0. The application of transfer learning and deep learning techniques to casting defect detection enables a great leap forward in this field.

45

# Endüstri 4.0 Kapsamında Döküm Hatalarının Tespiti İçin Transfer Öğrenme Modeli

**Öz:** Döküm, çeşitli endüstrilerin ana üretim süreçlerinden biridir ve hatalarının ortadan kaldırılması büyük önem taşır. Geleneksel döküm kusur tespiti süreçleri genellikle manuel olarak gerçekleştirilir, bu da hem zaman alıcı hem de insan hatalarına açıktır. Bu çalışmada, döküm ürünlerinin imalat sürecinde transfer öğrenme ile muayene sürecini otomatikleştirerek "manuel muayene" darboğazının ortadan kaldırılıp kaldırılamayacağını doğrulayacağız.Motivasyon, manuel inceleme süreçlerinde doğruluk ve verimlilik değerlerini arttırmaktır. Üretim hatalarını azaltma ve genel üretim verimliliğini artırma ihtiyacı, Endüstri 4.0'ın temel hedefleridir.Bu çalışma, bu hedeflere ulaşma yolunda önemli bir adımı temsil edebilir ve derin öğrenme ve transfer öğrenmeyi kullanarak döküm hatası tespitini otomatikleştirmeyi ve böylece manuel incelemenin zaman alıcı ve hataya eğilimli doğasını ortadan kaldırmayı hedeflemektedir. Derin öğrenme mimarilerini ve transfer öğrenme tekniklerini kullanarak, döküm görüntülerini iki ayrı sınıfa ayırarak, bu süreçte daha önce hiç ulaşılmamış bir doğruluk düzeyine ulaşıyoruz. Bu çalışmanın yenilikçi yönü, transfer öğrenme ve derin öğrenme tekniklerini döküm kusur tespitine uygulayan ilk çalışmalardan biri olmasıdır. Bu, döküm sürecindeki kusur tespitinin otomatikleşmesi ve genel üretim verimliliğinin artırılmasında büyük bir potansiyel sunmaktadır. Dahası, bu çalışma, bu teknolojilerin Endüstri 4.0'ın hedefleri doğrultusunda üretim süreçlerinin daha geniş bir çerçevede nasıl iyileştirilebileceğini gösterir.

Bu yaklaşımın faydaları, manuel muayene süreçlerini otomatikleştirebilme ve bu sayede üretim sürecini hızlandırabilme, doğruluğu artırabilme ve insan hatalarını azaltabilme yeteneğidir. Bu, nihai ürünlerin kalitesini kontrol etmenin daha verimli bir yolu olarak Endüstri 4.0 kapsamında önerilmektedir. Transfer öğrenme ve derin öğrenme tekniklerinin döküm kusur tespitine uygulaması, endüstrinin bu alanda büyük bir adım atmasını sağlar.

# 1. INTRODUCTION

In casting products, it is very important to distinguish faulty products from defect-free products. While visual inspection of castings is slow and inefficient in mass production, automatic and reliable defect detection improves and positively affects the quality control process. However, casting defect detection is a challenge due to the diversity and variability in the appearance of defects. It is quite easy to achieve this work, which is normally done manually, with deep learning networks. Overall, using deep learning for this purpose has the potential to be more accurate and efficient than traditional audit methods and can help reduce the cost of quality control. Casting defects can have a significant impact on the quality and performance of the final product, so it is important to detect and correct these defects as early in the manufacturing process as possible. Deep learning algorithms can analyze castings images and identify defects such as voids, porosity, and inclusions. These algorithms can be trained on large image datasets labeled with various types of defects, and once trained, they can be used to classify new images and detect defects in real-time. Using deep learning to detect casting defects is a promising approach that can improve the accuracy and efficiency of defect detection in casting processes.

For error detection in casting, convolutional neural networks (CNNs), recurrent neural networks (RNNs), and autoencoders are used. There are several types of deep learning architectures that can be used. A convolutional neural network (CNN) was used in the study [1] to classify casting defects in aluminum alloy casting images. The study found that CNN was able to achieve an accuracy of 93.33% in the classification task, outstripping other machine learning algorithms such as support vector machines and k-nearest neighbors. The study [2] used a CNN to classify casting images into four different categories: good, surface defect, internal defect, and other. The model was trained on a dataset of more than 7,000 images and was able to achieve an accuracy of 92.3% on a test set of 1,000 images. The study [3] have proposed a two-stage convolution model with DenseNet to classify casting products using defective and non-defective casting image dataset. At the end of the study, they achieved 99% accuracy. In the study [4] four powerful CNN-based models (VGG16, ResNet50, DenseNet121, and InceptionResNetV2) were applied to the dataset and produced the feature maps. The extracted features were classified into various classifiers. Error detection was performed on the cast images using a neural network model. The model has been trained to detect errors in the given images and high accuracy rates have been achieved. In the study [5] the best model was selected by applying three different models from CNN-based models to the feature maps obtained from different casting materials, by comparing the three types of CNN algorithms, the accuracy can be obtained as follows. Basic Architecture (Accuracy - 98%), Alex Net (Accuracy - 51%), Le Net (Accuracy - 99%). At the end of this project model. They were able to obtain the best determined maximum accuracy from the Le Net

Algorithm. In [13], an enhanced domain adaptive Faster R-CNN model was introduced with its superior capability to detect void and inclusion defects in spacecraft composite structures (SCSs). In [14], different pre-trained and custom-built architectures were compared and contrasted with model size, performance In [13], an enhanced domain adaptive Faster R-CNN model was introduced with its superior capability to detect void and inclusion defects in spacecraft composite structures (SCSs). In [14], different pre-trained and custom-built architectures were compared and contrasted with model size, performance, and CPU latency in detecting defective casting products. In [15], the problem of identifying small defects during an industrial inspection was defined. The current study investigated complex transfer learning (TL) strategies, allowing for the automatic detection and categorization of product defects in the production process using industrial product specimens. This study suggested a multitype damage detection model for containers on the basis of transfer learning and MobileNetV2 [16].

The current work makes the following main contributions:

- ✓ The study creates a deep learning-based detection system for classifying casting defects for industry 4.0 products.
- ✓ A framework is proposed, improving the detection capability of supervised learning approaches based on ResNet50, MobilnetV2, and InceptionV3, hybrid architectures for learning casting errors effectively.
- ✓ The current work presented a new framework where the learning and combination of features are carried out. The features chosen are employed to predict error detection in casting.
- ✓ We studied how to use Deep Neural Network (DNN) models for the purpose of predicting defects with high accuracy rates.

The rest of this paper is organized as follows. Section 2 explains the proposed method. The results and discussions are shown in Section 3. Section 4 describes the discussion. The conclusion and future studies are presented in Section 5.

## 2. THE PROPOSED METHOD

### 2.1. Methodology

This research suggested a hybrid model classify images of industrial casting products. Before creating the hybrid model, classification was made with various deep learning architectures, and the three highest ones were used in the hybrid model. In this study, out of 1300 images taken from the impellers of submersible pumps, 781 of them are faulty and 519 of them are normal, and feature mapping was created with 2-class image set deep learning models. The classification was made with the proposed hybrid model. The feature maps extracted from the deep learning models used for the hybrid model were combined. The newly formed feature map o dimension

1300*3001. The classification of the obtained feature map was performed with three various machine learning classifiers. Figure 1 shows the suggested model's block diagram.
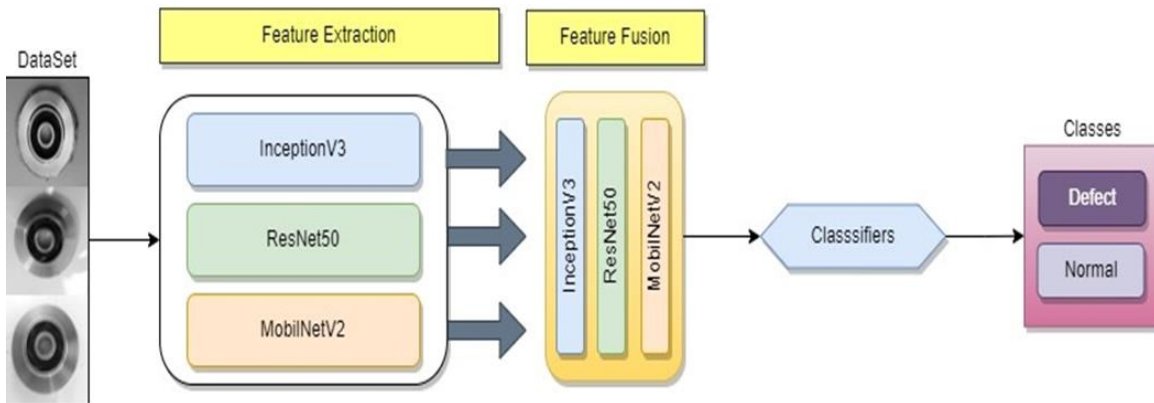


**Figure 1:** Architecture of the Proposed Model.

Deep neural networks are commonly utilized in numerous artificial intelligence applications, such as speech recognition, computer vision, and robotics. A frequently preferred form of the deep neural network is a convolutional neural network consisting of multiple convolutional layers [7]. In this study, Deep learning architectures were used effectively to detect casting errors. Three different models were used as a basis while creating the hybrid model we proposed. These models are ResNet50, MobilnetV2, and InceptionV3, architectures.

MobileNetV2 networks are developed for mobile, IoT, or devices with low hardware specifications. While maintaining the classification performance, these networks offer a significant improvement in the number of parameters and processing complexity. Its architecture consists of linear bottleneck and inverted residual blocks. The convolution layer consists of deep access and point access layers [8].

Resnet50 is a specific type of neural network introduced in [12] to facilitate the training of networks that are significantly deeper. ImageNet represents a 50-layer network that is trained on the dataset. Instead of utilizing 2 (3x3) convolutions, the ResNet model utilizes convolution layers (1x1), (3x3), and (1x1) [9]. In the study [10] development of the InceptionV3 architecture was performed. The said model comprises roughly three sections: the first block, the convolution block, and the classifier block. Comprising 315 layers, the architecture in question takes 299x299 input images. SVM, a supervised machine learning method, classifies the feature map created from the developed hybrid model. [6, 11]. In addition, to measure the performance values of other classifiers, k-Nearest Neighbors (KNN) [12], Neural Networks, and Logistic Regression were also classified.

# 3. RESULTS AND DISCUSSION

## 3.1. Datasets

This dataset contains images of impellers of submersible pumps. Our casting product data includes top-view JPEG images of cast submersible pump impellers provided by Pilot Technocast. Images were taken with a Canon EOS 1300D DSLR camera. Each image is 300×300 pixels in size and is already labeled def_front (defective dumps) or ok_front (non-perfect). There are 1300 images in total. When making the classification model, we have already divided the data into two parts for training and testing. Defected production images total 781, and Normal production images are 519.



**Figure 2:** Samples of Dataset.

Feature mapping was done using MobilnetV2, InceptionV3, and Resnet architectures. Later, these feature maps were combined to create a new feature map with the size of 1300x3001. The features extracted from the proposed hybrid model were classified by smart classification methods with different supervision which is shown in Table 1. Cubic SVM achieved the highest accuracy with 100%. Linear Discriminant followed, with 99.7%, while Naive Bayes achieved the lowest result with 81.1%. The performances of these methods were compared using Precision, F1-Score, Accuracy, and specificity metrics.

**Table 1.** Performance results of deep learning algorithms

| Model | Accuracy | Precision | Specificity | F1-Score |
|---|---|---|---|---|
| CNN+ CUBIC SVM | 100 | 100 | 100 | 100 |
| CNN+KNN | 98,46 | 97,70 | 96,64 | 98,71 |
| CNN+NEURAL NETWORK | 99,46 | 99,10 | 98,67 | 99,55 |
| CNN+LINEAR DISCRIMANT | 99,7 | 99,62 | 99,43 | 99,81 |
| CNN+ENSEBLE | 99,6 | 99,49 | 99,24 | 99,74 |
| CNN+NAIVE BAYES | 81,17 | 80,79 | 74,23 | 84.19 |
| CNN+LOGISTIC REGRESYON KERNEL | 98,53 | 98,72 | 98,06 | 98.53 |
| CNN+BOOSTED TREE | 98.14 | 97.70 | 96,61 | 98,45 |



| CNN+SVM | | | CNN+LINEAR DISCRIMANT | | | CNN+KNN | | |
|---|---|---|---|---|---|---|---|---|
| 1 | 781 | | 1 | 778 | 3 | 1 | 776 | 5 |
| 2 | | 519 | 2 | | 519 | 2 | 2 | 517 |
| | 1 | 2 | | 1 | 2 | | 1 | 2 |

| CNN+NEURAL NETWORK | | | CNN+ENSEBLE | | | CNN+LOGISTİC REGRESSION | | |
|---|---|---|---|---|---|---|---|---|
| 1 | 780 | 1 | 1 | 777 | 4 | 1 | 682 | 99 |
| 2 | 1 | 518 | 2 | | 519 | 2 | 87 | 432 |
| | 1 | 2 | | 1 | 2 | | 1 | 2 |

| CNN+NAIVE BAYES | | | CNN +LOGİSTİC REGRESYON KERNEL | | | CNN+BOOSTED TREE | | |
|---|---|---|---|---|---|---|---|---|
| 1 | 631 | 150 | 1 | 771 | 10 | 1 | 763 | 18 |
| 2 | 87 | 432 | 2 | 13 | 506 | 2 | 6 | 513 |
| | 1 | 2 | | 1 | 2 | | 1 | 2 |

**Figure 3:** Confusion Matrix of the Proposed Model

In the current research, constant coefficients were employed in all experiments. Furthermore, in the experiments, the cross-validation coefficient was found to be 5. The experiments were conducted on a computer having an i5 processor, 16 GB RAM, 5 GB graphics card, and Windows 10 operating system. Confusion matrices were utilized with the objective of measuring the performance of the deep and hybrid models. The Error and Normal classes are represented as 1 and 2, respectively, in confusion matrices. In this study, 5 different pre-trained state-of-the-art models were used. The same parameters were used in the whole study. The parameters used in these architectures are shown in Table 2.

**Table 2.** Paramaters of of deep learning algorithms

| Environment | Max Epochs | Mini Batch Size | Learn Rate | Optimization |
|---|---|---|---|---|
| Matlab 2022b | 5 | 8 | 1e-4 | Sgdm |

### 3.2. Results and Discussion

The data set was divided into two as 30% testing and 70% training. The accuracy rates obtained from the architectures were MobileNetV2 98.97%, InceptionV3 98.46, Resnet50 97.95%, and Efficientnetb0 84.10%. The truth table obtained from deep learning architectures is shown in Table 3

**Table 3.** Performance of Deep Learning algorithms

| Model | Accuracy (%) |
|---|---|
| Efficientnetb0 | 85.00% |
| InceptionV3 | 98.08% |
| MobilenetV2 | 99.62% |
| Resnet50 | 97.85% |
| Alexnet | 94.62% |

In this study, Mobilnetv2 architecture achieved the highest accuracy with 99.62%. It was followed by InceptionV3 with 98.08%, Resnet50 with 97.85%, Alexnet with 94.62%, and efficient in the last place with 85.00%. Confusion matrices obtained from deep learning architectures are shown in Table 5. When these matrices are examined; While MobilnetV2 architecture classified 153 of the incorrect images correctly, it showed 3

incorrect images as error-free. Likewise, it classified 102 of 104 error-free images as error-free and misclassified 1 of them as error-free. We see that different deep learning networks can give different results even if the same parameters are used.

**Table 4.** Performance of proposed algorithms

|  | Softmax(%) | LD(%) | BT(%) | KNN(%) | NN(%) | SVM(%) | ENS(%) | LG(%) |
|---|---|---|---|---|---|---|---|---|
| **Proposed Model** | - | 99.70 | 83.90 | 97.40 | 97.60 | **98.20** | 98.00 | |

**Table 5.** Confusion Matrix of Deep Learning algorithms

| InceptionV3 | MobilenetV2 | Resnet50 | Alexnet | Efficententb0 |
|---|---|---|---|---|



**Table 6.** Performance of relative studies

| Ref. | Methos | Accuracy(%) |
|---|---|---|
| [5] | AlexNet | 51 |
| | Lenet | 95.72 |
| [1] | CNN | 93.33 |
| [12] | Resnet34 | 83.80 |
| [3] | DenseNet | 99 |
| [14] | Custom Model | 99.44 |
| [16] | InceptionV3 | 92.92 |
| | MolileNetV2 | 89.41 |
| **Proposed Model** | **(MobilNetV2+ Resnet50+ InceptionV3) +SVM (Cubic)** | **100** |

In order to compare the success of the method, the methods and success rates of previous studies using deep learning methods for casting defect detection are given in Table 6. We emphasize that the proposed hybrid model can detect more defective production images compared with other methods represented in Table 6. We can see that (MobilNetV2+ Resnet50+ InceptionV3) +SVM (Cubic) outperforms the other models in six recent studies conducted in analyzing images of castings defects using deep learning.

## 4. DISCUSSION

When compared with the models and accuracy rates presented in the studies discussed earlier, the proposed model that integrates MobilNetV2, Resnet50, InceptionV3, and a Support Vector Machine (SVM) with a cubic kernel, demonstrates superior performance with an extraordinary accuracy of 100%.

In the study [1], a CNN achieved an accuracy of 93.33%. This suggests that while the CNN performed admirably, the proposed hybrid model outperforms it by a significant margin. Similarly, the CNN model in the study [2], which achieved 92.3% accuracy, is outstripped by the hybrid model's performance.

Study [3] employed a two-stage convolution model with DenseNet, reporting a remarkable accuracy of 99%. Yet,

the proposed model still slightly outperforms it with an additional 0.7% in accuracy.

In the study [4], where four powerful CNN-based models were used, the accuracy achieved is not explicitly stated, but it's clear that the proposed hybrid model's performance likely surpasses any achieved in that study.

Lastly, the three different CNN-based models used in the study [5] yielded varied accuracy rates: Basic Architecture (98%), Alex Net (51%), and Le Net (99%). Here, the proposed model equals or surpasses these results, particularly outdoing the relatively low accuracy achieved by the Alex Net model.

In summary, the hybrid architecture that integrates MobilNetV2, Resnet50, InceptionV3, and an SVM with a cubic kernel showcases the excellent performance, surpassing or equaling those reported in the referenced studies. This indicates the effectiveness and robustness of combining different deep learning models with classical machine learning methods. It also underscores the potential of such combinations in improving the accuracy of defect detection in casting processes.

# 5. CONCLUSION

This research paper has presented a novel hybrid method that harnesses the power of Convolutional Neural Networks (CNN) and transfers learning architectures to detect defects in the casting manufacturing process using advanced deep learning techniques. Leveraging the proficiency of cutting-edge deep learning models such as Resnet50, MobilnetV2, and InceptionV3, this work proposes an innovative approach with the potential to significantly boost the precision and efficiency of defect identification within casting procedures.

Our approach effectively combines CNN and supervised learning architectures to enable accurate defect detection as well as the automated categorization of images from the casting process. The method has been designed to analyze dump images in order to identify anomalies and errors that may occur during the casting process. This not only ensures a high level of quality control but also minimizes human intervention, thus reducing the likelihood of user errors and increasing the overall efficiency of the casting process. The performance metrics of our method reveal a promising success rate, indicating its potential to be a practical tool for determining general casting efficiency. By identifying and rectifying defects early in the process, our method could facilitate faster turnaround times and improve overall manufacturing outcomes.

In terms of future work, our goal is to further enhance the detection of errors and defects. We plan to work with newer and potentially more effective deep learning architectures and expand our datasets to be more comprehensive. The prospect of harnessing more diverse and extensive data could enable our system to learn from a broader range of defects and improve its capability to generalize across different casting scenarios. It is our expectation that, with these improvements, the effectiveness and accuracy of defect detection in the casting process will be substantially increased

## Acknowledgement

# REFERENCES

[1] Lili Jiang, Yongxiong Wang, Zhenhui Tang, Yinlong Miao, Shuyi Chen, Casting defect detection in X-ray images using convolutional neural networks and attention-guided data augmentation,Measurement,Volume 170, 2021

[2] C. Hu, Y. Wang, K. Chen, Y. Qin, H. Shao and J. Wang, "A CNN Model Based on Spatial Attention Modules for Casting Type Classification on Pseudo-color Digital Radiography Images," 2019 Chinese Automation Congress (CAC), Hangzhou, China, 2019, pp. 4585-4589

[3] Dilliraj Ekambaram, Vijayakumar Ponnusamy. (2022). Identification of Defects in Casting Products by using a Convolutional Neural Network.

IEIE Transactions on Smart Processing & Computing, 11(3), 149-155.

[4] HABIBPOUR, Maryam, et al. An Uncertainty-Aware Deep Learning Framework for Defect Detection in Casting Products. arXiv preprint arXiv:2107.11643, 2021.

[5] M Shanthalakshmi, Susmita mishra, V Jananee, P Narayana Perumal, S Manoj Jayakar5.(2022). Identification of Casting Product Surface Quality Using Alex net and Le-net CNN Models.

[6] Suykens, J.A.K., Vandewalle, J. (1999). Least squares support vector machine classifiers. Neural Processing Letters, 9(3): 293-300.

[7] Gürkan, H., Hanilçi, A. 2020. Evrişimli sinir ağı ve QRS imgeleri kullanarak EKG tabanlı biyometrik tanıma yöntemi. Pamukkale Üniversitesi Mühendislik Bilimleri Dergisi, 26(2), 318-327.

[8] Eryılmaz, F. & Karacan, H. (2021). Akciğer X-Ray Görüntülerinden COVID-19 Tespitinde Hafif ve Geleneksel Evrişimsel Sinir Ağ Mimarilerinin Karşılaştırılması . Düzce Üniversitesi Bilim ve Teknoloji Dergisi , ICAIAME 2021 , 26-39 . DOI: 10.29130/dubited.1011829

[9] D. Theckedath and R. Sedamkar, "Detecting affect states using vgg16, resnet50 and se-resnet50 networks," SN Computer Science, vol. 1, no. 2, pp. 1–7, 2020.

[10] Szegedy, C., Ioffe, S., Vanhoucke, V., Alemi, A. (2017). Inception-v4, inception-ResNet and the impact of residual connections on learning. Thirty-first AAAI Conference on Artificial Intelligence, pp. 4278-4284.

[11] Özyurt, F., Sert, E., Avci, D. (2022). Ensemble residual network features and cubic-SVM based tomato leaves disease classification system. Traitement du Signal, 39(1): 71-77.

[12] He, K., Zhang, X., Ren, S., & Sun, J. (2015). Deep Residual Learning for Image Recognition. arXiv.

[13] Yanfeng Gong, Jun Luo, Hongliang Shao, Zhixue Li, A transfer learning object detection model for defects detection in X-ray images of spacecraft composite structures, Composite Structures,Vol.284, 2022

[14] Bolla, B. K., Kingam, M., & Ethiraj, S. (2022). Efficient Deep Learning Methods for Identification of Defective Casting Products. arXiv.

[15] U. K. Lilhore, S. Simaiya, J. K. Sandhu, N. K. Trivedi, A. Garg and A. Moudgil, "Deep Learning-Based Predictive Model for Defect Detection and Classification in Industry 4.0," 2022 International Conference on Emerging Smart Computing and Informatics (ESCI), Pune, India, 2022, pp. 1-5, doi: 10.1109/ESCI53509.2022.9758280.

[16] Mesbah, Mahmoud, Wang, Zixin,Gao, Jing,Zeng, Qingcheng, Sun, Yuhui, 2021, Multitype Damage Detection of Container Using CNN Based on Transfer Learning,Hindawi

[17] İ. E. Parlak, E. Emel, "Deep learning-based detection of aluminum casting defects and their types", Engineering Applications of Artificial Intelligence, Vol.118, 2023, ISSN 0952-1976

[18] Z. Zhao, T. Wu, "Casting Defect Detection and Classification of Convolutional Neural Network

Based on Recursive Attention Model", Scientific Programming, vol. 2022, Article ID 4385565, 11 pages, 2022

[19] A. R.Dakak, V. Kaftandjian, P. Duvauchelle, P. Bouvet, Insight - Non-Destructive Testing and Condition Monitoring, Vol. 64, No. 11, 2022, pp. 647-658, The British Institute of Non-Destructive Testing

[20] I. Raouf, P. Kumar, H. Lee, H.S. Kim, Transfer Learning-Based Intelligent Fault Detection Approach for the Industrial Robotic System. Mathematics 2023, 11, 945.

[21] M. S. Azari, F. Flammini, S. Santini and M. Caporuscio, "A Systematic Literature Review on Transfer Learning for Predictive Maintenance in Industry 4.0," in IEEE Access, vol. 11, pp. 12887-12910, 2023, doi: 10.1109/ACCESS.2023.3239784.

**Türk Doğa ve Fen Dergisi**
**Turkish Journal of Nature and Science**
www.dergipark.gov.tr/tdfd

# Comparison of Different Supervised Classification Algorithms for Mapping Paddy Rice Areas Using Landsat 9 Imageries

## Melis INALPULAT[1,2]* (iD)

[1] Çanakkale Onsekiz Mart University, Faculty of Agriculture, Department of Agricultural Structures and Irrigation, Agricultural Remote Sensing Laboratory (AGRESEL), Çanakkale, Türkiye
[2] Çanakkale Onsekiz Mart University, Computer-Agriculture-Environment-Planning (ComAgEnPlan) Study Group, Çanakkale, Türkiye
Melis INALPULAT ORCID No: 0000-0001-7418-1666

*Corresponding author: melissacan@comu.edu.tr

**Abstract:** Rice is known to be one of the most essential crops in Türkiye, as well as many other countries especially in Asia, whereas paddy rice cropping systems have a key role in many processes ranging from human nutrition to environment-related perspectives. Therefore, determination of cultivation area is still a hot topic among researchers from various disciplines, planners, and decision makers. In present study, it was aimed to evaluate performances of three classifications algorithms among most widely used ones, namely, maximum likelihood (ML), random forest (RF), and k-nearest neighborhood (KNN), for paddy rice mapping in a mixed cultivation area located in Biga District of Çanakkale Province, Türkiye. Visual, near-infrared, and shortwave-infrared bands of Landsat 9 acquired on July 04, 2022 was utilized. The classification scheme included six classes as dense vegetation (D), sparse vegetation (S), agricultural field (A), water surface (W), residential area – base soil (RB), and paddy rice (PR). The performances were tested using the same training samples and accuracy control points. The reliability of each classification was evaluated through accuracy assessments considering 150 equalized randomized control points. Accordingly, RF algorithm could identify PR areas with over 96.0% accuracy, and it was followed by KNN with 92.0%. Using one-date Landsat 9 imagery seemed to have potential for PR area determination at high accuracy levels. In conclusion, RF algorithm is strongly suggested for reliable distinction of PR areas from neighbor classes under similar climate, soil and terrain conditions with comparable cultivation patterns, whereas Landsat 9 presents valuable data set for similar studies by being free of charge.

52

# Landsat 9 Kullanılarak Çeltik Alanlarının Haritalanması için Farklı Kontrollü Sınıflandırma Algoritmalarının Karşılaştırılması

**Öz:** Asya' da bulunan birçok ülkede olduğu gibi Türkiye' de de çeltik esansiyel bitkilerden biri olup, tava üretim sistemleri insan beslenmesinden çevresel perspektifte bir çok süreç için kilit role sahiptir. Bu nedenle, üretim alanlarının belirlenmesi farklı disiplinlerden birçok araştırmacı, planlayıcı ve karar vericiler yönünden hala önemli bir konu teşkil etmektedir. Çalışmada Çanakkale ili Biga ilçesinde konumlanan karışık üretim alanların içerisindeki çeltik alanlarının belirlenmesinde en çok kullanılan sınıflama algoritmaları arasından en büyük olabilirlik (ML), rastsal orman (RF) ve k-en yakın komşu (KNN)' nun performans değerlendirmesi amaçlanmıştır. 04 Haziran 2022 tarihinde çekilen Landsat 9 görüntüsünün görünür, yakın kızılötesi ve kısa dalgaboylu kızılötesi bantlarından yararlanılmıştır. Sınıflama, yoğun vejetasyon (D), seyrek vejetasyon (S), tarım alanları (A), su yüzeyi (W), yerleşim alanı – çıplak toprak (RB) ve çeltik (PR) olmak üzere 6 sınıfı içermektedir. Performanslar, aynı eğitim örnekleri ve aynı doğruluk kontrol noktaları ile test edilmiştir. Her bir sınıflamanın güvenilirliği doğruluk analizleri ile 150 rastgele eşit dağılımlı noktanın kontrolü ile yapılmıştır. Buna göre RF algoritması çeltik alanlarını %96.0' nın üzerinde doğrulukla ve ardından gelen KNN ise %92.0 doğrulukla belirleyebilmiştir. PR alanlarının yüksek doğrulukta belirlenmesinde tek tarihli Landsat 9 görüntüsünün kullanım potansiyeli olduğu görülmüştür. Sonuç olarak, benzer iklim, toprak ve arazi koşulları ile kıyaslanabilir ürün deseni koşulları altında PR alanlarının komşu sınıflardan güvenilir şekilde ayrıştırılması için RF algoritması kuvvetle önerilmekte olup, ücretsiz olması sebebiyle benzer çalışmalar için Landsat 9 önemli bir veri seti teşkil etmektedir.

# 1. INTRODUCTION

Paddy rice (PR) production has a vital role in food security, and it is a significant crop for over half of global population, whereby almost 20% of energy per capita sourced from rice consumption [1-3]. A great majority is growing in Asian countries, and the produced amount corresponds to 80% of world's total production and consumption rates [4-5]. However, many countries import rice due to their supply amount is not sufficient to meet the demands of the living population [6]. As it was cited by Semerci and Everest [7], rice production meets 80% of rice demand in Türkiye according to latest reports, whereby the gaps in the supply is met by import of approximately 150 thousand tons. Thence, prediction of rice production before harvest became an important point for forecasting the gap between production and expected consumption. On the other hand, identification of paddy rice cultivation areas is not important only in terms of nutrition or economic views, but also for controlling cropping system related environmental issues. The primary effect of paddy rice cultivation on the environment comprises from the large amount of irrigation water requirement since it is the main water intensive crop, and reported to consume almost one-fourth of world's freshwater resources [8]. In another point of view, it is one of the major contributors of anthropogenic greenhouse gas emissions, in particular, methane, whereby it is declared to be responsible for the 11% of methane emissions [9]. Therefore, up-to-date and reliable monitoring of rice planting areas has great importance in policies of food and environmental sustainability. In this context, remotely sensing data provides rapid, accurate, and relatively economic analysis of rice plantation.

Several studies have been conducted for paddy rice determination starting from 80s through different sensors, ranging from Landsat series to synthetic aperture radar data. Different techniques have developed for PR mapping in different regions of the world including particularly Asia [10], Mediterranean countries [11] and Australia [12], within the last decades [13]. Recent studies have dealt with comparison of varietal machine learning algorithms for classification of various LULC classes, as well as PR [14]. For instance, Mishra et al. [15] used knowledge-based decision tree approach, Onojeghuo et al. [16] considered support vector machines (SVM) and random forest (RF) algorithms, and Karkee et al. [17] utilized artificial neural networks. Present study focused on evaluation of different classification algorithms for paddy rice distinction using Landsat 9 imagery. Performances of three most widely used algorithms; maximum likelihood (ML), RF, and k-nearest neighborhood (KNN) were evaluated in the test site located within Biga District of Çanakkale Province, Türkiye. Although there are studies on comparison of different classifiers in the literature for different LULC types or a specific crop, they mostly based on at least a set of imageries or time series that covering different phenological stages of plants. However, it usually presents a limitation for many Landsat-based studies due to relatively low temporal resolution, whereas cloud cover may reduce the number of imageries within the growing season. Therefore, the study aimed to compare the performances of ML, RF and KNN algorithms, and investigate the potential of using one-date Landsat 9 imagery instead of multi-temporal imageries acquired in certain intervals during the growth period, for distinction of PR from other land use/land cover (LULC) classes. . To achieve this aim, the area was separated into six main LULC class including PR, the same training samples from each class were used in ML, RF, and classification steps, and accuracy of the same reference points were controlled to ensure that different performances are sourced from the properties of used algorithms.

# 2. MATERIAL AND METHOD

## 2.1. Study Area

The study was conducted within the specified area in Biga District of Çanakkale Province (40°20'12'' N - 27°17'24'' E). Figure 1 represents the location of the study area within Biga, Çanakkale and Türkiye. The 2021 year reports of Turkish Statistical Institute have revealed that Çanakkale Province includes 9.35% of Türkiye' s paddy rice cultivation areas with 121091 hectares (ha), while Biga takes the first place among 12 districts with 96341 ha, corresponding to 79.7% of whole province paddy rice areas [18]. The specified area was selected due to its complex surface properties, which represents a mixture of different LULC types that can give similar signatures with each other especially for irrigated fields, and covers an area of approximately 16380 ha.



**Figure 1.** Location of study area

## 2.2. Data Collection, Image Processing, and Supervised Classification

Landsat 9 imagery has 11 bands covering different channels in between visible and thermal infrared regions of electromagnetic spectrum. Even though the band properties of Landsat 8 and Landsat 9 are near-identical to each other, enhancements in radiometric resolution led to better identification of dark surfaces, such as; water bodies. In present study, Landsat 9 imagery acquired on 04 June, 2022 is downloaded freely from United States Geological Survey website [19], and the path/row number of the imagery is 181/32 to determine paddy rice fields in the area. Level-2 production that has been geometrically, radiometrically, and atmospherically corrected was used (UTM Zone 35). The imagery was A total of six bands (6B) visible, near-infrared and shortwave-infrared bands were stacked prior to subset of the study area.

53

A classification scheme was composed depending on the variations in LULC types in the specified area. Accordingly, six main LULC class determined including dense vegetation (D), sparse vegetation (S), agricultural field (A), water surface (W), residential area – base soil (RB), and paddy rice (PR). The D class was consisted of dense tree cover. The S class included all types of shrubs, bushes, and harvested crop residues. The A class covered all types of agricultural production fields, except paddy rice. The W class represents water surfaces of sea or stream or open channels. The RB class covered residential areas together with bare lands, which were spectrally similar. The PR class includes the paddy rice within the specified area.

Training sample polygons from each LULC class were collected manually for the classification process depending on visual interpretation of high-resolution images from closest date of Google Earth. Supervised classification procedures were applied using three different algorithms of ML [20], RF [21], and KNN [22]. The ML algorithm calculates the likelihood allocations of classes [23]. The RF known to be a common machine learning algorithm for classification studies [24], and it's capable of increasing classification accuracy by creating multiple decision trees. The KNN classifies the unknown data by finding K-closest data from the image with the help of Euclidean distance [25]. Different parameters have tested and the most appropriate LULC maps were selected to be exposed to accuracy assessment procedures.

## 2.3. Accuracy Assessment

Finally, accuracy assessments were conducted subsequent to image classification to evaluate reliabilities of the LULC maps (LULC$_{ML}$, LULC$_{RF}$, and LULC$_{KNN}$). High-resolution Google Earth imagery with closest date was used as the reference image. In this process, accuracies of 150 randomized control points, with 25 points for each LULC class were assessed by transferring on Google Earth application (Figure 2). The well-known measures for accuracy assessment, overall accuracy (OA, %) (1), overall kappa (K) coefficient ( 2), user's accuracy (UA, %) (3), and producer's accuracy (PA, %) (4), that obtained from error matrices were evaluated for each LULC map to state the classification performances of considered algorithms. The methodological workflow is given in Figure 3.

$$OA = \frac{\sum NoCC_P}{\sum NoR_P} \times 100 \qquad (1)$$

$$UA = \frac{\sum NoCC_{PLULC}}{\sum NoR_{PLULC}} \times 100 \qquad (2)$$

$$PA = \frac{\sum NoCC_P}{\sum NoC_{PLULC}} \times 100 \qquad (3)$$

$$K = \frac{P_0 - P_C}{1 - P_C} \qquad (4)$$

Where, $\Sigma NoCC_P$ represents total number of correctly classified pixels, $\Sigma NoR_P$ total number of reference pixels, $\Sigma NoCC_{PLULC}$ total number of correctly classified pixels in a certain LULC class, $\Sigma NoR_{PLULC}$ total number of reference pixels in the same class, $\Sigma NoC_{PLULC}$ total number of classified pixels in the same class, $P_O$ probability of correct classification, $P_C$ probability of change agreement.
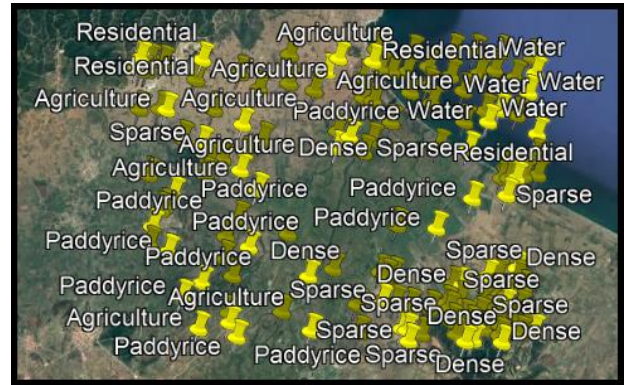


**Figure 2.** Distribution of accuracy check points
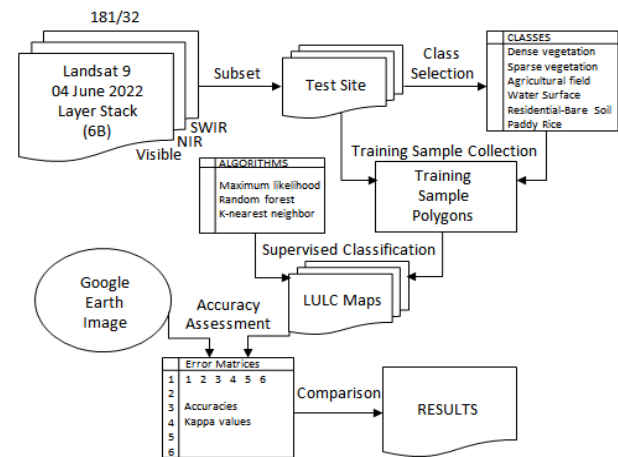


**Figure 3.** Flowchart for the supervise classification and performance comparison

## 3. RESULTS AND DISCUSSION

### 3.1. LULC Classifications

Classification of LULC is known to be one of the most widely used analyses within the frame of remote sensing, whereas Landsat imageries have long been used in several studies particularly for identification of various plants [26]. One of the main challenges for obtaining confidential LULC maps is the duration of processing time especially dealing with medium resolution imageries likewise Landsat series, which are available free of charge [27-28]. The produced maps of LULC$_{ML}$, LULC$_{RF}$, LULC$_{KNN}$ are given in Figure 4, Figure 5, and Figure 6, respectively. Areas of the LULC classes were calculated in hectares (ha) and percentages (%) (Table 1), and compared to each other. Accordingly, the area was predominantly covered by A and PR class in all classifications, whereby total area of mentioned classes corresponds to at least 55% of whole study area. Furthermore, water surface area differed slightly due to discrimination capabilities of considered algorithms for

the limited number of wet pixels on stream lines. Depending on $LULC_{ML}$, A areas seemed to cover major part of the area (29.3%), and it was followed by PR class (27.9%). Other vegetation types including dense and sparse vegetation were found as 3.5% and 19.0%, respectively, whereby the proportion of RB class was 9.6%. In comparison with $LULC_{ML}$, investigation of the class areas obtained from $LULC_{RF}$ has shown that PR class areas were quite higher than A class areas with a difference of 6.6%. Moreover, sparse and dense vegetation coverages calculated as 20.7 and 4.3%, which were both higher than $LULC_{ML}$ classification. Conversely, classification of RB areas through RF resulted in 4% lower coverage than ML. On the other hand, the class area coverages were more consistent for $LULC_{RF}$ and $LULC_{KNN}$ when compared with $LULC_{ML}$. Based on $LULC_{KNN}$, it was seen that majority of the study area was classified as PR (31.2%), while A class has the lowest share within all classifications (24.7%). The coverage of sparse vegetation showed highest value with 22.8% among all classifications. Dense vegetation was slightly lower than $LULC_{RF}$ and calculated as (4.9%). It was denoted that most effective components of supervised classification of LULC are training samples and classifiers, as well as ancillary of supplementary datasets when they are available [29]. In present study, the same training samples were utilized for all classifications for a systematic assessment of performances by avoiding the differences sourced from use of variant datasets. Therefore, the differences between LULC maps are only resulted from the discrimination properties of different classifiers, whereby the performances were determined through accuracy assessment procedures. Visual interpretations have revealed that, the RB area was overestimated especially for $LULC_{ML}$, and led to underestimation of PR class area, as well as A class. Similar situation was seen in $LULC_{KNN}$ for the misclassifications between RB and A classes, but the PR classification seemed more accurate in comparison with $LULC_{ML}$. Conversely, the $LULC_{RF}$ gave more precise results in all LULC types. Moreover, it was noticed that there were observable confusions between S and A classes in all classifiers in different rates.
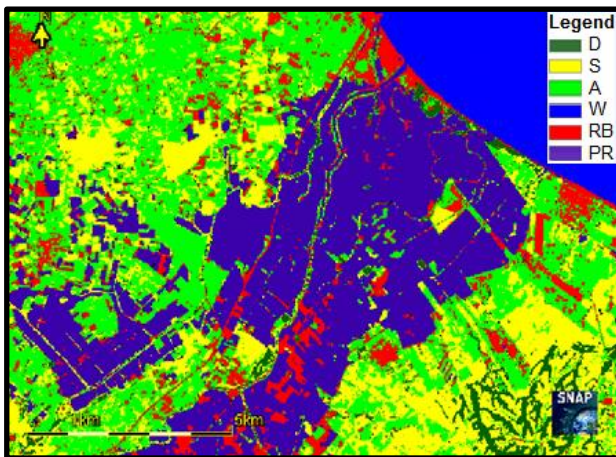

**Figure 4.** The distribution of classes from $LULC_{ML}$
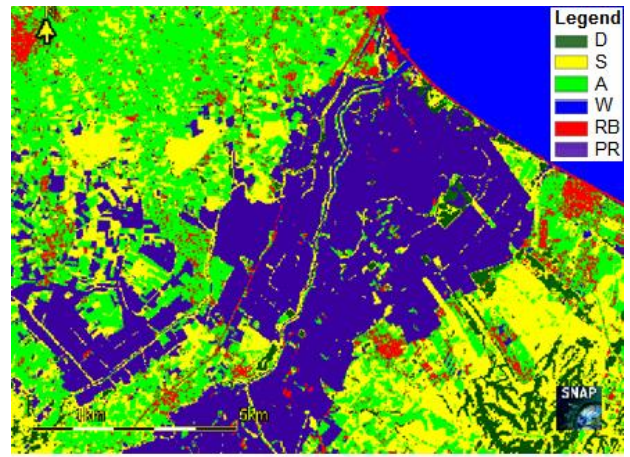

**Figure 5.** The distribution of classes from $LULC_{RF}$
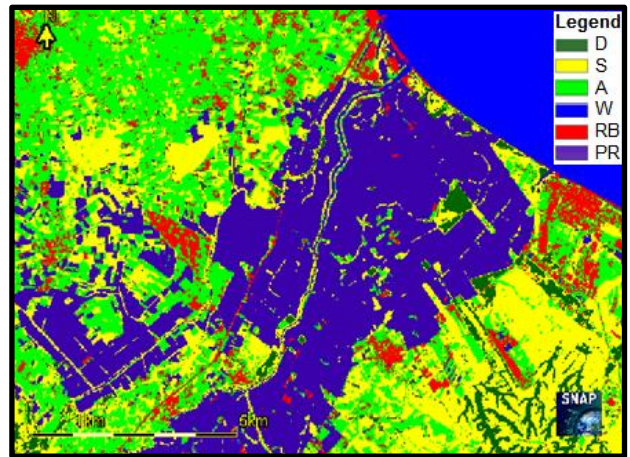

**Figure 6.** The distribution of classes from $LULC_{KNN}$

55

**Table 1**. Areas (ha, %) of LULC classes based on $LULC_{ML}$, $LULC_{RF}$, and $LULC_{KNN}$

| LULC CLASS | $LULC_{ML}$ Area | | $LULC_{RF}$ Area | | $LULC_{KNN}$ Area | |
|---|---|---|---|---|---|---|
| | ha | % | ha | % | ha | % |
| D | 569.3 | 3.5 | 706.2 | 4.3 | 680.6 | 4.2 |
| S | 3106.0 | 19.0 | 3388.5 | 20.7 | 3732.3 | 22.8 |
| A | 4805.0 | 29.3 | 4265.0 | 26.0 | 4053.2 | 24.7 |
| W | 1754.6 | 10.7 | 1760.5 | 10.7 | 1768.4 | 10.8 |
| RB | 1565.5 | 9.6 | 919.3 | 5.6 | 1041.3 | 6.4 |
| PR | 4577.4 | 27.9 | 5338.3 | 32.6 | 5102.0 | 31.2 |
| Total | 16377.8 | 100.0 | 16377.8 | 100.0 | 16377.8 | 100.0 |

### 3.2. Accuracy Assessments

The performances of different algorithms were identified through accuracy assessments. Using random sampling, the randomized points from each class were distributed over the study area to guarantee the uniform and appropriate representation of the classes [30]. Determination of rice via using satellite images usually face with difficulties due to the confusions between plantations with similar color and texture [31]. The error matrices representing confusions between the classes are given in Table 2, Table 3 and Table 4 for $LULC_{ML}$, $LULC_{RF}$, and $LULC_{KNN}$ classifications, respectively. Due to the fact that the study area was composed of different types of agricultural fields, the spectral signatures were highly mixed. Furthermore, relatively small sizes of the mentioned fields were also present a handicap for the study against relatively low resolution of imagery. Thus, there were confusions between in all

LULC maps in different rates. The overall accuracies (OA) of LULC$_{ML}$, LULC$_{RF}$, and LULC$_{KNN}$ were 84.7%, 93.3% and 88.0%, respectively. Furthermore the overall kappa (OK) values were calculated as 0.816, 0.920, and 0.856 with the same order. Even though all the classifications seemed reliable since they were over the threshold kappa coefficient value, it can be clearly seen that the lowest classification performance was obtained from LULC$_{ML}$ not only for PR, but also for A classification based on the tables. The UA and PA were calculated as 80.0% and 86.9% for PR class, whereas the values were found to be 72.0% and 75.0% for A class. The confusions were occurred particularly between PR and RB class, where the water level, the height and coverage of the plants were considerably low. Moreover, there were also misclassifications in A and S classes, as well as A and RB classes. The confusions may seem relatively low due small size of study area, and thus, limited number of control points. However, greater size of test areas together with higher number of considered LULC types expected to reduce the accuracy of ML classifications in areas with similar properties.

The LULC$_{RF}$ classification gave the most reliable results for all LULC types, and accuracy indicators have shown that the distribution of classes was strongly close to real situation (93.3%). However, the most observable finding among the selected LULC types was the near-perfect classification of PR class, which was correctly classified (100%), one out of twenty six reference points was accurate, which means that and only one control point from W class was misclassified as PR. Depending on the finding, in can be confidently said that the RF can be used for PR classifications within complex areas due to considerably low error rates, which may not be significantly affected from increase of the sampling size dependent to its discrimination capability.

The investigation of error matrices for LULC$_{KNN}$ has revealed that, although the general classification were highly accurate with high OA and OK values (88.0% and 0.856), some misclassifications in PR class, in addition to low performance of classifying complex structured A class areas. Nevertheless, the use of the algorithm instead of ML is probable to give more satisfactory results in the further studies, but seemed to be less confident in comparison with RF algorithm for such purposes with 92.0 % UA and PA values for PR, and 76.0% UA and PA for A classes, respectively.

Previous studies conducted in different locations have shown that paddy rice phenology mapping is the most effective method for optical remote sensing related PR mapping with high OA [32]. Different machine learning algorithms were utilized for PR mapping, namely SVM, decision trees (DT), and RF, while advanced algorithms were also developed for obtaining classifications with higher accuracies, as it is mentioned by Zhang et al. [33] In present study, the PR determination through RF and was also prosperous with high UA and PA. In fact, as it was cited by Phan et al. [34], Mahdianpari et al. [35] and Xia et al. [36] have declared that various studies have agreed on the view of RF is considered as one of the most preferred LULC classifier over the last 20 years due to many capabilities of such as performance of higher accuracy in comparison with SVM, KNN or MLC [37-38], and rapid processing by selection of significant variables [339]. On the other hand, Zhu et al. [40] proposed a combination method consisting of phenology and machine learning approaches for determination of PR areas, and succeed with 88.8% OA, which was quite lower from the RF and KNN accuracies of present study. Furthermore, crops were identified through RF algorithm by Yao et al. [41] with OA and K values of 87.0% and 0.82, respectively, whereby the accuracies were significantly improved by combining RF and deep neural networks. In the lights of above mentioned situations, findings of the study were coherent with the literature, and believed to present a basis for further researches.

**Table 2.** Error matrix of LULC$_{ML}$

| Class | D | S | A | W | RB | PR | Total | UA (%) | PA (%) |
|-------|----|----|----|----|----|----|-------|--------|--------|
| D | 24 | 0 | 1 | 0 | 0 | 0 | 25 | 96.0 | 100.0 |
| S | 0 | 21 | 2 | 0 | 2 | 0 | 25 | 84.0 | 91.3 |
| A | 0 | 2 | 18 | 0 | 4 | 1 | 25 | 72.0 | 75.0 |
| W | 0 | 0 | 0 | 21 | 2 | 2 | 25 | 84.0 | 100.0 |
| RB | 0 | 0 | 2 | 0 | 23 | 0 | 25 | 92.0 | 66.1 |
| PR | 0 | 0 | 1 | 0 | 4 | 20 | 25 | 80.0 | 86.9 |
| Total | 24 | 23 | 24 | 21 | 35 | 23 | 150 | | |
| OA | 84.7% | | | | | | | | |
| OK | 0.816 | | | | | | | | |

**Table 3.** Error matrix of LULC$_{RF}$

| Class | D | S | A | W | RB | PR | Total | UA (%) | PA (%) |
|-------|----|----|----|----|----|----|-------|--------|--------|
| D | 24 | 0 | 1 | 0 | 0 | 0 | 25 | 96.0 | 96.0 |
| S | 0 | 22 | 2 | 0 | 1 | 0 | 25 | 88.0 | 96.0 |
| A | 1 | 1 | 20 | 0 | 3 | 0 | 25 | 80.0 | 87.0 |
| W | 0 | 0 | 0 | 24 | 0 | 1 | 25 | 96.0 | 100 |
| RB | 0 | 0 | 0 | 0 | 25 | 0 | 25 | 100.0 | 86.2 |
| PR | 0 | 0 | 0 | 0 | 0 | 25 | 25 | 100.0 | 96.0 |
| Total | 25 | 23 | 23 | 24 | 29 | 26 | 150 | | |
| OA | 93.3% | | | | | | | | |
| OK | 0.920 | | | | | | | | |

**Table 4.** Error matrix LULC$_{KNN}$

| Class | D | S | A | W | RB | PR | Total | UA (%) | PA (%) |
|-------|----|----|----|----|----|----|-------|--------|--------|
| D | 23 | 0 | 2 | 0 | 0 | 0 | 25 | 92.0 | 85.2 |
| S | 3 | 20 | 2 | 0 | 0 | 0 | 25 | 80.0 | 95.2 |
| A | 1 | 1 | 19 | 0 | 3 | 1 | 25 | 76.0 | 76.0 |
| W | 0 | 0 | 0 | 24 | 0 | 1 | 25 | 96.0 | 92.0 |
| RB | 0 | 0 | 2 | 0 | 23 | 0 | 25 | 92.0 | 88.5 |
| PR | 0 | 0 | 0 | 2 | 0 | 23 | 25 | 92.0 | 92.0 |
| Total | 27 | 21 | 25 | 26 | 26 | 25 | 150 | | |
| OA | 88.0% | | | | | | | | |
| OK | 0.856 | | | | | | | | |

## 4. CONCLUSIONS

Determination of PR areas has great importance in various terms, such as, yield forecast, maintenance of resources, water management, and reducing gas emissions for mitigation of climate change effects. In comparison with traditional methods, remote sensing is known to be a valuable tool for gathering information on land surface properties, whereby generation of LULC maps including different classes, comprises rapid and reliable assessment of PR areas and their effects within the concepts agricultural or environmental perspectives. On this account, along with the properties of utilized remotely sensed data; collection of training dataset, selection of appropriate classifier, and implementation of validation procedures are the most essential points of supervised classification techniques. Thereby, the major objective of present study was to compare some of the most widely used classification algorithms, namely, ML, RF, and KNN, for identifying the best performing classifier for PR detection in specified area with complex spectral structure due to spatial characteristics. Accuracy assessment procedures were conducted through the same randomized control points for $LULC_{ML}$, $LULC_{RF}$, and $LULC_{KNN}$ that collected equally from each LULC classes. Depending on the magnitude of area, a total of 150 points from the six classes were concluded to adequate and representative for evaluation of the reliability. Using the same control points in comparison step of the actual statuses with classified ones have enabled identification of best performed classification since the control points were mutual, as well as training samples, for all LULC maps. Thence, the differences between accuracies guaranteed to source from the algorithms. Findings have revealed that the most successful classification was obtained from $LULC_{RF}$ in terms of OA, K, UA, and PA with values of 93.3%, 0.920, 100.0%, and 96.0%, respectively. It was followed by KNN classifier 88.0%, 0.856, 92.0% and 92.0% with the same order, whereby the ML algorithm gave the less accurate results in all categories. The use of ML classifier in larger areas seemed probable to led reduced level of accuracy with the increment in control points and complexity level of the LULC. In present study only six LULC classes were taken into account. On the other hand, the classification scheme can be modified in different locations depending on climatic and geographic circumstances in respect to properties of land surface within the studied areas, data quality, and availability of supplementary satellite-based, aerial or ground truth data. Therefore, a further study is planned for exploring the accuracy of classification considering more LULC classes with higher number of training samples in a wider area of interest by using high-resolution datasets and derived vegetation indices. In conclusion, findings of the study findings believed to serve as a basis for future researchs by designating appropriate algorithm for the most recent Landsat data.

## REFERENCES

[1] Song Y, Wang Y, Mao W, Sui H, Yong L, Yang D, et al. Dietary cadmium exposure assessment among the Chinese population. PLoS ONE 2017;12:e0177978.

[2] Halder D, Saha JK, Biswas A. Accumulation of essential and non-essential trace elements in rice grain: Possible health impacts on rice consumers in West Bengal, India. Science of the Total Environment 2020;706:135944.

[3] Wei J, Cui Y, Luo W, Luo Y. Mapping paddy rice distribution and cropping intensity in China from 2014 to 2019 with Landsat images, effective flood signals, and Google Earth Engine. Remote Sensing, 2022;14:759.

[4] Muthayya JD, Sugimoto SD, Montgomery S, Maberly GF. An overview of global rice production, supply, trade, and consumption. Annals of the New York Academy of Sciences 2014;1324(1):7-14.

[5] Xia L, Zhao F, Chen J, Yu L, Lu M, Yu Q, et al. A full resolution deep learning network for paddy rice mapping using Landsat data. ISPRS Journal of Photogrammetry and Remote Sensing 2022;194:91-107.

[6] Saltık B, Genc L. Rice area determination using Landsat-based indices and land surface temperature values. International Journal of Agricultural and Biosystems Engineering 2016;10(7):462-470.

[7] Semerci A., Everest B. Econometric analysis of paddy production in Çanakkale Province. Türk Tarım ve Doğa Bilimleri Dergisi 2021;8(3):576-584.

[8] Cao J, Cai X, Tan J, Cui Y, Xie H, Liu F, et al. Mapping paddy rice using Landsat time series data in the Ganfu Plain irrigation system, Southern China, from 1988-2017. International Journal of Remote Sensing 2021;42(4):1556-1576.

[9] Smartt AD, Brye KR, Rogers CW, Norman RJ, Gbur EE, Hardke JT, et al. Previous crop and cultivar effects on methane emissions from drill-seeded, delayed-flood rice grown on a clay soil. Applied and Environmental Soil Science 2016:9542361.

[10] Dong J, Xiao X, Menarguez MA, Zhang G, Qin Y, Thau D, et al. Mapping paddy rice planting area in northeastern Asia with Landsat 8 images, phenology-based algorithm and Google Earth Engine. Remote Sensing of Environment 2016;185:142-154.

[11] Nguyen DB, Wagner W. European rice cropland mapping with Sentinel-1 data: the Mediterranean region case study. Water 2017;9:372.

[12] McCloy KR, Smith FR, Robinson MR. Monitoring rice areas using Landsat MSS data. International Journal of Remote Sensing 1987;8:741-749.

[13] Thorp KR, Drajat D. Deep machine learning with Sentinel satellite data to map paddy rice production stages across West Java, Indonesia. Remote Sensing of Environment 2021;265:112679.

[14] Basheer S, Wang X, Farooque AA, Nawaz RA, Liu K, Adekanmbi T, et al. Comparison of land use

57

land cover classifiers using different satellite imagery and machine learning techniques. Remote Sensing 2022;14:4978.

[15] Mishra VN, Prasad R, Kumar P, Srivastava PK, Rai PK. Knowledge-based decision tree approach for mapping spatial distribution of rice crop using C-band synthetic aperture radar-derived information. Journal of Applied Remote Sensing 2017;11:046003.

[16] Onojeghuo AO, Blackburn GA, Wang QM, Atkinson PM, Kindred D, Miao XY. Mapping paddy rice fields by applying machine learning algorithms to multi-temporal Sentinel-1A and Landsat data. International Journal of Remote Sensing 2018;39:1042-1067.

[17] Karkee M, Steward BL, Tang L, Aziz SA. Quantifying sub-pixel signature of paddy rice field using an artificial neural network. Computers and Electronics in Agriculture 2009;65:65-76.

[18] Turkish Statistical Institute [Internet] 2022 [Cited 2023 January 24]. Available from: https://biruni.tuik.gov.tr/medas/?locale=tr

[19] United States Geological Survey [Internet] 2022 [Cited 2022 December 16]. Available from: https://earthexplorer.usgs.gov

[20] Richards JA, Jia X. Remote sensing digital image analysis: An introduction. Berlin: Springer Verlag; 2006.

[21] Breiman, L. Random forests. Machine Learning, 2001;45(1):5-32.

[22] Fix E, Hodges JL. Discriminatory Analysis, Nonparametric Discrimination: Consistency Properties; Technique Report No. 4; U.S. Air Force School of Aviation Medicine, Randolf Field Texas: Universal City, TX, USA; 1951. p. 238-247.

[23] Erdanaev E, Kappas M, Wyss D. The identification of irrigated crop types using support vector machine, random forest and maximum likelihood classification methods with Sentinel-2 data in 2018: Tashkent Province, Uzbekistan. International Journal of Geoinformatics, 2022;18(2):37-53.

[24] Berhane TM, Lane CR, Wu Q, Autrey BC, Anenkhonov OA, Chepinoga VV, et al. Decision-tree, rule-based, and random forest classification of high-resolution multispectral imagery for wetland mapping and inventory. Remote sensing 2018;10(4):580.

[25] Kalpana YB, Nandhagopal SM. LULC image classifications using k-means clustering and knn algorithm. Dynamic Systems and Applications 2021;30(10):1640-1652.

[26] Hedayati A, Mohammad HV, Behzadi S. Paddy lands detection using Landsat-8 satellite images and object-based classification in Rasht city, Iran. The Egyptian Journal of Remote Sensing and Space Science 2022;25(1):73-84.

[27] Gomez C, White JC, Wulder AA. Optical remotely sensed time series data for land cover classification: A review. ISPRS Journal of Photogrammetry and Remote Sensing 2016;116:55-72.

[28] Yuh YG, Tracz W, Matthews HD, Turner SE. (Application of machine learning approaches for land cover monitoring in northern Cameroon. Ecological Informatics, 2023;74:101955.

[29] Johnson B. Scale issues related to the accuracy assessment of land use/land cover maps produced using multi-resolution data: Comments on "The improvement of land cover classification by thermal remote sensing". Remote Sensing 2015, 7, 8368-8390. Remote Sensing 2015;7:13436-13439.

[30] Zhao Y, Gong P, Yu L, Hu L, Li X, Li C, et al. Towards a common validation sample set for global land-cover mapping. International Journal of Remote Sensing, 2014;35:4795-4814.

[31] Abdi-Sukmono A. Identification of rice field using multi-temporal NDVI and PCA method on Landsat 8 (Case Study: Demak, Central Java). IOP Conf. Ser.:Earth and Environmental Science 2017;54:012001.

[32] Zhao R, Li Y, Ma M. Mapping Paddy Rice with Satellite Remote Sensing: A Review. Sustainability 2021;13:503.

[33] Zhang M, Lin H, Wang G, Sun H, Fu J. Mapping paddy rice using a convolutional neural network (CNN) with Landsat 8 datasets in the Dongting Lake Area, China. International Remote Sensing, 2018;10:1840.

[34] Phan TN, Kuch V, Lehnert LW. Land cover classification using Google Earth Engine and random forest classifier - the role of image composition. Remote Sensing 2020;12:2411.

[35] Mahdianpari M, Salehi B, Mohammadimanesh F, Motagh M. Random forest wetland classification using ALOS-2 L-band, RADARSAT-2 C-band and TerraSAR-X imagery. ISPRS Journal of Photogrammetry and Remote Sensing 2017;130:13-31.

[36] Xia J, Falco N, Benediktsson JA, Du P, Chanussot J. Hyperspectral image classification with rotation random forest via KPCA. IEEE Journal of Selected Topics in Applied Earth Observations and Remote Sensing 2017;10(4): 1601-1609.

[37] Rodriguez-Galiano VF, Chica-Rivas M. Evaluation of different machine learning methods for land cover mapping of a Mediterranean area using multi-seasonal Landsat images and Digital Terrain Models. International Journal of Digital Earth 2012;7:492-509.

[38] Abdel-Rahman EM, Mutanga O, Adam E, Ismail R. Detecting Sirex noctilio grey-attacked and lightning-struck pine trees using airborne hyperspectral data, random forest and support vector machines classifiers. ISPRS Journal of Photogrammetry and Remote Sensing 2014;88:48-59.

[39] Van-Beijma S, Comber A, Lamb A. Random forest classification of salt marsh vegetation habitats using quad-polarimetric airborne SAR, elevation and optical RS data. Remote Sensing of the Environment 2014;149:118-129.

[40] Zhu A-X, Zhau F-X, Pan H-B, Liu J-Z. Mapping rice paddy distribution using remote sensing by coupling deep learning with phenological characteristics. Remote Sensing 2021;13(7):1360.

58

[41] Yao J, Wu J, Xiao J, Zhang Z, Li J. The Classification Method Study of Crops Remote Sensing with Deep Learning, Machine Learning, and Google Earth Engine. Remote Sensing, 2022;14:2758.

**Türk Doğa ve Fen Dergisi**
**Turkish Journal of Nature and Science**

www.dergipark.gov.tr/tdfd

# Application of Economic Load Dispatch to Power Systems with the Artificial Bee Colony Algorithm Approach

**Mustafa Yasin ERTEN[1]** iD **, İbrahim EKE[1*]** iD

[1] Kırıkkale University, Faculty of Engineering and Natural Sciences, Electrical and Electronics Engineering Department, Kırıkkale, Türkiye
Mustafa Yasin ERTEN ORCID No: 0000-0002-5140-1213
İbrahim EKE ORCID No: 0000-0003-4792-238X

*Corresponding author: eke@kku.edu.tr*

**Abstract:** The economic dispatch problem has received increasing attention with the development of modern power systems. It is an optimization problem that aims to find the most economical schedule of generating units while satisfying load demand and operational constraints. In this paper, the application of the Artificial Bee Colony (ABC) algorithm to the economic dispatch problem is presented. The proposed method is demonstrated using a six-unit system. Additionally, the results obtained from the proposed method are compared with those from other optimization methods applied to the same problem.

## Yapay Arı Kolonisi Algoritması Yaklaşımı ile Ekonomik Yük Dağıtımının Güç Sistemlerine Uygulanması

**Öz:** Modern güç sistemlerindeki gelişmelerle birlikte ekonomik yük dağıtımı araştırmacıların ilgisini çekmeye başlamıştır. Ekonomik yük dağıtımı ise yük talebi ve diğer işletme kısıtlarını sağlama koşulları altında üretim üniteleri arasında en ekonomik dağıtımı yapan bir optimizasyon problemidir. Bu çalışmada kayıpları olan iletim hattı şebekesini besleyen 6 üniteli sistemin optimum çalışma noktaları Yapay Arı Kolonisi (YAK) algoritması yardımıyla belirlenmiştir. Elde edilen sonuçlar aynı problemin farklı optimizasyon problemleri sonuçlarıyla karşılaştırılmıştır.

## 1. INTRODUCTION

With the increase in industrialization and the development of technology, the need for energy is increasing day by day. Moreover, the spread of urbanization and the acceleration of migration from villages to cities have increased energy usage in daily life. In fact, Turkey's national energy plan envisages a 39.5% increase in primary energy consumption in 2035 compared to 2020 [1]. This situation creates an additional burden for countries to meet the demand. Therefore, the efficient use of the energy produced, the reduction of losses, and energy consumption with minimum cost have become crucial issues.

Since Economic Load Dispatch (ELD) is made to dispatch the energy demanded by consumers among generators with the lowest possible cost, finding a solution to this

problem has strategic importance for the power system. Therefore, ELD conditions can be met by minimizing generation and transmission costs. The power generation cost function is obtained by combining fuel, idle, and start-up costs. When minimizing the fuel costs of generators in power systems, it is desired to produce power at the most appropriate value between the maximum and minimum values. Recently, heuristic methods, which are reliable, fast, and effective optimization algorithms, have been used as an alternative to the mathematical approaches used in solving the Economic Dispatch (ED) problem [2].

Bouzeboudja et al. solved the economic dispatch problem in IEEE's 25 busbar system by using a real coded genetic algorithm with different methods [3]. Abido dealt with the environmental/economic dispatch problem with the genetic algorithm, pareto genetic algorithm and pareto

evolution algorithm in nonlinear optimization solutions in IEEE's 30 busbar system [4]. Türkay examined the ELD problem with a genetic algorithm to feed generators at minimum cost [5]. Alrashidi and El-Hawary solved the environmental/economic dispatch problem of particle swarm optimization in IEEE's 30 busbar power system and compared the results with different methods [6]. Wang and Singh [7] studied the ED problem in a four-zone power system. It is used a modified particle swarm optimization algorithm, taking into account environmental effects in IEEE's 30-bus power system. Bouktir et al. investigated the environmental and economic load dispatch problem using the multi-particle swarm optimization algorithm. Vishwakarma et al. have studied the solution to the ELD problem by using Simulation Annealing Algorithm [8]. Cai et al. [9] solved the ED problem using the chaotic ant swarm optimization algorithm.

Ozyon et al. addressed the environmental power dispatch problem on an IEEE 6 generator 30 busbar test system. The multi-objective optimization problem was transformed into a single-objective optimization problem with the weighting process, and its solution was provided by the Artificial Bee Colony (ABC) algorithm. The results were examined by evaluating whether losses were included or not on the test system [10].

Öztürk et al. have realized an ELD problem that minimizes the energy cost for the load provided by a three-unit thermal power plant with the ABC algorithm. The results showed that the ABC algorithm produces economic results in determining the output power of the generator units [11].

Eminoğlu and Karahan developed an interface to solve the ELD problem in their study. Through this interface, the study solved the ELD problem with Differential Improvement Algorithm (DGA) and Particle Swarm Optimization (PSO) and compared the performances of the algorithms. The results revealed that the PSO algorithm performs better in the ELD problem [12].

Özyon discussed the environmental and economic load dispatch problem by adding wind and solar energy generation resources to the thermal power plants in the IEEE 30-bus-6 generator power system. The optimization results of the system were obtained by using the Charged System Search (CSS) algorithm, including both renewable energy sources and only thermal power [13]. Andic et al. solved the ELD problem with the Crow Search Algorithm (CAA) by incorporating the valve point effects of steam turbines. However, it is emphasized that the solution they developed was more successful compared with Genetic Algorithm (GA) and Symbiotic Organisms Search (SOS) [14].

Dixit et al. examined the generation system consisting of 18 thermal units with a second-order (Convex) cost function, a standard IEEE 30 bus system, and 15 power generation units with emission restrictions in the island of Crete the ABC method they proposed. They compared the obtained results with different algorithms and revealed

that the ABC method is easy to integrate, has fast convergence, and has a high ability to perform searches close to the optimum solution [15].

Turgut and Demir addressed the ELD problem by applying Artificial Cooperative Search (ACS) to two different test power generation systems. They showed lower operating costs with LFS compared to other algorithms [16].

Özyön investigated the effects of wind power plants on the ELD problem using DGA. The results were compared with other studies in the literature, which was carried out on two separate test systems by considering and neglecting the transmission losses [17].

ABC is an algorithm with very few control parameters based on swarm intelligence, which can be used for solving numerical and discrete problems. In this study, the ELD problem, one of the optimization problems, is solved using the heuristic method ABC. The problem is based on the data of the study conducted in Turkey. The obtained results are compared with the results of different optimization problems of the same problem. In this study, it has been seen that heuristic methods give more reliable and better results than traditional methods and can successfully solve the economic dispatch problem in a power system used in Turkey. Furthermore, the proposed method is applied to a system with six generators, and the results are obtained and compared with the results obtained from other available studies. As a result, it has been shown how the ABC algorithm and program can be successfully applied in solving the economic load dispatch problem.

## 2. MATERIAL AND METHOD

The solution to the ELD problem involves operating the generators in power systems within specific limit values in response to increasing load demand while minimizing the overall system cost. The economic dispatch aims to determine the optimal allocation for each unit at intervals of 3 to 5 minutes based on the load requirements [2]. Figure 1 depicts the connection diagram of thermal power plants on a transmission line in relation to the load demand.
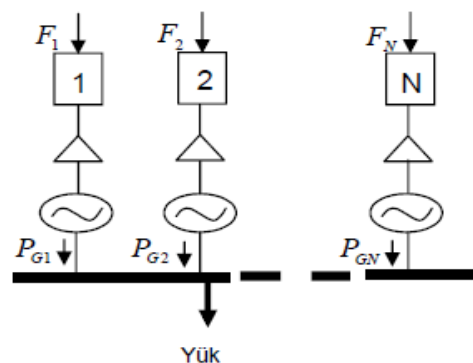


**Figure 1.** Connection diagram of thermal power plants to the transmission line

61

The ELD problem in energy systems is a power allocation problem characterized by large-scale linear and nonlinear constraints. The input of the fossil fuel generator is defined as a function of the output power, which can be represented by linear, piecewise, exponential, or polynomial functions. In this study, the input-output characteristic is modeled using a quadratic equation. The objective of ELD is to minimize the operating cost of the entire group of generators. Mathematically, the operating cost of the total generators can be expressed as follows.

$$Min \sum_{i=1}^{N} F_i(P_i) = Min \sum_{i=1}^{N} a_i + b_i P_i + c_i P_i^2 \qquad (1)$$

The objective function (cost function) given by Equation 1 is solved depending on the following constraints. The output power of the generators must be greater than or equal to the minimum active power value or less than or equal to the maximum active power value within the limit values determined as shown in Equation 2.
Power balance constraint :

$$\sum_{i=1}^{N} P_i - P_D - P_L = 0 \qquad (2)$$

Here, the loss of the transmission line is found as follows.

$$P_L = \sum_{i=1}^{N} B_i - P_i^2 \qquad (3)$$

Output power capacity of generators: The generator's output power must be greater than or equal to the minimum allowable power value or less than or equal to the maximum allowable power value.

$$P_{min,i} \leq P_i \leq P_{max,i} \qquad (4)$$

The cost function of the ED problem, as indicated in Equation 1, serves as the objective function in ABC and chaotic ABC (CABC). The variables utilized in the objective function are assigned randomly within the limit values specified in Equation 2. Equation 3 represents the total active power loss of the transmission line, while Equation 4 presents the active power balance equation of the transmission line. In ED problems, the constraints described in Equations 3 and 4 are also taken into account and employed as penalty functions in ABC and CABC.

$$P_L = \sum_{i=1}^{N} \sum_{j=1}^{N} P_i B_{ij} P_j + \sum_{i=1}^{N} B_{i0} P_i + B_{00} \qquad (5)$$

$$D = \sum_{i=1}^{N} P_{Gi} - P_D - P_L = 0 \qquad (6)$$

In the above equations:
$P_{Gi}$ : Output power of the $i^{th}$ generator
$a_i, b_i, c_i$ : Price coefficients of the $i^{th}$ generator
$F_i(P_{Gi})$ : The price required for the generator to produce $P_i$ power
$N$ : Number of groups
$P_{Gi}^{min}$ : Minimum output power of $i^{th}$ generator
$P_{Gi}^{max}$ : Maximum output power of the $i^{th}$ generator
$P_L$ : Loss of transmission line
$B_{ij}$ : Transmission line loss coefficient matrix
$B_{0i}$ : The vector of the same length as P
$B_{00}$ : Constant
$P_D$ : The demanded power

## 3. ARTIFICIAL BEE COLONY ALGORITHM (ABC)

ABC was initially developed by Derviş Karaboğa in 2005 as an optimization algorithm based on the behavior of bee colonies for real parameter optimization [18]. In a bee colony's natural life, there is a division of tasks among bees collecting honey. Worker bees, observer bees, and scout bees carry out distinct roles within the colony. Worker bees are responsible for visiting honey sources, collecting flower essences, and depositing the honey they gather into the hive. Additionally, worker bees have the task of communicating the quality of the honey source they collect to the observer bees. Observer bees, in turn, identify new honey sources and guide the worker bees towards them. To identify new sources, observer bees rely on the previous observations made by worker bees, which are then analyzed. Scout bees, on the other hand, wander randomly and search for new honey sources solely based on their own observations. In the algorithm, the process of determining the address of the nectar source is presented as a solution to the optimization problem. The size of the nectar source is considered as the degree of suitability in the relevant solution. According to the algorithm, each honey source is collected by a single worker bee, thus the number of solutions in the population is equal to the number of employed bees [18].

The algorithm operates through the following five fundamental steps:
1. Determining the initial values of honey source regions,
2. Directing the worker bees to the designated honey sources,
3. Conducting probability calculations for candidate regions that could become honey sources,
4. Observer bees determining new honey sources based on the information conveyed by the worker bees,
5. Decision-making regarding decommissioning existing honey sources.

In the algorithm, the initial values of the honey source regions are assigned using Equation 7 [18].

$$x_{ij} = x_j^{min} + rand(0,1)(x_j^{max} - x_j^{min}) \qquad (7)$$

In the equation, j represents the number of produced resources, while i represents the number of optimization parameters.

During the second step, the worker bee gathers nectar from the designated honey source. Additionally, it assesses the quality of a new source by analyzing a nearby honey source. The calculation for the exploration of the new honey source is provided in Equation 8, where $\phi$ is a random real number within the range of [-1, 1] [18].

$$v_{ij} = x_{ij} + \phi_{ij}(x_{ij} - x_{kj}) \qquad (8)$$

If the value of ij v exceeds the pre-defined parameter limits during the evaluation process, the translation is performed based on Equation 9. Subsequently, the suitability of the solution cost is calculated using Equation 10 [18].

$$v_{ij} = \begin{cases} x_j^{min}, & v_{ij} < x_j^{min} \\ v_{ij}, & x_j^{min} \le v_{ij} \le x_j^{max} \\ x_j^{max}, & v_{ij} > x_j^{max} \end{cases} \qquad (9)$$

$$fitness_i = \begin{cases} 1/(1 + f_i, & f_i \ge 0 \\ 1 + abs(f_i), & f_i < 0 \end{cases} \qquad (10)$$

The observer bees evaluate the cost/availability ratios of the hive, and a probability-based selection is made based on the amount of nectar. In the basic ABC algorithm, the roulette wheel method is used for probability-based selection. Consequently, the size of each slice depends on the fitness value it represents. The final stage of the algorithm involves determining the depleted honey source. After completing the search process of the worker and observer bees, the algorithm can identify a honey source that has been depleted. Counters that are updated during the search process are utilized for this purpose. If the counter for any honey source exceeds the control parameter, referred to as the limit and determined by the algorithm, that particular source is deemed exhausted and abandoned. As a result, the worker bee associated with the abandoned region is removed from the algorithm. The scout bee that discovers a new source transform into a worker bee, collecting honey from the newfound source, and the limit value for that source is reset. Only one scout bee is allowed to emerge per cycle. There are two criteria for terminating the algorithm. These conditions can be defined as either reaching the maximum number of cycles or exceeding a specified fault tolerance value, as determined by the user [18].

# 4. APPLICATION OF ABC ALGORITHM TO ELD SYSTEM

When searching for a solution to an optimization problem, general optimization techniques are employed to minimize or maximize objective functions based on available data. In the case of a classical economic load dispatch problem, the objective is to achieve maximum power output at the lowest cost while maintaining power balance. However, traditional optimization methods may not be adequate for solving such problems. Therefore, in this article, the economic load dispatch problem is addressed using the ABC method. The ABC algorithm, known for its minimal control parameters and reliance on swarm intelligence, can effectively tackle numerical and discrete problems. The economic load dispatch problem is implemented using the ABC method in the Matlab environment, and the problem-solving process is depicted in Figure 2, illustrating the flow diagram designed for this purpose.

The algorithm begins by creating a random colony with a size determined by the number of variables and bees. Half of the colony consists of worker bees, while the other half represents observer bees. Worker bees select random sources, calculate their positions, and store them in temporary memory. In each cycle, a worker bee discards the data in its memory if it achieves better results in the subsequent cycle, retaining only the best result. Nectar amounts are calculated by the bees based on the best source positions, and these amounts are stored in memory throughout the cycles, with the best solution determined at the end of the maximum cycle.

Observer bees visit sources and calculate nectar amounts based on information received from the worker bees. Worker bees, in search of better nectar around a selected source, visit neighboring sources up to a defined limit and compare the nectar amounts. If a newly found source is superior, the worker bee discards the previous nectar amount and considers the new source as the center for the next cycle. If no improvement is found, one of the worker bees becomes a scout bee and searches for a new source.

This study addresses the economic load dispatch problem using the ABC method. A test system with 6 generators is employed to evaluate the proposed method's performance. The obtained results are compared with those from different methods. The details and limitations of the test system can be found in Table 1.

**Table 1. The data and limitations of the test system**

| Unit | A | B | C | Pmin | Pmax |
|------|--------|------|-----|------|------|
| 1 | 0.007 | 7 | 240 | 100 | 500 |
| 2 | 0.0095 | 10 | 200 | 50 | 200 |
| 3 | 0.0090 | 8.5 | 220 | 80 | 300 |
| 4 | 0.0090 | 11 | 200 | 50 | 150 |
| 5 | 0.0080 | 10.5 | 220 | 50 | 200 |
| 6 | 0.0075 | 12 | 190 | 50 | 120 |

63
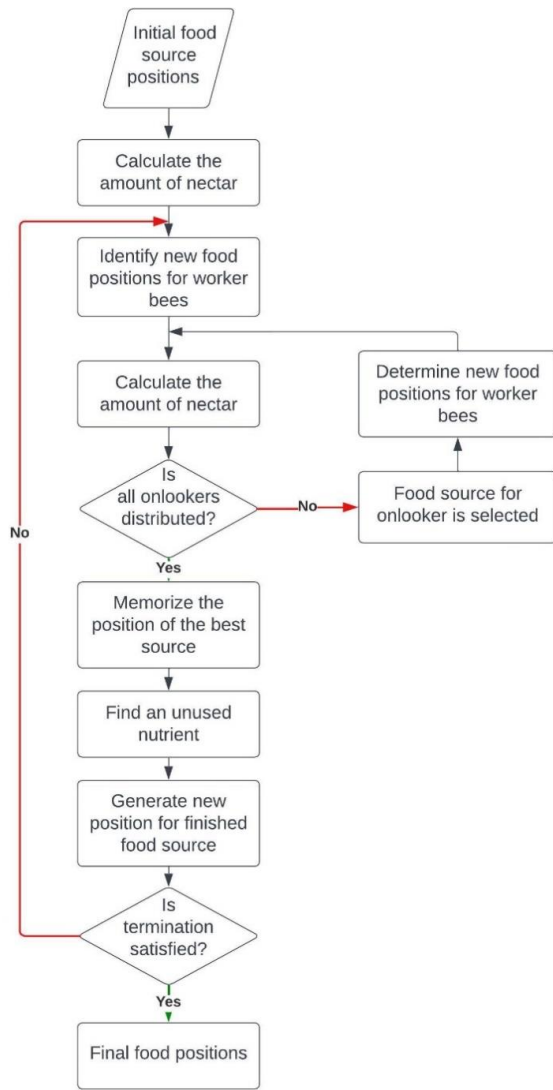
**Figure 2.** Flow diagram of ABC algorithm for ELD problem

The program worked in 1001 steps; the objective value was found to be 15445.9011. The output power values to be produced for each generator are presented in Table 2.

**Table 2. The output power for each generator**

| Generator | ABC | CABC |
|-----------|-----------|------------|
| $Pg_1$ | 444.1615 | 441.7425 |
| $Pg_2$ | 162.0570 | 180.9894 |
| $Pg_3$ | 258.2421 | 257.4831 |
| $Pg_4$ | 150.0000 | 149.9746 |
| $Pg_5$ | 175.7886 | 159.3187 |
| $Pg_6$ | 85.1814 | 85.68010 |
| Total loss | 12.4250 | 12.1885 |
| Total cost | 15453.0979 | 15445.9011 |

The Chaotic Artificial Bee Colony (CABC) algorithm utilizes chaotic maps in comparison to the traditional Artificial Bee Colony (ABC) algorithm, providing several advantages such as enhanced convergence speed, improved solution distribution, sensitivity to initial values, and adaptability. The utilization of chaotic maps based on chaos theory equips the CABC algorithm with stronger search and exploration capabilities. Chaos theory focuses on randomness and irregularity in dynamic systems, allowing for better dispersion of solutions. This enables the algorithm to approach global optima more

swiftly and effectively. Additionally, the impact of chaotic maps facilitates faster convergence and aids in solving complex problems more expeditiously in CABC. The sensitivity to initial values allows CABC to yield better results in a shorter time, enhancing its responsiveness to initial conditions. Furthermore, its adaptability enables the algorithm to perform better in specific problems and may prove more effective for diverse types of optimization problems.

Considering factors such as problem size, complexity, computational power, and initial values in the context of the addressed ELD problem, it is evident that the results obtained through the CABC algorithm are more successful compared to those achieved using ABC.

## 5. DISCUSSION AND CONCLUSION

To solve the ELD problem using the ABC algorithm, multiple attempts were made within the algorithm, and the best result obtained was considered as the solution for the ELD problem. The ABC algorithm was executed multiple times until the stopping criterion was satisfied, and the values that yielded the optimal solution were recorded as the final result. In this study, the number of cycles was adopted as the stopping criterion. By running the algorithm "i" times, it was observed that the desired result could be achieved within approximately "n" cycles. To ensure reliability, a total of 1001 cycles were selected.

The CABC algorithm, through the utilization of chaotic maps based on chaos theory, exhibits improved convergence speed, better solution distribution, sensitivity to initial values, and adaptability. As demonstrated in Table 2, these capabilities enable the algorithm to yield more successful cost function responses and lower loss values.

In future works, the integration of renewable energy resources into the existing thermal power units will be explored, and the impact of renewable energy sources on the system's operation will be investigated.

## REFERENCES

[1] ETKB. (2023). "Türkiye Ulusal Enerji Planı" Yayımlanmıştır. https://enerji.gov.tr/duyuru-detay?id=20317.

[2] Döşoğlu, M. K., Duman, S., & Öztürk, A. (2009). Genetik algoritma kullanarak ekonomik dağıtım analizi: Türkiye uygulaması. Politeknik Dergisi, 12(3), 167-172.

[3] Bouzeboudja, H., Chaker, A., Allali, A., & Naama, B. (2005). Economic dispatch solution using a real-coded genetic algorithm. Acta Electrotechnica et informatica, 5(1), 4.

[4] Abido, M. A. (2003). A niched Pareto genetic algorithm for multiobjective environmental/economic dispatch. International journal of electrical power & energy systems, 25(2), 97-105.

64

[5] Türkay, B. (2002). Economic dispatch at the ambarli power plant using genetic algorithm. IU-Journal of Electrical & Electronics Engineering, 2(1), 395-399.

[6] AlRashidi, M. R., & El-Hawary, M. E. (2006, July). Economic dispatch with environmental considerations using particle swarm optimization. In 2006 Large Engineering Systems Conference on Power Engineering (pp. 41-46). IEEE.

[7] Wang, L., & Singh, C. (2008). Balancing risk and cost in fuzzy economic dispatch including wind power penetration based on particle swarm optimization. Electric Power Systems Research, 78(8), 1361-1368.

[8] Vishwakarma, K. K., Dubey, H. M., Pandit, M., & Panigrahi, B. K. (2012). Simulated annealing approach for solving economic load dispatch problems with valve point loading effects. International Journal of Engineering, Science and Technology, 4(4), 60-72.

[9] Cai, J., Ma, X., Li, L., Yang, Y., Peng, H., & Wang, X. (2007). Chaotic ant swarm optimization to economic dispatch. Electric Power Systems Research, 77(10), 1373-1380.

[10] Özyön, S., Yasar, C., Özcan, G., & Temurtas, H. (2011). An artificial bee colony algorithm (ABC) approach to nonconvex economic power dispatch problems with valve point effect. In National Conference on Electrical, Electronics and Computer (FEEB'11) (pp. 294-299).

[11] Öztürk, A., Çobanlı, S., Duman, S., Tosun, S., & Döşoğlu, K. (2011, May). Yapay arı kolonisi algoritması ile elektrik güç sistemi optimal yakıt maliyetinin belirlenmesi. In 6th International Advanced Technologies Symposium (IATS'11) (Vol. 16, p. 18).

[12] Eminoğlu, U., & Karahan, O. (2017). Metasezgisel metotlar kullanılarak ekonomik yük dağıtımı probleminin çözümü: grafiksel kullanıcı arayüzü uygulaması. Politeknik Dergisi, 20(4), 827-835.

[13] Özyön, S. (2020). Yenilenebilir Enerji Üretim Birimleri İçeren Çevresel-Ekonomik Güç Dağıtımı Probleminin Yüklü Sistem Arama Algoritması ile Çözümü. Avrupa Bilim ve Teknoloji Dergisi, (18), 81-90.

[14] Andiç, C., Öztürk, A., & Tosun, S. Karga Arama Algoritmasi Kullanilarak Valf Nokta Etkili Ekonomik Yük Dağitimi Probleminin Çözülmesi. IV. Uluslararasi Bilimsel ve Mesleki Çalişmalar Kongresi – Mühendislik (BILMES EN 2019), Ankara, Türkiye, 7 - 09 Kasım 2.

[15] Dixit, G. P., Dubey, H. M., Pandit, M., & Panigrahi, B. K. (2011). Economic load dispatch using artificial bee colony optimization. International Journal of Advances in Electronics Engineering, 1(1), 119-124.

[16] Turgut, M. S., & Demir, G. K. (2017). Ekonomik Yük Dağıtımı Probleminin Yapay İşbirlikçi Algoritması ile Çözümü. Dokuz Eylül Üniversitesi Mühendislik Fakültesi Fen ve Mühendislik Dergisi, 19(55), 16-27.

[17] Özyön, S., & Yaşar, C. Ekonomik Güç Dağıtım Problemlerine Rüzgâr Enerji Santrallerinin Etkisinin Diferansiyel Gelişim Algoritmasıyla İncelenmesi The Examination of the Influence of the Wind Power Plants on Economic Power Dispatch Problems by Differential.

[18] Karaboga, D. (2010). Artificial bee colony algorithm. scholarpedia, 5(3), 6915.

65

## Türk Doğa ve Fen Dergisi
## Turkish Journal of Nature and Science
### www.dergipark.gov.tr/tdfd

# Determination of Mixed Virus Infection in Honey Bees from Erzurum, Türkiye

**Zeynep SELVİTOPİ** [iD] **, Gözde Büşra EROĞLU[1*]** [iD]

[1] Erzurum Technical University, Faculty of Science, Department of Molecular Biology and Genetics, Erzurum, Türkiye
Zeynep SELVİTOPİ ORCID No: 0000-0001-5297-1579
Gözde Büşra EROĞLU ORCID No: 0000-0001-8988-1315

*Corresponding author: gozdebusra.eroglu@erzurum.edu.tr

**Abstract:** Honeybees are one of the most important pollinators of agricultural products Especially the worker bees, which make up the majority of the honey bee population, produce products with high economic value such as honey, pollen, propolis, royal jelly, bee venom, and beeswax. Mass deaths are observed in honey bees grown in Erzurum province, where beekeeping activities are carried out intensively in the Eastern Anatolia region of Türkiye. Epidemic diseases seen in honey bees in Erzurum have a very negative effect on the development and progress of beekeeping activities. Most of the diseases that cause epidemics in bees and cause sudden death and colony loss are of viral origin. In this study, viral pathogens that cause death in honey bees in Erzurum province were investigated and it was determined that two honeybee viruses, the black queen cell virus (BQCV), and the deformed wing virus, caused intense epidemics. In addition, phylogenetic analyzes revealed that all BQCV isolates found in this study clustered quite far from BQCV isolates previously isolated from Türkiye, while DWV isolates clustered close to Hakkari and Lithuania isolates.

66

# Erzurum, Türkiye Bal Arılarında Karışık Virüs Enfeksiyonunun Belirlenmesi

**Öz:** Bal arıları tarımsal ürünlerin en önemli tozlaştırıcılarıdır. Özellikle bal arısı popülasyonunun büyük bir çoğunluğunu oluşturan işçi arılar bal, polen, propolis, arı sütü, arı zehri ve bal mumu gibi oldukça çeşitli ve ekonomik değeri yüksek ürünler üretmektedir. Türkiye'nin Doğu Anadolu bölgesindeki arıcılık faaliyetlerinin yoğun olarak gerçekleştirildiği Erzurum ilinde yetiştirilen bal arılarında toplu ölümler görülmektedir. Erzurum ili bal arılarında görülen salgın hastalıklar arıcılık faaliyetlerinin gelişimini ve ilerlemesini oldukça olumsuz etkilemektedir. Arılarda salgın oluşturarak ani ölüm ve koloni kayıplarına yol açan hastalıkların büyük bir çoğunluğu viral kaynaklıdır. Bu çalışmada Erzurum ili bal arılarında ölüme neden olan viral patojenler araştırılmış ve siyah kraliçe hücre virüsü ve deforme kanat virüsü olmak üzere iki adet bal arısı virüsünün yoğun salgına neden olduğu belirlenmiştir. Ayrıca filogenetik analizler bu çalışmada bulunan tüm BQCV izolatlarının daha önce Türkiye'den izole edilen BQCV izolatlarına oldukça uzak kümelendiğini, DWV izolatlarının ise Hakkari ve Lithuania izolatlarına yakın kümelendiğini ortaya koymuştur.

## 1. INTRODUCTION

Türkiye is known as one of the 12 bee gene centers in the world due to its geographical location and rich flora diversity. It also contains 20% of the honey bee species found in the world [1]. Since the products obtained from bees have a high commercial value, beekeeping has been an important source of income in Anatolia since ancient times. However, sudden bee deaths and colony losses occur due to diseases frequently seen in colonies. Beekeeping producers often use broad-spectrum chemical drugs without knowing the origin or the cause of the disease. Toxic drugs used leave residues in bee products and cause resistance development in vectors (*Varroa destructor*) [2]. The most common factors causing colony collapse and disease in bees are viral pathogens [3, 4]. While some of the viral pathogens seen in honey bees continue to exist silently without showing any specific symptoms, some of them cause important

diseases such as deformation in the wings of bees, paralysis in their legs, death, and even colony destruction [5, 6]. These viruses are pathogenic for all life stages of bees and are frequently seen in mixed infections in which an individual is infected with more than one virus at the same time [6]. Although conventional PCR methods using specific primers were used commonly for the determination of honeybee viruses, new-generation sequencing technologies developed in recent years have increased the number of known honeybee viruses. Thanks to this method, which is particularly suitable for the detection of asymptomatic viruses, the number of known honeybee viruses exceeded 30 [7-9]. The majority of these viruses have an RNA genome and are found in the Dicistroviridae and Iflaviridae families [10, 11]. The viral diseases that cause the most important problems in honey bee breeding, are DWV and BQCV. The viral pathogens in question can be transmitted to bees by the varroa mite, as well as the bee trade [12]. These two viruses are also very common in Turkish honey bees. DWV and BQCV viruses were detected for the first time in the Black Sea region in studies conducted in 2009-2010 in Türkiye [13, 14]. Although viral diseases of honey bees grown in many localities of Türkiye were detected, there are no studies on diseases and pathogens of honey bees in Erzurum, which has honey forests in the Eastern Anatolia region and is one of the attraction centers of beekeeping. This study, it was aimed to determine viral diseases to be obtained from apiaries located at different points in Erzurum province.

## 2. MATERIAL AND METHOD

### 2.1. Sample Source and RNA Isolation

A total of 37 queens and 279 worker bee samples were collected from 48 apiaries in Erzurum city center and its districts (Table 1).

The collected samples were brought to the laboratory on ice. It was stored at -80 °C until RNA isolation. Indispin/Cador pathogen kit was used to isolate RNA from samples (Indical Bioscience Cat. No: SP54104). Before proceeding to the manufacturer's instructions, every bee, 1 ml of PBS, and sterile steel balls were placed in each microcentrifuge tube and waited in the tissue lyser (Qiagen) device until the bees were

completely disintegrated. Afterward, the tissue pieces were precipitated by centrifugation at 6000 rcf at 4°C for 3 minutes and the supernatant was taken into a clean tube. After this stage, the kit was used. Nanodrop was used to determine the quality and density of RNA. Samples with good quality and density were stored at -80 °C until used in the next step.

Table 1. Sample numbers collected from localities

| Locality | Apiaries | Sample (Queen/worker) |
|---|---|---|
| Aşkale | 1 | 0/10 |
| Aziziye | 2 | 1/14 |
| Çat | 2 | 4/19 |
| Hınıs | 2 | 0/10 |
| Horasan | 2 | 1/10 |
| İspir | 3 | 2/14 |
| Köprüköy | 3 | 2/16 |
| Narman | 1 | 0/10 |
| Palandöken | 4 | 3/21 |
| Pasinler | 5 | 4/17 |
| Pazaryolu | 5 | 3/15 |
| Olur | 1 | 1/10 |
| Oltu | 2 | 1/20 |
| Şenkaya | 4 | 6/12 |
| Tekman | 1 | 0/13 |
| Tortum | 2 | 2/20 |
| Uzundere | 4 | 4/26 |
| Yakutiye | 4 | 3/22 |
| **Total** | **48** | **37/279** |

### 2.2. One-step Reaction and Phylogenetic Analysis

One-step reaction kit (EURx Cat. No: E0803-02) was used to synthesize the isolated RNAs into complementary DNA (cDNA) and to perform the polymerase chain reaction. The reaction prepared according to the kit procedure is as follows: in 25 µL of reaction volume with 60 ng of RNA, 1 µL of 10 µM sense and reverse primers, 12.5 µL of 2x master buffer mix, 1 µL of Master Enzyme mix, and up to 25 µL of nuclease-free water. The PCR condition was as follows: 94 °C for 5 min. for pre-denaturation, 35 cycles of 94 °C for 30 s, 55 °C for 30 s, 72 °C for 30 s, and a final extension at 72 °C for 5 min. The information of the primers used in the reaction is given in Table 2. After the reaction was finished, the banded samples were loaded onto a 1% agarose gel treated with ethidium bromide and run at 75 V for 45 min. Afterward, the gel was visualized in the imaging system under ultraviolet light.

Table 2. Primers set data used in virus screening of honey bees

| Primers and target genes | Sequences | tm | References |
|---|---|---|---|
| CBPV (RdRP) | **F:** GCAAACTGCCCACCAATAGT<br>**R:** TGGTACGGAAGGTGTGTCAA | | |
| SBV (cp gene) | **F:** TATTCAGGGGGACGCTACAC<br>**R:** AGTGCTGCTTGAAACCCTGT | | |
| IAPV (cp gene) | **F:** TTGGCGTGCAACTATGTGTT<br>**R:** TCTTCTGCCCACTTCCAAAC | | |
| BQCV (cp gene) | **F:** GACAGCGTGCCAAAGAGAG<br>**R:** GCGAACCCGTCCAATACTTA | 55°C | [15] |
| KBV (cp gene) | **F:** CACATTCCGAACAATAA<br>**R:** GCGATAGGAATTTTGCGGTA | | |
| DWV (Non-structural protein) | **F:** TTGGTATGCTCCGTTGACTG<br>**R:** ATTCCTCAGAAGTTGGTTTCG | | |
| ABPV (cp gene) | **F:** GTATGGAAGTGGGCTGAGGA<br>**R:** CGCGGTACTAAAAAGCTACGA | | [16] |

The samples obtained from the band were sent to Sentebiolab (Ankara, Türkiye) for sequence analysis. The name of the isolates was confirmed using the nucleotide blast program after trimming the head and end parts of the sequence results with low quality. In addition, access numbers were obtained for each isolate and recorded in the National Center for Biotechnology Information (NCBI) database. For phylogenetic analysis, the samples in the database and detailed information in Table 3 were used. In addition, Israel acute bee paralysis virus (IAPV) in the same family (Dicistroviridae) was used as the outgroup for BQCV, and Sacbrood virus (SBV) in the same family (Iflaviridae) with it was used as the outgroup for DWV. The nucleotide sequences of polyprotein for DWV and BQCV isolates were aligned using the program BioEdit (7.1.3.0). For phylogenetic relationship analysis, the Maximum Composite Likelihood model with 1000 bootstrap in the Neighbor-joining method was used to generate a phylogenetic tree using the MEGA 11 program.

**Table 3.** Information of the viruses used in phylogenetic analyzes

| Virus | Origin | Accession number | References |
|---|---|---|---|
| DWV | Lithuania | KF840794 | [17] |
| | Hakkari, Türkiye | KP835214 | [15] |
| | Erzincan, Türkiye | MW962981 | [18] |
| | | MW962982 | |
| | Van, Türkiye | KU521779 | [19] |
| | | KU521782 | |
| | Erzurum, Türkiye | OQ475006 | This study |
| | | OQ475007 | |
| | | OQ475005 | |
| | | OQ475004 | |
| | | OQ475003 | |
| | | OQ475002 | |
| | | OQ475011 | |
| | | OQ475012 | |
| | | OQ475013 | |
| | | OQ475014 | |
| | Italy | KF311109 | [20] |
| | Switzerland | JF346617 | [21] |
| | Sweden | JF346611 | |
| | Yugoslavia | JF346630 | |
| | China | JF346640 | |
| SBV (outgroup) | France | AH012541 | unpublished |
| BQCV | Tasmania | MF004373 | [22] |
| | Belgium | HG764797 | [23] |
| | Italy | MK238795 | [24] |
| | Syria | LT844588 | [25] |
| | Japan | KT717337 | [26] |
| | China | MF092814 | [27] |
| | USA | KY627847 | [28] |
| | France | MH133351 | unpublished |
| | Isparta, Türkiye | MW433904 | [29] |
| | Karaman, Türkiye | MW433911 | |
| | Konya, Türkiye | MW433906 | |
| | Niğde, Türkiye | MW433915 | |
| | Aksaray, Türkiye | MW433916 | |
| | Bingöl, Türkiye | MZ357974 | [30] |
| | Van, Türkiye | KU521775 | [19] |
| | Erzurum, Türkiye | OQ475008 | This study |
| | | OQ475009 | |
| | | OQ475010 | |
| | | OQ475015 | |
| | | OQ475016 | |
| IAPV (outgroup) | Russia | OL314256 | unpublished |

## 3. RESULTS

### 3.1. PCR Reactions

The samples in which BQCV and DWV diseases were determined were found in 7 apiaries in 4 different localities of Erzurum (Cat, Pasinler, Pazaryolu, Uzundere). As a result of the PCR reactions performed for virus screening, DWV was detected in 10 samples (3%) and BQCV was detected in 5 samples (1.6%) (Figure 1). Besides, samples collected from the Çat yolu locality were found to have mixed infections with both DWV and BQCV (Table 3). However, the presence of other bee viruses (CBPV, SBV, KBV, ABPV, and IAPV) was not detected in Erzurum.
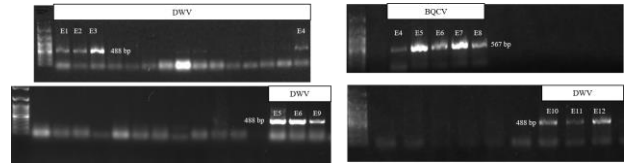


**Figure 1.** Samples with virus-positive band detected in PCR analysis

The nucleotide sequencing samples were deposited in the database with the accession numbers indicated in Table 3. In addition, it was determined that the sequences showed 98% BQCV and 99% for DWV similarity with the samples in the database, respectively (Table 4).

**Table 4.** Informations about samples with virus detected

| District | Sample code | Virus | Accession number | Similarity rate |
|---|---|---|---|---|
| Catyolu | E1 | DWV | OQ475002 | 99% |
| | E2 | | OQ475003 | 99% |
| | E3 | | OQ475004 | 99% |
| | **E4** | DWV | OQ475005 | 99% |
| | | BQCV | OQ475008 | 98% |
| | **E5** | DWV | OQ475006 | 99% |
| | | BQCV | OQ475009 | 98% |
| | **E6** | DWV | OQ475007 | 99% |
| | | BQCV | OQ475010 | 98% |
| Uzundere | E7 | BQCV | OQ475015 | 98% |
| | E8 | | OQ475016 | 98% |
| Pasinler | E9 | DWV | OQ475011 | 99% |
| | E10 | | OQ475012 | 99% |
| | E11 | | OQ475013 | 99% |
| Pazaryolu | E12 | | OQ475014 | 99% |

*Samples with mixed infections are indicated in bold.

### 3.2. Phylogenetic analyses

Phylogenetic similarity tree results Erzurum DWV isolates clustered close to Hakkari, Türkiye and Lithuania isolates (Figure 2a). Erzurum BQCV isolates clustered quite far from all BQCV isolates previously isolated from Türkiye (Figure 2b).
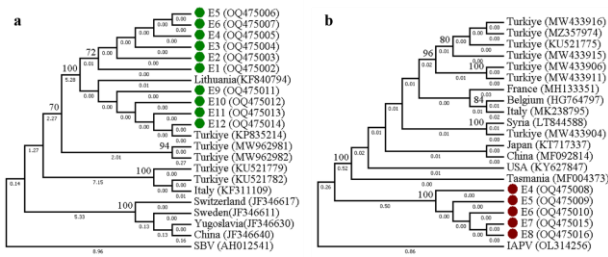
**Figure 2.** Phylogenetic analysis of honey bee viruses in Erzurum **a.** DWV isolates, **b.** BQCV isolates

## 4. DISCUSSION AND CONCLUSION

BQCV, which is in the family of Dicistroviridae, has taken this name because it was first detected in queen bees in Australia [31]. However, later studies in France and Austria reported that this virus was seen in the larval stages [6, 32]. DWV in the Iflaviridae family was first isolated from *Apis cerena*, a honey bee species found in the fareast [33]. Subsequently, this virus has spread to regions of Europe, North America, South America, Africa, Asia, and the Middle East [34, 35]. The most important findings of the disease are shrinkage and wrinkling of the wings caused by wear and tear. In the advanced stages of infection, deterioration in the body size of the bee and color change is also observed. This virus causes infection not only in the honey bee, but also in *Bombus* bees, which are known as important pollinators of tomatoes [36-38].

It is known that BQCV and DWV have a high prevalence worldwide. Choe et al. (2012) reported that BQCV virus is the most common pathogen in Korean honey bees [39]. Wang et al. (2016) declared that the prevalence of BQCV is high in the Yunnan region of China [40]. Ghorani et al. (2017) found that DWV is the most common honeybee virus in Iran (Mazandaran, Hormozgan, Kurdistan and Khorasan Razavi) [41]. Truong et al. (2023) reported that the three most common viruses were DWV (52.63%), BQCV (55.26%), and SBV (52.63%) as a result of their study on the prevalence of honeybee pathogens and parasites in South Korea between 2017-2021 [42].

Studies on the detection of viral pathogens that cause disease in honey bees have been carried out in our country for the last 15 years. Within the scope of these studies, Gülmez et al. (2009) detected DWV for the first time in Türkiye as a result of their study on honey bees in Ordu province [13]. Muz and Muz (2009) identified DWV in Hatay province [43]. Gümüşova et al. (2010) reported the presence of BQCV and CBPV in honey bees for the first time in Türkiye in their study in the Black Sea regions [14]. Rüstemoğlu and Sipahioğlu (2016) defined ABPV from honey bees in Hakkari province [16]. Muz and Muz (2018) detected BQCV in honey bees collected from different cities in Türkiye [44]. Oguz et al. (2017) determined the prevalence of Nosema and BQCV in honey bees reared in Van [45]. Karapınar et al. (2018) detected four viruses (ABPC, CBPV, DWV, BQCV) in Van honey bees [19]. Kalaycı et al. (2019) detected SBV in honey bees from Muğla province [46]. Rüstemoglu and Sipahioglu (2019)

defined 6 viruses (BQCV, DWV, SBV, CBPV, KBV, IAPV) in honey bees in Hakkari province [15]. Çağırgan et al. (2020) detected BQCV, DWV and ABPV disease in Burdur honey bees [47]. Kalaycı et al. (2020) reported that the DWV pathogen was the most common in honey bee samples from Adana, Aydın, Bursa, Izmir, Kütahya, Muğla, and Manisa, while the CBPV pathogen was less common [48]. Aydın (2020) determined that the honey bees of Malatya and Elazığ provinces were infected with DWV and BQCV [45]. Avcı et al. (2022) determined BQCV, DWV, and ABPV in honey bees in Konya, Karaman, Aksaray, Niğde, and Isparta [29]. Güller et al. (2022) detected SBV and BQCV pathogens in their study with honey bees in Bingöl province [30]. Utkan and Eroğlu (2023) declared that 2 different viruses (DWV, CBPV) in honey bees in Amasya province [50]. In addition, Eroglu (2023) determined that honey bee viruses (BQCV and KBV) were found in some wasps (*Vespula germanica*) found collectively dead in Erzurum [51].

Considering the literature studies, it was seen that viral pathogens are common in many beekeeping provinces in our country, and mainly DWV and BQCV pathogens were determined in these studies. In this study conducted in Erzurum, 7 bee viruses common worldwide were scanned by PCR in 316 healthy bees and dead/sick in front of the hive, and two viruses (DWV and BQCV) were detected. When the phylogenetic relationship of these viruses with other isolates in the NCBI database was examined, it was determined that BQCV isolates clustered quite far from BQCV isolates isolated from Türkiye. In addition, it was determined that DWV isolates clustered close to Hakkari and Lithuania isolates. Mixed infection of honeybee viruses has been known since the 1990s and is a frequent occurrence both in the world and in our country [52]. In mixed infection, more than one virus can be present in the same bee individual at the same time. Chen et al. (2004) reported for the first time that four bee viruses (BQCV, DWV, KBV, and SBV) were found in the same sample [53]. In our country, it has been declared in various studies that double, triple, quadruple and quintuple virus infections are seen [15, 48]. In this study, it was determined that both DWV and BQCV were found in the samples taken from Çat locality. The mixed infection will undoubtedly cause bees to die and diseases to spread faster. For this reason, in order to protect bees from viral infections, there is a need for careful hive cleaning and transported beekeeping, as well as vaccine production studies.

The results obtained showed that two viruses (BQCV and DWV) caused an epidemic in Erzurum honey bees and even mixed infections were observed in some samples at the same time. Thus, this study will shed light on the studies planned to prevent viral bee diseases that are common in the region and to protect bee health.

## REFERENCES

[1] Ruttner F. Biogeography and Taxonomy of Honeybees. 1th ed. Berlin, Germany: Springer; 1988.

[2] Dietemann V, Pflugfelder J, Anderson D, Charrière JD, Chejanovsky N, Dainat B, ... & Neumann P. Varroa destructor: research avenues towards sustainable control. Journal of Apicultural Research. 2012; 51:125-132.

[3] Dogaroglu M. Modern arıcılık. Anadolu Matbaa ve Ambalaj San. Tic. Ltd. Şti. İstanbul; 1999.

[4] Antunez K, D'Alessandro B, Corbella E, Ramallo G, Zunino P. Honey bee viruses in Uruguay. Journal of Invertebrate Pathology. 2006;93:67–70.

[5] De Miranda JR, Bailey L, Ball BV, Blanchard P, Budge GE, Chejanovsky N, et al. Standard methods for virus research in Apis mellifera. Journal Of Apicultural Research. 2013;52:1-56.

[6] Berenyi O, Bakonyi T, Derakhshifar I, Koglberger H, Nowotny N. Occurrence of six honeybee viruses in diseased Austrian apiaries. Applied and environmental microbiology. 2006;72(4):2414-2420.

[7] Galbraith DA, Zachary LF, Allyson MR, Axel B, Maryann F, Mary WG, et al. Investigating the Viral Ecology of Global Bee Communities with High-Throughput Metagenomics. Scientific Reports. 2018;8:1-14.

[8] McMenamin AJ, Flenniken ML. Recently identified bee viruses and their impact on three bee pollinators. Current Opinion Insect Science. 2018;26:120–129.

[9] Schoonvaere K, De Smet L, Smagghe G, Vierstraete A, Braeckman BP, de Graaf DC. Study of the Metatranscriptome of Eight Social and Solitary Wild Bee Species Reveals Novel Viruses and Bee Parasites. Published in Front. Microbiol. Biology, Medicine Frontiers in Microbiology. 2018;9:1-12.

[10] Eroglu GB. Phylogeographic Relationship of Honey Bee Dicistroviruses. Bee World. 2022;99(3):99-102.

[11] Eroglu GB. RNA Viruses in Honey Bees. In: Erdemir F, Ayar MK, editors. Distinguished Research from Different Disciplines. Gelenbevi Scientific Research Journal Announcements; 2022. p. 133-147.

[12] Beaurepaire A, Piot N, Doublet V, Antunez K, Campbell E, Chantawannakul P, et al. Diversity and global distribution of viruses of the western honey bee, Apis mellifera. Insects. 2020;11(4), 239.

[13] Gülmez Y, Bursalı A, Tekin S. First molecular detection and characterization of deformed wing virus (DWV) in honeybees (Apis mellifera L.) and mite (Varroa destructor) in Turkey. African Journal of Biotechnology. 2009;8(16).

[14] Gümüşova SO, Albayrak H, Kurt M, Yazıcı Z. Prevalence of three honey bee viruses in Turkey. Veterinarski Arhiv. 2010;80:779-785.

[15] Rüstemoğlu M, Sipahioğlu HM. Occurrence and prevalence of six honey bee viruses in Hakkari (Turkey) and their genomic divergence. Munis Entomology & Zoology. 2019;14(2):574-583.

[16] Rüstemoğlu M, Sipahioğlu HM. Occurrence and molecular characterization of acute bee paralysis virus (ABPV) in honeybee (Apis mellifera) colonies in Hakkari province. Yuzuncu Yıl University Journal of Agricultural Science. 2016;26(2):174-182

[17] Blazyte-Cereskiene L, Skrodenyte-Arbaciauskiene V, Radziute S, Cepulyte-Rakauskiene R, Apsegaite V, Buda V. A three-year survey of honey bee viruses in Lithuania. Journal of Apicultural Research. 2016;55(2):176-184.

[18] Güller A, Usta M, Cakar G, Kurt Z. Molecular characterization of Deformed wing viruses identified in honeybee (Apis mellifera L.) colonies in Erzincan province of Turkey. European Journal of Science and Technology. 2021;(27):186-192.

[19] Karapınar Z, Oguz B, Dincer E, Oztürk C. Phylogenetic analysis of black queen cell virus and deformed wing virus in honeybee colonies infected by mites in Van, Eastern Turkey. Praca oryginaina. 2018;74(7):460-465.

[20] Mazzei M, Carrozza ML, Luisi E, Forzan M, Giusti M, Sagona S, et al. Infectivity of DWV associated to flower pollen: experimental evidence of a horizontal transmission route. PLoS one. 2014;9(11):e113448.

[21] Forsgren E, De Miranda JR, Isaksson M, Wei S, Fries I. Deformed wing virus associated with Tropilaelaps mercedesae infesting European honey bees (Apis mellifera). Experimental and Applied Acarology. 2009;47:87-97.

[22] Fung E, Hill K, Hogendoorn K, Hingston AB, Glatz RV. Co-occurrence of RNA viruses in Tasmanian-introduced bumble bees (Bombus terrestris) and honey bees (Apis mellifera). Apidologie. 2018;49:243-251.

[23] Ravoet J, De Smet L, Meeus I, Smagghe G, Wenseleers T, de Graaf DC. Widespread occurrence of honey bee pathogens in solitary bees. Journal of Invertebrate Pathology. 2014;122:55-58.

[24] Mazzei M, Cilia G, Forzan M, Lavazza A, Mutinelli F, Felicioli A. Detection of replicative Kashmir bee virus and Black queen cell virus in Asian hornet Vespa velutina (Lepelieter 1836) in Italy. Scientific Reports. 2019;9(1):10091.

[25] Abou Kubaa R, Molinatto G, Khaled B, Daher-Hjaij N, Heinoun K, Saponari M. First detection of black queen cell virus, Varroa destructor macula-like virus, Apis mellifera filamentous virus and Nosema ceranae in Syrian honey bees Apis mellifera syriaca. Bull. Insectol. 2018;71:217-224.

[26] Traiyasut P, Mookhploy W, Kimura K, Yoshiyama M, Khongphinitbunjong K, Chantawannakul P. First detection of honey bee viruses in wax moth. Chiang Mai J. Sci. 2016;43(4).

[27] Yang SA, Gayral P, Zhao H, Wu Y, Jiang X, Wu Y, et al. Occurrence and molecular phylogeny of honey bee viruses in Vespids. Viruses. 2019;12(1):6.

[28] Murray EA, Burand J, Trikoz N, Schnabel J, Grab H, Danforth BN. Viral transmission in honey bees and native bees, supported by a global black queen cell virus phylogeny. Environmental microbiology. 2019;21(3):972-983.

[29] Avcı O, Oz ME, Dogan M. Silent threat in honey bee colonies: infection dynamics and molecular epidemiological assessment of black queen cell virus in Turkey. Archives of Virology. 2022;167(7):1499-1508.

[30] Güller A, Kurt Z. Occurrence and Molecular Phylogeny of Economically Relevant Viruses Infecting Honey Bees (L.) of Bingöl Province, Turkey. Journal of Apicultural Science. 2022;66(1):85-96.

[31] Anderson DL. Pathogens and queen bees. Aust. Beekeeper. 1993;94:292–296.

[32] Tentcheva D, Gauthier L, Zappulla N, Dainat B, Cousserans F, Colin ME, et al. Prevalence and seasonal variations of six bee viruses in Apis mellifera L. and Varroa destructor mite populations in France. Applied and Environmental Microbiology. 2004;70(12):7185-7191.

[33] Bailey L, Ball BV. Cultivation and Purification of Bee Viruses. In: Honey Bee Pathology; 1991.

[34] Allen M, Ball B. The incidence and world distribution of honey bee viruses. Bee World. 1996;77(3):141-162.

[35] Antunez K, Anido M, Garrido-Bailon E, Botias C, Zunino P, Martinez Salvador A, et al. Low prevalence of honeybee viruses in Spain during 2006 and 2007. Research in Veterinary Science. 2012;93(3):1441-1445.

[36] Genersch E, Yue C, Fries I, De Miranda JR. Detection of Deformed wing virus, a honey bee viral pathogen, in bumble bees (Bombus terrestris and Bombus pascuorum) with wing deformities. Journal of Invertebrate Pathology. 2006; 91(1):61-63.

[37] Li J, Peng W, Wu J, Strange JP, Boncristiani H, Chen Y. CrossSpecies Infection of Deformed Wing Virus Poses a New Threat to Pollinator Conservation. Journal of Economic Entomology. 2011;104(3):732-739.

[38] Peng W, Li J, Boncristiani H, Strange JP, Hamilton M, Chen Y. Host range expansion of honey bee Black Queen Cell Virus in the bumble bee, Bombus huntii. Apidologie. 2011;42, 650-658.

[39] Choe SE, Nguyen LTK, Noh JH, Koh HB, Jean YH, Kweon CH, Kang SW. Prevalence and distribution of six bee viruses in Korean Apis cerana populations. Journal of Invertebrate Pathology. 2012; 109(3):330-333.

[40] Wang M, Bi J, Wang L, Zhou D, Ma X, Li W, ... He S. Prevalence of four common bee RNA viruses in Eastern bee populations in Yunnan Province, China. Journal of Veterinary Science and Technology. 2016; 7(1).

[41] Ghorani M, Madadgar O, Langeroudi AG, Rezapanah M, Nabian S, Akbarein H. et al. The first comprehensive molecular detection of six honey bee viruses in Iran in 2015-2016. Archives of Virology. 2017; 162:2287-2291.

[42] Truong AT, Yoo MS, Seo SK, Hwang TJ, Yoon SS, Cho YS. Prevalence of honey bee pathogens and parasites in South Korea: A five-year surveillance study from 2017 to 2021. Heliyon. 2023; 9(2).

[43] Muz D, Muz MN. Survey of the occurrence of Deformed Wing Virus and multiple parasites of queens (Apis mellifera L.) in apiaries with collapsed colonies in Hatay, Turkey. Journal of Apicultural Research. 2009;48(3):204-208.

[44] Muz D, Muz MN. A molecular epidemiological study of black queen cell virus in honeybees (Apis mellifera) of Turkey: the first genetic characterization and phylogenetic analysis of field viruses. Apidologie. 2018;49(1):89-100.

[45] Oğuz B, Karapınar Z, Dinçer E, Değer MS. Molecular detection of Nosema spp. and black queen-cell virusin honeybees in Van Province, Turkey. Turkish Journal of Veterinary & Animal Sciences. 2017;41(2):221-227.

[46] Kalaycı G, Çağırgan AA, Pekmez K, Özkan B, Kaplan M. Molecular detection and phylogenetic analysis of the honeybee (Apis mellifera) sacbrood virus in Turkey. Turkish Journal of Veterinary & Animal Sciences. 2019; 43(4):551-554.

[47] Çağırgan AA, Yıldırım Y, Usta A. Phylogenetic analysis of deformed wing virus, black queen cell virus and acute bee paralysis viruses in Turkish honeybee colonies. Medycyna Weterynaryjna. 2020;76(08).

[48] Kalaycı G, Cağırgan AA, Kaplan M, Pekmez K, Beyazıt A, Özkan B, ... Arslan F. The role of viral and parasitic pathogens affected by colony losses in Turkish apiaries. Kafkas Üniversitesi Veteriner Fakültesi Dergisi. 2020;26(5).

[49] Aydın S. Detection and of molecular characterizatın of bee viruses in Malatya and Elazıg provinces (Master thesis). Malatya Turgut Özal University Institute of Graduate Studies Department of Plant Protection; 2020.

[50] Utkan NG, Eroğlu GB. Molecular identıfıcatıon of microbıal pathogens in honey bees from Amasya. Uludag Bee Journal. 2023;23 (1).

[51] Eroğlu GB. Detection of honey bee viruses in Vespula germanica: Black queen cell virus and Kashmir bee virus. Biologia 2023;1-5.

[52] Anderson DL. Pests and pathogens of the honeybee (Apis mellifera L.) in Fiji. Journal of Apicultural Research. 1990; 29(1):53-59.

[53] Chen Y, Zhao Y, Hammond, J, Hsu HT, Evans J, Feldlaufer M. Multiple virus infections in the honey bee and genome divergence of honey bee viruses. Journal of invertebrate pathology. 2004; 87(2-3):84-93.

71

## Türk Doğa ve Fen Dergisi
## Turkish Journal of Nature and Science
www.dergipark.gov.tr/tdfd

# Synthesis of TiO₂ Nanotubes and Examination of Photodiode Device Properties

**Lütfi Bilal TAŞYÜREK[1*]** (iD)

[1] Malatya Turgut Ozal University, Darende Bekir Ilicak V.H.S., Department of Opticians, Malatya, Türkiye
Lütfi Bilal TAŞYÜREK ORCID No: 0000-0003-0607-648X

*Corresponding author: bilaltasyurek@gmail.com*

**Abstract:** In this study, titanium dioxide (TiO₂) nanotubes were produced by anodization method using glycerol-based electrolyte. Structural characterization was investigated with SEM images and XRD pattern. The rectifying properties of n-type semiconductor TiO₂ nanotubes were investigated. Current-voltage (I-V) measurements of the Pt/TiO₂ nanotubes/Ti device were made at room temperature, in the dark and under different illumination conditions. The basic diode parameters were calculated by using thermionic emission (TE), Cheung and Norde functions from the I-V measurements of the devices in dark conditions. The ideality factors and barrier height of the Pt/TiO₂ nanotubes/Ti device were calculated 1.25 and 0.91 eV, respectively by the TE method. According to the results obtained, the Pt/TiO₂ nanotubes contact has a rectifying feature. In addition, the photovoltaic properties of the devices were examined by making I-V measurements at illumination intensities between 30 and 100 mW/cm². As a result, it has been evaluated that the device can also be used as a photodiode.

# TiO₂ Nanotüplerin Sentezi ve Fotodiyot Aygıt Özelliklerinin İncelenmesi

**Öz:** Bu çalışmada, gliserol bazlı elektrolit kullanılarak anotlama yöntemi ile titanyum dioksit (TiO₂) nanotüpler üretilmiştir. Yapısal karakterizasyon, SEM görüntüleri ve XRD deseni ile incelenmiştir. N-tipi yarı iletken özellik gösteren TiO₂ nanotüplerin doğrultucu özellikleri incelenmiştir. Pt/TiO₂ nanotüpler/Ti cihazının akım-voltaj (I-V) ölçümleri oda sıcaklığında, karanlıkta ve farklı aydınlatma koşullarında yapılmıştır. Cihazların karanlık koşullarda I-V ölçümlerinden termiyonik emisyon (TE), Cheung ve Norde fonksiyonları kullanılarak temel diyot parametreleri hesaplanmıştır. TE yöntemi ile Pt/TiO₂ nanotüp/Ti cihazının idealite faktörleri ve bariyer yüksekliği sırasıyla 1,25 ve 0,91 eV olarak hesaplanmıştır. Elde edilen sonuçlara göre Pt/TiO₂ nanotüp kontağı doğrultucu özelliğe sahiptir. Ayrıca 30 ile 100 mW/cm² arasındaki aydınlatma şiddetlerinde I-V ölçümleri yapılarak cihazların fotovoltaik özellikleri incelenmiştir. Sonuç olarak cihazın fotodiyot olarak da kullanılabileceği değerlendirilmiştir.

## 1. INTRODUCTION

Metal oxides are used as interface layer to improve the electrical parameters of photodiodes. Photodiodes are sensitive to high-energy particles and photons. Thus, they convert light into electric current and find a wide place in optoelectronic technology. If the luminous energy exceeds the band gap energy of the semiconductor layer, electron-hole pairs are formed. When these pairs drift in opposite directions, a photocurrent is formed [1]. Titanium dioxide (TiO₂) thin films are widely used in solar cells [2], gas sensors [3], photocatalysis [4], etc., due to their electrical and optical properties. It is an n-type semiconductor suitable for various applications such as TiO₂ has three different crystal structures as rutile, anatase

and brookite, with an indirect band gap of 3.0-3.2 eV. Thanks to this feature, its chemical, electrical and optical properties can be adapted for various applications [5]. In addition, TiO₂ is non-toxic and has a high dielectric constant and photocatalytic activity, increasing research opportunities.

Due to their properties, photodiodes have been investigated by many researchers to improve their performance [6], [7]. The electrical parameters of diodes using metal oxide nanostructures at their interfaces can be affected by the oxide layer [8]. Research has been carried out on diodes using TiO₂ as an interfacial [9].

While the values of the ideality factor and barrier height of the structure in dark conditions have been investigated, they have not been sufficiently investigated in illuminated conditions.

Despite many studies on $TiO_2$, the development of new materials for high-efficiency optoelectronic structures and their modeling remain hot research topics for current technologies. Thanks to their porous structure, $TiO_2$ nanoparticles provide large contact areas to adsorb dye molecules. This provides fast electron transfer and a large number of electrons [10]. Grain boundaries can cause photocurrent loss and lead to electron recombination in the near infrared region, which can result in loss of light absorption [11]. As an alternative to $TiO_2$ nanoparticles, $TiO_2$ nanotubes have been recognized as a promising option for photovoltaic applications. $TiO_2$ nanotubes attract attention with their features such as high surface/volume ratio, low cost and easy synthesis. The tubular porous structure of nanotubes provides a wide range of applications for light adsorption [12]. For photovoltaic applications, $TiO_2$ nanotubes offer advantages such as increased light scattering, fast electron transport and reduction of trap zones [13].

Rectifying contacts formed between metal and semiconductor have been a subject of extensive research in electronics for decades. Depending on the metal used as the contact, a Schottky barrier may form at the metal-metal oxide nanotube interface. Thus, the Fermi level may decrease [5]. Liu and Chen calculated the barrier height for Ag/$TiO_2$ nanoparticle contacts in their study [14]. Ling et al. [15] and Kwon et al. [16] examined the hydrogen sensor application of Au/$TiO_2$ and Pt/$TiO_2$ Schottky barrier diodes respectively. Mao et al. reported increased hydrogen sensor sensitivity of Pd decorated Ag/$TiO_2$ nanotube Schottky barrier diodes [17].

In our study, $TiO_2$ nanotubes were synthesized by anodization method using glycerol-based electrolyte and their morphological properties were determined. The electrical properties of the Schottky contact were investigated by making current-voltage (I-V) measurements and using different methods. Recently, nanostructures have been more intensively investigated in the fields of photovoltaic applications. Therefore, $TiO_2$ nanotubes are expected to contribute to the literature in photodetectors and photosensing devices. Finally, $TiO_2$ will be recommended to possible future research areas for the development of nanotube-based photovoltaic applications. In this way, it will be ensured that new nanotubes will be the subject of research such as this one.

## 2. MATERIAL AND METHOD

Glycerol electrolyte-based anodization method was applied to produce $TiO_2$ nanotubes. The cleaning procedure of commercial pure Ti foil (99%) with a size of 10x25 $mm^2$ and a thickness of 0.1 mm was applied for 15 minutes in an ultrasonic bath in acetone, isopropyl alcohol and deionized (DI) water, respectively. After each step of the cleaning procedure, the Ti foils were dried with high purity nitrogen ($N_2$) gas. 0.5 $wt$% $NH_4F$ was added to the

glycerol solution containing 15 $wt$% $H_2O$ and mixed with a magnetic stirrer for 15 minutes at 20 ºC. The solution prepared in a teflon beaker was placed in a thermostat bath at 20 ºC Pt mesh (99.9%, Sigma-Aldrich) as anode and Ti foil as cathode were placed in the solution at a distance of 2 cm from each other and 40 V voltage was applied for 2 hours with DC power supply. After the anodization process, the removed foil was washed with DI water and dried with $N_2$ gas. Thus, the synthesis of $TiO_2$ nanotubes, which will serve as the interface in the device design, was completed.

Finally, $TiO_2$ nanotubes were coated with 100 nm thick Pt metal by DC magnetron sputtering method with shadow mask to take I-V measurements. Pt electrodes help to conduct electric current. The schematic representation of the produced Pt/$TiO_2$ nanotubes/Ti devices and the measurement system is shown in Figure 1.
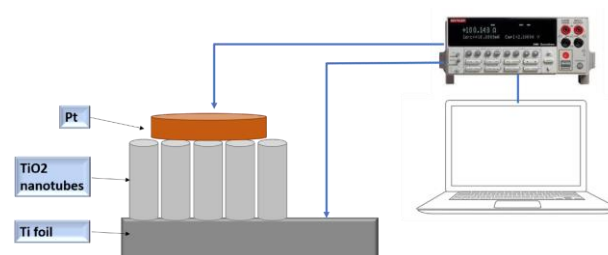


**Figure 1.** Schematic representation of Pt/$TiO_2$ nanotubes/Ti devices and measurement system

## 3. RESULTS

In Figure 2(A), the characteristic peaks of $TiO_2$ in x-ray diffraction (XRD) pattern are $2\theta$=35.06º (100), 38.46º (002), 40.18º (101), 53.02º (102), 62.96º (110), 70.66º (103), 76.2º (112), 76.46º (201) seen [18]–[20]. After anodization, the surface morphology of the $TiO_2$ nanotubes was characterized by scanning electron microscopy (SEM). Nanotubes were formed on the entire surface of the Ti foil. It is clear that there is a difference between the diameters of the nanotubes in the SEM images and the nanotubes show a slight contraction in Figure 2 (B) and (C). The average nanotube diameters are between 160-170 nm. It shows that there is still some irregularity in the pore formation process. Some pores do not appear to have grown completely straight and some abrasion marks are visible on the surface. There are also undulations on the walls of the tubes that are not very rough, but not very rough. This is due to the self-organization of the nanotubes and diffusion through the pores. In addition, some anodization parameters need to be optimized [21], [22]. As seen from the SEM images, the nanotubes are homogeneously formed. However, the diameters of the tubes were not formed in the same dimensions. In order for the tube diameters to be the same, parameters such as anodization temperature, application voltage, application time can be optimized [23].
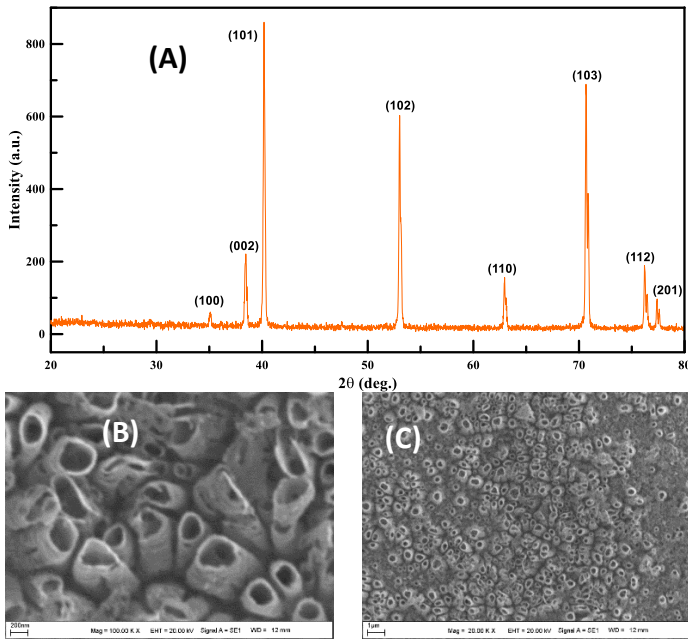
**Figure 2. (A)** XRD pattern and **(B-C)** SEM images of TiO$_2$ nanotubes



**Figure 3.** Semi-logarithmic I-V characteristic of Pt/TiO$_2$ nanotubes/Ti device at room tempeature

Thermionic emission theory (TE) in the linear region of the forward biased semi-logarithmic I-V plot (at low voltage) was used at both dark and illumination [24]–[26];

$$I = I_0 \left[ exp \left( \frac{q(V-IR_s)}{nkT} \right) - 1 \right] \qquad (1)$$

where $I_0$ is the saturation current found given by;

$$I_0 = AA^*T^2 exp \left( \frac{q\Phi_b}{kT} - 1 \right) \qquad (2)$$

The following equation is used to calculate the ideality factor ($n$) and the barrier height ($\Phi_b$);

$$n = \frac{q}{kT} \frac{dV}{d(ln\,I)} \qquad (3)$$

$$q\Phi_b = kT\,ln \left( \frac{AA^*T^2}{I_0} \right) \qquad (4)$$

In the above equations; $q$ is the charge of the electron, $k$ Boltzmann constant ($8.625 \times 10^{-5}$ eVK$^{-1}$), $A$ is the effective diode field (0.00785 cm$^2$), $A^*$ Richardson constant ($A^* \sim 1200$ Acm$^{-2}$K$^{-2}$ for TiO$_2$) [27] and $T$ is temperature in Kelvin.

The $n$ value (for ideal diodes, $n$=1) is calculated from the slope of the linear portion in the low voltage region in the forward direction of the semi-logarithmic I-V characteristic. For the Pt/TiO$_2$ nanotubes/Ti device, the $n$ value calculated using the curve in Figure 3 is 1.25 and the $\Phi_b$ value is 0.95 eV at room temperature. The $n$ value greater than one can be explained by the inhomogeneity of the barrier, the properties of the interface layer and the effect of series resistance ($R_s$) [28]–[30].

In order to understand the electrical characteristics of the Pt/TiO$_2$ nanotubes contact, it is not sufficient to examine only the linear region of the I-V graph in Figure 3. The $R_s$ effect is seen, where the graph moves away from linearity in forward bias. One of the methods used to investigate the $R_s$ effect is the Cheung functions [31]. The Cheung functions applied in the high voltage region are as follows;

$$\frac{dV}{d(ln\,I)} = \frac{nkT}{e} + IR_s \qquad (5)$$

$$H(I) = V - n \left( \frac{kT}{q} \right) ln \left( \frac{I}{AA^*T^2} \right) = n\Phi_b + IR_s \qquad (6)$$

The $n$ value is calculated from the point where the dV/d(lnI )-I slope intersects the vertical axis and the $\Phi_b$ value is calculated from the point where the H(I)-I slope intersects the vertical axis in Figure 4. The $R_s$ values are also calculated from the slopes of these graphs. The $n$ value calculated from the dV/d(lnI )-I slope is 2.69 and the $R_s$ value is 1867 kΩ. The $\Phi_b$ value calculated from the H(I)-I slope is 1.02 eV, and the $R_s$ value is 1650 kΩ. Electrical parameters calculated by Cheung method were higher than those calculated by TE method. This is due to the fact that the I-V regions where the calculation is made are different. In addition, the $R_s$ effect between Pt/TiO$_2$ nanotubes can be attributed to the increase in charge flow at high voltage and the inhomogeneity of the barrier height [32], [33].

74
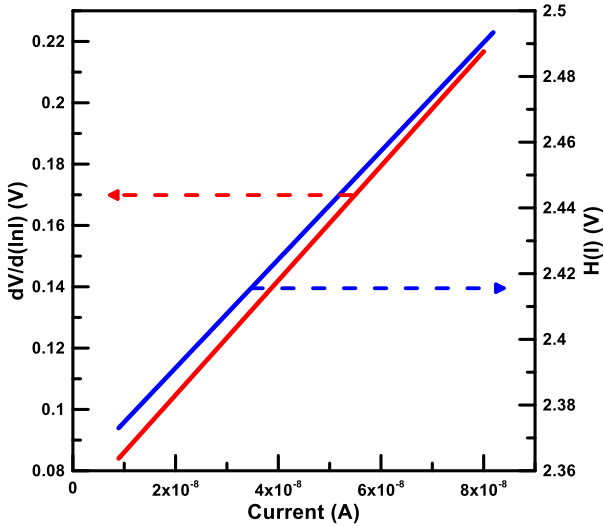
**Figure 4.** The graphs of of Pt/TiO₂ nanotubes/Ti device using Cheung functions at room temperature

Another method used to examine the $R_s$ effect is the Norde functions [34]–[36] The linear and sloped region of the I-V graph in forward bias is used together to calculate the Norde functions and $\Phi_b$ and $R_s$ values. Norde functions are given below;

$$F(V) = \frac{V}{\gamma} - \frac{kT}{q} ln\left(\frac{I(V)}{AA^*T^2}\right) \quad (7)$$

$$\Phi_b = F(V_0) + \frac{V_0}{\gamma} - \frac{kT}{q} \quad (8)$$

$$R_s = \frac{kT(\gamma - n)}{qI_{min}} \quad (9)$$

where γ is an integer greater than the ideality factor, I(V) is the current from the forward slope of the I-V curve, F(V0), V0 and Imin correspond to the minimum value of F(V). $R_s$ =31332 kΩ and $\Phi_b$ =0.98 eV obtained with the help of Norde functions from the F(V)-V graphs shown in Figure 5 of Pt/TiO₂ nanotubes/Ti device. The results are generally in agreement with those obtained in previous methods. The main reason for the difference in the calculated values is that the Norde functions are applied to the entire forward-voltage region. It may also be due to the free carrier concentration caused by carriers at the interface between Pt/TiO₂ nanotubes [37]–[39].
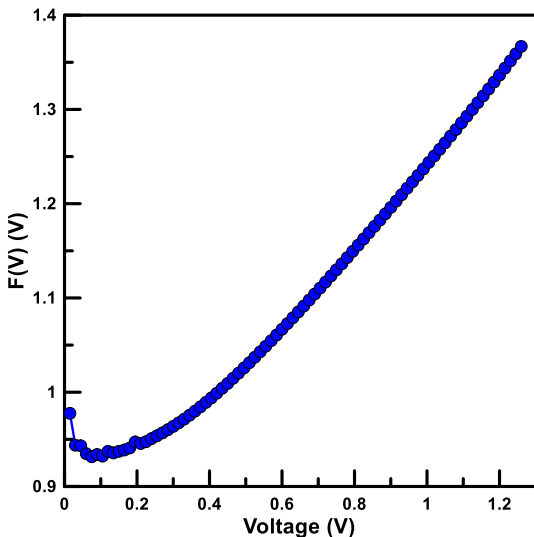


**Figure 5.** The graphs of of Pt/TiO₂ nanotubes/Ti device using Norde functions at room temperature

Figures 6 and 7 show the I-V characteristic of the Pt/TiO₂ nanotubes/Ti device at room temperature under 30, 40, 60, 80 and 100 mW/cm² light, respectively, in the dark. The $n$ and $\Phi_b$ values at 100 mW/cm² illumination were calculated as 2.04 and 0.89 eV by using the I-V characteristic with TE method. The departure of the I-V plots under illumination from the linear region is attributed to the series resistance effect in the bending region . It is not fully linear as it is affected by the series resistance in the contact region [8]. It is understood from the graphs that they show rectifying properties. The saturation current ($I_0$) has small values ($I_0$=8.22 x 10⁻¹¹ A). According to the reverse I-V graph, the increase in the current with the increase of the illumination intensity is explained by the photovoltaic behavior of the device. The movement of electron-hole pairs in the Pt/TiO₂ nanotubes contact is more pronounced in reverse bias than in forward bias. The energy of the photons is greater than the band gap energy, which can lead to the formation of electron-hole fences. The movement of these pairs can give useful information about the contact structure. The electron-hole pairs released along the contact can be separated by the electric field and move across the barrier [8], [40]–[42].
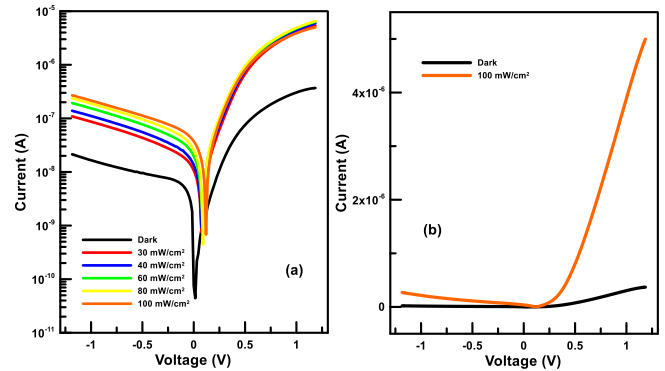


**Figure 6. (a)** Semi-logarithmic **(b)** lineer I-V grap of the Pt/TiO₂ nanotubes/Ti device in dark and different illuminations
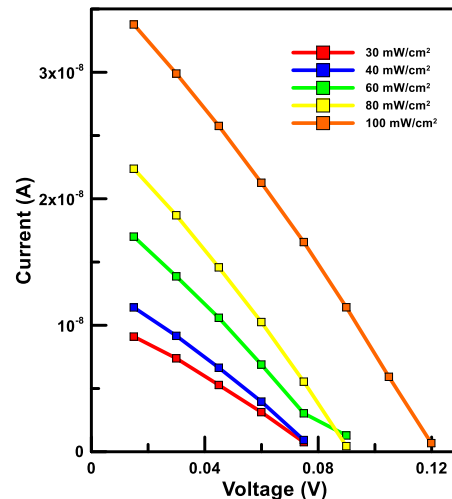
**Figure 7.** I-V grap of the Pt/TiO₂ nanotubes/Ti device in different illuminations

## 4. DISCUSSION AND CONCLUSION

In this study, TiO₂ nanotubes were produced by anodization method using glycerol-based electrolyte. XRD pattern and SEM images were examined to see the structural properties of TiO₂ nanotubes. The electrical characterization of TiO₂ nanotubes from the

nanostructured metal oxide group was investigated by three different methods (TE, Cheung and Norde functions). Photodiode performance and optical characterization were investigated under different lighting conditions. Then, $\Phi_b$, $n$ and $R_s$ parameters were calculated from the I-V properties of the Pt/TiO$_2$ nanotubes contact. The $n$ and $\Phi_b$ values of the Pt/TiO$_2$ nanotubes contact was measured as 1.25 and 0.91 eV, respectively by the TE method,. The results of I-V calculations by various methods were consistent. As a result, Pt/TiO$_2$ nanotubes showed rectifying properties. Photocurrent evaluation gave positive results for photodiode applications.

## Acknowledgement

## REFERENCES

[1]    İ. Orak, "The performances photodiode and diode of ZnO thin film by atomic layer deposition technique," Solid State Communications, vol. 247, pp. 17–22, 2016.

[2]    Y. Alivov, P. Xuan, and Z. Y. Fan, "TiO 2 nanotube height effect on the efficiency of dye-sensitized solar cells," 2011, doi: 10.1007/s11051-011-0627-1.

[3]    N. Kılınç, E. Şennik, M. Işık, A. Ş. Ahsen, O. Öztürk, and Z. Z. Öztürk, "Fabrication and gas sensing properties of C-doped and un-doped TiO2 nanotubes," Ceramics International, vol. 40, no. 1, Part A, pp. 109–115, 2014, doi: https://doi.org/10.1016/j.ceramint.2013.05.110.

[4]    M. Szkoda, K. Siuzdak, A. Lisowska-Oleksiak, J. Karczewski, and J. Ryl, "Facile preparation of extremely photoactive boron-doped TiO2 nanotubes arrays," Electrochemistry Communications, vol. 60, pp. 212–215, 2015.

[5]    M. Yilmaz, B. B. Cirak, S. Aydogan, M. L. Grilli, and M. Biber, "Facile electrochemical-assisted synthesis of TiO2 nanotubes and their role in Schottky barrier diode applications," Superlattices and Microstructures, vol. 113, pp. 310–318, 2018.

[6]    J. Cai, X. Chen, R. Hong, W. Yang, and Z. Wu, "High-performance 4H-SiC-based pin ultraviolet photodiode and investigation of its capacitance characteristics," Optics Communications, vol. 333, pp. 182–186, 2014.

[7]    K. F. Brennan, J. Haralson II, J. W. Parks Jr, and A. Salem, "Review of reliability issues of metal-semiconductor-metal and avalanche photodiode photonic detectors," Microelectronics Reliability, vol. 39, no. 12, pp. 1873–1883, 1999.

[8]    A. Karabulut, İ. Orak, and A. Türüt, "The photovoltaic impact of atomic layer deposited TiO2 interfacial layer on Si-based photodiodes," Solid-State Electronics, vol. 144, pp. 39–48, 2018.

[9]    S. B. K. Aydin, D. E. Yildiz, H. K. Çavuş, and R. Şahingöz, "ALD TiO 2 thin film as dielectric for Al/p-Si Schottky diode," Bulletin of Materials Science, vol. 37, pp. 1563–1568, 2014.

[10]   W.-Q. Wu et al., "Hydrothermal fabrication of hierarchically anatase TiO2 nanowire arrays on FTO glass for dye-sensitized solar cells," Scientific reports, vol. 3, no. 1, pp. 1–7, 2013.

[11]   J. Maçaira, L. Andrade, and A. Mendes, "Review on nanostructured photoelectrodes for next generation dye-sensitized solar cells," Renewable and Sustainable Energy Reviews, vol. 27, pp. 334–349, 2013.

[12]   X. Hou, K. Aitola, and P. D. Lund, "TiO2 nanotubes for dye-sensitized solar cells—A review," Energy Science & Engineering, vol. 9, no. 7, pp. 921–937, 2021.

[13]   G. K. Mor, O. K. Varghese, M. Paulose, K. Shankar, and C. A. Grimes, "A review on highly ordered, vertically oriented TiO2 nanotube arrays: Fabrication, material properties, and solar energy applications," Solar Energy Materials and Solar Cells, vol. 90, no. 14, pp. 2011–2075, 2006.

[14]   J. Liu and F. Chen, "Plasmon enhanced photoelectrochemical activity of Ag–Cu nanoparticles on TiO2/Ti substrates," Int. J. Electrochem. Sci, vol. 7, no. 9560, p. e9572, 2012.

[15]   Y. Ling, F. Ren, and J. Feng, "Reverse bias voltage dependent hydrogen sensing properties on Au–TiO2 nanotubes Schottky barrier diodes," International Journal of Hydrogen Energy, vol. 41, no. 18, pp. 7691–7698, 2016, doi: https://doi.org/10.1016/j.ijhydene.2016.02.007.

[16]   H. Kwon, J. H. Sung, Y. Lee, M.-H. Jo, and J. K. Kim, "Wavelength-dependent visible light response in vertically aligned nanohelical TiO2-based Schottky diodes," Applied Physics Letters, vol. 112, no. 4, p. 43106, 2018.

[17]   [17]      S. Mao et al., "High performance hydrogen sensor based on Pd/TiO2 composite film," International Journal of Hydrogen Energy, vol. 43, no. 50, pp. 22727–22732, 2018.

[18]   J. M. Macak, L. V Taveira, H. Tsuchiya, K. Sirotna, J. Macak, and P. Schmuki, "Influence of different fluoride containing electrolytes on the formation of self-organized titania nanotubes by Ti anodization," Journal of electroceramics, vol. 16, no. 1, pp. 29–34, 2006.

[19]   L. Özcan, T. Mutlu, and S. Yurdakal, "Photoelectrocatalytic degradation of paraquat by Pt loaded TiO2 nanotubes on Ti anodes," Materials, vol. 11, no. 9, p. 1715, 2018.

[20]   X. Xiao, T. Tian, R. Liu, and H. She, "Influence of titania nanotube arrays on biomimetic deposition apatite on titanium by alkali treatment," Materials Chemistry and Physics, vol. 106, no. 1, pp. 27–32, 2007, doi: https://doi.org/10.1016/j.matchemphys.2007.05.014 .

[21]   R. Narayanan, T. Y. Kwon, and K. H. Kim, "TiO2 nanotubes from stirred glycerol/NH4F electrolyte: Roughness, wetting behavior and adhesion for implant applications," Materials Chemistry and Physics, vol. 117, no. 2–3, pp. 460–464, 2009, doi: 10.1016/j.matchemphys.2009.06.023.

[22]   J. M. Macak et al., "TiO2 nanotubes: Self-organized electrochemical formation, properties and applications," Current Opinion in Solid State and Materials Science, vol. 11, no. 1–2, pp. 3–18, 2007,

doi: 10.1016/j.cossms.2007.08.004.

[23] E. Isik, L. B. Tasyurek, I. Isik, and N. Kilinc, "Synthesis and analysis of TiO2 nanotubes by electrochemical anodization and machine learning method for hydrogen sensors," Microelectronic Engineering, vol. 262, p. 111834, 2022, doi: https://doi.org/10.1016/j.mee.2022.111834.

[24] R. T. Tung, "Recent advances in Schottky barrier concepts," Materials Science and Engineering: R: Reports, vol. 35, no. 1–3, pp. 1–138, 2001.

[25] A. Turut, D. E. Yıldız, A. Karabulut, and İ. Orak, "Electrical characteristics of atomic layer deposited Au/Ti/HfO 2/n-GaAs MIS diodes in the wide temperature range," Journal of Materials Science: Materials in Electronics, pp. 1–11, 2020.

[26] S. M. Sze, Semiconductor devices: physics and technology. John wiley & sons, 2008.

[27] G. Rawat, H. Kumar, Y. Kumar, C. Kumar, D. Somvanshi, and S. Jit, "Effective Richardson constant of sol-gel derived TiO 2 Films in n-TiO 2/p-Si heterojunctions," IEEE Electron Device Letters, vol. 38, no. 5, pp. 633–636, 2017.

[28] D.-N. Bui, J. Mu, L. Wang, S.-Z. Kang, and X. Li, "Preparation of Cu-loaded SrTiO3 nanoparticles and their photocatalytic activity for hydrogen evolution from methanol aqueous solution," Applied surface science, vol. 274, pp. 328–333, 2013.

[29] Z. Çaldıran and L. B. Taşyürek, "The role of molybdenum trioxide in the change of electrical properties of Cr/MoO3/n-Si heterojunction and electrical characterization of this device depending on temperature," Sensors and Actuators A: Physical, p. 112765, 2021.

[30] A. R. Deniz, Z. Çaldıran, Ö. Metin, K. Meral, and Ş. Aydoğan, "The investigation of the electrical properties of Fe3O4/n-Si heterojunctions in a wide temperature range," Journal of colloid and interface science, vol. 473, pp. 172–181, 2016.

[31] S. K. Cheung and N. W. Cheung, "Extraction of Schottky diode parameters from forward current-voltage characteristics," Applied Physics Letters, vol. 49, no. 2, pp. 85–87, 1986.

[32] R. K. Gupta, K. Ghosh, and P. K. Kahol, "Fabrication and electrical characterization of Au/p-Si/STO/Au contact," Current Applied Physics, vol. 9, no. 5, pp. 933–936, 2009.

[33] A. TÜRÜT, "On current-voltage and capacitance-voltage characteristics of metal-semiconductor contacts," Turkish Journal of Physics, vol. 44, no. 4, pp. 302–347, 2020.

[34] H. Norde, "A modified forward I-V plot for Schottky diodes with high series resistance," Journal of Applied Physics, vol. 50, no. 7, pp. 5052–5053, 1979.

[35] A. Kocyigit, I. Orak, Z. Çaldıran, and A. Turut, "Current–voltage characteristics of Au/ZnO/n-Si device in a wide range temperature," Journal of Materials Science: Materials in Electronics, vol. 28, no. 22, pp. 17177–17184, 2017.

[36] A. Karabulut, A. Sarilmaz, F. Ozel, İ. Orak, and M. A. Şahinkaya, "A novel device fabricated with Cu2NiSnS4chalcogenide: Morphological and temperature-dependent electrical characterizations,"

Current Applied Physics, vol. 20, no. 1, pp. 58–64, 2020, doi: https://doi.org/10.1016/j.cap.2019.10.011.

[37] Y. S. Ocak, C. Bozkaplan, H. S. Ahmed, A. Tombak, M. F. Genisel, and S. Asubay, "Temperature dependent electrical characterization of RF sputtered MoS2/n-Si heterojunction," Optik, vol. 142, pp. 644–650, 2017.

[38] [38] A. Gencer Imer et al., "Interface controlling study of silicon based Schottky diode by organic layer," Journal of Materials Science: Materials in Electronics, vol. 30, pp. 19239–19246, 2019.

[39] E. Aldırmaz et al., "Cu-Al-Mn shape memory alloy based Schottky diode formed on Si," Physica B: Condensed Matter, vol. 560, pp. 261–266, 2019.

[40] A. A. M. Farag, H. S. Soliman, and A. A. Atta, "Analysis of dark and photovoltaic characteristics of Au/Pyronine G (Y)/p-Si/Al heterojunction," Synthetic metals, vol. 161, no. 23–24, pp. 2759–2764, 2012.

[41] A. G. Al-Sehemi, A. Karabulut, A. Dere, A. A. Al-Ghamdi, and F. Yakuphanoglu, "Photodiode performance and infrared light sensing capabilities of quaternary Cu2ZnSnS4 chalcogenide," Surfaces and Interfaces, vol. 29, p. 101802, 2022, doi: https://doi.org/10.1016/j.surfin.2022.101802.

[42] E. Özcan et al., "Fabrication of hybrid photodiode systems: BODIPY decorated cyclotriphosphazene covalently grafted graphene oxides," Inorganic Chemistry Frontiers, vol. 7, no. 16, pp. 2920–2931, 2020.

**Türk Doğa ve Fen Dergisi**
**Turkish Journal of Nature and Science**
www.dergipark.gov.tr/tdfd

# Taguchi Approach on Stress-Displacement Analyses of the Mounted Type Chassis Used in Agricultural Sprayer Machine

**Ali Rıza BUĞDAYCI[1]** , **Ali ÖNAL[1]** , **Bekir YALÇIN[2]** *

[1] Önallar Agricultural Machinery Company, Design Center, Konya, Türkiye
[2] Afyon Kocatepe University, Technology Faculty, Mechanical Engineering Department, Afyonkarahisar, Türkiye
Ali Rıza BUĞDAYCI ORCID No: 0000-0002-0167-562X
Ali ÖNAL ORCID No: 0009-0005-7312-0171
Bekir YALÇIN ORCID No: 0000-0003-0102-7769

*Corresponding author: bekiryalcin@aku.edu.tr*

**Abstract:** The optimum design for effective and economical use of agricultural sprayer machinery is becoming increasingly important. In order to reduce weight of agricultural sprayer machinery, safe designing has been continuously developed on chassis and sprayer boom by related engineers. The purpose of study aim is to determine how much boom and tank weights the mounted type chassis can carry. By the way, the stress strain analyses of the developed mounted type chassis design for agricultural sprayer machine were carried out with finite elements analyses (FEA) after doing related literature survey. The Taguchi orthogonal array design (L16, $2^4$) for eight FEA is done. After doing FEA according to Taguchi experimental design, von-Mises stress and shear stress together with displacements on mounted type chassis were obtained. As a result, the effect of the weights of pesticide tank and sprayer boom on stresses and displacement determined. The effect on equivalent von-Mises stress of pesticide tank and boom weights obtained as 5.89% and 87.38% sequentially from variance analyses. Moreover, the boom width, tank capacity and safety factor on the developed chassis were predicted via FEA before manufacturing.

78

# Tarımsal İlaçlama Makinelerinde Kullanılan Asılır Tip Şaside Gerilme ve Yerdeğiştirme Analizi Üzerine Taguchi Yaklaşımı

**Anahtar Kelimeler**
Tarımsal ilaçlama makinesi,
Asılır tip şasi,
Gerilme ve yer değiştirme analizi

**Öz:** Tarımsal ilaçlama makinelerinin performanslı ve ekonomik kullanımı için optimum tasarımın önemi giderek artmaktadır. Bu bağlamda, konuyla ilgili mühendisler tarımsal ilaçlama makinelerinin ağırlığını azaltmak için şasi ve ilaç püskürtücü kanatların emniyetli tasarımını geliştirmeye devam etmektedirler. Bu çalışmanın amacı, yeni asılır tip şasinin taşıyabileceği tarımsal ilaç püskürtücü ve ilaç deposu ağırlıklarını belirmektir. Bu bağlamda, gerekli literatür araştırmasından sonra asılır tip tarımsal ilaçlama makinesinin şasisi için statik gerilme-yer değiştirme analizi sonlu elemanlar yöntemi kullanılarak gerçekleştirilmiştir. Sistematik sonlu elemanlar analizi için Taguchi ortogonal dizin deney tasarımı (L16, $2^4$) yapılmış ve neticede geliştirilen asılır tip şaside oluşan bileşke gerilme ve kayma gerilmesi ile birlikte yer değiştirme değerleri elde edilmiştir. Varyans analizinden, püskürtücü ve ilaç tankı ağırlıklarının bileşke gerilme üzerine etkisi sırasıyla 87.38% ve 5.89% elde edilmiştir. Sonlu elemanlar analizleri sonucunda, imalat öncesi ilaç püskürtücü kanadın ve ilaç tank ağırlıklarının gerilme ve yer değiştirme üzerine etkisi ve püskürtücü kanat genişliği, ilaç tank kapasitesi ve güvenlik faktörü tahmin edilmiştir.

## 1. INTRODUCTION

Today agricultural machine and its equipment sector has turned into a unique sector rather than a sub-branch of machinery sector. Agricultural spraying machine is one of the agricultural machines affecting agricultural yield. Moreover, with the adaptation of the automation and controlling systems to the agricultural spraying machine, the conventional spraying machines have been

transformed into high value-added technology. For example; Akgül et al [1] developed the GPS aided proportional controller unit used in agricultural spraying. In their study, they declared that the amount of pesticide per unit agricultural area with low margin error and commercialization of this technology. Ilıca and Boz [2] developed an agricultural nozzle-height control test system using a permanent magnet tubular linear synchronous motor. They experimentally tested this control system that the developed system keeps the distance between differently sized plants and the nozzle at the set point with minimum error. It was mentioned in another study [3] that the automatic boom control systems were developed to check dynamic and static behaviour of spray boom and its suspension. Besides, it was reported [4] that the artificial intelligent and image processing technologies started to be used to detect and separate weeds from plants and also autonomous agricultural aircraft spraying system in the pesticide control. The opportunity to improve the control of the suspended center frame and boom system has dramatically increased using the hydraulic cylinders, spring-damper systems, sensor instrumentation and programmable controllers increase the potential for better management and control of a suspended boom system [5].

The sprayer boom system has four main mechanical components: the fixed center frame, suspended center frame, right and left boom wing. Agricultural spraying quality depends on a stability these mechanical components together with operation and land conditions, control and suspension systems. All mechanical components, suspended and control systems are assembled to the chassis of sprayer. Researcher and engineer have interested to understand a stability and stress-strains behaviours of mechanical components in agricultural sprayer machine in order to develop new suspension and control systems [6-12]. For example, Erdoğan et al [6], an increase in sprayer boom length caused increasing the stress on the connection of boom elements due to wing beat and cross displacements obtained from finite element analyses for sprayer boom. Therefore, they preferred to support the boom with swing bearing and chain link to sprayer chassis and center section in the booms wider than 15 meter. Miles 2018 [13] reported that it is important to control the boom height due to maintaining problem a level boom as when driving over uneven terrain with a wider boom and at faster speeds. Also, the related manufacturer started to manufacture agricultural spraying machining having larger pesticide tank, wider booms, faster drive and more acres spraying [13] to meet consumer demands and to improve this technology. Therefore, various boom and frame designs have been developed to control the boom height in the sector. For example, in one study [14] emphasized that the stability and level of the boom greatly depend on the chassis and suspension of the sprayer to maintain the optimum nozzle height. There are different methods to mount the boom to allow the boom rotate around pivot location on the machine chassis. These are known as rigid, fixed, pendulum, trapeze, inverted trapeze, and a combination of

pendulum and trapeze of boom center designs. It is claimed that the fixed boom center mounted chassis may be useful to carry extra load on the boom and to attach some auto height-control system study [14]. Another study gives information on the structural analyses result about transport chassis of sprayer machine that safety factor calculated as between 0.33 and 1.34. [15]. Koç 2015 [16] studied on the structural analyses of field sprayer boom that he emphasized using aluminium for active boom suspension system for field sprayer boom produced more favourable structural results than steel.

In this study, the main aim is to investigate stress and displacement analyses in mounted type chassis of agricultural sprayer machinery by static finite elements analyses (FEA) before manufacturing. FEA sets were planned to simulate real condition by Taguchi orthogonal array design (L16 $2^4$). Total eight FEA were realized by using ANSYS programme under different loads occurred with different the pesticide tank capacities and sprayer boom length. After doing literature survey, the mounted type chassis construction were designed to carry the fixed boom center with Solid program and then were transferred to ANSYS structural analyses, and also material constant and other finite elements modelling arrangement such as element type, element size, support type and locations, the calculated all loads and its locations. After 16 trials of FEA analyses, von-Mises stress, shear stress and displacement results for each FEA trial were obtained and then these results were used to analyze of Taguchi to predict the stress and displacements consecration in the chassis at the design stage. According to FEA results and Taguchi analyses, important information for design and manufacturing to mounted chassis were obtained.

## 2. MATERIAL AND METHOD

The mounted type chasses was modelled in real size which can be seen in Figure 1. Figure 1a shows the front left side view of chasses including upper and lower connecting points, points of mass. Mass points are the surfaces where the spraying tank is placed and carries the tank. Chassis is mounted with upper and lower connection point on the tractor suspension arms. After modelling the chasses, the optimum and homogeneous meshing were carried out which was given in Figure 1c. FEA were conducted with Ansys program after reviewing structural analyses workings, and also the meshing was realized by selection quadrilateral triangle elements in optimum condition.

The mesh sizes, which will negligible affect the stress and strain results, was determined as 8 mm. To improve the mesh quality, standard mechanical and high smooting modes on automatic method used. The steel material of St37 for the mounted chassis was selected. Afterwards, the homogenous mesh structure was obtained by preliminary preparing of finite elements which was given in Figure 1c.

79
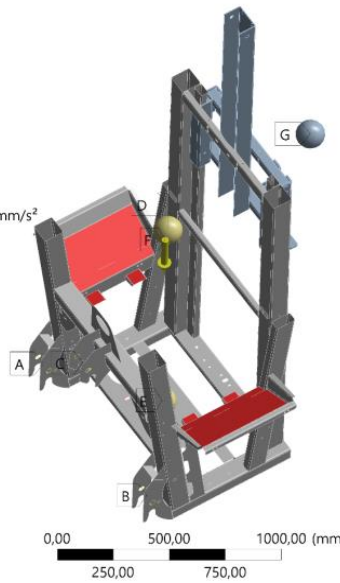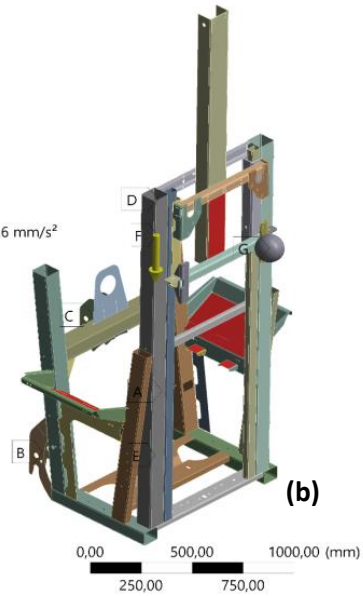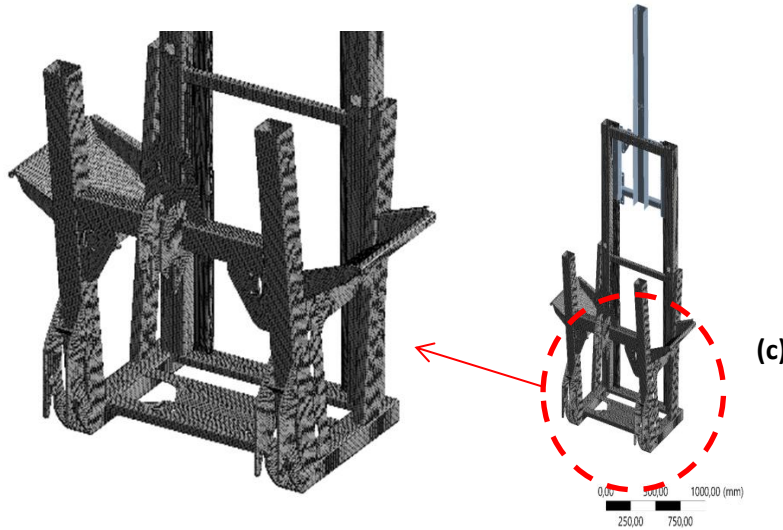
**Figure 1.** a) Front left side view of the mounted chasses, b) Back right side view of it, c) Mesh structure.

Total elements of 135064 elements and nodes of 137855 were produced after doing FEA of spraying machine with mounted chassis. Later, the cylindrical support was applied to the lower and upper connection points of chassis model. FEA was systematically done with L16 ($2^4$) Taguchi orthogonal array design (Table 1).

Tank and boom construction weights, which may be possible mounting to the chassis, have been determined by taking into account the application information. Taguchi orthogonal array design is a practical method to determine the effect of main input parameters on target outputs of analyse and experiment research, to determine the sub-level of main input variables.

**Table 1.** Taguchi orthogonal array design for FEA, input variables and levels.

| Input Variables | Force (kgf) | Levels | | | |
|---|---|---|---|---|---|
| | STW (kgf) | 1200 | 1500 | 2400 | 3000 |
| | SBW (kgf) | 450 | 600 | 900 | 1200 |
| **FEA Trials** | | | | | |
| FEA No | STW (kgf) | SBW (kgf) | | | |
| 1 | 1200 | 450 | | | |
| 2 | 1200 | 600 | | | |
| 3 | 1200 | 900 | | | |
| 4 | 1200 | 1200 | | | |
| 5 | 1500 | 450 | | | |
| 6 | 1500 | 600 | | | |
| 7 | 1500 | 900 | | | |
| 8 | 1500 | 1200 | | | |
| 9 | 2400 | 450 | | | |
| 10 | 2400 | 600 | | | |
| 11 | 2400 | 900 | | | |
| 12 | 2400 | 1200 | | | |
| 13 | 3000 | 450 | | | |
| 14 | 3000 | 600 | | | |
| 15 | 3000 | 900 | | | |
| 16 | 3000 | 1200 | | | |

It is well known that traditional experiment and analyze design plan is time-consuming and cause the high costs and complexity while determining the cause-effect

relationship [17].In the Taguchi orthogonal design, two input parameters of spraying tank weight (STW) with levels of 1200, 1500, 2400, 3000 kgf and sprayer boom weight (SBW) with levels of 450, 600, 900, 1200 kgf were selected. Spraying tank weigh is the full weight with pesticide. Boom weights of 450, 600, 900, 1200 kgf vary with length of 12, 16, 20, 24 m, respectively. Thereby, the pesticide capacity and spraying width of the mounted chassis planned to be manufacture have been determined. As can be seen Table 1, total 16 analyses were conducted to determining the effect of input variables on output variables of von-Mises stress, shear stress and displacements for the mounted spraying machine chassis. According to Table 1, Taguchi analyse was performed by using the stress and displacement values obtained from FEA. The relationship between

input variables with stress and displacement on sprayer chassis tried to determine.

## 3. RESULTS

After doing FEA, the total 80 values about shear stress, von-Mises stress and displacement results for each FEA trial were obtained. Firstly, the screen samples of stresses and displacements distributions were given in Figure 2 for the obtained minimum loading condition of 1st and 16th trials, respectively. According to 1st FEA results which was conducted under 450 kgf of boom weight and 12 m of its width and 1200 kgf of pesticide tank weight; 178.44 MPa of maximum von-Mises stress, 58.87 MPa of shear stress and 7.6727 mm of total displacement were occurred on the chassis construction, respectively.
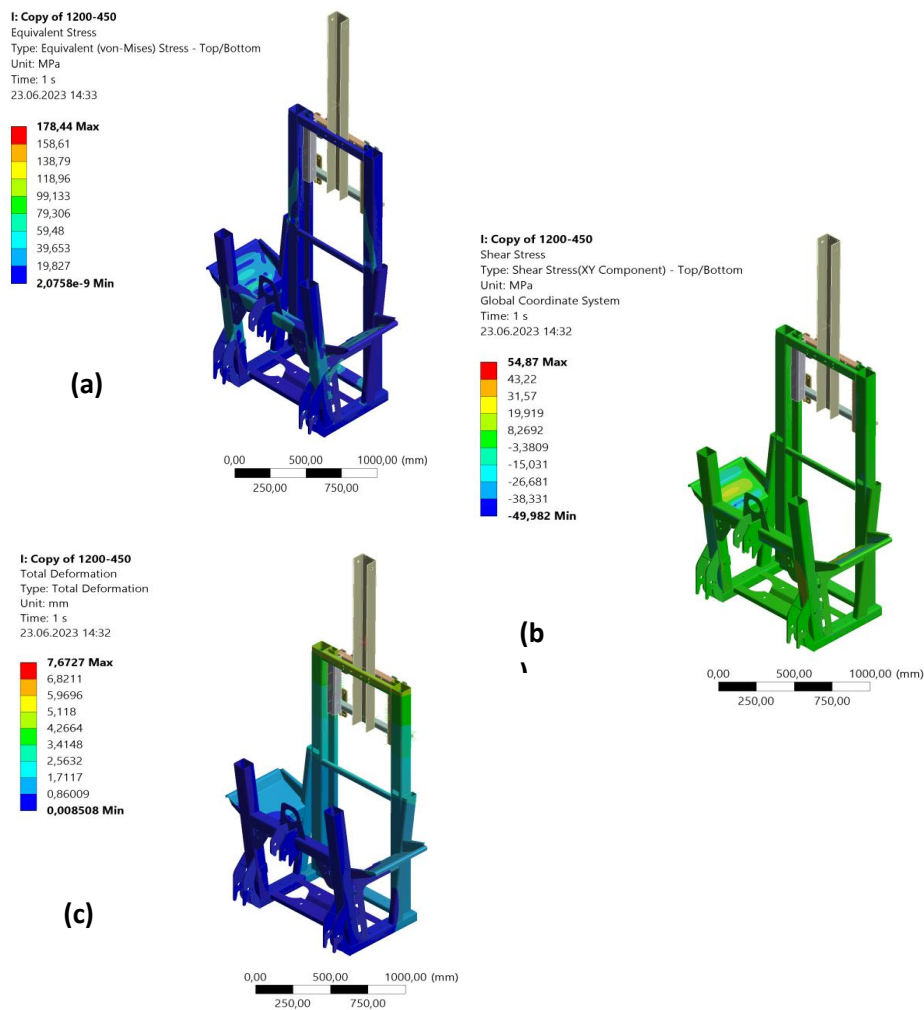
**Figure 2.** FEA result screens for minimum loading condition (1st FEA).

While the stresses concentrated on surfaces where the pesticide tank is placed, displacements occurred in vertical profile close to the sliding mechanism that adjusts the spraying level. In this situation, Taguchi analyse is performed to determine the effect of pesticide tank and boom weights on stress and displacement. The contributions values on equivalent von-Mises stress of pesticide tank and boom weights obtained as 87.38% and 5.89% sequentially from variance analyses realized using results of FEA analyses (Table 2). The effect of sprayer boom weight on von-Mises stress is seen more and this can be understood from the P-values of 0.0002 and 0.114770, respectively. R-Sq values of 93.26%, error of 6.74%, R-Sq (adj) of 88.77 and R-Sq (pred.) of 78.71% were obtained from variance analyses which are within the acceptable values [18]. As can be seen in Figure 3, the sprayer boom weight is more effective than pesticide tank weight in the Taguchi analyses by adopting "smaller is better". The reason interpreted that sprayer boom caused especially bending stress together with shear stress on the chassis of sprayer machine since the boom is mounted behind the chassis. Mises stresses relatively increased with increasing from 450 kgf to 600

kgf, on the other hand, the boom weight above 600 kgf increased von-Mises stresses dramatically.

**Table 2.** The contributions values on equivalent von-Mises stress of pesticide tank and boom weights.

| Source | DF | Seq SS | Contribution | Adj SS | Adj MS | F-Value | P-Value |
|---|---|---|---|---|---|---|---|
| Pesticide Tank Weight (kgf) | 3 | 11185 | 5.89% | 11185 | 3728 | 2.62 | 0.11470 |
| Sprayer Boom Weight (kgf) | 3 | 165989 | 87.38% | 165989 | 55330 | 38.92 | 0.00002 |
| Error | 9 | 12796 | 6.74% | 12796 | 1422 | | |
| Total | 15 | 189970 | 100.00% | | | | |

This state can be seen in Figure 3a. 1200 kgf and 1500 kgf of pesticide tank weight caused smiliar von-Mises stress values, and also the pesticide tank weight above 1500 kgf relatively increased. Thereby, the boom widht and boom weight to be monted on the agricaltural spraying machine should be evaluated more in terms of safe chassis design and rigidty.
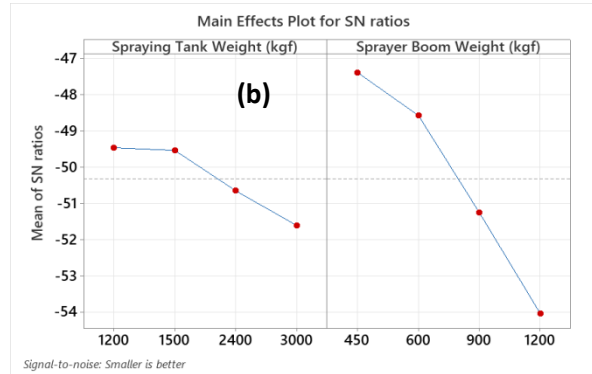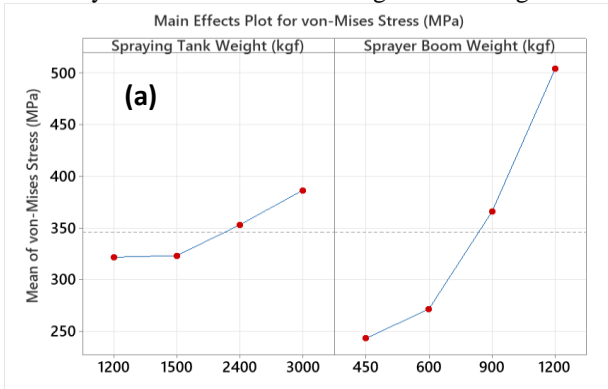


Figure 3. The curves of main effect and SN ratios for von-Mises stresses.
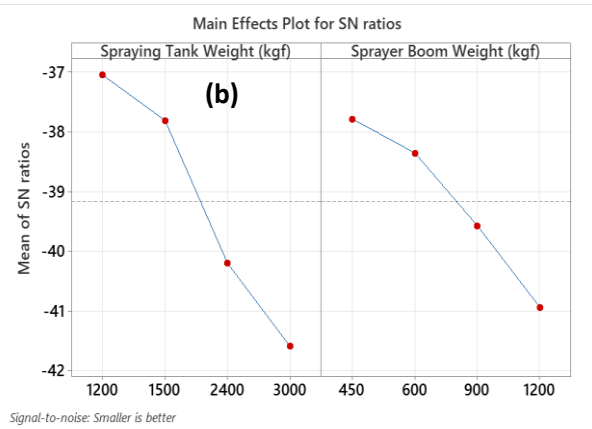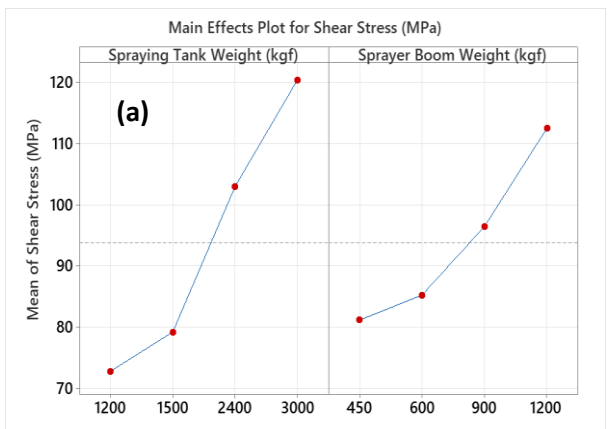


Figure 4. The curves of main effect and SN ratios for shear stresses obtained from Taguchi analyses.

Figure 4 shows the main effect and SN curves for shear stress occured on the chassis obtained from FEA analyses. In contrast to the von-Mises stress situation, the pesticide spraying tank weight is more effective on shear stresses. Because, sprayer thank is mounted on the chassis of agricultural sprayer. The shear stresses increased and bending stresses less than the effect of boom due to loading on the chassis. The shear stress increased dramatically when more than 1500 kgf of spraying tank is placed on the chassis. As similar, the

boom weight above 600 kgf increased dramatically shear stresses. The effect of main input parameters on displacement of chassis is shown in Figure 5. According to Figure 5, sprayer boom weight has more influence on displacement of chassis. The effect of pesticide spraying tank weight between 1200 kgf and 2400 kgf on displacement of chassis is almost the same, and also, after loading 2400 kgf, the displacement tends to increase. On the other hand, in case of increasing the

sprayer boom weight depending on its width, chassis displacement dramatically increase.
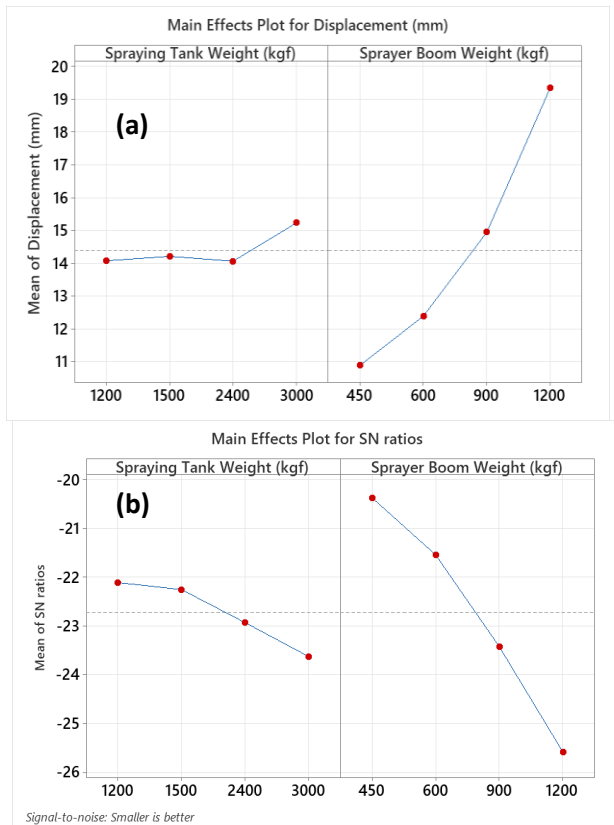


**Figure 5.** The main effect and SN ratio of main input parameters on displacement of chassis.

As can be seen in Figure 6, the lowest displacements (7.6727 mm and 7.9685 mm) of chassis were respectively obtained from 1st and 5th FEA trials, which are 1200 kgf of tank weight, 450 kgf of boom weight and 1500 kgf of tank weight, 450 kgf of boom weight, respectively. The highest displacement values of 22.862 mm and 22.857 mm occurred in 4th and 8th of FEA trials, which are 1200 kgf of tank weight, 1200 kgf of boom weight and 1500 kgf of tank weight, 1200 kgf of boom weight, respectively. Indeed, the displacement values in sprayer chassis are found to be between 8 mm and 16 mm.

The combined effect of two input parameters on von-Mises stress, shear stress and displacement can be seen in Figure 7. When 600 kfg of sprayer boom and around 2200 kgf of tank capacity is mounted on the sprayer chassis, the obtained von-Mises stresses was found to be lower than the yield strengt (around 230 MPa) of chassis materials St37 steel which can be seen in Figure 7a. The chassis construction has been forced with around 80 MPa of shear stress under same loading for 600 kfg of sprayer boom and around 2200 kgf of tank capacity. Over these loads caused the stresses above yield strenght (YS) of sprayer chassis. Figure 8 shows stresses for 16 FEA trials and in can be interpreted the safety factor of sprayer chassis.
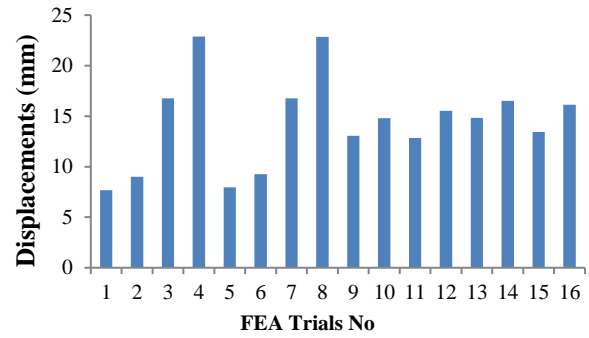


**Figure 6.** Displacement values in sprayer chassis for 16th FEA trials.
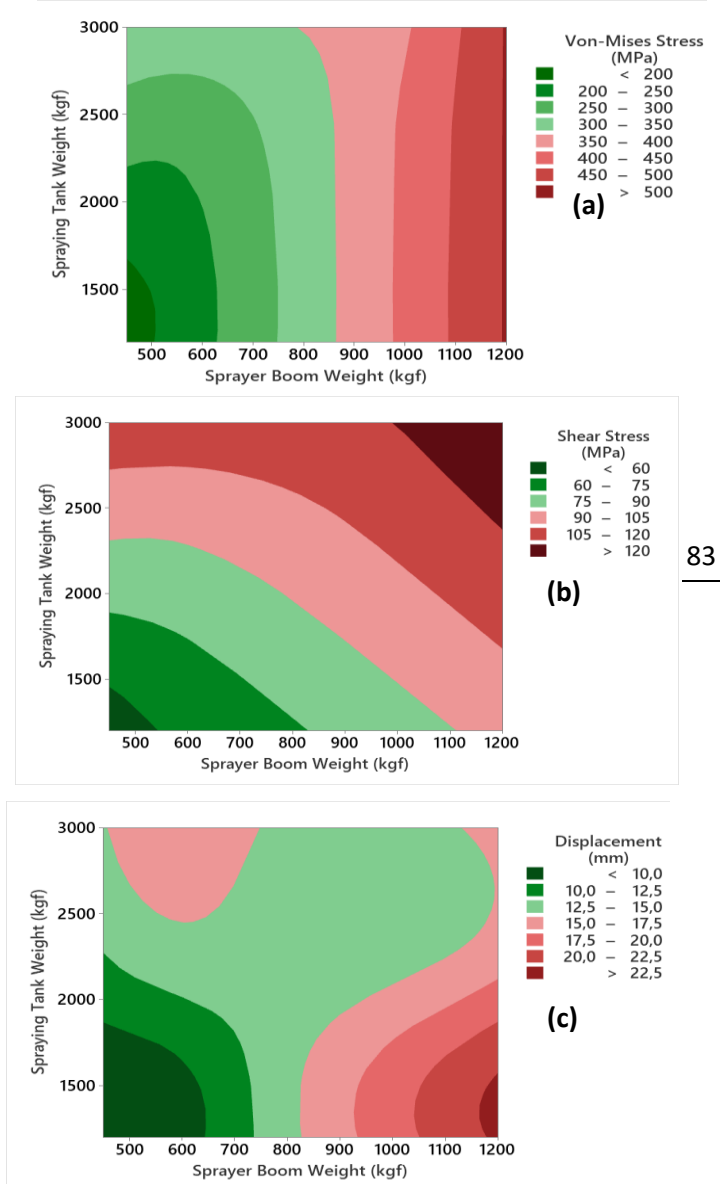


**Figure 7.** The combined effect of two input parameters on von-Mises stress (a), shear stress (b) and displacement (c).

83
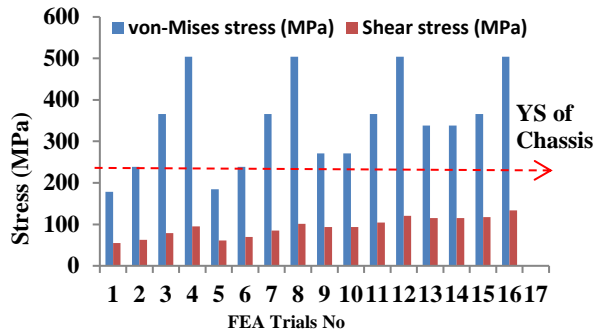
**Figure 8.** Von-Mises stress and shear stress values obtained from FEA of sprayer chassis.

## 4. CONCLUSION

In this study, which was performed to estimate the stress-displacement occurring in the designed mounted type agricultural spraying machine chassis before manufacturing, the following results were obtained:

➢ Firstly, safe the pesticide tank capacity and sprayer boom width of new one designed mounted type spraying chassis is determined by obtained FEA. The lowest displacements (7.6727 mm and 7.9685 mm) of chassis are respectively obtained from 1st and 5th FEA trials, which are 1200 kgf of tank weight, 450 kgf of boom weight and 1500 kgf of tank weight, 450 kgf of boom weight, respectively.

➢ While the stresses concentrated on surfaces where the pesticide tank is placed, displacements occurred in vertical profile close to the sliding mechanism that adjusts the spraying level.

➢ The effect on equivalent von-Mises stress of pesticide tank and boom weights obtained as 5.89% and 87.38% sequentially from variance analyses. The combined effect of sprayer boom and sprayer tank weights has the most influence on shear stress in sprayer chassis, secondly von-Mises stress and finally displacement values.

➢ Finally, the safety factors for new design of mounted type agricultural spraying machine chassis has been determined as 1.35 and 1.3 from 1st and 5th of finite elements analyses according to the obtained maximum von-Mises stress. It is alleged that the value of required safety factor of $1.3 - 1.35$ was adopted as a mean value from the range of factors for very accurate calculations, uniform material and fine design [19].

### Acknowledgement

## REFERENCES

[1] Akgül G. Aladağ NC. Taşkıran A. Yalçın B. Tarımsal ilaçlamada kullanılmak üzere GPS destekli oransal kontrolcü biriminin geliştirilmesi. Türk Tarım ve Doğa Bilimleri Dergisi. 2023; 10(3): 481–490.

[2] Allıca I. Boz A.F. Design of a nozzle-height control system using a permanent magnet tubular linear synchronous motor. Tarım Bilimleri Dergisi.2018; 24: 374-385.

[3] Herbst A. Osteroth HJ. Stendel, H. A novel method for testing automatic systems for controlling the spray boom height. Biosystems Engineering. 2018; 174: 115-125.

[4] Keskin M. and Şekerli YE. Tarımda Yabancı Ot Mücadelesinde Hassas, Otonom ve Akıllı Sistemler. Akiteck 4.0 Dergisi. 2022; 1 (1): 32-36.

[5] Blaylock KR. Active air spring control as a method of agricultural sprayer boom system suspension. Iowa State University. Master Theses. Agricultural and Biosystems Engineering. 2020.

[6] Erdoğan H. Sayrugaç A. Yalçın B. Tarımsal ilaçlamada X tipi katlanabilen ve geleneksel kanatlarda oluşan gerilmenin tahmini ve taguchi analizi. Afyon Kocatepe Üniversitesi Fen ve Mühendislik Bilimleri Dergisi. 2023; 23; 798-810.

[7] Ooms D. Ruter R. Lebeau F. Destain MF. Impact of the horizontal movements of a sprayer boom on the longitudinal spray distribution in field conditions. Crop Protection. 2003; 22: 813–820.

[8] Anthonis J. Audenaert J. Ramon H. Design optimisation for the vertical suspension of a crop sprayer boom. Biosystems Engineering. 2005; 90 (2): 153–160.

[9] Benez RC. Antuniassi UR. Chechetto RG. Motta AAB. Carvalho FK. Behavior of a sprayer boom stabilization system in vertical and horizontal movements. Energia na Agricultura. 2016; 31 (1): 1–9.

[10] Cui LF. Xue XY. Ding SM. Le FX. Development of a DSP-based electronic control system for the active spray boom suspension, Comput. Electron. Agric. 2019; 166; 105024.

[11] Lipinski AJ. Lipinski S. Burg P. Sobotka SM. Influence of the instability of the field crop sprayer boom on the spraying uniformity. Journal of Agriculture and Food Research. 2022;10;10432.

[12] Sunar B. Akıllı tarım uygulamalarında kullanılan ilaçlama sistemlerinin araştırılması. Afyon Kocatepe Üniversitesi, Makine Mühendisliği Bölümü, Bitirme Tezi. Afyonkarahisar Türkiye. 2020.

[13] Miles LT. Developing general procedure to quantitatively analyze boom height control performance on self-propelled agricultural sprayers. Iowa State University, Agricultural Engineering. Master Theses. USA, 2018.

[14] Betts G. and Gordon B. 2020. Boom stability and height control: the importance of design and control, Grain Research Development Corperation, Australia, 24.

[15] Yılmaz D. Hamamcı E. Salık D. Ahıskalı Y. Structural analyses of agricultural machinery: Case study for a transport chassis of a spraying machine. Journal of Agricultural Machinery Science. 2011;7 (4):405-409.

[16] Koca C. Structural Analysis of Field Sprayer Booms. Journal of Agricultural Sciences. 2017;23:147-155.

84

[17] Bolat Ç. Karakılınç U. Yalçın B. Öz Y. Yavaş Ç. Ergene B. Ercetin A. Akkoyun, F. Effect of drilling parameters and tool geometry on the thrust force and surface roughness of aerospace grade laminate composites. Journal of Micromachines. 2023; 14: 1427-1438.

[18] Montgomery DC. Design and analysis of experiments. 5th ed. John Wiley & Sons Inc, 2001.

[19] Szulca M. Malujdaa I. Talaśkaa K. Method of determination of safety factor on example of selected structure. Procedia Engineering. 2016; 136: 50 – 55.

**Türk Doğa ve Fen Dergisi**
**Turkish Journal of Nature and Science**
www.dergipark.gov.tr/tdfd

# Methods, Equipment and Other Methods Used by Healthcare Professionals to Protect from New Type of Coronavirus (SARS-Cov-2)

**Semih ERİTEN[1*]** , **Berna ERİTEN[2*]**

[1] Department of  Emergency, Sultanbeyli State Hospital, Sultanbeyli, İstanbul, Türkiye
[2] Department of Pathology, Şehit Prof. Dr. İlhan Varank Sancaktepe Training and Research Hospital, Sancaktepe, İstanbul, Türkiye
Semih ERİTEN ORCID No: 0000-0001-8516-372X
Berna ERİTEN ORCID No: 0000-0003-3710-1502

*Corresponding author: semiheriten@hotmail.com*

**Abstract:** In this study, it was aimed to examine the knowledge and protection levels of healthcare workers against COVID-19 disease. The study population consisted of 203 healthcare workers (Doctor: 30, Nurse: 104, Janitor: 21, Midwife: 48) who accepted to participate in the study in the Emergency Department of Malatya Training and Research Hospital between August 06 and December 31, 2020. According to the current findings of the study, it was observed that there may be a relationship between COVID-19 and the method used to protect healthcare workers and personal protective equipment. We believe that the findings of the study will help to develop protection strategies for workers in the event of a COVID-19 pandemic. In light of the ongoing global impact of the COVID-19 pandemic, it is imperative to proactively devise interventions and implement well-considered strategies aimed at safeguarding the health and well-being of healthcare professionals.

# Sağlık Çalışanlarının Yeni Tip Koronavirüsten (SARS-Cov-2) Korunmak için Kullandıkları Yöntemler, Ekipmanlar ve Diğer Yöntemler

**Öz:** Bu çalışmada sağlık çalışanlarının COVID-19 hastalığına karşı bilgi ve korunma düzeylerinin incelenmesi amaçlanmıştır. Çalışma evrenini 06 Ağustos - 31 Aralık 2020 tarihleri arasında Malatya Eğitim ve Araştırma Hastanesi Acil Servisinde çalışmaya katılmayı kabul eden 203 sağlık çalışanı (Doktor: 30, Hemşire: 104, Hizmetli: 21, Ebe: 48) oluşturmuştur. Çalışmanın mevcut bulgularına göre COVID-19 ile sağlık çalışanlarını korumak için kullanılan yöntem ve kişisel koruyucu ekipman arasında bir ilişki olabileceği gözlemlenmiştir. Çalışmanın bulgularının, bir COVID-19 pandemisi durumunda çalışanlar için koruma stratejileri geliştirilmesine yardımcı olacağına inanıyoruz. COVID-19 pandemisinin devam eden küresel etkisi ışığında, sağlık çalışanlarının sağlığını ve refahını korumayı amaçlayan müdahalelerin proaktif olarak tasarlanması ve iyi düşünülmüş stratejilerin uygulanması zorunludur.

## 1. INTRODUCTION

Pneumonia cases first appeared in Wuhan, China in December 2019, and were later discovered to be caused by a new form of coronavirus (SARS-CoV-2) agent [1]. SARS-CoV-2, which is believed to be the first cause of infection in wild animals, can be spread easily from person to person and can be carried asymptomatically [2]. COVID-19 is the name of the virus-caused disease table. Fever, cough, and shortness of breath are the most common symptoms, but gastrointestinal symptoms can also occur [3]. The virus has spread from China to the rest of the world due to the possibility of human-to-human transmission during the asymptomatic period [4]. The World Health Organization (WHO), in its statement on March 11, 2020, claimed that more than 118 thousand cases and 4291 deaths were seen in 114 countries, and Covid described 19 as a pandemic [5]. The first case was detected in Turkey reported on 11 March 2020 [6]. The number of cases continues to increase.

Healthcare workers have also started to be infected with SARS-CoV-2 since the outbreak had started. It was stated that 2055 healthcare workers were infected in China on February 20, 2020 [7]. As of 8 April 2020, the World Health Organization reported that a total of 22.073 healthcare workers from 52 different countries were infected [8]. It is predicted that the number in the world is much higher than this number. It has been announced that 15 thousand 315 healthcare workers were infected in Italy on April 10, 2020, and this number corresponds to 11% of the total infected patients [8,9]. In Turkey, on April 29 2020, according to the statement of the minister of health, 7 thousand 428 health care workers were recorded to be infected [6].

The duration of contact and the amount of virus found to be correlated with infection rates in studies conducted on infected healthcare workers [10]. Caring for a large number of infected patients over a long period of time increases the risk of infection [11]. Departments operating at the frontline and conducting processes that produce aerosols are especially vulnerable during the pandemic [12]. In a research conducted in the United States of America and England, it was presented that healthcare workers working in the front phase are at least 3 times more likely to be infected than the rest of the population. Although the use of personal protective equipment reduced the risk, it did not reduce the likelihood of infection to the same level as in the general population [13].

During the pandemic, healthcare workers' daily working patterns had to be fully altered. Prior to COVID-19, healthcare professionals who deal with patients in respiratory distress did not use routine personal protective equipment (PPE). As shown by COVID-19 patients with atypical presentations, the use of personal protective equipment (PPE) by healthcare professionals has become routine, depending on the risks of the department in which they work. The methods of triage used in hospital applications have changed. Patients with high fever and COVID-19-like complaints like shortness of breath and cough were quickly evaluated separately from other patients and began to be taken into isolated environments [14,15].

During this period, healthcare professionals are advised to use personal protective equipment such as masks, goggles, gloves, visors, and aprons during their working periods [16]. It is thought that the insufficiency of PPE increases the incidence of infection in healthcare workers [17]. In addition to protective equipment, hand hygiene is regarded as one of the most vital steps to prevent infection. Healthcare workers with insufficient hand hygiene after contact with patients have been found to have a higher risk of contracting COVID-19 disease [18].

Due to a rise in the number of infected patients, healthcare professionals from each department have been assigned to identify and treat COVID-19 patients that are outside of their area of expertise. One of the reasons for the high infection rates among healthcare workers in China is a failure to provide sufficient information and training to

front-line healthcare workers, as well as an inability to provide infection controls due to emergency situations [19].

The asymptomatic carriage has been found to have a significant place in SARS-CoV-2 transmission (20). Since healthcare workers are at higher risk of infection, it has been shown that they can become contagious with asymptomatic carriage [21]. This situation has yielded many healthcare professionals to distance themselves from their families and relatives. In Turkey, together with the world's health workers in many countries, thinking that they pose a risk in their homes, they left or were forced to isolate themselves from the vicinity of their homes in the pandemic period.

COVID-19 can be spread by droplets and interaction with polluted surfaces, putting healthcare workers at risk [22]. They must wear personal protective equipment such as masks, goggles, visors, and overalls to stay safe [23]. This condition raises the possibility of psychological issues in healthcare workers. Healthcare workers in hospitals, especially those diagnosed with COVID-19 and caring for suspected patients, may experience mental health problems as a result of their fear of infecting the virus and spreading it to others [24].

In order to carry out all strategies in epidemic management, it is critical to protect healthcare workers from the factor. Infection among healthcare workers would have a negative impact on the delivery of healthcare facilities, resulting in a reduction in the health system's response to the epidemic and an uncontrolled rise in the incidence rate [20]. Healthcare professionals in hospitals and pre-hospital areas, in particular, have no way of knowing if the patient or injured they are in close contact with has COVID-19, and they are competing with time, so they are more likely to become infected [25]. Based on this context, the purpose of the study is to examine the knowledge and protection levels of healthcare professionals against COVID-19 disease.

## 2. MATERIAL AND METHOD

This study was approved by the ethics committee of Malatya Training and Research Hospital (approval number: 23536505-000-13874). All the study subjects were assured that participation in the study was voluntary and that all information provided would remain confidential.

### 2.1. Design

One of the quantitative research techniques used in this study was the relational scanning model. The aim of relational scanning is to find the levels of variance in two or more variables. The relational screening model is described as "a research model that aims to determine whether there is a shift between two or more variables and, if there is, the degree of this change" [26]. The study population consisted of 203 healtycare professionals (Doctor: 30, Nurse: 104, Janitor: 21, Midwife: 48)

between 06 August and 31 December, 2020 who agreed to participate in the study.

## 2.2. Data Collection Tools

The literature on healthcare personnel's knowledge and protection levels against COVID 19 was scanned as the research's data collection tool, and appropriate modifications were made based on the opinions of field experts.

A questionnaire with 17 questions was utilized to assess the duties of the healthcare professionals who made up the study's sample, as well as their knowledge and protection levels against COVID-19.

The questions in the questionnaire form used within the scope of the research include whether or not healthcare professionals have received COVID-19 training, the country and year in which COVID-19 spread, the risk of transmission of COVID-19, is about their self-protection status (social distance, frequency of cleaning their hands with disinfectant during working hours, protective equipment they use) in hospital work areas, the status of passing and passing COVID-19 disease.

## 2.3. Statistical Analysis

In this study, various analyses were conducted using SPSS 25 statistical analysis software. First, the demographic characteristics of the participants were analyzed using frequency analysis and percentage calculations. Then, the Chi-square test was used to assess the associations between having COVID-19 disease and variables such as hand hygiene, compliance with social distancing rules and changing work clothes, and use of protective equipment.

## 3. RESULTS

The distribution of demographic characteristics of the healthcare professionals included in the study is given in Table 1.

**Table 1.** The distribution of demographic characteristics of the healthcare professionals

| | | n | % |
|---|---|---|---|
| Profession | Doctor | 30 | 14.8% |
| | Nurse | 104 | 51.2% |
| | Janitor | 21 | 10.3% |
| | Midwife | 48 | 23.6% |
| Training on COVID-19 disease | Online | 49 | 24.5% |
| | Face to face | 60 | 30.0% |
| | Online and face to face | 17 | 8.5% |
| | None | 74 | 37.0% |
| With the emergence of COVID-19 disease; Did you change yourself in terms of protection in the working area in the hospital in the period before the appearance of COVID-19 disease? | Yes | 196 | 96.6% |
| | No | 7 | 3.4% |
| How many times do you wash your hands with soap during your working hours? | 5> | 3 | 1.5% |
| | 5-10 | 48 | 23.6% |
| | 10-15 | 51 | 25.1% |
| | 15< | 101 | 49.8% |

| | | | |
|---|---|---|---|
| How many times do you clean your hands with disinfectants during your working hours? | 5> | 27 | 13.3% |
| | 5-10 | 45 | 22.2% |
| | 10-15 | 56 | 27.6% |
| | 15< | 75 | 36.9% |
| Do you obey the social distance rule with the patients? | Yes | 174 | 85.7% |
| | No | 29 | 14.3% |
| Do you obey the social distance rule with the employees? | Yes | 137 | 67.5% |
| | No | 66 | 32.5% |
| Do you change the clothes you wear while coming to work in the hospital or do you work with the clothes you come from home? | I come to the hospital in my workwear | 43 | 21.2% |
| | I come to the hospital with my regular clothes. I wear work clothes at the hospital | 148 | 72.9% |
| | I come to the hospital in normal clothes and work with these clothes without changing. | 12 | 5.9% |
| Have you had a PCR test for COVID-19 disease? | Yes | 115 | 56.7% |
| | No | 88 | 43.3% |
| Do you currently have COVID-19 disease? | Yes | 3 | 1.5% |
| | No | 200 | 98.5% |
| Have you had COVID-19 disease? | Yes | 10 | 4.9% |
| | No | 193 | 95.1% |
| Using Protective Equipment | Mask | Yes | 203 | 100% |
| | | No | - | - |
| | Apron | Yes | 48 | 23.6% |
| | | No | 155 | 76.4% |
| | Gloves | Yes | 39 | 19.2% |
| | | No | 164 | 80.8% |
| | Shoe Cover | Yes | 39 | 19.2% |
| | | No | 164 | 80.8% |
| | Bonnet | Yes | 115 | 57.5% |
| | | No | 85 | 42.5% |
| | Visor | Yes | 91 | 44.8% |
| | | No | 112 | 55.2% |
| | Overalls | Yes | 39 | 19.2% |
| | | No | 164 | 80.8% |
| Total | | 203 | 100% |

The distribution of the answers given according to the condition of having COVID-19 disease was examined by Chi-square analysis in Table 2. According to Table 2., there is a significant correlation between the distribution of the answers given according to the conditions and having COVID-19 disease ($p < 0.05$).

**Table 2.** The distribution of the answers given according to the condition of having COVID-19 disease

| | | Had a COVID-19 Disease | | | | p |
|---|---|---|---|---|---|---|
| | | Yes | | No | | |
| | | n | % | n | % | |
| How many times do you wash your hands with soap during your working hours? | 5> | 0 | 0.0% | 3 | 1.6% | 0.000 |
| | 5-10 | 10 | 100.0% | 38 | 19.7% | |
| | 10-15 | 0 | 0.0% | 51 | 26.4% | |
| | 15< | 0 | 0.0% | 101 | 52.3% | |
| How many times do you clean your hands with disinfectants during your working hours? | 5> | 3 | 30.0% | 24 | 12.4% | 0.002 |
| | 5-10 | 0 | 0.0% | 45 | 23.3% | |
| | 10-15 | 7 | 70.0% | 49 | 25.4% | |
| | 15< | 0 | 0.0% | 75 | 38.9% | |
| Do you obey the social distance rule with the patients? | Yes | 10 | 100.0% | 164 | 85.0% | 0.206 |
| | No | 0 | 0.0% | 29 | 15.0% | |
| Do you obey the social distance rule with the employees? | Yes | 3 | 30.0% | 134 | 69.4% | 0.015 |
| | No | 7 | 70.0% | 59 | 30.6% | |
| Do you change the clothes you wear while coming to work in the hospital or do you work with the clothes you come from home? | I come to the hospital with my work clothes such as apron and uniform. | 0 | 0.0% | 43 | 22.3% | 0.142 |
| | I come to the hospital in my regular clothes. I change it with uniform at the hospital. | 10 | 100.0% | 138 | 71.5% | |
| | I come to the hospital in normal clothes and work with these clothes without changing. | 0 | 0.0% | 12 | 6.2% | |

The relationship between the health personnel's status of having COVID-19 disease and using protective equipment is given in Table 3. According to Table 3., there is no significant correlation between using protective equipment and having COVID-19 disease (p> 0.05).

**Table 3.** Relationship between healthcare professionals' status of having COVID-19 disease and using protective equipment

| Using Protective Equipment | | Had a COVID-19 Disease | | | | p |
|---|---|---|---|---|---|---|
| | | Yes | | No | | |
| | | n | % | n | % | |
| Mask | No | 0 | 0.0% | 0 | 0.0% | - |
| | Yes | 10 | 100.0% | 193 | 100.0% | |
| Apron | No | 4 | 40.0% | 44 | 22.8% | 0.188 |
| | Yes | 6 | 60.0% | 149 | 77.2% | |
| Gloves | No | 4 | 40.0% | 35 | 18.1% | 0.102 |
| | Yes | 6 | 60.0% | 158 | 81.9% | |
| Shoe Cover | No | 10 | 100.0% | 154 | 79.8% | 0.112 |
| | Yes | 0 | 0.0% | 39 | 20.2% | |
| Bonnet | No | 6 | 60.0% | 79 | 41.6% | 0.205 |
| | Yes | 4 | 40.0% | 111 | 58.4% | |
| Visor | No | 4 | 40.0% | 108 | 56.0% | 0.253 |
| | Yes | 6 | 60.0% | 85 | 44.0% | |
| Overalls | No | 10 | 100.0% | 154 | 79.8% | 0.112 |
| | Yes | 0 | 0.0% | 39 | 20.2% | |

Table 4. shows the association between healthcare professionals' COVID-19 disease training and their level of knowledge and protection against COVID-19 disease. According to Table 4., a statistically significant relationship has been found between whether healthcare personnel receives training for COVID-19 disease and their knowledge and protection levels against COVID-19 disease. Furthermore, whether or not healthcare personnel received COVID-19 disease training and used protective equipment such as an apron, gloves, shoe cover, bonnet, visor, and overalls (p<0.05) was found to have a statistically significant relationship.

**Table 4.** Relationship between healthcare professionals' knowledge and protection against COVID-19 disease and whether or not they receive training on COVID-19 disease

| | | Having training of COVID-19 Disease | | | | | | | | p |
|---|---|---|---|---|---|---|---|---|---|---|
| | | Online | | Face to face | | Online and face to face | | No training | | |
| | | n | % | n | % | n | % | n | % | |
| How many times do you wash your hands with soap during your working hours? | 5> | 0 | 0.0% | 0 | 0.0% | 0 | 0.0% | 3 | 4.1% | 0.046* |
| | 5-10 | 7 | 14.3% | 20 | 33.3% | 6 | 35.3% | 12 | 16.2% | |
| | 10-15 | 10 | 20.4% | 15 | 25.0% | 3 | 17.6% | 23 | 31.1% | |
| | 15< | 32 | 65.3% | 25 | 41.7% | 8 | 47.1% | 36 | 48.6% | |
| How many times do you clean your hands with disinfectants during your working hours? | 5> | 4 | 8.2% | 7 | 11.7% | 3 | 17.6% | 13 | 17.6% | 0.001* |
| | 5-10 | 9 | 18.4% | 20 | 33.3% | 0 | 0.0% | 13 | 17.6% | |
| | 10-15 | 21 | 42.9% | 4 | 6.7% | 6 | 35.3% | 25 | 33.8% | |
| | 15< | 15 | 30.6% | 29 | 48.3% | 8 | 47.1% | 23 | 31.1% | |
| Do you obey the social distance rule with the patients? | Yes | 37 | 75.5% | 49 | 81.7% | 17 | 100.0% | 68 | 91.9% | 0.134 |
| | No | 12 | 24.5% | 11 | 18.3% | 0 | 0.0% | 6 | 8.1% | |
| Do you obey the social distance rule with the | Yes | 30 | 61.2% | 42 | 70.0% | 14 | 82.4% | 48 | 64.9% | 0.000* |
| | No | 19 | 38.8% | 18 | 30.0% | 3 | 17.6% | 26 | 35.1% | |

| | | | | | | | | | | |
|---|---|---|---|---|---|---|---|---|---|---|
| employees? | | | | | | | | | | |
| Do you change the clothes you wear while coming to work in the hospital or do you work with the clothes you come from home? | I come to the hospital with my work clothes such as apron and uniform. | 19 | 38.8% | 5 | 8.3% | 3 | 17.6% | 13 | 17.6% | |
| | I come to the hospital in my regular clothes. I change the uniform to work clothes at the hospital. | 30 | 61.2% | 55 | 91.7% | 14 | 82.4% | 49 | 66.2% | 0.000* |
| | I come to the hospital in normal clothes and work with these clothes without changing. | 0 | 0.0% | 0 | 0.0% | 0 | 0.0% | 12 | 16.2% | |
| Mask | No | 0 | 0.0% | 0 | 0.0% | 0 | 0.0% | 0 | 0.0% | - |
| | Yes | 49 | 100.0% | 60 | 100.0% | 17 | 100.0% | 74 | 100.0% | |
| Apron | No | 7 | 14.3% | 12 | 20.0% | 3 | 17.6% | 26 | 35.1% | 0.037* |
| | Yes | 42 | 85.7% | 48 | 80.0% | 14 | 82.4% | 48 | 64.9% | |
| Gloves | No | 0 | 0.0% | 20 | 33.3% | 0 | 0.0% | 19 | 25.7% | 0.000* |
| | Yes | 49 | 100.0% | 40 | 66.7% | 17 | 100.0% | 55 | 74.3% | |
| Shoe cover | No | 43 | 87.8% | 38 | 63.3% | 17 | 100.0% | 63 | 85.1% | 0.000* |
| | Yes | 6 | 12.2% | 22 | 36.7% | 0 | 0.0% | 11 | 14.9% | |
| Bonnet | No | 9 | 19.6% | 19 | 31.7% | 6 | 35.3% | 48 | 64.9% | 0.000* |
| | Yes | 37 | 80.4% | 41 | 68.3% | 11 | 64.7% | 26 | 35.1% | |
| Visor | No | 11 | 22.4% | 39 | 65.0% | 11 | 64.7% | 48 | 64.9% | 0.000* |
| | Yes | 38 | 77.6% | 21 | 35.0% | 6 | 35.3% | 26 | 35.1% | |
| Overalls | No | 46 | 93.9% | 35 | 58.3% | 17 | 100.0% | 63 | 85.1% | 0.000* |
| | Yes | 3 | 6.1% | 25 | 41.7% | 0 | 0.0% | 11 | 14.9% | |

## 4. DISCUSSION AND CONCLUSION

First of all, life must be maintained in order to protect human existence. It is critical to protect his health in order to accomplish this. While healthcare workers provide services to benefit patients and enhance their health, they must first protect their own health because the work environment and nature of their employment expose them to numerous risks and dangers [27]. Hospitals are high-risk workplaces for infectious diseases, and the likelihood of healthcare workers being exposed to occupational risks varies depending on the occupational group they work in, the job they do, and the department in which they work. Considering the working areas of healthcare professionals, the health risks of those who are in a position to directly care for the sick person are quite high [28,29]. When healthcare personnel comes into touch with percutaneous (piercing-cutting) injuries, mucous membranes, blood, tissues, or other contagious body fluids, they are exposed to infectious diseases [30]. Although the virus is most commonly found in blood, it can also be found in saliva, semen, and feces. A contaminated needle or another sharp instrument, a percutaneous stick, splashing on the skin or mucous membranes, or being swallowed are all possible routes of infection [31]. During the 2014-2015 Ebola pandemic in West Africa, almost 28,000 people were infected with the virus, with over 11,000 deaths. Most of the deaths have occurred among healthcare professionals with a high risk of infection [32]. In the COVID-19 pandemic, which is the subject of our study, which affects the whole world, the risk of respiratory transmission has affected many healthcare workers.

The careful use of personal protective equipment (PPE) by all healthcare professionals is very significant both for the patient and for his own health [33]. A recent study reported approximately 50% of hand or neck contamination during the removal of gloves, masks, and clothing. The amount of spontaneous contamination may vary depending on the type of PPE and the insertion technique, as well as other factors [34,35,36].

Points that were significantly associated with the method used to protect healthcare workers and personal protective equipment in the COVID-19 outbreak were observed, based on the present findings of our study. We believe that our findings will support the development of employee protection strategies in the event of a COVID-19 pandemic. Measures that can be taken during this time include providing a safe and healthy working environment, detecting risks and taking precautions, providing personal protection equipment, training, supporting, and promoting employee awareness.

A limitation of this study was its focus on healthcare professionals in hospitals in a single setting (Turkey). Thus, the results cannot be generalized to other settings. As the global COVID-19 pandemic continues, it is vital to plan early intervention and appropriate strategies to protect healthcare workers' health, as well as to provide them with adequate working environments and protective equipment. With the modifications and interventions made, healthcare staff will be able to go through this tough process with the least damage. We think that conducting similar studies on bigger samples in order to offer ideal settings for healthcare professionals to be less affected by possible similar conditions will have extremely significant outcomes.

## REFERENCES

[1] Zhu N, Zhang D, Wang W, et al. A novel coronavirus from patients with pneumonia in China, 2019. New England Journal of Medicine. 2020.

[2] Chan JF-W, Yuan S, Kok K-H, et al. A familial cluster of pneumonia associated with the 2019 novel coronavirus indicating person-to-person transmission: a study of a family cluster. The Lancet. 2020;395 (10223):514-23.

[3] Guan W-j, Ni Z-y, Hu Y, et al. Clinical characteristics of coronavirus disease 2019 in China. New England journal of medicine. 2020;382 (18):1708-20.

[4] Rothe C, Schunk M, Sothmann P, et al. Transmission of 2019-nCoV infection from an asymptomatic contact in Germany. New England Journal of Medicine. 2020;382 (10):970-1.

[5] WHO Organization. WHO Director-General's opening remarks at the media briefing on COVID-19-11 March 2020. 2020.

[6] TCS Bakanlığı. "Koronavirüs, Alacağımız Tedbirlerden Güçlü Değildir" 2020, https://www.saglik.gov.tr/TR,64383/koronavirus-alacagimiz-tedbirlerden-guclu degildir.html.

[7] WHO Organization. Organization WH. Report of the WHO-China joint mission on coronavirus disease 2019 (COVID-19). Geneva; 2020.

[8] WHO Organization. Coronavirus disease 2019 (COVID-19): situation report, 51. 2020.

[9] WHO Organization. Coronavirus disease 2019 (COVID-19): situation report, 82. 2020.

[10] Liu M, He P, Liu H, et al. Clinical characteristics of 30 medical workers infected with new coronavirus pneumonia. Zhonghua jie he he hu xi za zhi= Zhonghua jiehe he huxi zazhi= Chinese journal of tuberculosis and respiratory diseases. 2020;43:E016-E.

[11] Wang J, Zhou M, Liu F. Reasons for healthcare workers becoming infected with novel coronavirus disease 2019 (COVID-19) in China. J Hosp infect. 2020;105 (1).

[12] Ran L, Chen X, Wang Y, et al. Risk factors of healthcare workers with corona virus disease 2019: a retrospective cohort study in a designated hospital of Wuhan in China. Clinical Infectious Diseases. 2020.

[13] Nguyen LH, Drew DA, Graham MS, et al. Risk of COVID-19 among front-line health-care workers and the general community: a prospective cohort study. The Lancet Public Health. 2020;5 (9):e475-e83.

[14] Adams JG, Walls RM. Supporting the health care workforce during the COVID-19 global epidemic. Jama. 2020;323 (15):1439-40.

[15] Grennan D. What Is a Pandemic? Jama. 2019;321(9):910.

[16] Livingston E, Desai A, Berkwits M. Sourcing personal protective equipment during the COVID-19 pandemic. Jama. 2020;323 (19):1912-4.

[17] Wang J, Zhou M, Liu F. Reasons for healthcare workers becoming infected with novel coronavirus disease 2019 (COVID-19) in China. J Hosp infect. 2020;105 (1).

[18] Ran L, Chen X, Wang Y, Wu W, Zhang L, Tan X. Risk factors of healthcare workers with corona virus disease 2019: a retrospective cohort study in a designated hospital of Wuhan in China. Clinical Infectious Diseases. 2020.

[19] Nguyen LH, Drew DA, Graham MS, Joshi AD, Guo C-G, Ma W, et al. Risk of COVID-19 among front-line health-care workers and the general community: a prospective cohort study. The Lancet Public Health. 2020;5 (9):e475-e83.

[20] Gandhi M, Yokoe DS, Havlir DV. Asymptomatic transmission, the Achilles' heel of current strategies to control COVID-19. Mass Medical Soc; 2020.

[21] Vahidy F, Sostman HD, Bernard D, et al. Prevalence of SARS-CoV-2 infection among asymptomatic healthcare workers in greater Houston: a cross-sectional analysis of surveillance data from a large healthcare system. medRxiv. 2020.

[22] Chang D, Xu H, Rebaza A, et al. Protecting health-care workers from subclinical coronavirus infection. The Lancet Respiratory Medicine. 2020;8 (3):e13.

[23] WHO Organization. Rational use of personal protective equipment (PPE) for coronavirus disease (COVID-19): interim guidance, 19 March 2020. World Health Organization; 2020.

[24] Xiang Y-T, Yang Y, Li W, et al. Timely mental health care for the 2019 novel coronavirus outbreak is urgently needed. The Lancet Psychiatry. 2020;7 (3):228-9.

[25] Livingston E, Desai A, Berkwits M. Sourcing personal protective equipment during the COVID-19 pandemic. Jama. 2020;323 (19):1912-4.

[26] Karasar N. Bilimsel araştırma yöntemi. Ankara: Nobel Akademik Yayıncılık, 2016.

[27] Rim KT., Lim CH. Biologically hazardous agents at work and efforts to protect workers' health: a review of recent reports. Safety and Health At Work. 2014; 5(2): 43-52.

[28] Beşer A., Topçu S. Sağlık alanında kişisel koruyucu ekipman kullanımı. Dokuz Eylül Üniversitesi Hemşirelik Yüksekokulu E Dergisi. 2013; 6(4): 241-247.

[29] Liu M, Cheng SZ, Xu KW et al. Use of personal protective equipment against coronavirus disease 2019 by healthcare professionals in Wuhan, China: cross sectional study. Bmj. 2020; 369.

[30] Yuan N, Yang WX, Lu JL. et al. Investigation of adverse reactions in healthcare personnel working in Level 3 barrier protection PPE to treat COVID-19. Postgraduate medical journal. 2021: 97(1148): 351-354.

[31] Wang J, Zhou M, Liu F, Exploring the reasons for healthcare workers infected with novel coronavirus disease 2019 (COVID-19) in China. J Hosp Infect 2020. PubMed PMID: 32147406.

[32] Hancı Hİ, Erdem Y., Polat S. Adli hemşirelik. Ankara: Seçkin Yayıncılık.

[33] Honda H, Iwata K, Personal protective equipment and improving compliance among healthcare workers in high-risk settings. Curr Opin Infect Dis 2016;29:400–6.

91

[34] Loibner M, Hagauer S, Schwantzer G, et al. Limiting factors for wearing personal protective equipment (PPE) in a health care environment evaluated in a randomised study. PLoS One 2019;14:e0210775.

[35] Bhoyrul B, Lecamwasam K, Wilkinson M, et al. A review of non-glove personal protective equipment-related occupational dermatoses reported to EPIDERM between 1993 and 2013. Contact Dermatitis 2019;80:217–21.

[36] Yuan N, Yang WX, Lu JL, et al. Investigation of adverse reactions in healthcare personnel working in Level 3 barrier protection PPE to treat COVID-19. Postgraduate Medical Journal, 2021; 97(1148): 351-354.

**Türk Doğa ve Fen Dergisi**
**Turkish Journal of Nature and Science**

BİNGÖL ÜNİVERSİTESİ

# The Effect of Subcutaneous Tunneling on External Lumbar Drainage Complications

## Ece UYSAL[1]*

[1] Health Sciences University, Prof. Dr. Cemil Tascioglu City Hospital, Neurosurgery Department, Istanbul, Türkiye
Ece UYSAL ORCID No: 0000-0002-2355-8395

*Corresponding author: dr.eceuysal.nrs@gmail.com

**Abstract:**
Patients with a lumbar catheter become prone to infection due to the outflow of CSF. This research aimed to investigate how tunneled lumbar drainage affected infection in patients undergoing lumbar drainage.This study was conducted on patients with lumbar drainage who were hospitalized for various clinical reasons. Subcutaneous drain length was measured by post-procedural lumbar tomography. The length of the lumbar drainage catheter, the duration of lumbar drainage, fever monitoring, CSF leaking, and biochemical blood tests, the length of hospitalization, infection were recorded.This study comprised a total of 93 cases with external lumbar drainage. 51 (54.8%) of the 93 cases were inserted using the classic technique, 42 (45.2%) were inserted using the tunneled technique. The rate of CSF leakage was decreased using the tunneling approach (p = 0.003). A significant correlation was established between CSF leakage around the drain and subcutaneous drain length. CSF culture was negative in 78.8% of patients with subcutaneous drain lengths between 0 cm and 3 cm, and 100% of patients with subcutaneous drain lengths of 5 cm or more. Seven days or less was the cutoff value for negative CSF culture.External lumbar draining can lead to issues such as infection and CSF leakage. The tunneling procedure is straightforward, affordable, and successfully prevents these complications.

# Subkutan Tünellemenin Eksternal Lomber Drenaj Komplikasyonlarına Etkisi

**Anahtar Kelimeler**
Lomber drenaj,
Lomber ponksiyon,
Beyin omurilik
sıvısı, Menenjit

Bel bölgesinde uzun süre kateter bulunan hastalar, BOS sıvısının dış ortama çıkışı nedeniyle enfeksiyona yatkın hale gelebilir. Bu araştırma, tünelli lomber drenajın lomber drenaj uygulanan hastalarda enfeksiyonu nasıl etkilediğini araştırmayı amaçladı. Bu çalışma, çeşitli klinik nedenlerle hastaneye yatırılan lomber drenajlı hastalar üzerinde yapılmıştır. Subkutan dren uzunluğu işlem sonrası lomber tomografi ile ölçüldü. Lomber drenaj kateterinin uzunluğu, lomber drenaj süresi, ardından ateş izlemi, lomber drenaj çevresinden BOS sızıntısı ve günlük biyokimyasal kan testleri, hastanede kalış süresi, enfeksiyon ve antibiyotik ihtiyacı kaydedildi. Bu çalışma eksternal lomber drenajı olan toplam 93 olguyu içermektedir. Doksan üç olgunun 51'i (%54.8) klasik teknikle, 42'si (%45.2) ise tünelli teknikle yerleştirildi. BOS kaçağı oranı, tünelleme yaklaşımı kullanılarak azaltıldı (p = 0.003). Hastanede kalış süresi açısından iki işlem arasında fark yoktu. Dren etrafındaki BOS sızıntısı ile subkutan dren uzunluğu arasında istatistiksel olarak anlamlı bir ilişki saptandı. Subkutan dren uzunluğu 0-3 cm arasında olan hastaların %78.8'inde, 5 cm ve üzeri dren uzunluğu olan hastaların ise %100'ünde BOS kültürü negatifti. Negatif BOS kültürü için cut-0ff değeri yedi gün olarak belirlendi. Dış lomber drenaj, enfeksiyon ve BOS sızıntısı gibi sorunlara yol açabilir. Tünel açma prosedürü basittir, ekonomiktir ve bu komplikasyonları başarılı bir şekilde önler.

# 1. INTRODUCTION

CSF (Cerebrospinal Fluid) diversion methods are commonly used in neurosurgery. External lumbar drainage was first introduced in 1963 as a technique to alleviate cerebral tension during surgical procedures and it has been widely adopted as a method of cerebrospinal fluid (CSF) diversion in various clinical contexts [1]. These include the management of post-traumatic CSF leaks, evaluation of normal pressure hydrocephalus, and skull base surgery. It can be utilized to treat CSF fistulas as well as traumatic or non-traumatic cases of high intracranial pressure [2,3]. It allows for the evacuation of cerebrospinal fluid from the lumbar area to the external environment, relieving intracranial pressure and CSF pressure. Because of the length of the treatment procedure, it may be necessary to remain attached to the patient for a longer amount of time. Although external lumbar drainage is an easy method, it has complications such as infection or CSF leakage due to contact with the external environment [4]. Patients with a catheter in the lumbar area for an extended period may become prone to infection due to the outflow of CSF fluid to the external environment. Because of retrograde infection, lumbar drains may result in the colonization of bacteria [5]. This research aimed to investigate how tunneled lumbar drainage, a previously suggested method, affected infection in patients undergoing lumbar drainage [6].

# 2. MATERIAL AND METHOD

## 2.1. Study Design

Our study adheres to the ethical principles outlined in the Helsinki Declaration of the World Medical Association and is approved by the Clinical Research Ethics Committee decision for Clinical Research at Istanbul Prof. Dr. Cemil Tascioglu City Hospital dated 06.03.2022 and numbered 38. This study was conducted on patients with lumbar drainage who were hospitalized at the neurosurgery clinic for various clinical reasons between 2019 and 2022. Only patients with lumbar drainage were included in our study. Patients with ventricular drainage, those with previous infection, those under antibiotics, those under immunosuppressants, and those with a known cancer history were excluded from our study. In 2021, due to a policy shift, the tunneled lumbar drainage method began to replace the traditional method, which had been in use since 2019. The acquired data for the study were retrospectively assessed. Sociodemographic information and causes of lumbar drainage in patients were recorded. Patients having infection prior to insertion of lumbar drainage, using immunosuppressants or antibiotics, and infection from another region following lumbar drainage were excluded from our study. The length of the lumbar drainage catheter was measured using post-procedure lumbar tomography and lumbar radiography. 0 cm indicates classic technique. The duration of lumbar drainage, subsequent fever monitoring, CSF leaking surrounding the lumbar drain, and daily biochemical blood tests were recorded. Meanwhile, CSF samples collected from the lumbar drainage catheter every two days as part of a standard drainage process were analyzed and documented. In the case of elevated infection parameters in CSF samples, lumbar drainage catheter CSF culture samples were also received. The length of hospitalization related to lumbar drainage and infection and the requirement for antibiotics were also evaluated. The patient's diagnosis determined the duration of lumbar drainage, and lumbar drainage was ended after the patient's therapy concluded.

## 2.2. CSF infection Criteria

A positive CSF culture, a CSF/blood glucose ratio of less than 0.5, a neutrophilic CSF pleocytosis (> 5 cells/L), and fever (body temperature of greater than 38°C) [3].

## 2.3. External Lumbar Drainage Placement Procedure

Before performing the surgery on any patient, informed consent was obtained. The procedure was conducted in an operating room by a neurosurgeon or a neurosurgical assistant with considerable experience. Before the procedure, patients received intravenous cefazolin as a prophylactic (vancomycin if allergic to penicillin). Patients were placed in the lateral decubitus or sitting position to measure distance. After the appropriate sterilizing, lidocaine was administered as a local anesthetic. Between L3 and L4, the subarachnoid region was reached with a spinal needle (Tuohy needle). A 10 to 15-cm catheter was inserted into the subarachnoid area when CSF was observed. After removing the drainage catheter from the area of the skin where the needle was directly implanted, fixation sutures were used to secure it to the skin. In patients who underwent tunneling, the drain was removed after it had been advanced laterally in the subcutaneous tissue for a while [6].

## 2.4. Statistical Examination

The statistical analysis was conducted with SPSS 15.0 for Windows. Descriptive statistics; number and percentage for categorical variables, and mean, standard deviation, median, minimum, and maximum for numerical variables. The Chi-Square Test was used to compare the group rates. The Mann-Whitney U test was used to compare numerical data between two independent groups since the assumption of a normal distribution was met. Since the parametric test condition was unsatisfied, the relationships between numerical variables were investigated using Spearman correlation. Cut-off value analysis was evaluated via ROC Curve Analysis. The significance level regarding statistical alpha was accepted as $p<0.05$.

# 3. RESULTS

This study comprised a total of 93 cases with external lumbar drainage. There were 32 (34.4%) females and 61 (65.6%) males, averaging 53,214.3. (20-87). 51 (54.8%) of the 93 cases were inserted using the classic technique, whereas 42 (45.2%) were inserted using the tunneled technique. The duration of the drainage varied from 5 to 8 days, with an average of 6.33 days. In 10 (10,8) cases, CSF was detected leaking around the drain. In 16 (17.2%) cases, infection was observed correlated with fever, CSF culture, CSF/blood glucose, and elevated CSF

neutrophils. All infected patients required antibiotics (17.2%). Hospital stays ranged from 7 to 23, with a mean of 9,65 days. The length of the subcutaneous drain ranged from 0 to 8 (Table 1).

**Table 1.** A breakdown of the demographics of the 93 patients

| | | |
|---|---|---|
| **Age** Mean ±SD (Min-Max) | | 53.2±14.3 (20-87) |
| **Gender** n (%) | **F** | 32 (34.4) |
| | **M** | 61 (65.6) |
| **Duration of drain** Mean± SD (Min-Max) | | 6.33±1.15 (5-8) |
| **Technque** n (%) | **Classic** | 51 (54.8) |
| | **Tunneled** | 42 (45.2) |
| **Fever** n (%) | **No** | 77 (82.8) |
| | **Yes** | 16 (17.2) |
| **CSF leakage around drain** n (%) | **No** | 83 (89.2) |
| | **Yes** | 10 (10.8) |
| **CSF culture** n (%) | **Negative** | 77 (82.8) |
| | **Positive** | 16 (17.2) |
| **CSF/Blood Glucose** Mean± SD (Min-Max) | | 0.61±0.17 (0.2-0.8) |
| **CSF Neutrophil >5** n (%) | **No** | 77 (82.8) |
| | **Yes** | 16 (17.2) |
| **Hospital Stay** Mean ±SD (Min-Max) | | 9.65±4.17 (7-23) |
| **Plus antibiotic need** n (%) | **No** | 77 (82.8) |
| | **Yes** | 16 (17.2) |
| **Subcutaneous drain length** Mean± SD (Min-Max) | | 2.74±3.27 (0-8) |

When comparing the classical and tunnel lumbar drainage techniques, it was found that the classical approach resulted in CSF leakage in 10 cases (19.6%) (Table 2). No CSF leakage was reported among individuals who utilized the tunnel approach. The rate of CSF leakage was statistically significantly decreased using the tunneling approach (p = 0.003). Regarding fever, CSF culture, CSF/blood glucose, and CSF neutrophil > 5, no statistically significant differences were detected between the approaches. There was no difference between the two procedures in terms of hospital stay.

**Table 2.** Comparison of classic and tunneled external lumbar drainage technique

| | Technique | | |
|---|---|---|---|
| | Classic | Tunneled | p |
| Fever n (%) | 11 (21.6) | 5 (11.9) | 0.219 |
| CSF leakage around drain n (%) | 10 (19.6) | 0 (0.0) | 0.002 |
| CSF culture n (%) | 11 (21.6) | 5 (11.9) | 0.219 |
| CSF/Blood Glucose* | 0.59±0.19 0.6 (0.2-0.8) | 0.63±0.15 0.7 (0.2-0.8) | 0.359 |
| CSF Neutrophil >5 n (%) | 11 (21.6) | 5 (11.9) | 0.219 |
| Plus antibiotic need n (%) | 11 (21.6) | 5 (11.9) | 0.219 |
| Hospital Stay* | 10.3±4.9 8 (7-23) | 8.8±2.9 8 (7-20) | 0.334 |

\* Mean.±SD (Median) Min-Max

Comparing the duration of the subcutaneous drain with infection parameters such as fever, CSF culture, and CSF neutrophil count >5 (p=0.037) showed significant differences (p=0.05) (Table 3). It was also discovered that decreasing the length of the subcutaneous drain increased the likelihood of cerebrospinal fluid (CSF) leakage from the edge of the drain (p=0.005). There was no statistically significant association between CSF/blood glucose levels and drain duration (p=0.329).

**Table 3.** The comparison of subcutaneous drain length on other parameters

| | | Subcutaneous drain length | | |
|---|---|---|---|---|
| | | Mean ±SD | Median (Min-Max) | p |
| **Fever** n (%) | No | 3.14±3.42 | 0 (0-8) | 0.037 |
| | Yes | 0.81±1.28 | 0 (0-3) | |
| **CSF leakage around drain** n (%) | No | 3.07±3.31 | 0 (0-8) | 0.005 |
| | Yes | 0.00±0.00 | 0 (0-0) | |
| **CSF culture** n (%) | Negative | 3.14±3.42 | 0 (0-8) | 0.037 |
| | Positive | 0.81±1.28 | 0 (0-3) | |
| **CSF Neutrofil >5** n (%) | No | 3.14±3.42 | 0 (0-8) | 0.037 |
| | Yes | 0.81±1.28 | 0 (0-3) | |
| **CSF/Blood Glucose** | | r:0.102 p=0.329 | | |

There was a statistically significant difference between the subcutaneous drain length levels and CSF culture rates (p<0.001) (Table 4). The length of subcutaneous drains for classical procedures was assumed to be 0 cm. CSF culture was negative in 78.8% of patients with subcutaneous drain lengths between 0 and 3 cm, and 100% of patients with subcutaneous drain lengths of >5 cm.

**Table 4.** The comparison of subcutaneous drain lengths with CSF

| | | CSF culture | | | | |
|---|---|---|---|---|---|---|
| | | Negative | | Positive | | |
| | | n | % | n | % | p |
| | **0** | 41 | 78.8 | 11 | 21.2 | **<0.001** |
| | **2** | 0 | 0 | 2 | 100 | |
| | **3** | 0 | 0 | 3 | 100 | |
| **Subcutaneous drain length (cm)** | **5** | 2 | 100 | 0 | 0 | |
| | **6** | 11 | 100 | 0 | 0 | |
| | **7** | 18 | 100 | 0 | 0 | |
| | **8** | 5 | 100 | 0 | 0 | |

As the duration of the drainage increases, there is a statistically significant increase in the likelihood of experiencing fever (p=0.001), CSF leaking around the drain (p=0.002), CSF culture (p=0.001), and CSF neutrophil >5 (p=0.001). There was a statistically significant inverse connection (p=0.001) between the duration of draining and the CSF/blood glucose level (Table 5).

**Table 5.** Comparison of the duration of external lumbar drainage and its effect on other parameters

| | | Duration of drainage | | |
|---|---|---|---|---|
| | | Mean ±SD | Median (Min-Max) | p |
| **Fever** n (%) | No | 6.14±1.09 | (6) 5-8 | |
| | Yes | 7.25±1.00 | (8) 5-8 | **0.001** |
| **CSF leakage around drain** n (%) | No | 6.20±1.10 | (6) 5-8 | |
| | Yes | 7.40±0.97 | (8) 5-8 | **0.002** |
| **CSF culture** n (%) | Negative | 6.14±1.09 | (6) 5-8 | |
| | Positive | 7.25±1.00 | (8) 5-8 | **0.001** |
| **CSF Neutrofil >5** n (%) | No | 6.14±1.09 | (6) 5-8 | |
| | Yes | 7.25±1.00 | (8) 5-8 | **0.001** |
| **CSF/Blood Glucose** | | r:-0.341 **p=0.001** | | |

There is a statistically significant association between the duration of drainage and the positive CSF culture (p=0.001). While the CSF culture negatives rate is high in patients with a length of 5 days (96.7%), it is low in patients with a duration of 8 days (55%) (Table 6).

**Table 6.** The assessment of CSF culture positive based on the duration of external lumbar draining.

| | | CSF culture | | | | |
|---|---|---|---|---|---|---|
| | Days | Negative | | Positive | | |
| | | n | % | n | % | p |
| **Drainage duration (day)** | 5 | 29 | 96.7 | 1 | 3.3 | **0.002** |
| | 6 | 19 | 86.4 | 3 | 13.6 | |
| | 7 | 18 | 85.7 | 3 | 14.3 | |
| | 8 | 11 | 55.0 | 9 | 45.0 | |

With 85.7% sensitivity and 56.7% specificity, seven days or less was established to be the cut-off value for negative CSF culture. Positive predictive value (PPV) was 90.4%, whilst negative predictive value (NPV) was 45% (Figure 1) (Table 7).
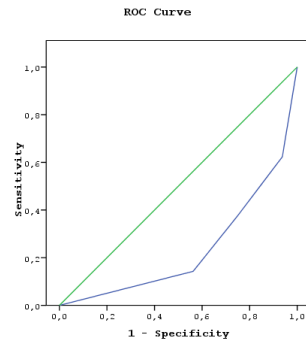


**Figure 1.** The ROC analyses for CSF culture negativity of <7 days of duration of the drainage

**Table 7.** Test Result Variable(s): Drainage duration

| Area Under the Curve | SE | p | 95% Confidence Interval | |
|---|---|---|---|---|
| 0.233 | 0.064 | 0.001 | 0.108 | 0.359 |

CSF culture Positive rate was 19.2 times greater among patients with CSF leakage around the drain (p<0.001 OR:19.2 95% CI 4.2-87.7) (Table 8).

**Table 8.** Comparison of CSF cultures according to the CSF leakage around the drain

| | | CSF leakage around drain | | | | |
|---|---|---|---|---|---|---|
| | | No | | Yes | | |
| | | n | % | n | % | p |
| **CSF culture** | **Negative** | 74 | 89.2 | 3 | 30.0 | **<0.001** |
| | **Positive** | 9 | 10.8 | 7 | 70.0 | |

## 4. DISCUSSION AND CONCLUSION

Continuous lumbar drainage systems are employed in the treatment of cerebrospinal fluid leaks [7]. These techniques also diagnose patients with hydrocephalus at standard pressure and benign intracranial hypertension [8, 9]. After inserting a needle into the lumbar area, typically at the L3-4 or L4-5 level, a catheter is advanced into the subarachnoid space. This catheter transports CSF to the external environment, and its pressure decreases [10]. Local infections, nerve root irritations, headaches, meningitis, retained catheter, symptomatic intracranial subdural collections, and symptomatic intracranial traumatic pattern subarachnoid hemorrhage may develop regardless of the straightforwardness of the procedure [11]. Meningitis, an infection of the central nervous system, is a severe problem requiring treatment. Our investigation determined that the infection detection rate among patients who were followed up with external lumbar drainage was 17.2%. These patients all needed further antibiotics. The observed infection rate was more significant than that reported in the literature. The high infection rate is associated with the sociodemographic composition and personal cleanliness.

Moreover, the drain can produce a permanent CSF fistula at the exact location of its implantation. Mainly, it is vital to take precautions against infection, such as prophylactic antibiotic use [12], revision of lumbar drainage at 5-day intervals [13], tunneled catheters [10], and antibiotic-impregnated lumbar catheters [14].

The long-tunneled approach was initially applied to the external ventricular catheter, another catheter constantly in contact with CSF. Khanna et al. were the initial group to describe this technique by extending the standard 5 cm subcutaneous tunnel [15]. While some research indicated that extended tunneling in EVD lowered the risk of infection [16], other studies did not detect a significant difference in infection risk [17, 18].

After that, its technical application in external lumbar drainage systems in contact with another CSF is described [6]. They reported that the eventual effectiveness of this tunneling approach in reducing infectious problems is debatable. However, it decreases CSF leakage at the exit site and raises the patient's tolerance for the indwelling catheter. In our series, we examined the infection rates of the classical and tunneling procedures. In this study, it was observed that the infection rate resulting from external lumbar drainage decreased from 21.6% to 11.6% through the implementation of the tunnelling technique. This result is also important in light of the literature's disagreements. Further and exhaustive research is required.

The tunneling procedure considerably impacts minimizing CSF leakage around the drain. There was no CSF leakage around the drain in catheters implanted using the tunneling technique. CSF leaks around the catheter considerably increased the risk of infection. In our study, the tunneling method avoids CSF leaks, hence minimizing infection rates. Comparing the lengths of subcutaneous drains revealed a substantial difference in infection formation and CSF leakage prevention surrounding the drain. There was no infection in those with at least 5 cm of tunneling. This threshold value demonstrates that 3 cm tunneling is equal to the conventional method and is insufficient to prevent infection. At least 5 cm of tunneling should reduce the incidence of infection.

Examining the effects of catheter duration on infection rates and CSF leakage around the catheter reveals that this period is statistically significant. The greater the danger of infection increases, the longer a catheter is left in place. Moreover, presumably due to epithelialization, CSF circumvents the catheter and causes leakage. Negative rates were increased in those with less than seven days of CSF culture. This indicates that catheterization for no more than seven days can lower the risk of infection. The infection rate increases dramatically when catheters are retained for longer than seven days.

External lumbar draining can lead to issues such as infection and CSF leakage. The tunneling procedure is straightforward, affordable, and successfully prevents these complications.

## REFERENCES

[1] Basauri LT, Concha-Julio E, Selman JM, Cubillos P, Rufs J. Cerebrospinal fluid spinal lumbar drainage: indications, technical tips, and pitfalls. Crit Rev Neurosurg. 1999 Jan 26;9(1):21-27. doi: 10.1007/s003290050104. PMID: 9933364.

[2] El Ahmadieh TY, Wu EM, Kafka B, Caruso JP, Neeley OJ, Plitt A, et al. Lumbar drain trial outcomes of normal pressure hydrocephalus: a single-center experience of 254 patients. J Neurosurg. 2019 Jan 4;132(1):306-312. doi: 10.3171/2018.8.JNS181059. PMID: 30611143.

[3] Guo X, Zhu Y, Hong Y. Efficacy and Safety of Intraoperative Lumbar Drain in Endoscopic Skull Base Tumor Resection: A Meta-Analysis. Front Oncol. 2020 May 7;10:606. doi: 10.3389/fonc.2020.00606. PMID: 32457833; PMCID: PMC7221155.

[4] Shakeyeva A, Kuzmin V, Lozovoy V. Improving Methods of Diagnosis and Treatment of Posthemorrhagic Hydrocephalus in Young Children. Pediatr Neurol. 2023 Aug 3;148:1-7. doi: 10.1016/j.pediatrneurol.2023.07.023. Epub ahead of print. PMID: 37625173.

[5] Hetem DJ, Woerdeman PA, Bonten MJ, Ekkelenkamp MB. Relationship between bacterial colonization of external cerebrospinal fluid drains and secondary meningitis: A retrospective analysis of an 8-year period. J Neurosurg 2010; 113:1309–1313

[6] Hahn M, Murali R, Couldwell WT. Tunneled lumbar drain. Technical Note. J Neurosurg. 2002 Jun;96(6):1130-1. doi: 10.3171/jns.2002.96.6.1130. PMID: 12066917.

[7] Nigrovic LE, Kimia AA, Shah SS, Neuman MI. Relationship between cerebrospinal fluid glucose and serum glucose. N Engl J Med 2012; 366: 576–578.

[8] Hussein M, Abdellatif M. Continuous Lumbar Drainage for the Prevention and Management of Perioperative Cerebrospinal Fluid Leakage. Asian J Neurosurg. 2019 Apr-Jun;14(2):473-478. doi:

10.4103/ajns.AJNS_265_18. PMID: 31143264; PMCID: PMC6516026.

[9] Stevens AR, Soon WC, Chowdhury YA, Toman E, Yim S, Veenith T, et al. External Lumbar Drainage for Refractory Intracranial Hypertension in Traumatic Brain Injury: A Systematic Review. Cureus. 2022 Oct 7;14(10):e30033. doi: 10.7759/cureus.30033. PMID: 36348893; PMCID: PMC9637378.

[10] Ginalis EE, Fernández LL, Ávila JP, Aristizabal S, Rubiano AM. A review of external lumbar drainage for the management of intracranial hypertension in traumatic brain injury. Neurochirurgie. 2022 Feb;68(2):206-211. doi: 10.1016/j.neuchi.2021.05.004. Epub 2021 May 26. PMID: 34051245.

[11] Governale LS, Fein N, Logsdon J, Black PM. Techniques and complications of external lumbar drainage for normal pressure hydrocephalus. Neurosurgery. 2008 Oct;63(4 Suppl 2):379-84; discussion 384. doi: 10.1227/01.NEU.0000327023.18220.88. PMID: 18981847.

[12] Karvouniaris M, Brotis A, Tsiakos K, Palli E, Koulenti D. Current Perspectives on the Diagnosis and Management of Healthcare-Associated Ventriculitis and Meningitis. Infect Drug Resist. 2022 Feb 28;15:697-721. doi: 10.2147/IDR.S326456. PMID: 35250284; PMCID: PMC8896765.

[13] Dasic D, Hanna SJ, Bojanic S, Kerr RS. External ventricular drain infection: the effect of a strict protocol on infection rates and a review of the literature. Br J Neurosurg. 2006 Oct;20(5):296-300. doi: 10.1080/02688690600999901. PMID: 17129877.

[14] Shekhar H, Kalsi P, Dambatta S, Strachan R. Do antibiotic-impregnated external ventriculostomy catheters have a low infection rate in clinical practice? A retrospective cohort study. Br J Neurosurg. 2016;30(1):64-9. doi: 10.3109/02688697.2015.1096903. Epub 2015 Oct 15. PMID: 26469715.

[15] Khanna RK, Rosenblum ML, Rock JP, Malik GM. Prolonged external ventricular drainage with percutaneous long-tunnel ventriculostomies. J Neurosurg 1995;83:791-4.

[16] Shekhar H, Kalsi P, Dambatta S, Strachan R. Do antibiotic-impregnated external ventriculostomy catheters have a low infection rate in clinical practice? A retrospective cohort study. Br J Neurosurg. 2016;30(1):64-9. doi: 10.3109/02688697.2015.1096903. Epub 2015 Oct 15. PMID: 26469715.

[17] Leung GK, Ng KB, Taw BB, Fan YW. Extended subcutaneous tunnelling technique for external ventricular drainage. Br J Neurosurg 2007;21:359-64.

[18] Cine HS, Suslu HT. Silviyan Araknoid Kist Tanısı İle Cerrahi Tedavi Ve Takip Yapılan Hastaların Semptomatik Ve Radyolojik Açıdan Retrospektif Olarak Değerlendirilmesi: Araştırma Makalesi. Acta Medica Ruha, 2023;1(2):116–125. https://doi.org/10.5281/zenodo.7964102

[19] Tahir MZ, Sobani ZA, Murtaza M, Enam SA. (2016). Long-tunneled versus short-tunneled external ventricular drainage: Prospective experience from a developing country. Asian Journal of Neurosurgery. 2016;11(2):114-117. https://doi.org/10.4103/1793-5482.145052

# Effects of Thymoquinone Against D- Galactose and Aluminum Chloride Induced Testicular Dysfunction in Rats

**Serkan Ali AKARSU[1*]** ![iD] **, Gökhan Doğukan AKARSU[2]** ![iD] **, Aysun ÇETİN[3]** ![iD]

[1] Atatürk University, Veterinary Faculty, Reproduction and Artificial Insemination Department, Erzurum, Türkiye
[2] Yozgat Bozok University, Vocational School of Health Servıces, Pharmacy Services Department, Yozgat, Türkiye
[3] Erciyes University, Medicine Faculty, Biochemistry Department, Kayseri, Türkiye
Serkan Ali AKARSU ORCID No: 0000-0003-4450-6540
Gökhan Doğukan AKARSU ORCID No: 0000-0002-6586-5748
Aysun ÇETİN ORCID No: 0000-0003-4959-7955

*Corresponding author: serkanaliakarsu@gmail.com

**Abstract:** Alzheimer's disease affects all tissues negatively. In this study, it was aimed to determine the effects of TQ on testicular toxicity in rats with experimental Alzheimer's disease. In the study, 33 Wistar Albino rats weighing 190-230 gr were used. Rats were 11 rats in each group; were divided into 3 equal groups as control, ALZ and ALZ+TQ. The control group was given saline by IP route for 28 days daily. The ALZ group was given 60 mg/kg D-gal + 40 mg/kg $AlCl_3$ IP for 28 days daily. The ALZ+TQ group was given 60 mg/kg D-gal + 40 mg/kg $AlCl_3$ for 28 days by IP + 20 mg/kg TQ by oral gavage for last 14 days daily. According to the findings of our study, a decrease in SOD, CAT, GPx activity and GSH levels and an increase in MDA levels were determined in the ALZ group. In the ALZ+TQ group, while SOD, GPx, CAT activities and GSH levels increased, MDA levels decreased. There was a decrease in sperm motility and sperm density in the ALZ group, and an increase in the rate of abnormal sperm and dead spermatozoa. In the ALZ+TQ group, sperm motility, abnormal sperm rate and dead spermatozon rate improved. As a result, it was determined that the decrease in semen quality and increase in oxidative stress induced by $AlCl_3$+D-Gal were suppressed by TQ, protecting the testicular tissue from oxidative damage and increasing semen quality.

99

# Sıçanlarda D-Galaktoz ve Alüminyum Klorürün Neden Olduğu Testis Fonksiyon Bozukluğuna Karşı Timokinonun Etkileri

**Anahtar Kelimeler**
Alzheimer,
AlCl3+D-Galaktoz,
Oksidatif stres,
Rat,
Sperm,
Timokinon

**Öz:** Alzheimer hastalığı tüm dokuları olumsuz etkilemektedir. Bu çalışmada deneysel alzheimer hastalığı modeli oluşturulan ratlarda testis toksisitesi üzerine TQ etkileri belirlenmesi amaçlanmıştır. Çalışmada ağırlıkları 190-230 gr arasında değişen 33 adet Wistar Albino cinsi rat kullanıldı. Sıçanlar, her grupta 11 sıçan olmak üzere kontrol, ALZ ve ALZ+TQ olarak 3 eşit gruba ayrıldı. Kontrol grubuna, 28 gün boyunca IP yoluyla serum fizyolojik günlük olarak verildi. ALZ grubuna 28 gün boyunca günlük olarak 60 mg/kg D-gal+40 mg/kg $AlCl_3$ IP verildi. ALZ+TQ grubuna 28 gün 60 mg/kg D-gal +40 mg/kg $AlCl_3$ IP+20 mg/kg TQ son 14 gün oral sonda ile günlük olarak verildi. Çalışma bulgularına göre ALZ grubunda SOD, CAT, GPx aktivitesi ve GSH düzeylerinde azalma, MDA düzeylerinde ise artış saptanmıştır. ALZ+TQ grubunda SOD, GPx, CAT aktiviteleri ve GSH seviyeleri artarken MDA seviyeleri azaldı. ALZ grubunda sperm motilite ve sperm yoğunluğunda azalma, anormal sperm ve ölü canlı spermatozoa oranında artış olduğunu göstermiştir. ALZ+TQ tedavi grubunda sperm hareketliliği, anormal sperm oranı ve ölü sperm oranı düzeldi. Sonuç olarak, $AlCl_3$+D-Gal'in neden olduğu semen kalitesindeki azalma ve oksidatif stres artışının TQ tarafından baskılandığı, testis dokusunu oksidatif hasardan koruduğu ve semen kalitesini arttırdığı belirlendi.

## 1. INTRODUCTION

Alzheimer's disease is characterized by memory loss and behavioral disorders [1]. Aluminum chloride ($AlCl_3$) and D-galactose (D-Gal) are administred to create Alzheimer's disease model [2]. Aluminum (Al) is one of the most toxic of these heavy metals [3]. Al compounds are used in many medical applications, such as antacids, phosphate binders, buffered aspirins, and vaccines [4]. Recent animal and clinical studies have reported that Al causes neuropathological changes in the central nervous system [5]. Al can accumulate in the liver and kidneys, causing hepatorenal toxicity [6]. Al also has pro-oxidative, excitotoxic, immunogenic, proinflammatory, and mutagenic effects [7]. Oral Al exposure causes a decrease in glutathione peroxidase (GPx), catalase (CAT) activities, glutathione (GSH) levels and an increase in malondialdehyde (MDA) content in rats [8]. Considered as a systemic toxic substance, $AlCl_3$ accumulates in target organs including the testicles and causes dysfunction [9]. In another study, $AlCl_3$ causes a decrease in sperm motility and density in rats, and an increase in the ratio of dead live sperm and abnormal spermatozoa [10]. D-Gal can cause aging in tissues such as the brain, kidney, and liver [11]. Moreover, D-Gal induces oxidative stress by increasing lipid peroxidation [12]. In addition $AlCl_3$ and D-Gal administration causes oxidative damage in testicular tissue of rats [13].

Medicinal plants and phytochemicals are used against neurodegenerative diseases [14]. Herbal substances are used because of their therapeutic properties against various toxicants [15-17]. One of the bioactive components of the Nigella sativa plant, from which black seed oil is obtained, is thymoquinone (TQ) [18]. TQ is known as an antioxidant, anti-neoplastic and anti-inflammatory agent [19]. In addition, TQ is one of the anti-cancer bioactive compounds [20]. TQ protects the histopathological structure of the testis by preventing oxidative damage from experimentally induced testicular damage in male rats [21]. In another study, it was reported that it improved sperm motility, density, abnormal spermatozoa rate and dead spermatozoa rate in male rats with TQ varicocele [22]. Similarly, TQ regulated the pituitary testis axis, adjusted oxidant balance, decreased apoptosis and improved sperm quality in rats with lead toxicity [23]. In line with these data, the aim of this study was to determine the effect of TQ against $AlCl_3$+ D-Gal on testicular toxicity, which was applied to create an experimental Alzheimer's model in rats.

## 2. MATERIAL AND METHOD

### 2.1. Animals and Ethical Permission

All chemicals used in the study were obtained from Sigma Chemical Co. (St. Louis, MO) unless otherwise stated. Ethical permission was obtained from the Erciyes University Animal Experiments Local Ethics Committee for the study (Protocol no:23/037). Thirty three Wistar Albino rats weighing 190-230 g were used in the study. Rats were housed in standard laboratory conditions ($25\pm2$ °C temperature, a relative humidity of %$60\pm5$ and, a 12-h

light-dark rhythm) throughout the study. Rats were fed commercial pellet feed ad libitum water throughout the study. Rats were divided into 3 groups: the control group, the ALZ group, and the ALZ+TQ group, with 11 rats in each group.

The control group received saline (0.9%) intraperitoneally (IP) daily for 28 days.

ALZ group received D-galactose at 60 mg/kg dose + $AlCl_3$ at 40mg/kg by IP daily for 28 days [24].
ALZ+TQ group received 60 mg/kg D-galactose + 40 mg/kg dose $AlCl_3$ by IP daily for 28 days + 20 mg/kg TQ by oral gavage for last 14 days daily [24].

After the end of the experimental phase, the rats were sacrificed under xylazine-ketamine anesthesia. The testicular tissue of each rat was removed and separated from the epididymis. Then, the cauda epididymis was taken into a petri dish containing 5 ml of saline and trimmed at 35°C. Trimmed semen was used for semen analysis [25].

### 2.2. Oxidative Stress Analysis

To determine the oxidant antioxidant status in testis tissue, SOD, CAT, GPx activities, GSH levels and MDA contents were analyzed. SOD activity was measured according to the Sun et al. [26] method. CAT activity was determined using Aebi's [27] method. GPx activity was determined by the method developed by Lawrence and Burk [28]. GSH levels were measured by the method of Sedlak and Lindsay [29]. Testicular tissue MDA content was measured by the method described by Goth [30].

### 2.3. Reproductive Parameters Analysis

Testicular tissues separated from the epididymis were weighed using a precision balance (Radwag PS 750 R2, Poland). Results are presented in mg [31]. A light microscope with a heating plate was used to evaluate sperm motility. A small amount of semen was dropped on the slide and covered with a coverslip. Motility estimates were calculated as % with the average of three different microscope fields [32].

For the rate of dead sperm and sperm abnormalities, 10 µl of eosin and nigrosin dye were dropped on 10 µL of semen and dried on a slide, mixed with a coverslip and smeared. 200 sperm cells were examined on each slide with a light microscope. Sperm cells whose heads were stained were considered dead [33, 34]. To determine the rate of dead spermatozoa for abnormalities in sperm cells, a total of 200 sperm cells were evaluated on the prepared slide and the abnormality rates were calculated as a percentage [35].

### 2.4. Statistical Analysis

Biochemical and spermatological data were analyzed by one-way ANOVA using the SPSS (version 26.0; Chicago, IL) program. Differences between groups were made using the Tukey multiple comparison test. Results were

presented as mean ± standard error (S.E.M). P<0.05 values and below were considered statistically significant.

## 3. RESULTS

### 3.1. Oxidant/Antioxidant Assessment

The oxidative stress results of the experimental groups were presented in Figure 1-5. The highest MDA levels was seen in the ALZ group. ALZ+TQ treatment group partially decreased MDA level (P<0.05). While GPx, CAT, SOD activity and GSH levels were generally highest in the control group, these parameters were found to decrease in the ALZ group. TQ treatment was found to improve these parameters.

### 3.2. Spermatological Evaluation

The epididymal sperm parameters of the rats in the experimental groups are presented in Table 1. Accordingly, while the highest total motility value was seen in the control group, a statistical difference was found between the other experimental groups (P<0.05). There was no difference between the groups in terms of epididymal semen density. While the rate of dead and abnormal sperm rate were found to be at the highest in the ALZ group, a statistically significant difference was observed between the other experimental groups (P<0.05). There was no difference between the groups in terms of testicular weight.



**Figure 1.** The malondialdehyde (MDA) levels results. Different superscript letters in the same column (a, b, c) indicate significant inter-group differences (p < 0.05)
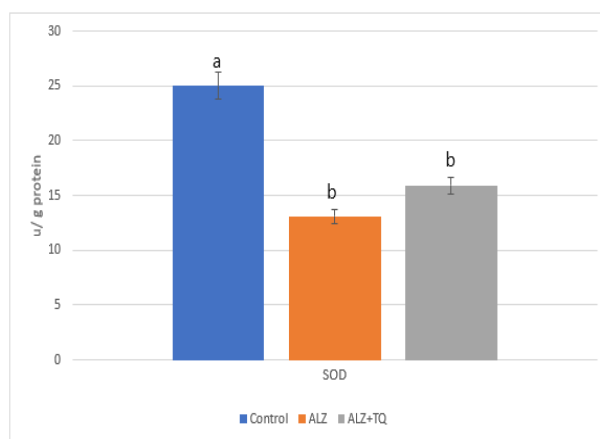


**Figure 2.** The superoxide dismutase (SOD) levels results. Different superscript letters in the same column (a, b) indicate significant inter-group differences (p < 0.05)



**Figure 3.** The glutathione (GSH) levels results. Different superscript letters in the same column (a, b) indicate significant inter-group differences (p < 0.05)



**Figure 4.** The glutathione peroxidase (GPx) levels results. Different superscript letters in the same column (a, b, c) indicate significant inter-group differences (p < 0.05)
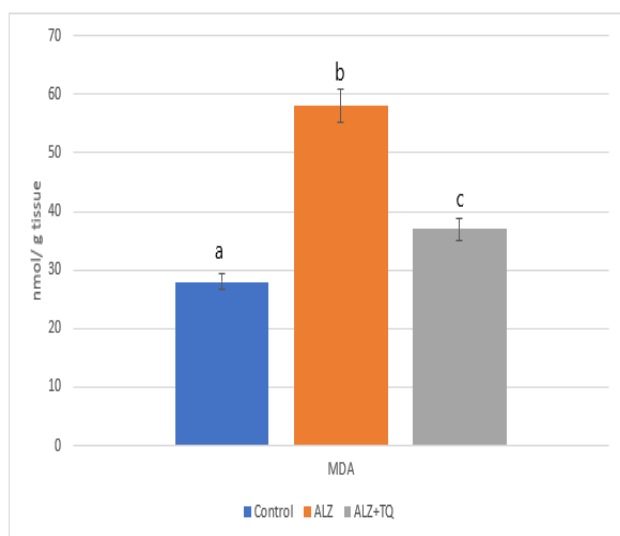
101

**Figure 5.** The catalase (CAT) levels results. Different superscript letters in the same column (a, b, c) indicate significant inter-group differences (p< 0.05)

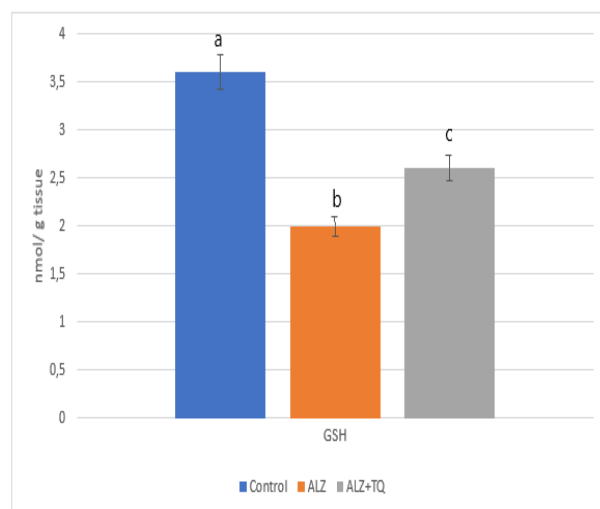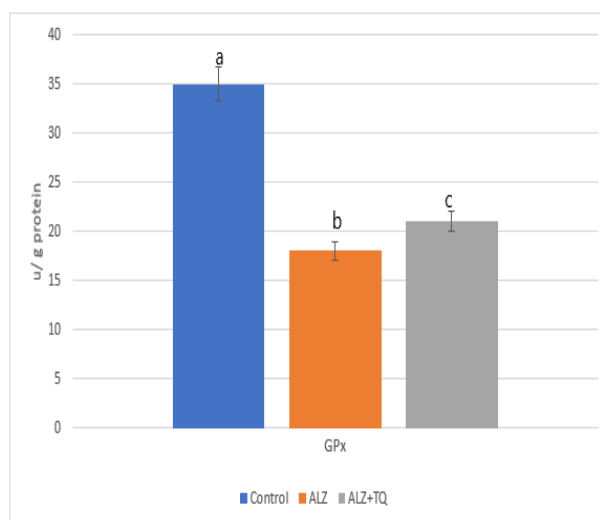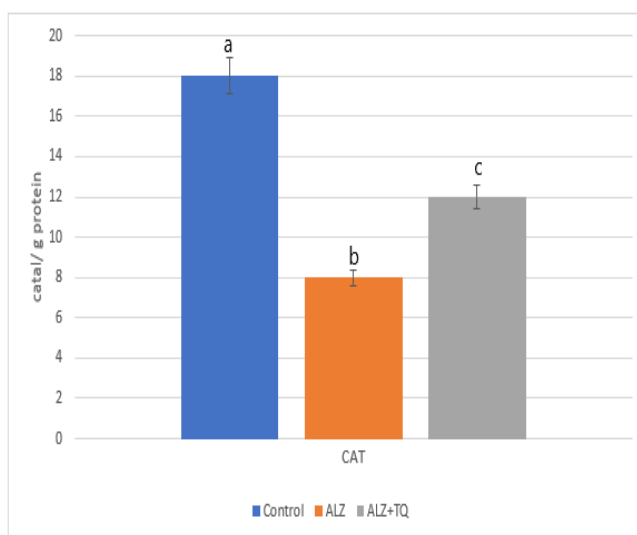**Table 1**. Sperm analysis results of the experimental groups

|  | **Control** | **ALZ** | **ALZ+TQ** |
|---|---|---|---|
| **Total Motility (%)** | 81.92±3.30[a] | 52.66±15.51[b] | 59.41±3.13[b] |
| **Density (%)** | 78,25±8,30 | 74,50±8,21 | 71,42±3,99 |
| **Dead sperm rate%** | 15.42±1.83[a] | 22,58±2,57[b] | 19,08±2,42[c] |
| **Abnormal sperm rate (%)** | 7,83±1,03[a] | 11,67±2,27[b] | 9,33±0,65[c] |
| **Right testis weight (mg)** | 1459,66±63,14 | 1413,75±33,75 | 1419,92±50,74 |
| **Left testis weight (mg)** | 1435,58±63,25 | 1394,62±39,45 | 1383,67±57,45 |

## 4. DISCUSSION AND CONCLUSION

Heavy metal pollution has significant adverse effects on the reproductive functions of both animals and humans [36-38]. Humans and animals are acutely or chronically exposed to heavy metals through food and water intake [39]. These toxic substances cause deterioration in endocrine mechanism and testicular functions [40]. D-Gal causes aging progression and nephropathy in the brain, kidney, and liver. It also induces oxidative stress by increasing lipid peroxidation [41]. In the present study, the effects of TQ on the changes caused by $AlCl_3$+D-Gal in the testicular tissue of rats, which were administried to create an experimental Alzheimer's model, were investigated.

Oxidative stress occurs when the balance between the antioxidant defense system and reactive oxygen species (ROS) is disrupted [42]. Oxidative stress at physiological limits is required for physiological interactions of sperm cells such as fertilization and sperm hyperactivation. However, excessive ROS induces lipid peroxidation [43]. Testis are one of the target organs for oxidative stress due to the high composition of polyunsaturated lipids in the membrane structure [44]. Antioxidant defense mechanisms protect mammalian germ cells against oxidative stress [45]. Enzymes such as SOD, CAT and GPx are the first defense mechanism against oxidative stress. GSH binds free radicals formed as a result of oxidative metabolism [46]. MDA is an important oxidant

parameter for testicles [47]. In previous studies, it has been stated that $AlCl_3$ weakens the antioxidant system in rats by increasing the MDA content [48, 49]. It is stated that D-Gal induces oxidative stress by increasing lipid peroxidation [11]. Presented study, the oxidant activity induced by $AlCl_3$+D-Gal was significantly reduced in the ALZ+TQ group. Parallel to this GSH level, CAT, GPx and SOD activity decreased. This confirms the TQ antioxidant property of this condition and exhibits lipid peroxidation-reducing antioxidant properties.

Environmental pollution adversely affects the structural and physiological integrity of the testicles and may cause infertility [36, 50]. Testicular oxidative stress is one of the main factors causing infertility [51]. It is reported that oxidative damage causes spermatozoal dysfunction [52]. It has been reported that Al-induced oxidative damage and Al cross the blood-testis barrier, induce lipid peroxidation, damage the sperm membrane [53] and cause inactivation of antioxidant enzymes [54]. It has been reported that oxidative damage in spermatozoa plays an important role in the deterioration of sperm function and infertility [45]. $AlCl_3$ increases oxidative stress in testicular tissue and thus has a negative effect on testicular physiology and sperm parameters [8, 55]. It is stated that $AlCl_3$ reduces sperm motility and increases the rate of abnormal sperm [56]. Consistent with previous studies, $AlCl_3$ administration decreased spermatozoa motility, increased dead sperm ratio and abnormal spermatozoa ratio in our study. The reason for this may be that $AlCl_3$ crosses the blood testicular barrier and impairs sperm metabolism and also increases lipid peroxidation due to the increase of free radicals. It can also be shown in the deficiency in the antioxidant defense system, which is necessary for sperm functions.

As a result, $AlCl_3$+D-Gal administration in rats caused an increase in oxidative stress in testis tissue, and decrease in sperm quality. TQ treatment, strengthened the antioxidant defense system in the testis, partially prevented oxidative damage and improved sperm quality.

102

## REFERENCES

[1] Supnet C, Bezprozvanny I. Presenilins function in ER calcium leak and Alzheimer's disease pathogenesis. Cell calcium. 2011;50(3):303-9.

[2] Zhang Y, Pi Z, Song F, Liu Z. Ginsenosides attenuate d-galactose-and AlCl3-inducedspatial memory impairment by restoring the dysfunction of the neurotransmitter systems in the rat model of Alzheimer's disease. Journal of ethnopharmacology. 2016;194:188-95.

[3] Ahmed SA, Mohammed WI. Carvedilol induces the antiapoptotic proteins Nrf2 and Bcl2 and inhibits cellular apoptosis in aluminum-induced testicular toxicity in male Wistar rats. Biomedicine & Pharmacotherapy. 2021;139:111594.

[4] Exley C. Does antiperspirant use increase the risk of aluminium-related disease, including Alzheimer's disease? Molecular Medicine Today. 1998;4(3):107-9.

[5] Sood PK, Nahar U, Nehru B. Curcumin attenuates aluminum-induced oxidative stress and mitochondrial dysfunction in rat brain. Neurotoxicity research. 2011;20:351-61.

[6] Tahari FZ, Lablack M, Hamadouche NA, Tahari Z, Aoues A. Protective effect of Haloxylon salicornicum on hepatic and renal functions of Wistar rats exposed to aluminium. African Journal of Biotechnology. 2016;15(9):293-302.

[7] Klein J, Mold M, Mery L, Cottier M, Exley C. Aluminum content of human semen: Implications for semen quality. Reproductive Toxicology. 2014;50:43-8.

[8] Güvenç M, Cellat M, Gökçek İ, Arkalı G, Uyar A, Tekeli İO, et al. Tyrosol prevents AlCl3 induced male reproductive damage by suppressing apoptosis and activating the Nrf-2/HO-1 pathway. Andrologia. 2020;52(2):e13499.

[9] Guo C-H, Huang C-J, Chen S-T, Hsu G-SW. Serum and testicular testosterone and nitric oxide products in aluminum-treated mice. Environmental toxicology and pharmacology. 2001;10(1-2):53-60.

[10] Türk E, Ozan Tekeli I, Özkan H, Uyar A, Cellat M, Kuzu M, et al. The protective effect of esculetin against aluminium chloride-induced reproductive toxicity in rats. Andrologia. 2021;53(2):e13930.

[11] Huang C-C, Chiang W-D, Huang W-C, Huang C-Y, Hsu M-C, Lin W-T. Hepatoprotective effects of swimming exercise against D-galactose-induced senescence rat model. Evidence-Based Complementary and Alternative Medicine. 2013.

[12] Hakimizadeh E, Hassanshahi J, Kaeidi A, Nematollahi MH, Taghipour Z, Rahmani M, et al. Ceftriaxone improves hepatorenal damages in mice subjected to D-galactose-induced aging. Life Sciences. 2020;258:118-9.

[13] Mohamed NE-S, Abd El-Moneim AE. Ginkgo biloba extract alleviates oxidative stress and some neurotransmitters changes induced by aluminum chloride in rats. Nutrition. 2017;35:93-9.

[14] Gezici S, Koçum D. Nörodejeneratif Hastalıkların Tedavisinde Nöroprotektif Ajan Olarak Tıbbi Bitkiler ve Fitokimyasallar. Türk Doğa ve Fen Dergisi. 2021;10(2):325-37.

[15] Varisli B, Caglayan C, Kandemir F, Gür C, Bayav I, Genc A. The impact of Nrf2/HO-1, caspase-3/Bax/Bcl2 and ATF6 /IRE1/ PERK/ GRP78 signaling pathways in the ameliorative effects of morin against methotrexate-induced testicular toxicity in rats. Molecular Biology Reports. 2022;49(10).

[16] Gür C, Kandemir O, Kandemir FM. Investigation of the effects of hesperidin administration on abamectin-induced testicular toxicity in rats through oxidative stress, endoplasmic reticulum stress, inflammation, apoptosis, autophagy, and JAK2/STAT3 pathways. Environmental Toxicology. 2022;37(3):401-12.

[17] Gür C, Kandemir FM, Genç A. Bortezomib ile kalp hasarı oluşturulan ratlarda berberinin oksidatif ve nitrozatif stres üzerine etkisi. Türk Doğa ve Fen Dergisi. 2020;9(2):118-26.

[18] Imran M, Rauf A, Khan IA, Shahbaz M, Qaisrani TB, Fatmawati S, et al. Thymoquinone: A novel strategy to combat cancer: A review. Biomedicine & Pharmacotherapy. 2018;106:390-402.

[19] Ahmad N, Ahmad R, Al-Layly A, Al-Shawi H, Al-Ali A, Amir M, et al. Ultra-high-performance liquid chromatography-based identification and quantification of thymoquinone in Nigella sativa extract from different geographical regions. Pharmacognosy Magazine. 2018;14.

[20] Ghosheh OA, Houdi AA, Crooks PA. High performance liquid chromatographic analysis of the pharmacologically active quinones and related compounds in the oil of the black seed (Nigella sativa L.). Journal of pharmaceutical and biomedical analysis. 1999;19(5):757-62.

[21] Gökçe A, Oktar S, Koc A, Yonden Z. Protective effects of thymoquinone against methotrexate-induced testicular injury. Human & experimental toxicology. 2011;30(8):897-903.

[22] Gür FM, Timurkaan S, Taskin E, Guven C, Gur HE, Senturk M, et al. Thymoquinone improves testicular damage and sperm quality in experimentally varicocele-induced adolescent rats. Andrologia. 2021;53(5):e14033.

[23] Hassan E, El-Neweshy M, Hassan M, Noreldin A. Thymoquinone attenuates testicular and spermotoxicity following subchronic lead exposure in male rats: Possible mechanisms are involved. Life sciences. 2019;230:132-40.

[24] Akarsu GD, Çetin A. The Effect of Thymoquinone on Oxidative Stress Parameters and Apolipoprotein E in Alzheimer Model in Rats. Dementia and Geriatric Cognitive Disorders. 2022;51(4):297-309.

[25] Omur A, Kirbas A, Aksu E, Kandemir FM, Dorman E, Kaynar O, et al. Effects of antioxidant vitamins (A, D, E) and trace elements (Cu, Mn, Se, Zn) on some metabolic and reproductive profiles in dairy cows during transition period. Polish journal of veterinary sciences. 2016.

[26] Sun Y, Oberley LW, Li Y. A simple method for clinical assay of superoxide dismutase. Clinical chemistry. 1988;34(3):497-500.

[27] Aebi H. Catalase. Methods of enzymatic analysis. Elsevier; 1974. p. 673-84.

[28] Lawrence RA, Burk RF. Glutathione peroxidase activity in selenium-deficient rat liver. Biochemical and biophysical research communications. 1976;71(4):952-8.

[29] Sedlak J, Lindsay RH. Estimation of total, protein-bound, and nonprotein sulfhydryl groups in tissue with Ellman's reagent. Analytical biochemistry. 1968;25:192-205.

[30] Goth L. A simple method for determination of serum catalase activity and revision of reference range. Clinica chimica acta. 1991;196(2-3):143-51.

[31] Türk G, Ateşşahin A, Sönmez M, Çeribaşi AO, Yüce A. Improvement of cisplatin-induced injuries to sperm quality, the oxidant-antioxidant system, and the histologic structure of the rat testis by ellagic acid. Fertility and sterility. 2008;89(5):1474-81.

[32] Aksu EH, Akman O, Özkaraca M, Ömür A, Ucar Ö. Effect of Maclura pomifera extract on cisplatin-

induced damages in reproductive system of male rats. Kafkas Univ Vet Fak Derg. 2015;21:397-403.

[33] Tuncer SÇ, Akarsu SA, Küçükler S, Gür C, Kandemir FM. Effects of sinapic acid on lead acetate-induced oxidative stress, apoptosis and inflammation in testicular tissue. Environmental toxicology. 2023.

[34] Bal R, Naziroğlu M, Türk G, Yilmaz Ö, Kuloğlu T, Etem E, et al. Insecticide imidacloprid induces morphological and DNA damage through oxidative toxicity on the reproductive organs of developing male rats. Cell biochemistry and function. 2012;30(6):492-9.

[35] Aksu E, Akman O, Ömür A, Karakuş E, Can I, Kandemir F, et al. 3, 3 diindolylmethane leads to apoptosis, decreases sperm quality, affects blood estradiol 17 β and testosterone, oestrogen (α and β) and androgen receptor levels in the reproductive system in male rats. Andrologia. 2016;48(10):1155-65.

[36] Akarsu SA, Türk G, Arkalı G, Çeribaşı AO, Yüce A. Changes in heavy metal levels, reproductive characteristics, oxidative stress markers and testicular apoptosis in rams raised around thermal power plant. Theriogenology. 2022;179:211-22.

[37] Caglayan C, Demir Y, Kucukler S, Taslimi P, Kandemir FM, Gulçin İ. The effects of hesperidin on sodium arsenite-induced different organ toxicity in rats on metabolic enzymes as antidiabetic and anticholinergics potentials: A biochemical approach. Journal of food biochemistry. 2019;43(2):e12720.

[38] Kandemir FM, Caglayan C, Darendelioğlu E, Küçükler S, İzol E, Kandemir Ö. Modulatory effects of carvacrol against cadmium-induced hepatotoxicity and nephrotoxicity by molecular targeting regulation. Life Sciences. 2021;277:119610.

[39] Li S, Han B, Wu P, Yang Q, Wang X, Li J, et al. Effect of inorganic mercury exposure on reproductive system of male mice: Immunosuppression and fibrosis in testis. Environmental Toxicology. 2022;37(1):69-78.

[40] PT Manfo F, A Nantia E, P Mathur P. Effect of environmental contaminants on mammalian testis. Current molecular pharmacology. 2014;7(2):119-35.

[41] Radmehr V, Ahangarpour A, Khorsandi L, Omidi M. Protective Effects of Myricitrin and Vitamin E on Nephropathy of Aging Mice Model Induced By D-Galactose. Duzce Medical Journal. 2021;23(3):270-5.

[42] Gülcin I. Antioxidant activity of food constituents: an overview. Archives of toxicology. 2012;86:345-91.

[43] Aksu EH, Kandemir FM, Küçükler S. Ameliorative effect of hesperidin on streptozotocin-diabetes mellitus-induced testicular DNA damage and sperm quality degradation in Sprague–Dawley rats. Journal of Food Biochemistry. 2021;45(10):e13938.

[44] Drasga RE, Einhorn LH, Williams SD, Patel DN, Stevens EE. Fertility after chemotherapy for testicular cancer. Journal of Clinical Oncology. 1983;1(3):179-83.

[45] Çağlayan C, Taslimi P, Demir Y, Küçükler S, Kandemir FM, Gulcin I. The effects of zingerone against vancomycin-induced lung, liver, kidney and testis toxicity in rats: The behavior of some metabolic enzymes. Journal of biochemical and molecular toxicology. 2019;33(10):e22381.

[46] El-Shenawy NS. Effects of insecticides fenitrothion, endosulfan and abamectin on antioxidant parameters of isolated rat hepatocytes. Toxicology in vitro. 2010;24(4):1148-57.

[47] Belhan S, Özkaraca M, Kandemir FM, Gülyüz F, Yildirim S, Ömür AD, et al. Effectiveness of hesperidin on methotrexate-induced testicular toxicity in rats. Kafkas Üniversitesi Veteriner Fakültesi Dergisi. 2017;23(5).

[48] Dera HA, Abushouk A. Protective effect of resveratrol against aluminium chloride (AlCl3) induced testicular damage in rats entails inhibition of intrinsic apoptotic pathway. Science of Advanced Materials. 2015;7(2):384-95.

[49] Khalaf HA, Elsamanoudy AZ, Abo-Elkhair SM, Hassan FE, Mohie PM, Ghoneim FM. Endoplasmic reticulum stress and mitochondrial injury are critical molecular drivers of AlCl3-induced testicular and epididymal distortion and dysfunction: protective role of taurine. Histochemistry and Cell Biology. 2022;158(1):97-121.

[50] Yilmaz O, Hikmet D. Ağır metallerin üreme sistemi üzerine etkileri. Yüzüncü Yıl Üniversitesi Veteriner Fakültesi Dergisi. 2013;24(2):91-4.

[51] Kandemir FM, Caglayan C, Aksu EH, Yildirim S, Kucukler S, Gur C, et al. Protective effect of rutin on mercuric chloride-induced reproductive damage in male rats. Andrologia. 2020;52(3):e13524.

[52] Küçükler S, Çomakli S, Özdemir S, Kandemir Fm. Ratlarda dosetaksel kaynaklı testis toksisitesi üzerine silimarinin etkileri: biyokimyasal, moleküler ve histopatolojik değerlendirme. F Ü Sağ Bil Vet Derg. 2020;34(1):13-21.

[53] Khattab FKI, Khattab I. Histological and ultrastructural studies on the testis of rat after treatment with aluminium chloride. Aust J Basic Appl Sci. 2007;1(1):63-72.

[54] Wagner H, Cheng JW, Ko EY. Role of reactive oxygen species in male infertility: An updated review of literature. Arab journal of urology. 2018;16(1):35-43.

[55] Praveen K, Poonam S. Protective role of Tribulus terrestris on aluminium chloride-induced reproductive toxicity in the male laboratory mouse. International Journal of Pharmaceutical Sciences and Research (IJPSR). 2015;6(6):2395-405.

[56] Alkhedaide A, Alshehri ZS, Sabry A, Abdel‐Ghaffar T, Soliman MM, Attia H. Protective effect of grape seed extract against cadmium-induced testicular dysfunction. Molecular medicine reports. 2016;13(4):3101-9.

104

**Türk Doğa ve Fen Dergisi**
**Turkish Journal of Nature and Science**
www.dergipark.gov.tr/tdfd

# Prevalence of *Cryptosporidium*, *Eimeria* Species and Gastrointestinal Helminths in Lambs and Sheeps in Erzurum Region

**Barış SARI[1]** (iD), **İbrahim BALKAYA[2]** (iD), **Gencay Taşkın TAŞÇI[1]** (iD), **Mükremin Özkan ARSLAN[3]** (iD),

**Sezin Beyza KÜÇÜKLER[2]\*** (iD)

[1]Department of Parasitology, Veterinary Faculty, Kafkas University, Kars, Türkiye
[2] Department of Parasitology, Veterinary Faculty, Ataturk University, Erzurum, Türkiye
[3] Department of Medical Parasitology, Medicine Faculty, Kafkas University, Kars, Türkiye
Barış SARI ORCID No: 0000-0001-9978-2513
İbrahim BALKAYA ORCID No: 0000-0002-1103-2812
Gencay Taşkın TAŞÇI ORCID No: 0000-0002-8590-1101
Mükremin Özkan ARSLAN ORCID No: 0000-0002-6447-5561
Sezin Beyza KÜÇÜKLER ORCID No: 0009-0005-3772-6395
*Corresponding author: sezinbeyzakucukler@gmail.com*

**Abstract:** This study was carried out in Pazaryolu, Pasinler and Ilıca districts of Erzurum from February to March 2009, and included 461 lambs (253 with diarrhea and 208 healthy, varying up to 1 month of age) and 397 sheeps (9 with diarrhea and 388 healthy), from 28 pens located in 11 focuses on the region. The fresh fecal samples taken from lambs and sheeps was examined microscopically. Of the 858 fecal samples examined, *Cryptosporidium* species were found in 397 (46.3%), *Eimeria* species in 313 (36.5%) and gastrointestinal helminth eggs were found in 21 (2.4%). Ten *Eimeria* species: *Eimeria ovinoidalis*, *E. parva*, *E. pallida*, *E. faurei*, *E. bakuensis*, *E. crandalis*, *E. ahsata*, *E. weybridgensis*, *E. intricata* and *E. granulosa* were detected in lamb and sheep feces. Additionally, in the samples examined, *Strongyloides papillosus*, *Nematodirus* spp. and *Trichuris* spp. eggs were found.

105

## Erzurum Yöresinde Kuzu ve Koyunlarda *Cryptosporidium, Eimeria* Türleri ve Gastrointestinal Helmintlerin Prevalansı

**Öz:** Bu çalışma 2009 yılının Şubat ve Mart aylarında Erzurum'un Pazaryolu, Pasinler ve Ilıca ilçelerinde yürütülmüş olup, yöredeki 11 odakta bulunan 28 ağıldan yaşları 1 aylığa kadar değişen 461 kuzu (253 ishalli, 208 sağlıklı) ve 397 (9 ishalli, 388 sağlıklı) koyundan alınan dışkı örneği mikroskobik olarak incelenmiştir. İncelenen 858 dışkı örneğinin 397'sinde (%46.3) *Cryptosporidium* türlerine, 313'ünde (%36.5) *Eimeria* türlerine ve 21'inde ise (%2.4) gastrointestinal helmint yumurtalarına rastlanmıştır. Kuzu ve koyun dışkılarında *Eimeria ovinoidalis, E. parva, E. pallida, E. faurei, E. bakuensis, E. crandalis, E. ahsata, E.weybridgensis, E. intricata* ve *E. granulosa* olmak üzere 10 *Eimeria* türü tespit edilmiştir. Ayrıca incelenen örneklerde *Strongyloides papillosus, Nematodirus* spp. ve *Trichuris* spp. yumurtalarına rastlanılmıştır.

## 1. INTRODUCTION

Cryptosporidiosis is a zoonotic protozoan disease that is common all over the world. Disease-causing agents are Apicomplexa subphylum, protozoa of the *Cryptosporidium* genus, which is in the Sporozoa class. It can affect a wide variety of animal species, including reptiles, birds, fish, and mammals. Transmission occurs

through increased consumption of water or food contaminated with oocysts [1].

Cryptosporidiosis is considered to be an important disease, leading to important economic losses in calves and lambs. Mild or severe yellowish, malodorous, diarrhea, and weight loss, depression, abdominal pain are seen clinically in sheep, and in general, it can cause death

in animals in one month old animals [2, 3]. The clinical course of the disease in lambs is similar to that in calves, and the agent development takes 3-4 days. Outbreaks are generally seen in 7-10 day old lambs. Risk factors such as farm management, herd size, farm type and hygiene, bedding type, colostrum feeding, season, age and contamination sources (e.g. water) play a role in the spread of *Cryptosporidium* spp [4-6].

Due to the small size of *Cryptosporidium* spp. oocysts, it is difficult to be noticed by inexperienced people. The most widely used diagnostic test is acid-fast staining of smears prepared from feces. The most used are the modified Ziehl–Neelsen (mZN) or modified Kinyoun staining technique. Recently, ELISA and PCR diagnostic methods have been widely used in diagnosis [7-9].

*Cryptosporidium parvum*, *C. xiaoi* and *C. ubiquitum* are the most common of the *Cryptosporidium* species found in sheep, whereas *C. hominis*, *C. andersoni*, *C. bovis*, *C. scrofarum*, *C. suis*, *C. fayeri* and *C. canis* are seen as sporadic [10-12]. *C. parvum* is the main species found in humans and animals. Anthroponotic *C. parvum* type I (*C. hominis*) is observed in humans, while *C. parvum* type II (*C. bovis*) is found zoonotically in humans and animals (especially ruminants). *C. parvum* type II causes infection in lambs [2, 10-12].

Ovine cryptosporidiosis was first described in diarrheic lambs 1-3 weeks olds in Australia in 1974 [13]. However, its role as the primary etiological agent of diarrhea in lambs was defined by different studies in the early 1980 [14]. In subsequent studies, infection has also been reported from different geographical regions; Its prevalence varies between 4% and 85% in the USA, Canada, Iran, Trinidad Tobago, Spain and Italy [15].

Studies performed in Turkey have reported the prevalence of *Cryptosporidium* agents in diarrheic and nondiarrheic lambs as follows: 38.8% in Kars, 79.1% in Aydın, 2.97% in Konya, 12% in Elazığ, , 23.3% in İzmir, and 13.17% in Van regions [6, 16-20].

Coccidiosis is a protozoan disease caused by protozoans belonging to the Eimeridae family [21, 22]. Coccidiosis, which is very common in many region of the world, is primarily seen in poultry, cattle, sheep, goats, dogs, cats, pigs and rabbits. Although it causes economic losses as it cause death in young animals, especially those who survived the disease play a carrier role because they become preimmune. Clinically, it may result in hemorrhagic diarrhea, depression, weight loss, and sometimes death, especially in young animals [21-23].

For the diagnosis of coccidiosis, the age of the animal, treatment and housing conditions and clinical findings are taken into consideration. Definitive diagnosis is made by detecting the presence of oocysts in fecal samples in line with clinical symptoms. For the diagnosis of *Eimeria* oocysts, simple flotation method is used for qualitative detection in fecal samples and Modified McMaster method is used for quantitative detection, while serological and molecular methods are also used for

diagnosis. The treatment phase in coccidiosis is based on killing the causative agent or preventing its development, eliminating fluid loss in animals and treating secondary infections. The most important factors in the prevention of coccidiosis are good business management, care-feeding and hygiene. Basic protection factors such as the number of animals in the barn or farm, the temperature in the barn, the presence of animals of different age groups in the same compartments, the diet and feed contents should be taken into account [21-25].

In the previous studies, it was detected that *Eimeria ovina*, *E. ahsata*, *E. crandalis*, *E. faurei*, *E. intricata*, *E. ovinoidalis*, *E. parva*, *E. granulosa*, *E. pallida*, *E. punctata*, *E. weybridgensis*, and *E. marsica* species caused coccidiosis in sheep [21-25]. It is commonly seen in sheep and 3-8 weeks old lambs almost all over the world. The prevalence of the disease in Turkey was detected between 12.6-100% (Kars, Aegean region, Elazig, Bursa, Antakya, Van, Bitlis) [25-31]. Different prevalence rates have been reported in various studies conducted in Kenya, Australia, Spain, and Iran it has been found to be widespread all over the world. [32-35].

Gastrointestinal helminths in sheep cause a decrease in meat, milk, skin, and wool products and even death. Gastrointestinal nematodes are also neglected in terms of a treatment since it usually progresses subclinically without causing sudden deaths. Mixed infections with other helminths have also been reported to have worsened the disease and increased the death rates [21, 36-38].

In the studies performed to determine the nematodiasis-causing species and their prevalence rates in the gastrointestinal system in sheep in Turkey were determined: *Trichostrongylus, Ostertagia, Teladorsagia, Marshallagia, Haemonchus, Nematodirus, Cooperia, Strongyloides, Bunostomum, Oesopagostomum, Gonglonema, Chabertia, Trichuris* species at the prevalence rate of 0.2-89.3%. The parasitological examination revealed that the most prevalent species was *Ostertagia* spp., followed by *Nematodirus* spp. and *Trichostrongylus* spp. [39, 40-43].

This study was carried out to determine the prevalence of *Cryptosporidium*, *Eimeria* Species and Gastrointestinal Helminths in Lambs and Sheeps in Erzurum Region.

## 2. MATERIAL AND METHOD

This study was carried out in Erzurum province during the birthing season in February and March 2009. Fresh fecal samples were collected from the rectums of 461 lambs (253 with diarrhea, 208 healthy, ages varying up to 1 month) and 397 (9 with diarrhea, 388 healthy) sheep from 28 sheep pens in 11 foci in the Erzurum region.

Fecal samples were examined using the zinc sulfate flotation method. Gastrointestinal helminth eggs and *Eimeria* oocysts were detected using this method. Fecal samples containing detected *Eimeria* oocysts were placed in petri dishes and allowed to sporulate in a laboratory oven after being treated with 2.5% potassium dichromate

[22, 24]. Sporulated oocysts were examined using centrifugal flotation under a 10-40 lens microscope. The shape, color, size, and state of the wall of the oocysts reported in the literature, as well as the shape and size of sporocysts and sporozoites, sporocyst and oocyst residue, stidea body, polar granule, micropyle, and cap, were examined under the immersion lens [22, 24, 44].

Identification of *Cryptosporidium* oocysts was made as follows: The portioned fecal samples were first homogenized with tap water at 3000 rpm for 5 minutes, then centrifuged, and smears were prepared from the sediment obtained at the end of the centrifuge, stained with the modified acid-fast method (MAF), and examined under a microscope with a 40 lens [45].

## 3. RESULTS

In the Erzurum region, 397 (46.3%) *Cryptosporidium* spp. oocyst, 313 (36.5%) *Eimeria* spp. oocyst, and 21 (2.4%) gastrointestinal helminth eggs were found in 858 fecal samples.

*Cryptosporidium* was found in 34.8% (88/253) of lambs with diarrhea. When the relationship between the appearance of oocysts in the fecal is evaluated, *Cryptosporidium* sp. oocysts were found at a higher rate. In lambs with normal fecals, this rate was determined to be 19.2% (40/208). *Cryptosporidium* was found in 55.6% (5/9) of diarrheal sheep and 68% (264/388) of healthy sheep during the periparturient period.

*Eimeria* species identified in lambs and sheep and their prevalence are as follows; *Eimeria ovinoidalis* (22%), *E. parva* (12.2%), *E. pallida* (11.9%), *E. faurei* (10.7%), *E. bakuensis* (9.7%), *E. crandalis* (3.0%), *E. ahsata* (0.7%), *E. weybridgensis* (0.3%), *E. intricata* (0.2%) and *E. granulosa* (0.1%). *Eimeria* was detected in 41/78 (52.6%) of sheep during the periparturient period. *Strongyloides papillosus* 12/21 (57.1%), *Nematodirus* spp. 7/21 (33.3%), and *Trichuris* spp. 2/21 (9.5%) species were detected in sheep, and no gastrointestinal helminth eggs were found in lambs.

Prevalence rates in lambs and sheep and their distribution according to age groups are given in Tables 1-4.

**Table 1.** Prevalence of *Cryptosporidium*, *Eimeria* and Gastrointestinal helminths in lambs.

|  | Diarrheic lamb | Healthy lamb |
|---|---|---|
| *Cryptosporidium* spp. | 88/253 (34.8%) | 40/208 (19.2%) |
| *Eimeria* spp. | 75/253 (29.6%) | 94/208 (45.29%) |
| Gastrointestinal helmint | 0/253 | 0/208 |

**Table 2**. Prevalence of *Cryptosporidium*, *Eimeria* and Gastrointestinal helminths in sheep.

|  | Preparturient Sheep | Postparturient Sheep |
|---|---|---|
| *Cryptosporidium* spp. | 74/78 (94.9%) | 195/319 (61.1%) |
| *Eimeria* spp. | 41/78 (52.6%) | 103/319 (32.3%) |
| Gastrointestinal helmint | 12/78 (15.4%) | 9/319 (2.8%) |

**Table 3**. According to age groups in lambs *Cryptosporidium* spp. prevalence.

|  | Diarrheic lamb | Healthy lamb | Total |
|---|---|---|---|
| **1 Week** | 12/45(26.7%) | 1/7 (14.3%) | 13/52 (25%) |
| **2 Week** | 14/46(30.4%) | 8/55(14.5%) | 22/101(21.8%) |
| **3 Week** | 23/75(30.7%) | 16/72(22.2%) | 39/147 (26.5%) |
| **4 Week** | 39/87(44.8%) | 15/74(20.3%) | 54/161 (33.5%) |

**Table 4** According to age groups in lambs *Eimeria* spp. prevalence.

|  | Diarrheic lamb | Healthy lamb | Total |
|---|---|---|---|
| **0-2 Week** | 10/91 (11%) | 24/62 (38.7%) | 34/153 (22.2%) |
| **3-4 Week** | 66/162 (40.7%) | 70/146 47.9%) | 136/308(44.2%) |

## 4. DISCUSSION AND CONCLUSION

*Cryptosporidium* species are highly important in domestic animals and are recognized as the principal etiological agent in the diarrhea cases of newborn lambs. It progresses with high morbidity and mortality in inadequate care and feeding. The postpartum period is the time when animals are most susceptible to natural infection [46]. The disease is controlled by the immune system, and it can be self-limiting in those with a developed immune system. It has been reported that risk factors such as herd size, rearing type, birth time and weaning are effective in the occurrence of oocysts. Farm management and hygiene are important in the prevention of infection [5, 6].

In a study performed on lamb diseases in the neonatal period in Turkey, it was reported that diarrhea cases ranked top with 15.4%. It has been observed that *Cryptosporidium* infections are one of the most important causes of neonatal lamb diarrhea. It has been reported that *Cryptosporidium* oocyst excretion has been observed to be high in animals affected with diarrhea [47].

In a study performed on the prevalence of *Cryptosporidium* was found a rate of 17.2% in sheep and lambs in Iran [5]. In studies performed in Spain, prevalence rates ranging from 14.7% to 45% in lambs with diarrhea and 59% in sheep were reported [48]. Another research revealed a prevalence of 2.6% with microscopic testing and 26.2% with PCR in lambs in Australia [49]. Other studies found that the prevalence of *Cryptosporidium* infection in lambs was 12.5% in

107

Zambia, 3.7% in Brazil, 10.1% in Poland, 42.1% in Serbia, 11.2% in Tunisia, and 23% in Canada [50-55].

According to studies done in various geographical and climatic regions of Turkey, the prevalance of *Cryptosporidium* agents in lambs with diarrhea is as follows: 12% in Elazığ, 23.3% in İzmir, 2.97% in Konya, 79.1% in Aydın and 3.63 percent in Van area, while in Kars region 21.05% and 38.8% were found in two different studies [6, 16-20]. In this study, the prevalence was found to be 46.3%. The difference in prevalence between studies is assumed to be caused by the number of materials used, the number of animals with diarrhea, and the age of the animals. The prevalence of *Cryptosporidium* infection has been reported to be between 4% and 85% in sheep worldwide [56]. Studies on the prevalence of *Cryptosporidium* have found prevalences ranging from 13.6% to 46.5% in Turkey [16, 57]. These studies indicate that *Cryptosporidium* infections in sheep and lambs are common in many areas across the world, including Turkey.

The age of the host animals is the most important risk factor influencing *Cryptosporidium* prevalence. Cryptosporidiosis is widespread in companies that keep a high number of calves, lambs, and kids, and the clinical picture is most common in lambs under one month old. *Cryptosporidium* oocysts are more common in 1-3 week old animals. It has been reported that the incidence of oocysts decreases with age [6, 18]. In this study, however, the prevalence was higher (33.5%) in 4-week-old lambs. The reason is based on the fact that the number of 4-week-old animals used is higher than the animals of other species.

The prevalence of *Eimeria* in sheep is high in all age groups. However, the disease is important in lambs from two weeks to three months old. It shows a latent course in the elderly. Among the key risk factors for the disease are hygiene, care, and feding [24-25, 30].

Coccidiosis in sheep and lambs is common infection in Turkey and many other countries across the world. The prevalence of coccidiosis in Turkey ranged from 12.6 to 100% (Antakya, Bitlis, Aegean region, Bursa, Elazig, Kars, Van). It was determined that nine different *Eimeria* species infect 29.9% of the sheep in Bursa. Nine *Eimeria* species of 94.8% of lambs in Elazig, seven different *Eimeria* species of 37.26% of sheep in Elazig, nine different *Eimeria* species of 100% of sheep in Van and 10 different *Eimeria* species of 93.9% of lambs and sheep in Kars province were detected [25-31]. In this study, the prevalence of *Eimeria* was found to be 36.5%, and it was determined that the animals were infected with 10 different *Eimeria* species. In the world, this rate was found to be between 12.7% and 97% [32-35]. The differences and prevalences among *Eimeria* species vary depending on climate, vegetation, immunity, age, species, farm management, other diseases and stress factors [29-30, 34].

Periparturient period is very important because of parasitic diseases. The immune system is suppressed during this period due to an increase in glucocorticoid and estrogen levels. Hormonal changes and stress increase the prevalence of parasite factors. Therefore, there is an increase in the excretion of *Cryptosporidium* and *Eimeria* oocysts in the periparturient period [46, 58]. In this study, the infection rate in sheep during the periparturient period, also known as the transition time in animals, was determined to be higher than in those during the postparturient period.

A prevalence of 0.2-89.3% was observed in studies done in Turkey to investigate the species causing gastro-intestinal nematodiosis and their prevalence rates in sheep [39-43]. This rate was determined to be 2.5% in present study. The prevalence of helminth infections varies according to several factors, including parasite (biological characteristics), host (genetic resistance, age, physiological state), and environmental factors (climate, altitude, breeding system). Factors such as pasture composition, animal diversity, the proportion of herds or herds in the same pasture, and pasture pollution play a very important role in the spread of helminths. In addition, antiparasitic drug usage, sample size, and coinfections impact the prevalence of parasitic infections. Age is another factor that affects the prevalence of gastrointestinal parasites. In general, adults are more resistant to parasitic infections than young animals due to age-related changes in host immunity [59-61]. However, infection was observed in sheep in this study.

The increased infection rate in adults can be attributed to the disease spreading across large areas during grazing, overfeeding in contaminated grassland, and exposure to stress factors [32, 59, 61].

In this study, *Cryptosporidium* spp. was found in 397 (46.3%) of 461 lambs (253 with diarrhea, 208 healthy) and 397 (9 with diarrhea, 388 healthy) sheep feces samples ranging from 28 sheep pens up to 1 month old in 11 foci in Erzurum region. *Eimeria* spp. (36.5%) and gastrointestinal helminth eggs (2.4%) were found. The prevalence of *Cryptosporidium* was determined as 34.8% (88/253) in lambs with diarrhea and 19.2% (40/208) in healthy lambs, and the prevalence of *Cryptosporidium* in sheep was 55.6% (5/9) in diarrheal lambs and 68% (264/388) in healthy ones. Furthermore, different *Eimeria* species were identified in this study. These species are as follows; *Eimeria ovinoidalis, E. parva, E. pallida, E. faurei, E. bakuensis, E. crandalis, E. ahsata, E. weybridgensis, E. intricata* and *E. granulosa. Strongyloides papillosus, Nematodirus* spp., and *Trichuris* spp. were found among the gastro-intestinal nematod eggs. These nematod eggs were not detected in lambs.

Care-hygiene, rearing type, pen condition, season, water resources, breeding season, long winter conditions, and prolonged stay of young animals in the barn were determineted as risk factors that determine the frequency of parasites in the region (Field Observations). Parasite density was reported especially in areas where the physical conditions of the pen were poor.

As a result, *Cryptosporidium* and *Eimeria* species have been identified as common in local lambs. It was determined that gastrointestinal helminth eggs were found at a low rate. The reason for this is the use of drugs against helminths to sheep following the return from grassland in the area.

It has been determined that *Cryptosporidium* and *Eimeria* species have been found to be common in asymptomatic sheep, and *Cryptosporidium* oocyst is excreted at least as much as diarrheal lambs with sheep feces throughout the periparturient period. For this reason, separating the lambs from their mothers and keeping them in separate compartments after birth will limit diarrhea cases and hence clinical cryptosporidiosis, preventing the disease from spreading.

## Acknowledgement

## REFERENCES

[1] Fayer R. Taxonomy and species delimitation in *Cryptosporidium*. Exp Parasitol. 2010; 124: 90-97.

[2] Ramirez NE, Ward LA, Sreevatsan S. A review of the biology and epidemiology of cryptosporidiosis in humans and animals. Microbes Infect. 2004; 6(8): 773-785.

[3] Castro-Hermida JA, Gonzalez-Warleta M, Mezo M. Natural infection by *Cryptosporidium parvum* and *Giardia duodenalis* in sheep and goats in Galacia (NW Spain). Small Rumin Res. 2007; 72: 96-100.

[4] Brook E, Hart CA, French N, Christley R. Prevalence and risk factors for *Cryptosporidium* spp. infection in young calves. Vet Parasitol. 2008; 152: 46-52.

[5] Nouri M, Karami M. Asyptomatic cryptosporidiosis in nomadic shepherds and their sheep. J Infect. 1991; 23(3): 331-333.

[6] Sarı B, Arslan MO, Gicik Y, Kara M, Tasci GT. The prevalence of *Cryptosporidium* species in diarrhoeic lambs in Kars province and potential risk factors. Trop Anim Health Prod. 2009; 41: 819–826.

[7] Diaz P, Quílez J, Robinson G, Chalmers RM, Díez–Banos P, Morrondo P. Identification of *Cryptosporidium xiaoi* in diarrhoeic goat kids (*Capra hircus*) in Spain. Vet Parasitol. 2010; 172: 132-134.

[8] Robert B, Ginter A, Antoine H, Collard A, Coppe P. Diagnosis of bovine cryptosporidiosis by enzyme linked immunosorbent assay. Vet Parasitol. 1990; 37: 1-8.

[9] Gibbons CL, Gazzard BG, Ibrahim M, Morris Jones S, Ong CSL, Awad Kareim FM. Correlation between markers of strain variation in *Cryptosporidium parvum*: evidence of clonality. Parasitol Int. 1998; 47: 139-147.

[10] Sarı B, Arslan MO. Sığır ve Koyunlarda Cryptosporidiosis. Turkiye Klinikleri J Vet Sci 2012; 3(2):9-15.

[11] Chen Y, Qin H, Huang J, Li J, Zhang L. The global prevalence of *Cryptosporidium* in sheep: A systematic review and meta-analysis. Parasitology 2022; 149(12): 1652-1665.

[12] Fayer, R. *Cryptosporidium*: a water-borne zoonotic parasite. Vet Parasitol. 2004; 126: 37-56.

[13] Barker IK, Carbonell PL. *Cryptosporidium agni* sp. n. from lambs, and *Cryptosporidium bovis* from a calf, with observations on the oocyst. Z Parasitenkd. 1974; 44(4): 289-298.

[14] Angus KW, Appleyard WT, Menzies JD, Campbell I, Sherwoofayerd D. An outbreak of diarrhoea associated with cryptosporidiosis in naturally reared lambs. Vet Record. 1982; 110(6): 129-130.

[15] De Graaf DC, Vanopdebbosch E, Ortega-Mora LM, Abbasi H, Peeters JE. A review of the importance of cryptosporidiosis in farm animals. Int J Parasitol. 1999; 29(8): 1269-1287.

[16] Ulutas B, Voyvoda, H. Cryptosporidiosis in diarrhoeic lambs on a sheep farm. T Parazitol Derg. 2004; 28(1): 15-17.

[17] Sevinc F, Uslu U, Derinbay O. The Prevalence of *Cryptosporidium parvum* in lambs around Konya. Turkish J Vet Anim Sci. 2005; 29: 1191-1194.

[18] Ozer E, Erdogmus SZ, Koroglu E. Investigation on the incidence of Cryptosporidia of calves and lambs in Elazig vicinity. Turkish J Vet Anim Sci. 1990; 14, 439-445.

[19] Erman N, Beyazit A, Oz I. Prevelance of cryptosporidiosis in lambs and goat kids in Izmir province. Bornova Vet Kont Araşt Enst Derg. 2000; 25: 33-38.

[20] Çiçek M, Körkoca H, Gül A. Van belediyesi mezbahasında çalışan işçilerde ve kesimi yapılan hayvanlarda *Cryptosporidium* sp.'nin araştırılması. T Parazitol Derg. 2008; 32(1):8-11.

[21] Soulsby EJL. Helminths, Arthropods & Protozoa of Domesticated Animals. 7th Edition, Bailliere Tindall, London, 1986.

[22] Levine ND. Veterinary Protozoology. Ames. Iowa State Universty. 1985;150-163.

[23] Gjerde B, Hele O. Effects of leucocyte extract, levamisole and sulphadimidine on natural coccidial infections (Eimeria spp.) in young lambs. Acta Vet Scand. 1987; 28(1): 33-45.

[24] Dinçer Ş. Coccidiosis. 7nd ed. İzmir: Türkiye Parazitol Derg; 2001. p. 201-218.

[25] Arslan MÖ, Umur Ş, Kara M. The prevalence of Coccidian Species in Sheep in Kars Province of Turkey. Trop Anim Hlth Prod. 1999; 31: 161-165.

[26] Sayın F, Kahyaoğlu T, Çakmak A. Ege bölgesinde (İzmir, Manisa, Aydın) koyun ve keçilerde Eimeria türlerinin tespiti. Ankara Üniv Vet Fak Derg. 1986; 33(1): 90-96.

[27] Güler S, Dumanlı N, Özer E, Erdoğmuş Z, Köroğlu E. Elazığ yöresinde kuzu ve oğlaklarda bulunan *Eimeria* türleri ve bunların yayılışı üzerine araştırmalar. Doğa-Tr J Vet Animal Sci. 1990; 14: 295-300.

109

[28] Demir S. Bursa Et ve Balık Kurumu mezbahasında kesilen koyunlarda *Eimeria* türlerinin tespiti. Turkiye Parazitol Derg. 1985; 19(1): 132-139.

[29] Kaya G. Prevalence of *Eimeria* Species in Lambs in Antakya Province. Turk J Vet Anim Sci. 2004; 28: 687-692.

[30] Gül A, Değer S. Van yöresi koyunlarında bulunan *Eimeria* türleri ve bunların prevalansı. Turk J Vet Anim Sci. 2002; (26): 859-864.

[31] Gül A. Bitlis Yöresinde Koyunlarda *Eimeria* Türlerinin Yaygınlığı. Turkiye Parazitol Derg. 2007; 31(1): 20-24

[32] Kanyari PWN. The relationship between coccidial and helminth infections in sheep and goats in Kenya. Vet Parasitol. 1993; 51(1,2): 137-141.

[33] Hidalgo-Arguello MR, Cordero Del Campillo M. Epizootology of *Eimeria ahsata* Coccidiosis in Leon (Spain). Vet Parasitol. 1988; 27(3,4): 183-191.

[34] O'Callaghan MG, O'Donoghue PJ, Moore E. Coccidia in Sheep in South Australia. Vet Parasitol. 1987; 24(3,4): 175-183.

[35] Mirzaei M, Dahmardeh E. The Prevalence of *Eimeria* Species in Sheep in Zabol city, Iran. Iranian Vet J. 2016; 11(4): 98-105.

[36] Radostits OM, Blood DC, Gay CC. Veterinary Medicine: A text book of disease of cattle, sheep, pigs, goats and horse. Baillere Tindall Publication, London, 1994.

[37] Güralp N. The Prelevance of Parasitic Diseases of Animals in Turkey. AÜ Vet Fak Derg. 1984; 31: 304-315.

[38] Torina A, Dara S, Marino AM, Spargano OAE, Vitale F, Reale S, et al. Study of Gastrointestinal Nematodes in Sicilian Sheep and Goats, Ann. N. Y. Acad. Sci. 2004; 1026:187-194.

[39] Vural A. Trakya Bölgesi Koyunlarındaki Helmint İnvazyonlarının Durumunun Tespiti ve Bunlara Karşı Etkili Kombine Bir Tedavi Sisteminin Geliştirilmesi. Pendik Vet Kont Arşt Enst Derg. 1970; 3(2): 33-55.

[40] Güralp N. Koyunlarımızda görülen Trichostrongylidae türlerine dair sistematik araştırmalar. Ankara Üniv. Vet. Fak. Yayınları, Yayın No: 64. 1955. Ankara.

[41] Zeybek H. Samsun Yöresi Koyun ve Kuzularında Paraziter Fauna Saptama Çalışmaları. AÜ Vet Fak Derg. 1980; 17: 215-236.

[42] Doğanay A, Öğe S. Türkiye'de koyun ve keçilerde görülen helmintler. Kafkas Univ Vet Fak Derg. 1997; 3(1): 97-114.

[43] Altaş M, Sevgili M, Gökçen A, Bayburs HC. Şanlıurfa yöresindeki koyunlarda sindirim sistemi nematodlarının yaygınlığı. Türkiye Parazitol Derg. 2006; 30(4): 317-321.

[44] Pellerdy LP. Coccidia and Coccidiosis. Paul Parey, Berlin und Hamburg and Academiai Kiado, Budapest, 1974, p. 771-809.

[45] Ok ÜZ, Girginkardeşler N, Kilimcioğlu A, Limoncu E. Dışkı İnceleme Yöntemleri. In: Özcel MA, Altıntaş N, Editors. Parazit Hastalıklarında Tanı. Türkiye Parazitol Dern. 1997; 1-61.

[46] Arslan MÖ, Sarı B, Kara M, Taşçı GT, Ekinci İtik A, Gündüz N. Kars Yöresinde Periparturient Dönemdeki İneklerde *Eimeria* ve *Cryptosporidium* Türlerinin Yaygınlığı Üzerine Araştırmalar. Kafkas Üniv Vet Fak Derg. 2012; 18(A): 65-70.

[47] Gökçe E, Erdoğan, H.M. An epidemiological study on neonatal lamb health. Kafkas Üniv Vet Fak Derg. 2009; 15: 225-236.

[48] Matos-Fernandez MJ, Pereira-Bueno J, Ortega-Mora LM, Pilar-Izquerdo M, Fere I, Roje-Vazquez FA. Prevalencia de la infeccion por *Cryptosporidium parvum* en corderos, cabritos y terneros en la provincia de Leon. Acta Parasitologica. 1993; 1: 211.

[49] Ryan UM, Bath C, Robertson I, Read C, Eliot A, Mcinnes L, Traub R, Besier, B. Sheep may not be an important zoonotic reservoir for *Cryptosporidium* and *Giardia* parasites. Apl Environ Microbiol. 2005; 71(9): 4992-4997.

[50] Goma FY, Geurden T, Siwila J, Phiri IGK, Gabriel S, Claerebout E, Vercruysse J. The prevalence and molecular characterisation of *Cryptosporidium* spp. in small ruminants in Zambia. Small Rum Res. 2007; 72: 77-80.

[51] Tembue AAM, Alves LC, Borges JCG, Faustino MA da G, Machado EL de C. *Cryptosporidium* spp. in sheep in Ibimirim District, Pernambuco State, Brazil. Ciencia Veterinaria nos Tropicos. 2006; 9(1): 41-43.

[52] Majewska AC. Werner A, Sulima P, Luty T. Prevalence of *Cryptosporidium* in sheep and goats bred on five farms in westcentral region of Poland. Vet Parasitol. 2000; 89: 269-275.

[53] Misic Z, Katic-Radivojevic S, Kulisic, Z. *Cryptosporidium* infection in lambs and goat kids in Serbia. Acta Vet Beograd. 2006; 56(1): 49-54.

[54] Soltane R, Guyot K, Dei-Cas E, Ayadi A. Prevalence of *Cryptosporidium* spp. (Eucoccidiorida: Cryptosporiidae) in seven species of farm animals in Tunisia. Parasite. 2007; 14(4): 335-338.

[55] Olson ME, Thorlakson CL, Deselliers L, Morck DW, McAllister TA. *Giardia* and *Cryptosporidium* in Canadian farm animals. Vet Parasitol. 1997; 68: 375-381.

[56] Zhang X, Jian Y, Li X, Ma L, Karanis G, Qigang C, et al. Molecular detection and prevalence of *Cryptosporidium* spp. infections in two types of domestic farm animals in the Qinghai-Tibetan plateau area (QTPA) in China. Parasitol Res. 2018; 117: 233-239.

[57] Ozdal N, Tanritanir P, Goz Y, Deger S, Kozat S. Parasitic protozoans (*Eimeria*, *Giardia*, and *Cryptosporidium*) in lambs with diarrhoea in the Van province, Turkey. Bull Vet Inst Pulawy. 2009; 53: 47-51.

[58] Arslan C, Tufan T. Geçiş dönemindeki süt ineklerinin beslenmesi I. Bu dönemde görülen fizyolojik, hormonal, metabolik ve immunolojik değişiklikler ile beslenme ihtiyaçları. Kafkas Üniv Vet Fak Derg. 2010; 16 (1): 151-158.

[59] Belina D, Giri A, Mengistu S, Eshetu A. Gastrointestinal Nematodes in Ruminants: The Parasite Burden, Associated Risk Factors and Anthelmintic Utilization Practices in Selected

110

Districts of East and Western Hararghe. Ethiopia. J Vet Sci. 2017; 8: 2-7.

[60] Kantzoura V, Kouam MK, Theodoropoulo H, Feidas H, Theodoropoulos G. Prevalence and Risk Factors of Gastrointestinal Parasitic Infections in Small Ruminants in the Greek Temperate Mediterranean Environment. Open Vet. 2012; 2: 25-33.

[61] Singh R, Bal MS, Singla LD, Kaur P. Detection of anthelmintic resistance in sheep and goat against fenbendazole by fecal egg count reduction test. J Parasit Dis. 2017; 41: 463-6.

**Türk Doğa ve Fen Dergisi**
**Turkish Journal of Nature and Science**
www.dergipark.gov.tr/tdfd

# The Effect Of Corset On Postoperative Pain Following Lumbar Disc Herniations

## Hidayet Safak CINE[1*] iD

[1] Istanbul Medeniyet University Goztepe Prof. Dr. Suleyman Yalcin City Hospital, Neurosurgery Department, Istanbul, Türkiye
Hidayet Safak CINE ORCID No: 0000-0002-0808-5921

*Corresponding author: cinesafak@gmail.com*

In this research, we aimed to investigate the effect of lumbar corsets on the postoperative pain of single and multiple-level lumbar disc herniations by the Visual analog scale (VAS) and the health outcomes via the Oswestry Disability Index (ODI). Patients (n=101) with a single or double-level unilateral lumbar disc hernia with no history of lumbar surgery were included in this study. All patients decided for operation have been administered non-steroidal NSAIDs and muscle relaxants for 4 – 6 weeks before the operation. All patients were recommended to use a lumbar corset in the postoperative period. A VAS and ODI were utilized to measure the clinical outcomes of corset usage. The first-week and first-month average VAS scores in the corsets group were statistically significantly lower than those who did not use corsets (p<0.001, p=0.002). No statistically significant difference was found in the first-week and first-month VAS changes of the patients who did not use corsets (p=0.059). The first-week and first-month average ODI scores in the corsets group were statistically significantly lower than those who did not use (p=0.012, p<0.001). The change in ODI scores from the first week to the first month was statistically significantly higher in patients wearing corsets (p<0.001). Early adoption of the corset in the postoperative period can help rest and promote the dynamic healing of aching back muscles. Our findings indicated that the use of corsets promoted early recovery from rehabilitation and returns to daily activities.

112

# Lomber Disk Hernisinde Postoperatif Ağrılarda Korsenin Etkisi

**Anahtar Kelimeler**
Lomber disk hernisi,
Korse,
Mikrodiskektomi,
Vizüel analog
skalası,
Oswestry disabilite
indeksi

Bu araştırmada, tek ve çok seviyeli lomber disk hernilerinde bel korselerinin postoperatif ağrı üzerine etkisini Visual analog skala (VAS) ile ve Oswestry Disabilite İndeksi (ODI) ile sağlık sonuçlarına etkisini araştırmayı amaçladık. Bu çalışmaya lomber cerrahi öyküsü olmayan, tek veya çift seviyeli unilateral lomber disk hernisi olan hastalar (n=101) dahil edildi. Operasyona karar verilen tüm hastalara operasyondan 4 – 6 hafta önce non-steroidal NSAİİ ve kas gevşetici verildi. Tüm hastalara postoperatif dönemde lomber korse kullanmaları önerildi. Korse kullanımının klinik sonuçlarını ölçmek için bir VAS ve ODI kullanıldı. Korse grubunda 1. hafta ve 1. ay ortalama VAS skorları korse kullanmayanlara göre istatistiksel olarak anlamlı derecede düşüktü (p<0.001, p=0.002). Korse kullanmayan hastaların 1. hafta ve 1. ay VAS değişimlerinde istatistiksel olarak anlamlı fark bulunmadı (p=0.059). Korse grubunda 1. hafta ve 1. ay ortalama ODI skorları kullanmayanlara göre istatistiksel olarak anlamlı derecede düşüktü (p=0.012, p<0.001). ODI puanlarının birinci haftadan birinci aya göre değişimi korse kullanan hastalarda istatistiksel olarak anlamlı derecede yüksekti (p<0,001). Postoperatif dönemde korsenin erken dönemde benimsenmesi, dinlenmeye yardımcı olabilir ve ağrıyan sırt kaslarının dinamik iyileşmesini destekleyebilir. Bulgularımız, korse kullanımının rehabilitasyondan erken iyileşmeyi ve günlük aktivitelere dönüşü desteklediğini göstermiştir.

# 1. INTRODUCTION

Lombar back pain is one of the most common musculoskeletal problems today. Approximately 70 – 85% of the adult population suffers from low back pain at some point in their lives. Low back pain has many causes. One of the most important causes is lumbar disc herniation (LDH). LDH is the displacement of material inside the intervertebral disc from the edges of the disc [1]. L4 – L5 and L5 – S1 segments are the most common levels of disc herniation. Typical symptoms are radiating pain, felting sensation, numbness, loss of sensation, loss of muscle strength, and functional limitation caused by all these symptoms [2].

Long-term low back pain causes activity restriction in individuals, causing atrophy, especially in the muscles in the waist region. This atrophy condition causes insufficiency in spinal stabilization activity in individuals. Studies have shown that individuals with chronic low back pain have fatigue in the posterior trunk muscles and weakness in the abdominal muscles [3]. Low back pain and sciatica can bring considerable consequences to human daily life, such as impairment of social and work abilities. Spinal degeneration, trauma, inflammation, and infection can be counted as the source of lumbar back pain [4]. LDH is a kind of spinal degeneration that can lead to sciatica or low back pain. Even if low back pain can be observed more frequently, the annual incidence of LDH can reach 2% [5].

Conservative and surgical methods treat LDH. Surgical methods are preferred in individuals with progressive neurological symptoms or cauda equina syndrome who cannot be successful with conservative methods. Among the surgical methods used, microdiscectomy is accepted as the gold standard for shorter operation time and faster return to working life [6]. The intervertebral disc is the largest aneural tissue in the body, so the pain does not occur due to problems in the disc in the early period. The presence of pain is an important parameter for determining the degree of degeneration, and the reduction of pain is an important parameter for recovery [7].

Almost 70% of patients with LDH experience an outstanding decrease in pain after four weeks of conservative medical treatment. Even though pain reduction can be achieved to 80% with the prolongation of conservative treatment, LDH may end up with surgery [6-8]. The decision of the surgery may be attached to many indefinite factors such as a positive leg raising test and long duration of symptoms. Once the surgery is performed, the fundamental purpose should be reducing the pain, at least in the first postoperative week. Although sciatica can usually decrease or even disappear after surgery, the low back pain may persist for a while and proceed to affect the patient's life [9].

Non-steroid anti-inflammatory drugs (NSAIDs) are preferred in these situations; however, opioids may cause undesirable side effects [10]. Even though they have been claimed not to affect spinal stabilization, lumbar corsets (braces) have been used long to reduce back pain, and indications have been discussed since then [11].

In the present study, we aimed to investigate the effect of lumbar corsets on the postoperative pain of single and multiple-level LDH by using the Visual analog scale (VAS) scores and the health outcomes via the Oswestry Disability Index (ODI) scores.

# 2. MATERIAL AND METHOD

A total of 101 patients who were operated on for LDH in our institution between June 2019 to July 2022 have been enrolled in this retrospective analysis. All procedures followed were in accordance with the ethical standards of the responsible committee on human experimentation (institutional and national) and with the Helsinki Declaration of 1975, as revised in 2008. Ethics committee approval has been granted from Istanbul Medeniyet University on 10.05.2023 with protocol number 0308.

Patients with a single or double-level unilateral LDH with no history of lumbar surgery were included in this study. Individuals were diagnosed via MRI. All patients decided for operation have been administered NSAIDs and muscle relaxants for 4 – 6 weeks before the operation. Persistent radiculopathy was the main driver in the surgery decision. The operations were performed by one neurosurgeon with the standard unilateral microdiscectomy procedure. The patients were divided into two groups according to the disc levels operated as single-level or double-level. All patients were recommended to use a lumbar corset in the postoperative period. A VAS was utilized to investigate low back pain in the first week and the first month after the operation. ODI was administered to measure the clinical outcomes of corset usage.

Individuals with other reasons for back pain, such as lumbar stenosis, lumbar listhesis, rheumatic diseases, osteoclasis, or joint inflammation, and patients on antipsychotics or other medication that could affect pain were excluded from the analysis.

## 2.1. Statistical Analysis

The statistical analysis was conducted using SPSS 15.0 for Windows. Numbers and percentages for categorical variables, and mean, standard deviation, minimum, maximum, and median for numerical variables. The Wilcoxon Test was used to analyze the differences in the dependent group because the normal distribution assumption was not met. The Mann-Whitney U test was used to compare numerical variables between two independent groups because the assumption of normal distribution was unmet. The acceptable significance level for alpha was $p < 0.05$.

# 3. RESULTS

A total of 101 patients who underwent LDH have been enrolled in this research. The mean age of the participants was 49.6±13.3 years (range 22 – 71). There

was no difference regarding gender; 48.5% (n=49) of the patients were female, and 51.5% (n=52) were male. The distribution of herniation was 47.5% (n=48) double level and 52.5% (n=53) single level. Approximately half of the subjects, 46.5% (n=47), wore corsets, while 53.5% (n=54) did not.

The first-week and first-month average VAS scores in the corsets group were statistically significantly lower than those who did not use corsets (p<0.001, p=0.002, respectively). No statistically significant difference was found in the first week and first-month VAS changes of the patients who did not use corsets (p=0.059) (Table 1, Table 2, Figure 1).

**Table 1.** Baseline demographics, VAS and ODI scores in the first week and month

| **Age** Mean±SD (Min-Max) | | 49.6±13.3 (22-71) |
|---|---|---|
| **Gender** n (%) | Female | 49 (48.5) |
| | Male | 52 (51.5) |
| **Level** n (%) | Double | 48 (47.5) |
| | Single | 53 (52.5) |
| **Corset** n (%) | No | 54 (53.5) |
| | Yes | 47 (46.5) |
| **VAS** Mean±SD/Min-Max (Median) | 1st week | 4.60±1.33 / 2-6 (5) |
| | 1st month | 2.19±1.05 / 1-4 (2) |
| | difference | 2.42±1.23 / 0-5 (2) |
| | p-value* | <0.001 |
| **ODI** Mean±SD/Min-Max (Median) | 1st week | 39.4±10.7 / 20-60 (40) |
| | 1st month | 18.9±13.6 / 0-60 (20) |
| | Difference | 20.5±12.2 / 0-40 (20) |
| | p-value* | <0.001 |

*Wilcoxon Test. VAS: Visual analog scale, ODI: Oswestry Disability Index*



**Figure 1:** The first-week and first-month average VAS scores in the corsets group were statistically significantly lower than those who did not use corsets (p<0.001, p=0.002, respectively). No statistically significant difference was found in the first-week and first-month VAS changes of the patients who did not use corsets (p=0.059). VAS: Visual analog scale, ODI: Oswestry Disability Index

The first-week and first-month average ODI scores in the corsets group were statistically significantly lower than those who did not use corsets (p=0.012, p<0.001,

respectively). The change in ODI scores from the first week to the first month was statistically significantly higher in patients wearing corsets (p<0.001) (Table 1, Table 2, Figure 2).

**Table 2.** The change in VAS and ODI scores regarding corset use

| | No Corset | | Wearing Corset | | |
|---|---|---|---|---|---|
| | Mean±SD | Min-Max (Median) | Mean±SD | Min-Max (Median) | p-value# |
| **1st week VAS** | 5.17±0.77 | 4-6 (5) | 3.96±1.55 | 2-6 (5) | <0.001 |
| **1st-month VAS** | 2.50±1.08 | 1-4 (2.5) | 1.83±0.89 | 1-4 (2) | 0.002 |
| **VAS difference** | 2.67±1.12 | 1-5 (2.5) | 2.13±1.30 | 0-4 (2) | 0.059 |
| **1st week ODI** | 42.2±10.4 | 30-60 (40) | 36.2±10.1 | 20-50 (40) | 0.012 |
| **1st month ODI** | 27.2±12.0 | 10-60 (30) | 9.4±7.6 | 0-20 (10) | <0.001 |
| **ODI difference** | 15.0±12.7 | 0-40 (10) | 26.8±7.8 | 10-40 (30) | <0.001 |

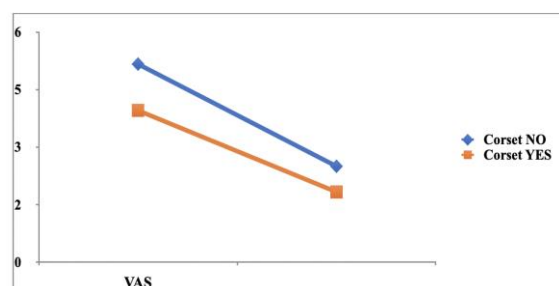*#Mann Whitney U Testi. VAS: Visual Analog Scale, ODI: Oswestry Disability Index*
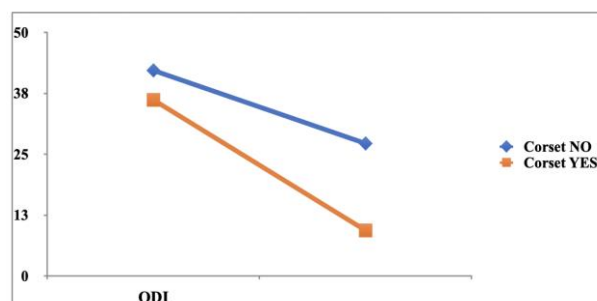


**Figure 2**: The first-week and first-month average ODI scores in the corsets group were statistically significantly lower than those who did not use corsets (p=0.012, p<0.001, respectively). The change of ODI scores from the first week to the first month was statistically significantly higher in patients wearing corsets (p<0.001). VAS: Visual Analog Scale, ODI: Oswestry Disability Index

In patients aged ≤65, the first-week average VAS score of patients wearing corsets was statistically significantly lower (p=0.002). There was no statistically significant difference in the first-week and first-month VAS changes of the patients who did and did not use corsets (p=0.142). The first-week average ODI scores of the patients wearing corsets were statistically significantly lower than those who did not (p=0.020). The change in ODI scores from the first week to the first month was statistically significantly higher in patients wearing corsets (p<0.001) (Table 3).

In patients aged >65 years, the first-week average VAS scores of patients wearing corsets were statistically significantly lower (p=0.048). There was no statistically significant difference in the first-week and first-month VAS changes of the patients who did and did not use corsets (p=0.533). There was no statistically significant difference in the first week's average ODI scores of the patients who did and did not use corsets (p=0.235). The first-week and first-month changes in ODI scores were statistically significantly higher in patients using corsets (p=0.001) (Table 3).

**Table 3.** The change in VAS and ODI scores regarding age

| Age Group | | No Corset Mean±SD | Min-Max (Median) | Wearing Corset Mean±SD | Min-Max (Median) | p-value# |
|---|---|---|---|---|---|---|
| **<65** | 1st week VAS | 5.20±0.79 | 4-6 (5) | 4.00±1.63 | 2-6 (5) | 0.002 |
| | VAS difference | 2.71±1.06 | 1-5 (3) | 2.18±1.36 | 0-4 (2) | 0.142 |
| | 1st week ODI | 42.0±10.6 | 30-60 (40) | 35.6±10.5 | 20-50 (40) | 0.020 |
| | ODI difference | 15.56±13.24 | 0-40 (10) | 26.2±8.2 | 10-40 (30) | <0.001 |
| **>65** | 1st week VAS | 5.00±0.71 | 4-6 (5) | 3.85±1.34 | 2-6 (3) | 0.048 |
| | VAS difference | 2.44±1.42 | 1-5 (2) | 2.00±1.15 | 0-4 (2) | 0.533 |
| | 1st week ODI | 43.3±10.0 | 30-60 (40) | 37.7±9.3 | 20-50 (40) | 0.235 |
| | ODI difference | 12.2±9.7 | 0-30 (10) | 28.5±6.9 | 20-40 (30) | 0.001 |

\* Mann Whitney U Testi. VAS: Visual Analog Scale, ODI: Oswestry Disability Index

In single-level patients, the first-week average VAS scores of those who used corsets were statistically significantly lower than those who did not (p<0.001). The first-week and first-month changes in VAS scores were statistically significantly lower in patients who used corsets (p<0.001). The first week average ODI scores of the patients who used corsets were statistically significantly lower than those who did not (p=0.002). The first-week and first-month changes in ODI scores were statistically significantly higher in patients who used corsets (p=0.006) (Table 4).

There was no statistically significant difference in the first-week average VAS scores of the double-level patients who did and did not use corsets (p=0.752). The first-week and first-month changes in VAS scores were statistically significantly higher in patients using corsets (p=0.012). There was no statistically significant difference in the first-week average ODI scores of the patients who did and did not use corsets (p=0.196). The first-week and first-month changes in ODI scores were statistically significantly higher in patients wearing corsets (p<0.001) (Table 4).

**Table 4.** The change in VAS and ODI scores regarding corset use and type of hernia

| Level | | No Corset Mean±SD | Min-Max (Median) | Wearing Corset Mean±SD | Min-Max (Median) | p-value# |
|---|---|---|---|---|---|---|
| **Single** | 1st week VAS | 5.00±0.83 | 4-6 (5) | 2.77±0.95 | 2-5 (3) | <0.001 |
| | VAS difference | 3.11±0.89 | 2-5 (3) | 1.42±0.99 | 0-3 (2) | <0.001 |
| | 1st week ODI | 37.8±8.0 | 30-50 (40) | 29.6±8.2 | 20-40 (30) | 0.002 |
| | ODI difference | 16.7±12.7 | 0-40 (20) | 25.4±8.6 | 10-40 (30) | 0.006 |
| **Double** | 1st week VAS | 5.33±0.68 | 4-6 (5) | 5.43±0.51 | 5-6 (5) | 0.752 |
| | VAS difference | 2.22±1.15 | 1-5 (2) | 3.00±1.10 | 1-4 (3) | 0.012 |
| | 1st week ODI | 46.7±10.7 | 30-60 (50) | 44.29±5.07 | 40-50 (40) | 0.196 |
| | ODI difference | 13.3±12.7 | 0-30 (10) | 28.6±6.5 | 20-40 (30) | <0.001 |

\* Mann Whitney U Testi. VAS: Visual Analog scale, ODI: Oswestry Disability Index

## 4. DISCUSSION AND CONCLUSION

LDH is a serious disease, as surgical treatment could cause complications and reduce the patient's quality of life. Studies conducted in LDH surgery; demonstrated to improve patients' quality of life [12]. Complications seen after LDH surgery can be elaborated as infection, increased motor deficit, disruption of the mechanical integrity of the vertebral column, spinal cord compression, bleeding, urinary retention, and paralytic ileus. Surgery-originated iatrogenic complications such as nerve root, dura mater, spinal cord, or other adjacent structure injuries may also occur [13]. Among the complications that may develop, the most important one is the recurrence of the disease due to reasons such as the technique applied, herniation level, patient selection unsuitable for surgery, and the patient's failure to act in accordance with post-operative body mechanics [14].

Patients with LDH surgery may also experience problems such as pain-related personal care, inadequacies in physical movements such as walking, standing, and lifting, and changes in their social lives. These deficiencies negatively affect the patient's daily activities and quality of life. In the previous literature, most studies on non-operative treatments in LDHs evaluated methods such as manipulation, epidural injections, nerve root blocks, corset, traction, lumbar school, or non-operative treatments published retrospectively [15].

The resorption process significantly improved clinical parameters by adding muscle relaxants, analgesics, and anti-inflammatory medications. However, there is no correlation between clinical improvement and disc size, and clinical improvement may occur before significant morphological changes are observed in the disc prior to radiological amelioration. This could be explained by the progressive decrease of pressure in the herniated disc and especially by the regression of the inflammation process accompanying the herniation [16].

In LDH, the effect of the treatment program, including physical therapy modalities, rest, drug therapy, and exercise on clinical parameters, starts in the early period. Later on, this treatment program may be effective in the natural course of herniation and can lead to morphological changes with the contribution of the process [17].

There are many studies in which lumbar corsets are used in postoperative care. Several studies have used a corset or waist corset following arthrodesis with

115

instrumentation [18-20]. However, the type, duration, and corset regime varied in these studies. The rationale for using a corset or corset depends on the goals of the treatment. Such goals may include limiting mobility, helping to relieve post-operative pain, improving fusion rates, or improving patient-reported functional outcomes [19]. Numerous authors have reported using corsets or splints following lumbar arthrodesis. In our study, regarding the pain and patient improvement parameters, the first-week and first-month average VAS scores in patients wearing corsets were statistically significantly lower. At the same time, no difference was found between patients who did not use corsets. Additionally, the first-week and first-month average ODI scores in the corsets group were statistically significantly lower than those who did not use corsets. The change in ODI scores from the first week to the first month was statistically significantly higher in patients wearing corsets.

As for the factors against using corsets, the main question is the muscular response to the corset. There are conflicting data in the literature because different reports indicate that the corset can strengthen or weaken the lumbar muscles or has no effect. However, none of these studies were specifically designed to study the effect of the corset in patients undergoing spinal surgery [21]. In previous articles by Yee et al. (2008) and Zoia et al. (2018), no significant benefit of the corset has been shown, contradicting our findings [22, 23]. Takasaki and Miki (2017) conducted a systematic review with a meta-analysis on lumbosacral orthoses and elaborated that no negative effect has been observed in 1 to 6 months. However, they also admitted that the quality of evidence was low, and quality trials were required to draw a definitive conclusion [24]. Our study obtained similar outcomes in the first-week average VAS scores of patients wearing corsets in patients aged >65 and ≤65 with single-level LDH. The first-week and first-month changes in VAS scores were significantly higher in patients using corsets with double-layer LDH.

Last but not least, we also assumed that the patient-reported benefit from corset utilization might be related to behavioral aspects of the study population. Turkish people use corsets, braces and similar traditional equipment in painful situations.

Early adoption of the corset in the postoperative period can help rest and promote the dynamic healing of aching back muscles. In addition, our findings indicated that the use of corsets promoted early recovery from rehabilitation and returns to daily activities.

## REFERENCES

[1] Al Qaraghli MI, De Jesus O. Lumbar Disc Herniation. 2023 Feb 12. In: StatPearls [Internet]. Treasure Island (FL): StatPearls Publishing; 2023 Jan–. PMID: 32809713.

[2] Carnevale JA, Goldberg JL, Schwarz J. Lumbar Herniated Disc. World Neurosurg. 2022;166:52-53. doi:10.1016/j.wneu.2022.07.059

[3] Grooten WJA, Boström C, Dedering Å, Halvorsen M, Kuster RP, Nilsson-Wikmar L, et al. Summarizing the effects of different exercise types in chronic low back pain - a systematic review of systematic reviews. BMC Musculoskelet Disord. 2022;23(1):801. Published 2022 Aug 22. doi:10.1186/s12891-022-05722-x

[4] Roiha M, Marjamaa J, Siironen J, Koskinen S, Koski-Palkén A. Favorable long-term health-related quality of life after surgery for lumbar disc herniation in young adult patients. Acta Neurochir (Wien). 2023;165(3):797-805. doi:10.1007/s00701-023-05522-9

[5] Zhao X, Yang Y, Yue R, Su C. Potential causal association between leisure sedentary behaviors, physical activity and musculoskeletal health: A Mendelian randomization study. PLoS One. 2023;18(3):e0283014. Published 2023 Mar 16. doi:10.1371/journal.pone.0283014

[6] Mörl F, Bradl I. Lumbar posture and muscular activity while sitting during office work. J Electromyogr Kinesiol. 2013;23(2):362-368. doi:10.1016/j.jelekin.2012.10.002

[7] Gibbs D, McGahan BG, Ropper AE, Xu DS. Back Pain: Differential Diagnosis and Management. Neurol Clin. 2023;41(1):61-76. doi:10.1016/j.ncl.2022.07.002

[8] Mescouto K, Olson RE, Hodges PW, Setchell J. A critical review of the biopsychosocial model of low back pain care: time for a new approach?. Disabil Rehabil. 2022;44(13):3270-3284. doi:10.1080/09638288.2020.1851783

[9] Hebelka H, Brisby H, Erkmar A, Lagerstrand K. Loading of the Spine in Low Back Pain Patients Does Not Induce MRI Changes in Modic Lesions: A Prospective Clinical Study. Diagnostics (Basel). 2022;12(8):1815. Published 2022 Jul 28. doi:10.3390/diagnostics12081815

[10] Alizadeh R, Sharifzadeh SR. Pathogenesis, etiology and treatment of failed back surgery syndrome. Neurochirurgie. 2022;68(4):426-431. doi:10.1016/j.neuchi.2021.09.005

[11] O'Keeffe M, Ferreira GE, Harris IA, Darlow B, Buchbinder R, Traeger AC, et al. Effect of diagnostic labelling on management intentions for non-specific low back pain: A randomized scenario-based experiment. Eur J Pain. 2022;26(7):1532-1545. doi:10.1002/ejp.1981

[12] Li WS, Yan Q, Cong L. Comparison of Endoscopic Discectomy Versus Non-Endoscopic Discectomy for Symptomatic Lumbar Disc Herniation: A Systematic Review and Meta-Analysis. Global Spine J. 2022;12(5):1012-1026. doi:10.1177/21925682211020696

[13] Masuda S, Fukasawa T, Takeuchi M, Fujibayashi S, Otsuki B, Murata K, et al. Reoperation Rates of Microendoscopic Discectomy Compared With Conventional Open Lumbar Discectomy: A Large-database Study. Clin Orthop Relat Res. 2023;481(1):145-154. doi:10.1097/CORR.0000000000002322

[14] Lew SM, Mehalic TF, Fagone KL. Transforaminal percutaneous endoscopic discectomy in the

treatment of far-lateral and foraminal lumbar disc herniations. J Neurosurg. 2001;94(2Suppl):216-220. doi: 10.3171/spi.2001.94.2.0216

[15] Jang JS, An SH, Lee SH. Transforaminal percutaneous endoscopic discectomy in the treatment of foraminal and extraforaminal lumbar disc herniations. J Spinal Disord Tech. 2006;19(5):338-343. doi:10.1097/01.bsd.0000204500.14719.2e

[16] Yeung AT, Tsou PM. Posterolateral endoscopic excision for lumbar disc herniation: Surgical technique, outcome, and complications in 307 consecutive cases. Spine (Phila Pa 1976). 2002;27(7):722-731. doi:10.1097/00007632-200204010-00009

[17] Imoto R, Umakoshi M, Yunoki M, Tatano M, Hirashita K, Yoshino K, et al. Surgical Outcomes of Full-Endoscopic Lumbar Discectomy in the Early Adoption Phase. Asian J Neurosurg. 2022;17(3):474-479. Published 2022 Sep 1. doi:10.1055/s-0042-1751012

[18] Holmström E, Moritz U. Effects of lumbar belts on trunk muscle strength and endurance: a follow-up study of construction workers. J Spinal Disord. 1992;5(3):260-266. doi:10.1097/00002517-199209000-00003

[19] Butler AJ, Munakomi S, Donnally III CJ. Discectomy. In: StatPearls. Treasure Island (FL): StatPearls Publishing; August 13, 2023.

[20] Kawaguchi Y, Gejo R, Kanamori M, Kimura T. Quantitative analysis of the effect of lumbar orthosis on trunk muscle strength and muscle activity in normal subjects. J Orthop Sci. 2002;7(4):483-489. doi:10.1007/s007760200084

[21] Fercho J, Krakowiak M, Yuser R, Szmuda T, Zieliński P, Szarek D, et al. Evaluation of Movement Restriction of Spinal Orthoses Using Inertial Measurement Units. Int J Environ Res Public Health. 2022;19(24):16515. Published 2022 Dec 8. doi:10.3390/ijerph192416515

[22] Yee AJ, Yoo JU, Marsolais EB, Carlson G, Poe-Kochert C, Bohlman HH, et al. Use of a postoperative lumbar corset after lumbar spinal arthrodesis for degenerative conditions of the spine. A prospective randomized trial. J Bone Joint Surg Am. 2008;90(10):2062-2068. doi:10.2106/JBJS.G.01093

[23] Zoia C, Bongetta D, Alicino C, Chimenti M, Pugliese R, Gaetani P. Usefulness of corset adoption after single-level lumbar discectomy: a randomized controlled trial. J Neurosurg Spine. 2018;28(5):481-485. doi:10.3171/2017.8.SPINE17370

[24] Takasaki H, Miki T. The impact of continuous use of lumbosacral orthoses on trunk motor performance: a systematic review with meta-analysis. Spine J. 2017;17(6):889-900. doi:10.1016/j.spinee.2017.03.003

## Türk Doğa ve Fen Dergisi
## Turkish Journal of Nature and Science

BİNGÖL ÜNİVERSİTESİ

# The Effect of Alumina Additive on the Properties of Sheep Hydroxyapatite

**Süleyman Serdar PAZARLIOĞLU[1*]** iD

[1] Marmara University, Technology Faculty, Metallurgy and Materials Science and Engineering Department, İstanbul, Türkiye

Süleyman Serdar PAZARLIOĞLU ORCID No: 0000-0002-7870-8418

*Corresponding author: spazarlioglu@marmara.edu.tr*

**Abstract:** In this study, the effect of alumina ($Al_2O_3$) addition, varying between 1-10% by weight, on the properties of hydroxyapatite obtained from sheep femur bones (SHA) was investigated. SHA decomposed at all sintering temperatures and the total decomposition rate increased from 1.4% to 4.1% with increasing temperature. The decomposition rate of SHAs with $Al_2O_3$ added increased to 60.1% with increasing $Al_2O_3$ and sintering temperature. Density (from $2.16\pm0.03$ to $2.98\pm0.02$ g/cm$^3$) and hardness (from $0.93\pm0.15$ GPa to $3.90\pm0.27$ GPa) of SHA increased with increasing temperatures, however; the highest compression strength ($82\pm5.05$ MPa) and fracture toughness ($0.70\pm0.11$ MPam$^{1/2}$) were obtained at a temperature of 1200ºC. Additions at amount of 1% and 2.5% $Al_2O_3$ to SHA contributed to obtaining better properties than 5% and 10%, however; the optimum $Al_2O_3$ ratio is 2.5% and the sintering temperature is 1200ºC. With the addition of $Al_2O_3$ at amount of 2.5%, the fracture toughness value of SHA increased from $0.70\pm0.11$ MPam$^{1/2}$ to $1.70\pm0.15$ MPam$^{1/2}$, and the compression strength increased from $82\pm5.05$ MPa to $207.85\pm5.85$ MPa. The brittleness index of SHA increased from $1.70\pm0.27$ to $7.10\pm0.50$ $\mu^{-1/2}$ with increasing temperature. It increased to $3.56\pm0.18$ $\mu^{-1/2}$ as the maximum value by the addition of $Al_2O_3$ to SHA. At the end of the 28-day immersion period, it was determined that, most of the SHA surface and the entire surface of the SHA-$2.5Al_2O_3$ composite were covered with apatite layer.

# Alumina İlavesinin Koyun Hidroksiapatitin Özelliklerine Etkisi

**Anahtar Kelimeler**
Koyun hidroksiapatit, Alumina, Sinterleme, Özellik

**Öz:** Bu çalışmada ağırlıkça %1-10 arasında değişmekte olan alumina ($Al_2O_3$) ilavesinin koyun femur kemiklerinden elde edilmiş olan hidroksiapatitin (SHA) özelliklerine etkisi incelenmiştir. SHA tüm sinterleme sıcaklıklarında dekompoze olmuş ve toplam dekompoze olma oranı artan sıcaklıkla %1.4' ten %4.1' e çıkmıştır. $Al_2O_3$ ilaveli SHA' lerde dekompoze olma oranı ise artan $Al_2O_3$ ve sinterleme sıcaklığı ile %60.1' e artmıştır. SHA' nın yoğunluğu (2,16±0,03' ten 2,98±0,02 g/cm³' e) ve sertliği (0,93±0,15 GPa' dan 3,90±0,27 GPa' ya) artan sıcaklık arttıkça artmış, ancak; en yüksek basma dayanımı (82±5,05 MPa) ve kırılma tokluğu (0,70±0,11 MPam$^{1/2}$) 1200ºC sıcaklıkta elde edilmiştir. SHA' ya %1 ve %2.5 oranında $Al_2O_3$ ilavesi, %5 ve %10' dan daha iyi özelliklerin elde edilmesine katkı sağladı; optimum $Al_2O_3$ oranı %2.5 ve sinterleme sıcaklığı 1200ºC' dır. %2.5 oranında $Al_2O_3$ ilavesi ile SHA' nın kırılma tokluğu değeri 0,70±0,11 MPam$^{1/2}$' den 1,70±0,15 MPam$^{1/2}$' ye, basma dayanımı 82.48±5.05 MPa' dan 207.85±5.85 MPa' ya yükselmiştir. SHA' nın kırılganlık indeksi artan sıcaklıkla 1.70±0.27'den 7.10±0.50 $\mu^{-1/2}$'ye yükseldi. SHA' ya $Al_2O_3$ ilavesiyle maksimum değer olarak 3,56±0,18 $\mu^{-1/2}$' ye yükseldi. 28 günlük daldırma süresi sonunda SHA yüzeyinin büyük bir kısmının, SHA-$2.5Al_2O_3$ kompozitinin yüzeyinin ise tamamının apatit tabakası ile kaplandığı belirlendi.

## 1. INTRODUCTION

Waste mineralized tissues (WMT) create an undesirable environmental impact [1]. The most effective method for

minimize the environmental impact of WMT is to transform their into useful and valuable substances through ecofriendly processes [2]. WMT, such as bone, teeth, antler and horn, are important elemental storage

sites in animals. These tissues contain necessary elements, both major, such as calcium (Ca), phosphorus (P), magnesium (Mg) and sulphur (S), and trace elements, such as iron (Fe), zinc (Zn), manganese (Mn) and cadmium (Cd). [3]. These ingredients serve as catalytic, structural, and electrochemical components in numerous applications. Furthermore, bones are utilized in food and biomedical sector due to their rich component. Waste bone derived hydroxyapatite (HA) has further usage in drug delivery agents, adsorbents, chemical sensors, bio-ceramics, chromatographic lighting materials, and powder carriers [4]. Waste bone of animals such as chicken [5], turkey [6], bovine [7], goat [8], and pork [9] can be used in the production of HA. Sheep bones are also suitable for medical research [10], because they have similar macrostructure to human bone [11]. Sheep bones can be also used as HA production resource [12]. HA is one of the non-toxic bioceramics that has biocompatibility and similarity in composition with human bones. Besides having advantages, HA has poor mechanical properties such as low values of hardness and fracture toughness and is brittle [13]. It has been stated by Demirkol, N., et al.[14] that SHA has the sintered density of 2.59 $g/cm^3$, the hardness of 189 HV and the compression strength of 69 MPa. These values restrict the use of SHA in the human body. The weak characteristic properties of SHA could be improved when it was reinforced with a material, which has higher mechanical reability than that of SHA [15]. Many studies have demonstrated that the addition of ceramics to SHA tends to enhance its mechanical performance and/or its biological properties [16]. For this purpose some ceramics such as niobium oxide [17], magnesium oxide [18], perlite [19] and bioactive glass [20] were used as reinforcement agent.

Alumina ($Al_2O_3$) is an advanced ceramics industry because of three key advantages: (i) it has an industrially high usable combination of mechanical, tribological, dielectric properties and chemical inertness; (ii) It is an inexpensive and easily available material [21]. Moreover, it has excellent properties, such as low thermal expansion coefficient, high chemical stability, and good high-temperature performance [22]. It has been declared that $Al_2O_3$ additive contributes the improvement of properties of dental [23] and femoral head of hip joint replacement materials [24]. Although $Al_2O_3$ has been used as a reinforcement agent for synthetic [25-27] and/or biologically derived HAs [28,29], its effect on SHA has not been investigated.

In the present study, the effect of alumina additive on the sinterability and properties of sheep derived hydroxyapatite was investigated using microstructural characterization techniques and mechanical testings.

## 2. MATERIAL AND METHOD

In the present study, hydroxyapatite was derived from sheep femur bones as shown in Figure 1. Sheep femur bones purchased from Migros (Kadıköy, Istanbul) were firstly cleaned to remove visible substances and then head parts of the bones were cut off and marrow in shafts removed via boiling within water in a pressure cooker for

4 h. After the boiling process, the retained shafts were deproteinized with sodium hidroxide (NaOH) for 1 h, washed with distilled water and then dried at 105ºC for 4h. before calcination treatment. Finally bones were calcinated at 800ºC for 2 h and then obtaining of HA was checked by XRD analysis. It is in good agreement with the ICDD Card No: 98-009-0247 for HA. The calcinated samples were firstly ground and then crushed in a mortar to between -63 µm to +45 µm to prepare the composites as shown in Figure 2.



**Figure 1.** Schematic presentation of the production of SHA powder

Figure 2 shows the processing steps of production of SHA with and without $Al_2O_3$ additives. Four different composites were prepared by adding $Al_2O_3$ to SHA, at amount of 1wt%, 2.5wt%, 5wt% and 10wt% , respectively. The prepared mixtures were homogenized with zirconia balls and ethyl alcohol at 180 rpm for 2 hours, with a powder/ball ratio of 1/7. SHA and composite powders were pelleted in accordance with British standard 7253 [30] using zinc stearate, and then dried at 105ºC. The green bodies were heated up to 300ºC to remove zinc stearate and sintered at the temperatures of 1100, 1150, 1200, 1250 and 1300ºC for 4 h.
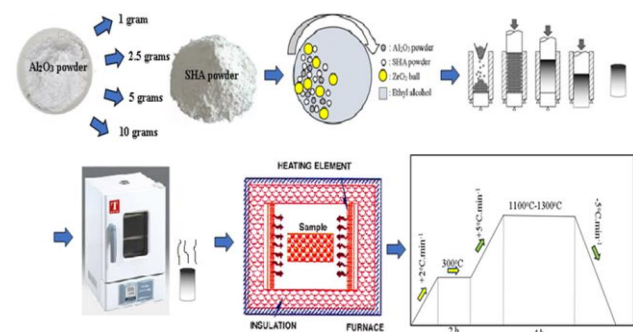


**Figure 2** Processing steps of production of SHA with and without $Al_2O_3$ additive

Density, porosity and relative densities of the sintered samples were measured using a Precisa XB 320 M precision balance according to the Archimedes principle. The theoretical density of SHA was taken as 3.156 g.cm$^{-3}$ [31] and the theoretical density of $Al_2O_3$ was taken as 3.970 g.cm-3 [32] to calculate the relative density of samples. Hardness of the samples were determined in the Future Tech FM301 device by using the Vickers (HV$_{0.2}$) method because it provided the formation of hardness indent without cracking. The sintered samples were ground with SiC papers (between 800 and 5000 mesh) and then polished with diamond paste up to 0.5 µ to obtain

mirror-like surfaces. Fracture toughness measurements were performed under a load of 2,943 N with a dwell time of 10 s and calculated according to Equation 1 [33].

$$K_{1c} = 0.203(c/a)^{-1.5}(H_V)(a)^{0.5} \qquad (E1)$$

Here; $K_{IC}$ is the fracture toughness (MPa.m$^{1/2}$), $c$ is the radial crack dimension measured from the center of the indent impression (m), $H_V$ is the hardness (MPa), and a is the half diagonal of the indentation (m). The brittleness index of the sintered samples was calculated by Equation 2 [34].

$$BI = (HV/K_{1c}) \qquad (E2)$$

Here; $B$ is brittleness index, $HV$ is the hardness, and $K_{1c}$ is the fracture toughness.

Compression strength of the sintered samples was calculated by Devotrans FU 50kN testing device under a loading rate of 2 mm.min$^{-1}$. The surface morphology and grain size measurements of the samples were performed using the FEI Sirion XL30 scanning electron microscope (SEM). The phases in the SHAs with and without $Al_2O_3$ additive were analyzed using a Philips X'Pert X-ray diffraction (XRD, Netherlands) device in the range of 2θ values between 20° and 50°. Rietvield analysis was performed to calculate the phase ratios in the samples.

## 3. RESULTS & DISCUSSION

Figure 3 shows the XRD analysis of the pure SHA depending on the sintering temperature. It is seen that β, α-TCP and CaO phases are formed when pure SHA is sintered at 1300ºC. The same regime had also confirmed in a previous study [35]. Thermal stability of biologically derived HAs depends on a number of factors, such as Ca/P ratio of HA [36], calcination temperature and time [37] and sintering atmosphere [38], cause its decomposition [39]. Thermal stability of synthetic HA is around 1100-1150ºC; above this temperature, it is possible to see phase transformations [40]. Bovine HA has been reported to decompose into β-TCP at approximately 1100°C [41]. The termal decomposition of HA is attributed to the vacancies formed by release of structural water [42], and it can be explained as shown in Reaction 1 [38] when sintering is performed at 1300ºC.
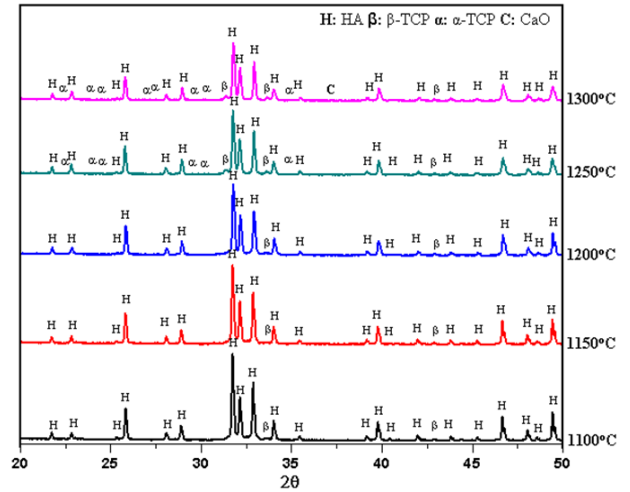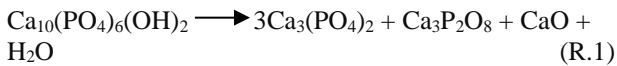
$$Ca_{10}(PO_4)_6(OH)_2 \longrightarrow 3Ca_3(PO_4)_2 + Ca_3P_2O_8 + CaO + H_2O \qquad (R.1)$$



**Figure 3.** XRD analysis of the pure SHA depending on the sintering temperature.

A study mentioned that HA at the sintering treatment of 1200°C has occurred with β-TCP [43]. Breaking of the bond between the calcium ion and the hydroxyl ion leads to removal of the hydroxyl ion from the crystal, and HA eventually decompose to generate β-TCP [44]. The formation of OH$^-$ vacancies accelerates the cation transport in the HA lattice and it increase the decomposition ratio of HA matrix material [45]. As shown in Table 1, the decomposition ratio of 1.4% of SHA at 1100ºC increased with ascent of sintering temperature and it was calculated as 4.1% at the sintering temperature of 1300ºC. It was declared by Lim, et al. [46] that the decomposition ratio of HA had 56% at the same temperature. However, a material produced to the human body applications should have a decomposition ratio lower than that of 10% according to ISO 13779-3:2018 standart [47]. There are several reasons for such a restriction: β-TCP existing in HA with low content helps for the rapid bonding of artificial bones to natural ones via rapid dissolution. Biphasic HA/β-TCP structures are being considered for filling periodontal osseous defects. The presence of a more bioactive phase (β-TCP) in the biphasic composite promotes a much faster osseointegration without complete implant resorption [48]. Too high content of β-TCP seriously deteriorates the mechanical properties and chemical stability of artificial bones. Thus, the precise control of β-TCP content in HAp is a critical issue in biomedical applications [49]. More than 10% of α-TCP in the HA matrix causes an increase in the number of nanopores, which severely reduces the strength of the sintered samples [50]. Moreover, the formation of a very high amount of highly soluble phase in HA ceramics, i.e. α-TCP, reduces the formation of an apatite-like layer in HA ceramics [51]. The presence of CaO in HA-based implants designed for medical applications is unacceptable for the following reasons. In contact with water molecules CaO converts into calcium hydroxide. That results in gradual tension and hair cracks in the ceramic material, its swelling and breaking and even some disintegration into individual particles and also generates strong alcalinity in the implant environment. The problem of the presence of CaO in the HA of animal origin is significant in respect of its applications as biomaterial [52].

**Table 1** Rietvield analysis of pure SHA depending on the sintering temperatures

| Temperature (°C) | Chemical composition (%) | | | | Total decomposition ratio (%) |
|---|---|---|---|---|---|
| | HA | β-TCP | α-TCP | CaO | |
| 1100 | 98.6 | 1.4 | - | - | 1.4 |
| 1150 | 98.0 | 2.0 | - | - | 2.0 |
| 1200 | 97.8 | 2.2 | - | - | 2.2 |
| 1250 | 97.4 | 1.0 | 1.6 | - | 2.6 |
| 1300 | 95.9 | 1.3 | 2.6 | 0.2 | 4.1 |

XRD patterns of Al$_2$O$_3$ added SHAs are presented in Figure 4. For the SHA/1Al$_2$O$_3$ composite, HA decomposed to β-TCP at 1100°C; and at 1200°C HA started to decompose the mixture of β- and α-TCP. After sintering at 1300°C, 5.0% of the HA tranformed into β-TCP and 3.0% of the HA tranformed into α-TCP in this composite as shown in Table 2. In the composites of SHA/2.5Al$_2$O$_3$ and SHA/5Al$_2$O$_3$, HA transformed to β-TCP. A transformation at about 8.1% for SHA/2.5Al$_2$O$_3$, and 17.6% for SHA/5Al$_2$O$_3$ after sintering at 1300°C was calculated. However; in the SHA/10Al$_2$O$_3$ composite, 19.2% of HA transformed into β-TCP and 1.0% of HA to α-TCP, after sintering was carried out at 1100°C. When it was sintered at 1300°C, the transformation rate of HA into β-TCP and α-TCP increased to 43.4% and 16.7%, respectively. In addition to β- and/ α-TCP, calcium aluminates (CaAl$_2$O$_4$ and Ca$_4$Al$_6$O$_{13}$) were detected in the SHA/Al$_2$O$_3$ composites. No CaO peak was observed in the SHA/Al$_2$O$_3$ composites. CaO in free form has observed in HA/ZrO$_2$ [53] and HA/TiO$_2$ [54] composites.
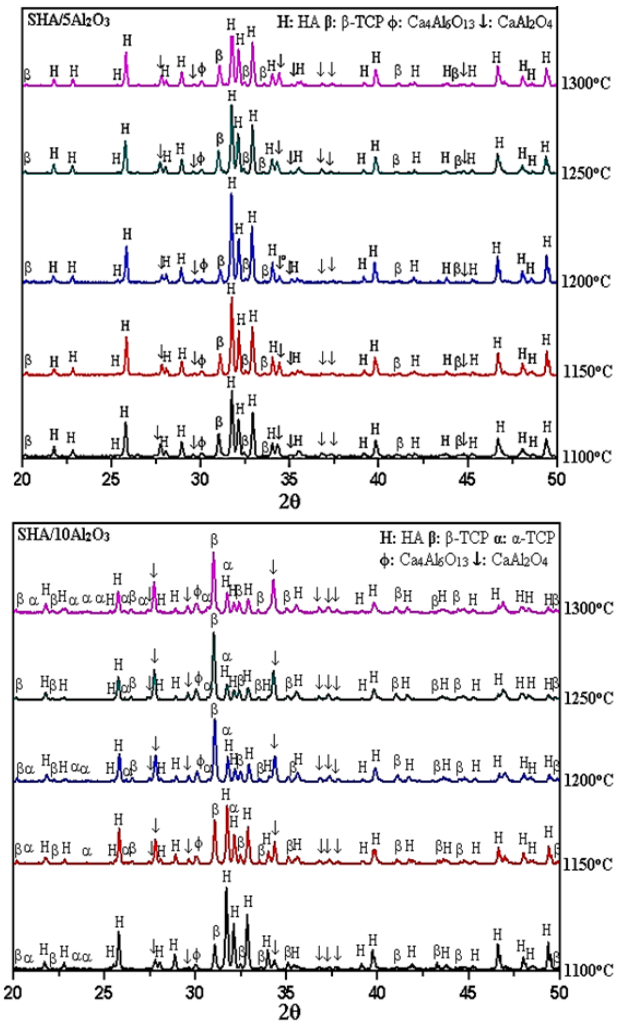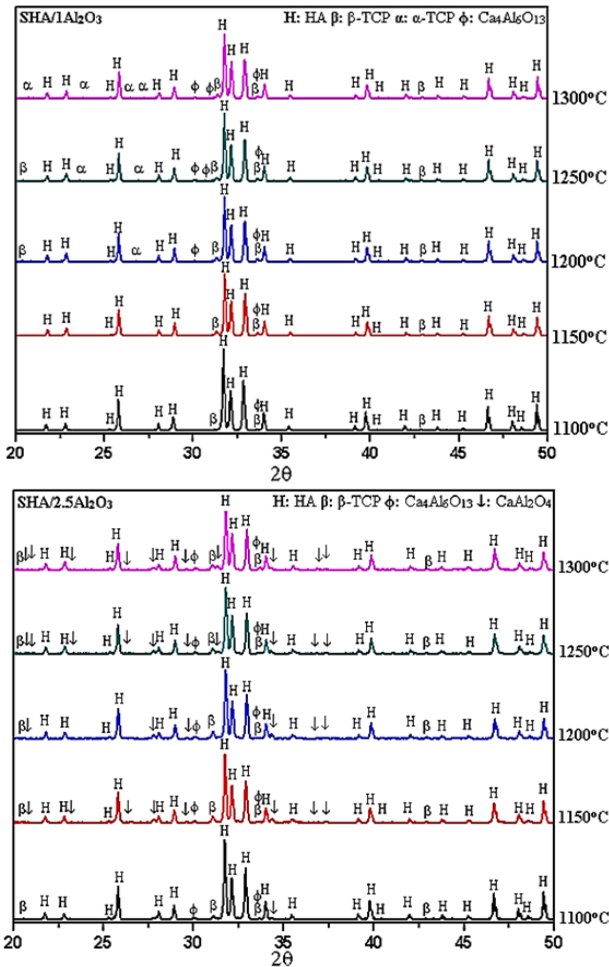




**Figure 4.** XRD patterns of Al$_2$O$_3$ added SHAs

**Table 2.** Rietvield analysis of SHA-Al$_2$O$_3$ composites depending on the sintering temperatures

| Temperature (°C) | Composite | Chemical composition (%) | | | | | Total decomposition ratio (%) |
|---|---|---|---|---|---|---|---|
| | | HA | β-TCP | α-TCP | Ca$_4$Al$_6$O$_{13}$ | CaAl$_2$O$_4$ | |
| 1100 | | 94.1 | 2.8 | - | 3.1 | - | 2.8 |
| 1150 | | 92.9 | 3.2 | - | 3.9 | - | 3.2 |
| 1200 | SHA-1Al$_2$O$_3$ | 90.5 | 3.7 | 1.7 | 4.1 | - | 5.4 |
| 1250 | | 88.7 | 4.1 | 2.4 | 4.8 | - | 6.5 |
| 1300 | | 87.0 | 5.0 | 3.0 | 5.0 | - | 8.0 |
| 1100 | | 92.9 | 3.1 | - | 3.8 | 0.2 | 3.1 |
| 1150 | | 91.1 | 4.5 | - | 4.0 | 0.4 | 4.5 |
| 1200 | SHA-2.5Al$_2$O$_3$ | 90.3 | 5.0 | - | 4.2 | 0.5 | 5.0 |
| 1250 | | 87.0 | 6.6 | - | 5.0 | 1.4 | 6.6 |
| 1300 | | 84.8 | 8.1 | - | 5.4 | 1.7 | 8.1 |
| 1100 | | 90.4 | 4.8 | - | 3.2 | 1.6 | 4.8 |
| 1150 | | 89.4 | 5.2 | - | 3.5 | 1.9 | 5.2 |
| 1200 | SHA-5Al$_2$O$_3$ | 85.6 | 7.5 | - | 4.9 | 4.0 | 7.5 |
| 1250 | | 79.1 | 13.7 | - | 4.2 | 5.0 | 13.7 |
| 1300 | | 74.5 | 17.6 | - | 3.8 | 8.9 | 17.6 |
| 1100 | | 71.6 | 19.2 | 1.0 | 1.2 | 7.0 | 20.2 |
| 1150 | | 62.5 | 25.8 | 2.9 | 1.4 | 7.4 | 28.7 |
| 1200 | SHA-10Al$_2$O$_3$ | 55.9 | 30.4 | 4.2 | 1.5 | 8.0 | 34.6 |
| 1250 | | 43.8 | 37.6 | 8.5 | 1.6 | 8.5 | 46.1 |
| 1300 | | 25.6 | 43.4 | 16.7 | 2.0 | 12.3 | 60.1 |

Figure 5 (a-c) shows the density, porosity and relative density of SHA and SHA/Al$_2$O$_3$ composites depending on the sintering temperatures, respectively. The density of pure SHA calculated as 2.16±0.03 g/cm$^3$ at 1100°C increased with increasing temperature and reached

$2.98\pm0.02$ g/cm$^3$ at 1300ºC. However, the highest densities in Al$_2$O$_3$ added SHAs could be obtained at different temperatures depending on the amount of Al$_2$O$_3$ additives. The highest density in composites was calculated as $2.95\pm0.00$ g/cm$^3$, and it belongs to SHA-1Al$_2$O$_3$. In general, a decrease in the densities of the composites was determined with the increase of the Al$_2$O$_3$ ratio. Similar behavior had also confirmed in Al$_2$O$_3$ added bovine HA [55] and synthetic HA [56]. The relative density of SHA at 1100ºC calculated as $68.58\pm0.74\%$ increased to $94.48\pm0.64\%$ when sintering temperature is 1300ºC. A maximum relative density value of $94.29\pm0.12\%$ could be achieved in Al$_2$O$_3$ added SHAs and it belongs to SHA-2.5Al$_2$O$_3$ composite sintered at 1200ºC. However, the relative density of this composite decreased to $90.96\pm0.54\%$ with increasing temperature. A similar situation has been observed in SHA-5Al$_2$O$_3$ composites, and its relative density decreased from $\%89.49\pm1.10$ to $\%82.61\pm1.71$ with the temperature increasing from 1200ºC to 1300ºC. The highest relative densities for SHA-1Al$_2$O$_3$ and SHA-10Al$_2$O$_3$ composites could be obtained at 1250ºC, and they were calculated as $93.65\pm0.14\%$ and $82.08\pm0.96\%$, respectively. As can be seen from these values, the density and partial density of Al$_2$O$_3$ added SHAs are affected by several factors. First, the increased Al$_2$O$_3$ ratio caused the decomposition rate of HA to increase from 2.8% to 60.1%, as seen in Table 2. The increase in the decomposition ratio resulted in the formation of β-TCP (3.07 g/cm$^3$ [57]), and α-TCP (2.866 g/cm3 [58]) phases, which have lower theoretical density values than that of HA (3.156 g/cm$^3$). Secondly, increasing Al$_2$O$_3$ ratio increases the formation of CaAl$_2$O$_4$ phase, which is one of the two detected calcium aluminate phases in SHA-Al$_2$O$_3$ composites. Because CaAl$_2$O$_4$ (2.98 g/cm$^3$ [59]) has a lower theoretical density than HA, just like β-TCP and α-TCP phases, the densification behavior of the composites has decreased. Moreover, it has an increasing effect on the decomposition of HA in HA-Al$_2$O$_3$ binary composites as seen in Reaction 2 [60].

$$Ca_{10}(PO_4)_6(OH)_2 + Al_2O_3 \longrightarrow 3Ca_3(PO_4)_2 + CaAl_2O_4 + H_2O \qquad (R.2)$$
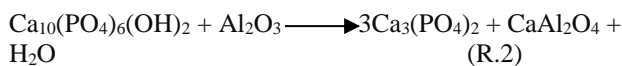
SHA-1Al$_2$O$_3$ and SHA-2.5Al$_2$O$_3$ composites have higher densification behavior than SHA-5Al$_2$O$_3$ and SHA-10Al$_2$O$_3$ composites because these composites contain higher amount of Ca$_4$Al$_6$O$_{13}$ as shown in Table 2. Ca$_4$Al$_6$O$_{13}$ has a higher theoretical density (3.548 g/cm$^3$ [61]) than CaAl$_2$O$_4$. The increase in CaAl$_2$O$_4$ ratio increases the release of OH$^-$ ions and causes a more porous structure [62]. Therefore, SHA-5Al$_2$O$_3$ and SHA-10Al$_2$O$_3$ composites are more porous than SHA-1Al$_2$O$_3$ and SHA-2.5Al$_2$O$_3$. The lowest porosity in SHA-5Al$_2$O$_3$ and SHA-10Al$_2$O$_3$ composites were calculated as $7.20\pm0.37\%$, and $11.15\pm1.19\%$, respectively. It was calculated as $2.45\pm0.60\%$ for SHA-1Al$_2$O$_3$, and $2.53\pm0.42\%$ for SHA-2.5Al$_2$O$_3$ composites.
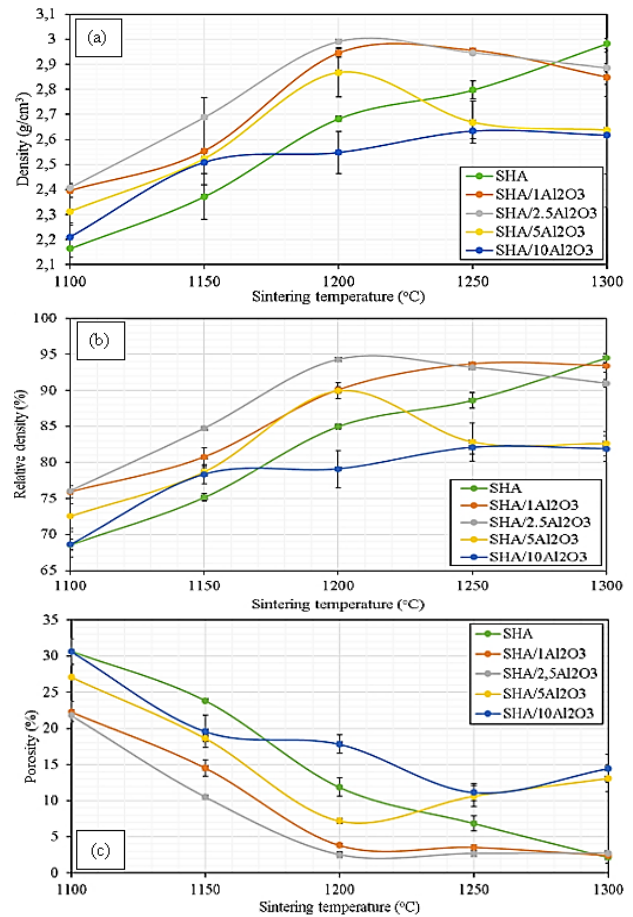


**Figure 5. (a)** Density, **(b)** porosity, and **(c)** relative density of SHA and SHA/Al$_2$O$_3$ composites depending on the sintering temperatures

Figure 6 shows the compression strength of SHA and SHA-Al$_2$O$_3$ composites. The compression strength of SHA calculated as $35.14\pm2.51$ MPa at 1100ºC increased to $82.48\pm5.50$ MPa at 1200ºC, but decreased to $73.55\pm4.04$ and $64.27\pm3.05$ MPa when sintering was carried out 1250 and 1300ºC. There are two reasons why the compression strength of SHA decreases at temperatures above 1200ºC: First is the decomposition of SHA into α-TCP and CaO phases, which have lower compression strength than β-TCP, as shown in **Table 3**. Second is the average grain size of 1.404 at 1200ºC showed a great deal with increasing temperature, and reached to $3.632\pm0.716$ μ, as shown in Figure 7.



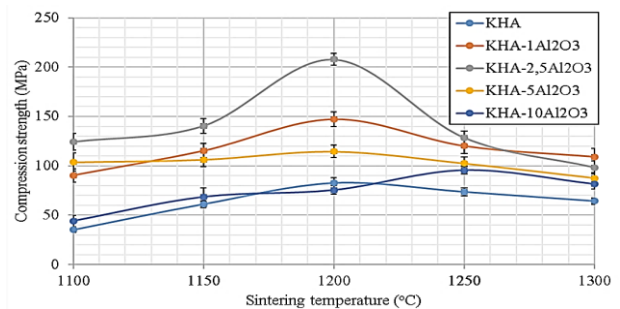**Figure 6.** Compression strength of SHA and SHA-Al$_2$O$_3$ composites.

**Table 3.** The mechanical properties of β-TCP, α-TCP and CaO

| Property | β-TCP | α-TCP | CaO |
|---|---|---|---|
| Compression strength (MPa) | 436 [63] | 42 [64] | 38.6 [65] |

In line with previously reported study, it has been observed that with increase in grain size such as from 1.3 μ to 3.5 μ [66], compression strength of HA decrease.
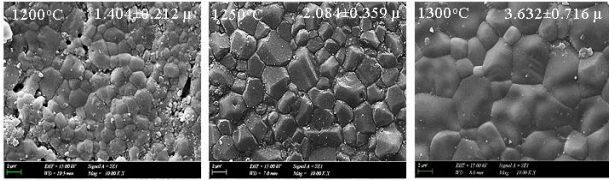


**Figure 7.** SEM images of SHA sintered at 1200ºC, 1250ºC and 1300ºC.

Figure 8 shows the SEM images of SHA-1Al$_2$O$_3$ and SHA-2.5Al$_2$O$_3$ composites sintered between 1200 and 1300ºC. It was determined that with the addition of 2.5% Al$_2$O$_3$ to SHA, the grain growth in SHA could be prevented at a higher rate than %1Al$_2$O$_3$. This can be attributed to the Ca$_4$Al$_6$O$_{13}$. As seen in Reaction 3, the Ca$_4$Al$_6$O$_{13}$ phase occurs in HA-Al$_2$O$_3$ composites from 900ºC to 1300ºC [59] and it has an inhibitory effect on grain growth.

$$4CaO + 3Al_2O_3 \longrightarrow Ca_4Al_6O_{13} \qquad (R.3)$$
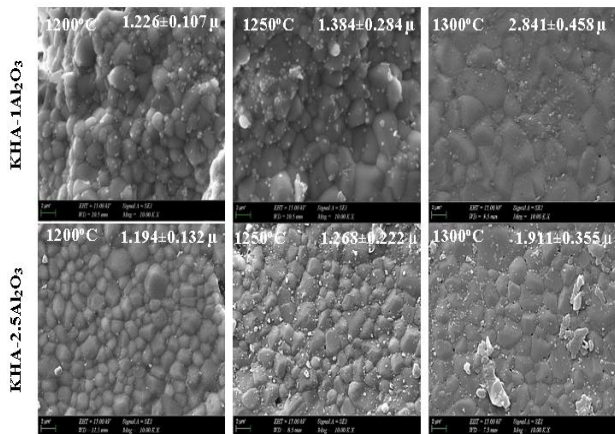


**Figure 8.** SEM images of SHA-1Al$_2$O$_3$ and SHA-2.5Al$_2$O$_3$ composites

For HA compacts mechanical properties are enhanced with decrease in grain size in sintered microstructure. With decrease in grain size, the inherent flaw size in sintered microstructure is reduced which leads to the enhancement of compressive strength. Again as the number of grain boundaries per unit volume is increased with decrease in grain size, finer grain sized compacts offer more resistance to crack propagation and dislocation motion resulting in higher hardness and fracture toughness [67]. The highest compression strength of SHA of 82.48±5.50 MPa could be increased to 147.29±7.50 MPa, 207.85±5.85 MPa, 114.50±6.16 MPa and 95.45±3.53 MPa by increase in Al$_2$O$_3$ ratio in the present study. The highest compression strength belongs to SHA-2.5Al$_2$O$_3$ composite and it is about 2.5 times higher than Bovine HA-Al$_2$O$_3$ composite [55]. Figure 9 a-c show the hardness, fracture tougness and brittleness index of SHA with and without Al$_2$O$_3$ additives. The hardness of SHA at 1100ºC calculated as 0.93±0.15 GPa increased to the highest value of 3.90±0.27 GPa when sintering was performed at 1300ºC. However, the highest fracture toughness for SHA was obtained by sintering at 1200ºC and it was calculated as 0.70±0.11 MPam$^{1/2}$. The highest

fracture toughness values were obtained at 1200ºC in Al$_2$O$_3$ added SHAs and they were calculated as 1.32±0.06, 1.70±0.15, 1.41±0.27 and 1.11±0.24 MPam$^{1/2}$ depending on the increasing Al$_2$O$_3$ ratio. As can be seen from these values, an increase in the fracture toughness of SHA between 1.5 and 2.5 times was achieved with the addition of Al$_2$O$_3$. There are several reasons for this: First is the Al$_2$O$_3$ (3.72 MPam$^{1/2}$ [68]) used as reinforcement material has higher fracture toughness than HA. Second, the calcium aluminate phases formed between HA and Al$_2$O$_3$ particles limit the propagation of post-indentation cracks [69]. Third is because the ratio of β-TCP in the composites is higher than that of pure SHA, the fracture toughness of β-TCP (1.28 MPam$^{1/2}$ [70]) is approximately 80% higher than HA, contributing to the increase in fracture toughness. The brittleness index of SHA without Al$_2$O$_3$ increased from 1.70±0.27 to 7.10±0.50 μ$^{-1/2}$ with increasing temperature. The brittleness index of SHA at 1200ºC, where the highest fracture toughness and compressive strength is obtained, is 4.26±0.50 μ$^{-1/2}$, and it is compatible with 4.85 found by Shaly et al. [71].
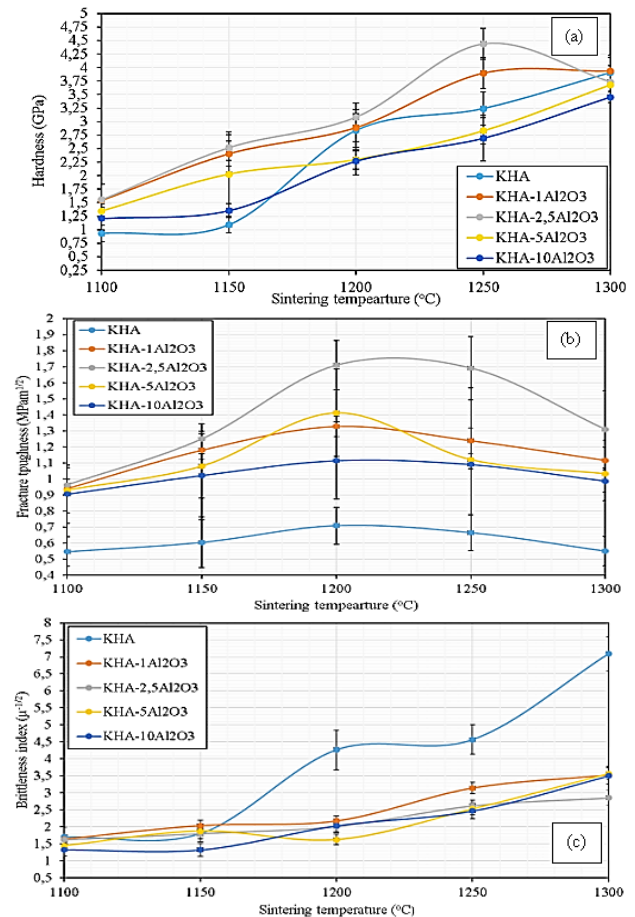


**Figure 9.** (a) Hardness, (b) fracture toughness, and (c) brittleness index of SHA with and without Al$_2$O$_3$ additives

The brittleness index of SHA-Al$_2$O$_3$ composites increased with increasing temperature, just as in pure SHA. However, it increased to 3.56±0.18 μ$^{-1/2}$ as the maximum value. As can be seen from this value, the maximum brittleness index of SHA was reduced by about 1/2. It is also compatible with MgO added synthetic HA calculated as 3.72 μ$^{-1/2}$ [72].

Figure 10 shows the SEM and EDS analysis of pure SHA and SHA-2.5Al$_2$O$_3$ composite subjected to SBF testing during immersion periods of 14 and 28 days, respectively. At the end of the 14 days immersion, the apatite layer with a Ca/P ratio of 1.77 was crystallized on the SHA surface. After 28 days, the Ca/P ratio decreased to 1.76 and most of the SHA surface was covered with apatite layer. However, the surface of SHA-2.5Al$_2$O$_3$ composite was mostly covered with apatite layer in both 14 and 28-day immersion times. While the Ca/P ratio of the apatite layer formed on the surface of the SHA-2.5Al$_2$O$_3$ composite after 14 days was 1.87, it was calculated as 1.69 at the end of 28 days. It has a Ca/P ratio closer to the ideal value of 1.67 [73]. It has been concluded that there may be several reasons why SHA with 2.5% Al$_2$O$_3$ addition exhibits better bioactivity than pure SHA. As stated by Sainz et al., average grain size and phases contained in the samples subjected to the SBF test affect the precipitation of apatite layers [74]. The smaller the average grain size, the higher the apatite layer precipitation on the surface of the samples subjected to the SBF testing [75]. The average grain sizes of SHA and SHA-2.5Al$_2$O$_3$ subjected to the SBF test in this study are 1.404±0.212 μ and 1.194±0.132 μ. As mentioned earlier, there are two phases that contribute to the formation of a lower grain size in the SHA-Al$_2$O$_3$ composite than in SHA: Ca$_4$Al$_6$O$_{13}$. As noted by García-Álvarez et al. [76] that CaAl$_2$O$_4$ exhibits a triggering effect on the apatite precipitation from the SBF solution.
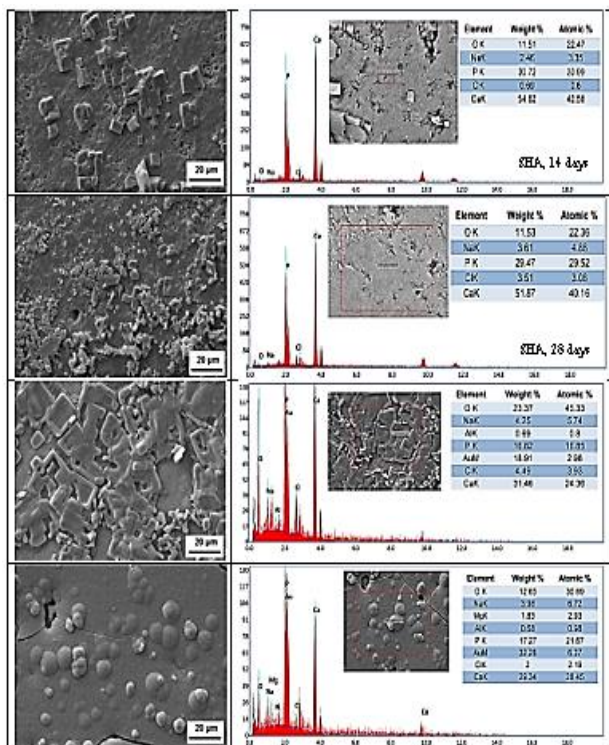


**Figure 10.** SEM and EDS analysis of pure SHA and SHA-2.5Al$_2$O$_3$ composite subjected to SBF testing during immersion periods of 14 and 28 days

## 4. CONCLUSIONS

In this study, the effects of Al$_2$O$_3$ addition at 4 different rates on the properties of SHA were examined and the following results were obtained:

1- SHA decomposed into β-TCP between 1100ºC-1200ºC, β- and α-TCP at 1250ºC and β- and α-TCP + CaO phases at 1300ºC, and the decomposition rate increased from 1.4% to 4.1% with increasing sintering temperature.

2- With increasing Al$_2$O$_3$ and sintering temperature, 60.1% of HA in the SHA-Al$_2$O$_3$ composites decomposed into β- and α-TCP phases.

3- Density, hardness and brittleness index properties of SHA without Al$_2$O$_3$ additive increased with increasing temperature, however; the highest compression strength and fracture toughness were obtained at 1200ºC.

4- With the addition of Al$_2$O$_3$ at amount of 2.5%, the highest fracture toughness and compression strength values of SHA were increased approximately 2.5 times.

5- The amount of apatite layer formed on the surface of SHA-2.5Al$_2$O$_3$ composite is higher than SHA due to its lower grain size and the phases it contains.

## REFERENCES

[1] Boutinguiza M., Pou J., Comesaña R., Lusquiños F., de Carlos A., León B. Biological hydroxyapatite obtained from fish bones. Mater. Sci. Eng. C. 2012;32:478-86.

[2] Hart A., Ebiundu K., Peretomode E., Onyeaka H., Nwabore O.F., Obileke K. Value-added materials recovered from waste bone biomass: technologies and applications. RSC Adv. 2022;12:22302-20.

[3] Buddhachat K., Klinhom S., Siengdee P., Brown J.L., Nomsiri R., Kaewmong P., Thitaram C., Mahakkanukrauh P., Nganvongpanit K. Elemental analysis of bone, teeth, horn and antler in different animal species using nonınvasive handheld X-ray fluorescence. PloS One. 2016; doi: 10.1371/journal.pone.0155458.

[4] Hussain F., Alshahrani S., Abbas M.M., Khan H.M., Jamil A., Yaqoob H., Soudagar M., Imran M., Ahmad M., Munir M. Waste animal bones as catalysts for biodiesel production; A mini review. Catalysts. 2021;11:630-45.

[5] Foroutan R., Peighambardoust S.J., Hosseini S.S., Akbari A., Ramavandi B. Hydroxyapatite biomaterial production from chicken (femur and beak) and fish bone waste through a chemical less method for Cd$^{2+}$ removal from shipbuilding waste water. J. Hazard. Mater. 2021;413:125428-40.

[6] Esmaeilkhanian A., Sharifianjazi F., Abouchenari A., Rouhani A., Parvin N., Irani M. Synthesis and characterization of natural nano-hydroxyapatite derived from turkey femur-bone waste. Appl. Biochem. Biotechnol. 2019;189:919-32.

[7] Herliansyah M.K., Dewo P., M. Shukor H.A., Ide-Ektessabi Ari. Development and characterization of bovine hydroxyapatite porous bone graft for biomedical applications. Adv. Mater. Res. 2011;277:59-65.

[8] Ismail S.A., Abdullah H.Z. Extraction and characterization of natural hydroxyapatite from goat bone for biomedical applications. Mater. Sci. Forum. 2020;1010:573-78.

124

[9] Buasri A., Inkaew T., Kodephun L., Yenying W., Loryuenyong V. Natural hydroxyapatite (NHAp) derived from pork bone as a renewable catalyst for biodiesel production via microwave irradiation. Key Eng. Mater. 2015;659:216-20.

[10] Sartoretto S.C., Uzeda M.J., Miguel F.B., Nascimento J.R., Ascoli F., Calasans-Maia M.D. Sheep as an experimental model for biomaterial implant evaluation. Acta Ortop Bras. 2016;24(5):262-66.

[11] Li Y., Chen S.K., Li L., Qin L., Wang X.L., Lai Y.X. Bone defect animal models for testing efficacy of bone substitute biomaterials. J. Orthop. Translat. 2015;3:95-04.

[12] Rehman I., Smith R., Hench L.L., Bonfield W. Structural evaluation of human and sheep, bone and comparison with synthetic hydroxyapatite by FT-Raman spectroscopy. J. Biomed. Mater. Res. 1995;29(10):1287-94.

[13] Indra A., Putra A.B., Handra N., Fahmi H., Nurzal A., Perdana M., Subardi A., Jon Affi J. Behavior of sintered body properties of hydroxyapatite ceramics: effect of uniaxial pressure on green body fabrication. Mater. Today Sustain. 2022;17:100100-08.

[14] Demirkol N., Oktar F.N., Kayali E.S. Influence of niobium oxide on the mechanical properties of hydroxyapatite. Key Eng. Mater. 2013;529-530: 29-33.

[15] Angioni D., Cannillo V., Orrù R., Cao G., Garroni S., Bellucci D. Bioactivity enhancement by a ball milling treatment in novel bioactive glass-hydroxyapatite composites produced by spark plasma sintering. J. Eur. Ceram. Soc. 2023;43:1220-29.

[16] Bazin T., Magnaudeix A., Mayet R., Carles P., Julien I., Demourgues A., Gaudon M., Champion E. Sintering and biocompatibility of copper-doped hydroxyapatite bioceramics. Ceram. Int. 2021;47:13644-54.

[17] Demirkol N., Oktar F.N., Kayali E.S. Mechanical and microstructural properties of sheep hydroxyapatite (SHA)-niobium oxide composites. Acta Phys. Pol. A. 2012;121(1):274-76.

[18] Akıllı A., Evlen H., Demirkol N. Biological and morphological effects of apatite kinds (Sheep/Synthetic) on MgO reinforced bone tissue with hydroxyapatite matrix. Acta Phys. Pol. A. 2022;142(2):201-10.

[19] Karip E., Muratoğlu M. A study on using expanded perlite with hydroxyapatite: Reinforced bio-composites. Proc. Inst. Mech. Eng. H: J. Eng. Med. 2021;235(5):574-82.

[20] Ekren N. Reinforcement of sheep-bone derived hydroxyapatite with bioactive glass. J. Ceram. Process. Res. 2017;18(1):64-68.

[21] Landek D., Ćurković L., Gabelica I., Mustafa M.K., Žmak I. Optimization of sintering process of alumina ceramics using response surface methodology. Sustainability. 2021;13:6739-53.

[22] Pan Y., Li H., Liu Y., Liu Y., Hu K., Wang N., Lu Z., Liang J. He S. Effect of holding time during sintering on microstructure and properties of 3D printed alumina ceramics. Front. Mater. 2020;7:54-66.

[23] Zhang L., Liu H., Yao H., Zeng Y., Chen J. Preparation, microstructure, and properties of $ZrO_2(3Y)/Al_2O_3$ bioceramics for 3D printing of all-ceramic dental implants by vat photopolymerization. Chin. J. Mech. Eng. 2022;1(2):100023-36.

[24] Visbal S., Lira-Olivares J., Sekino T., Niihara K., Moon B.K., Lee S.W. Mechanical properties of $Al_2O_3$-$TiO_2$-SiC nanocomposites for the femoral head of hip joint replacement. Mater. Sci. Forum. 2005;486-487:197-00.

[25] Aminzare M., Eskandari A., Baroonian M.H., Berenov A., Hesabi Z.R., Taheri M., Sadrnezhaad S.K. Hydroxyapatite nanocomposites: Synthesis, sintering and mechanical properties. Ceram. Int. 2013;39:2197-06.

[26] Epure L.M., Dimitrievska S., Merhi Y., Yahia L.H. The effect of varying $Al_2O_3$ percentage in hydroxyapatite/$Al_2O_3$ composite materials: Morphological, chemical and cytotoxic evaluation. J. Biomed. Mater. Res. 2007;83A(4):1009-23.

[27] Ji H., Marquis P.M. Preparation and characterization of $Al_2O_3$ reinforced hydroxyapatite. Biomaterials. 1992;13(11):744-48.

[28] Öksüz K.E., Özer A. Microstructural and phase study of $Y_2O_3$ doped hydroxyapatite/$Al_2O_3$ biocomposites. Dig. J. Nanomater. Biostructures. 2016;11(1):167-72.

[29] Mezahi F.Z. Effect of $ZrO_2$, $TiO_2$, and $Al_2O_3$ additions on process and kinetics of bonelike apatite formation on sintered natural hydroxyapatite surfaces. Int. J. Appl. Ceram. Technol. 2012;9(3):529-40.

[30] British Standard Non-Metallic Materials for Surgical Implants. Part 2: Specifications for Ceramic Materials Based on Alumina, BS 7253: Part 2: 1990 ISO 6474-1981.

[31] Majling J., Znáik P., Palová A., Stevĭk S., Kovalĭk S., Agrawal D.K., Roy R. Sintering of the ultrahigh pressure densified hydroxyapatite monolithic xerogels. J. Mater. Res. 1997;12(1):198-02.

[32] Rahimiana M., Ehsani N., Parvin N., Baharvandi H.R. The effect of particle size, sintering temperature and sintering time on the properties of Al-$Al_2O_3$ composites, made by powder metallurgy. J. Mater. Process. Technol. 2009;209:5387-93.

[33] Niihara K. Indentation microfracture of ceramics-its application and problems. J. Ceram. Soc. Jpn. 1985;20:12-18.

[34] Pandey A., Nigam V.K., Balani K. Multi-length scale tribology of hydroxyapatite reinforced with ceria and silver. Wear. 2018;404-405:12-21.

[35] Demirkol N., Turan M. Production and characterization of ternary sheep hydroxyapatite (SHA)-wollastonite (W)-commercial inert glass (CIG) biocomposite. Res. Eng. Struct. Mater. 2019;5(2):167-74.

[36] Kim S.R., Lee J.H., Kim Y.T., Riu D.H., Jung S.J., Lee Y.J., Chung S.C., Kim Y.H. Synthesis of Si, Mg substituted hydroxyapatites and their sintering behaviors. Biomaterials. 2003;24:1389-99.

[37] Herliansyah M.K., Hamdi M., Ide-Ektessabi A., Wildan M.W., Toque J.A. The influence of sintering temperature on the properties of compacted bovine hydroxyapatite. Mater. Sci. Eng. C 2009;29:1674-80.

[38] Liao C.J., Lin F.H., Chen K.S., Sun J.S. Thermal decomposition and reconstitution of hydroxyapatite in air atmosphere. Biomaterials. 1999;20:1807-13.

[39] Rapacz-Kmita A., Paluszkiewicz C., Ślósarczyk A., Paszkiewicz Z. FTIR and XRD investigations on the thermal stability of hydroxyapatite during hot pressing and pressureless sintering processes. J. Mol. Struct. 2005;744-747:653-56.

[40] Göller G., Oktar F.N. Sintering effects on mechanical properties of biologically derived dentine hydroxyapatite. Mater. Lett. 2002;56:142-47.

[41] Niakan A., Ramesh S., Tan C.Y., Hamdi M., Teng W.D. Characteristics of sintered bovine hydroxyapatite. Appl. Mech. Mater. 2013;372:177-80.

[42] Rao R.R., Kannan T.S. Synthesis and sintering of hydroxyapatite–zirconia composites. Mater. Sci. Eng. C 2002;20:187-93.

[43] Indrani D.J., Soegijono B., Adi W.A., Trout N. Phase composition and crystallinity of hydroxyapatite with various heat treatment temperatures. Int. J. App. Pharm. 2017;9(2):87-91.

[44] Wei L., Pang D., He L., Deng C. Crystal structure analysis of selenium-doped hydroxyapatite samples and their thermal stability. Ceram. Int. 2017;43:16141-48.

[45] Xu J.L., Khor K.A. Chemical analysis of silica doped hydroxyapatite biomaterials consolidated by a spark plasma sintering method. J. Inorg. Biochem. 2007;101:187-95.

[46] Lim K.F., Muchtar A., Mustaffa R., Tan C.Y. Sintering of HA/Zirconia composite for biomedical and dental applications: A review. Adv. Mater. Res. 2013;686:290-95.

[47] The British Standards Institution 2018, ISBN 978 0 580 86939-6

[48] Santos J.D., Silva P. L., Knowles J. C., Talal S., Monteiro F. J. Reinforcement of hydroxyapatite by adding $P_2O_5$-CaO glasses with $Na_2O$, $K_2O$ and MgO. J. Mater. Sci.: Mater. Med. 1996;7:187-89.

[49] Sung Y.M., Lee J.C., Yang J.W. Crystallization and sintering characteristics of chemically precipitated hydroxyapatite nanopowder. J. Cryst. Growth. 2004;262:467-72.

[50] Ou S.F., Chiou S.Y., Ou K.L. Phase transformation on hydroxyapatite decomposition. Ceram. Int. 2013;39:3809-16.

[51] Youness R.A., Taha M.A., Ibrahim M.A. Effect of sintering temperatures on the in vitro bioactivity, molecular structure and mechanical properties of titanium/carbonated hydroxyapatite nano biocomposites. J. Mol. Struct. 2017;1150:188-95.

[52] Sobczak-Kupiec A., Wzorek Z. The influence of calcination parameters on free calcium oxide content in natural hydroxyapatite. Ceram. Int. 2012;38:641-47.

[53] Evis Z., Usta M., Kutbay I. Improvement in sinterability and phase stability of hydroxyapatite and partially stabilized zirconia composites. J. Eur. Ceram. Soc. 2009;29:621-28.

[54] Nath S., Tripathi R., Basu B. Understanding phase stability, microstructure development and biocompatibility in calcium phosphate-titania composites, synthesized from hydroxyapatite and titanium powder mix. Mater. Sci. Eng. C 2009;29(1):97-07.

[55] Oktar F.N., Agathopoulos S., Ozyegin L.S., Gunduz O., Demirkol N., Bozkurt Y., Salman S. Mechanical properties of bovine hydroxyapatite (BHA) composites doped with $SiO_2$, MgO, $Al_2O_3$, and $ZrO_2$. J. Mater. Sci: Mater. Med. 2007;18:2137-43.

[56] Tayyebi S., Mirjalili F., Samadi H., Nemati A. A review of synthesis and properties of hydroxyapatite/alumina nano composite powder. J. Chem. 2015;5(2):20-28.

[57] Bohner M., Santoni B.L.G., Döbelin N. β-tricalcium phosphate for bone substitution: Synthesis and properties. Acta Biomater. 2000;13:23-41.

[58] Sinusaite L., Renner A.M., Schütz M.B., Antuzevics A., Rogulis U., Grigoraviciute-Puroniene I., Mathur S., Zarkov A. Effect of Mn doping on the low-temperature synthesis of tricalcium phosphate (TCP) polymorphs. J. Eur. Ceram. Soc. 2019;39(10):3257-63.

[59] Kahlenberg V., Fischer R.X., Shaw C.S.J. High-pressure $Ca_4Al_6O13$: An example of a calcium aluminate with three different types of coordination polyhedra for aluminum. Am. Mineral. 2000;85:1492-96.

[60] Kumar P.N., Ferreira J.M.F., Kannan S. Phase transition mechanisms involved in the formation of structurally stable β-$Ca_3(PO_4)_2$-α-$Al_2O_3$ composites. J. Eur. Ceram. Soc. 2017;37:2953-63.

[61] Mei H., Zhong Y., Wang P., Jia Z., Li C., Cheng N. Electronic, optical, and lattice dynamical properties of tetracalcium trialuminate ($Ca_4Al_6O_{13}$). Materi. 2018;11:449-61.

[62] Salomão R., Ferreira V.L., Costa L.M.M., de Oliveira I.R. Effects of the initial $CaO$-$Al_2O_3$ ratio on the microstructure development and mechanical properties of porous calcium hexaluminate. Ceram. Int. 2017;42(2):2626-31.

[63] Akao M., Aoki H., Kato K., Sato A. Dense polycrystalline β-tricalcium phosphate for prosthetic applications. J. Mater. Sci. 1982;17:343-46.

[64] Takahashi K., Fujishiro Y., Yin S., Sato T. Preparation and compressive strength of a-tricalcium phosphate based cement dispersed with ceramic particles. Ceram. Int. 2004;30:199-03.

[65] Mimi M. M., Shakil A.-M.-O.-R., Haque M. R., Hasan, M. R. Effect of addition of CaO on compressive strength of high-volume fly ash concrete. J. Civ. Eng. Sci. Technol. 2003;14(1):64-76.

[66] Trzaskowska M., Vivcharenko V., Przekora A. The impact of hydroxyapatite sintering temperature on its microstructural, mechanical, and biological properties. Int. J. Mol. Sci. 2023;24:5083-04.

126

[67] Dasgupta S., Tarafder S., Bandyopadhyay A., Bose S. Effect of grain size on mechanical, surface and biological properties of microwave sintered hydroxyapatite. Mater. Sci. Eng. C 20123;33:2846-54.

[68] Szutkowska M. Fracture toughness of advanced alumina ceramics and alumina matrix composites used for cutting tool edges. J. Achiev. Mater. Manuf. Eng. 2012;54(2):202-10.

[69] Afzal M.A.F., Kesarwani P., Reddy K.M., Kalmodia S., Basu B., Balani K. Functionally graded hydroxyapatite-alumina-zirconia biocomposite: Synergy of toughness and biocompatibility. Mater. Sci. Eng. C 2012;32:1164-73.

[70] Akao M., Miura N., Aoki H. Fracture toughness of sintered hydroxyapatite and $\beta$-tricalcium phosphate. JCS-Japan. 1984;92(107):672-74.

[71] Shaly A.A., Priya G.H., Mahendiran M., Linet J.M., Arul J., Mani M. An intrinsic analysis on the nature of alumina ($Al_2O_3$) reinforced hydroxyapatite nanocomposite. Physica B: Condensed Matter. 2022;642(1):414100.

[72] Shaly, A.A., Priya, G.H., Linet, J.M.: An exploration on the configurational and mechanical aspects of hydrothermally procured MgO/HA bioceramic nanocomposite. Phys. B 2021;617:413131

[73] Chien C.S., Liao T.Y., Hong T.F., Kuo T.Y., Chang C.H., Yeh M.L., Lee T.M. Surface microstructure and bioactivity of hydroxyapatite and fluorapatite coatings deposited on Ti-6Al-4V substrates using Nd-YAG laser. J. Med. Biol. Eng. 2014; 34(2):109-15.

[74] Sainz M.A., Pena P., Serena S., Caballero A. Influence of design on bioactivity of novel $CaSiO_3$-$CaMg(SiO_3)_2$ bioceramics: In vitro simulated body fluid test and thermodynamic simulation. Acta Biomater. 2010;6:2797-07.

[75] Wu C., Chang J. Synthesis and in vitro bioactivity of bredigite powders. J. Biomater. Appl. 2007;21: 251-63.

[76] García-Álvarez J., Escobedo-Bocardo C., Cortés-Hernández D.A., Almanza-Robles J. M. Bioactivity and mechanical properties of scaffolds based on calcium aluminate and bioactive glass. Int. J. Mater. Res. 2018;110(4):343-50.

127

# Synthesis of Li$_7$P$_3$S$_{11}$ Solid Electrolyte for All-Solid-State Lithium-Sulfur Batteries

**Çağrı Gökhan TÜRK$^{1,2}$ , Mahmud TOKUR$^{2,3,4*}$**

$^1$Sakarya University, Institute of Natural Sciences, Sakarya, Türkiye
$^2$Sakarya University, Research, Development and Application Center, Sakarya, Türkiye
$^3$Sakarya University, Department of Metallurgical & Materials Engineering, Sakarya, Türkiye
$^4$NESSTEC Energy & Surface Technologies A.S., Technology Development Zones, Sakarya, Türkiye
Çağrı Gökhan TÜRK ORCID No: 0000-0001-9940-6948
Mahmud TOKUR ORCID No: 0000-0003-3612-5350

*Corresponding author: mtokur@sakarya.edu.tr

**Abstract:** Solid electrolytes containing sulfur are gaining increasing traction among researchers and are growing in popularity with each passing day. Recently, Li$_7$P$_3$S$_{11}$, Li$_{10}$GeP$_2$S$_{12}$, and Li$_{11}$Si$_2$PS$_{12}$ solid electrolytes have been of great interest in literature. The ionic conductivity of these electrolytes can attain a value as high as $10^{-2}$ S/cm. For this purpose, this study employed the mechanical alloying method to synthesize the Li$_7$P$_3$S$_{11}$ solid electrolyte for use in all-solid-state lithium-sulfur batteries. To accomplish this, Li$_2$S and P$_2$S$_5$ ingredients were mixed in a ball mill at certain stoichiometric ratios. The crystallization temperatures of the obtained powders were determined by the DSC thermal analysis method, and they were crystallized under a protective atmosphere at the appropriate crystallization temperature. Subsequently, the acquired powders, known for their high sensitivity to ambient conditions, underwent XRD and Raman analysis within a specially designed enclosure to prevent exposure to open atmosphere. Powders that underwent structural characterization were subjected to electrochemical testing through electrochemical impedance spectroscopy and cyclic voltammetry analyses in a special solid-state cell. Notably, the cyclic voltammetry analysis unveiled an impressive electrochemical window extending to a minimum of 5 V. Additionally, the total conductivity of the Li$_7$P$_3$S$_{11}$ pellet was quantified at 1.1 mS cm$^{-1}$ at room temperature, further emphasizing its favorable electrochemical properties. The results exhibited compatibility with existing literature, confirming the synthesized electrolyte's viability as a fitting candidate for lithium-sulfur batteries.

128

## Tam Katı Hal Lityum-Sülfür Piller için Li$_7$P$_3$S$_{11}$ Katı Elektrolit Sentezi

**Anahtar
Kelimeler**
Enerji
depolama,
Lityum-Sülfür
pil,
Li$_7$P$_3$S$_{11}$ Katı
elektrolit

**Öz:** Sülfür içeren katı elektrolitler, bilim insanları için oldukça caziptir ve her geçen gün cazibesi artmaktadır. Son zamanlarda Li$_7$P$_3$S$_{11}$, Li$_{10}$GeP$_2$S$_{12}$ ve Li$_{11}$Si$_2$PS$_{12}$ katı elektrolitleri literatürde büyük ilgi görmektedir. Bu elektrolitlerin iyonik iletkenliği $10^{-2}$ S/cm seviyelerine bile ulaşabilmektedir. Bu amaçla, bu çalışmada tamamen katı hal Lityum Sülfür piller için mekanik alaşımlama yöntemi ile Li$_7$P$_3$S$_{11}$ katı elektroliti sentezlenmiştir. Bunun için Li$_2$S ve P$_2$S$_5$ bileşenleri bir bilyalı değirmende belirli stokiyometrik oranlarda karıştırılmıştır. Elde edilen tozların kristalleşme sıcaklıkları DSC termal analiz yöntemi ile belirlenmiş ve uygun kristalleşme sıcaklığında koruyucu atmosfer altında kristallendirilmiştir. Daha sonra elde edilen ve açık atmosfere karşı oldukça hassas olan tozlar özel yapım bir tutucu ile XRD ve Raman analizine tabi tutulmuştur. Yapısal olarak karakterize edilen tozlar, özel bir katı hal hücresinde elektrokimyasal empedans spektroskopisi ve çevrimsel voltammetri analizleri ile elektrokimyasal olarak test edilmiştir. Sonuçların literatürle uyumlu olduğu görülmüş ve sentezlenen elektrolitin lityum sülfür piller için uygun bir aday olarak kullanılabileceği belirlenmiştir.

## 1. INTRODUCTION

Elemental sulfur (S) is emerging as a captivating contender for the cathode component of batteries, exhibiting promising outcomes in the realm of next-generation battery technologies. The non-toxic and environmentally benign nature of sulfur, coupled with its abundant presence in nature and cost-effectiveness, amplifies its allure for next-generation technologies and further clears the path ahead. With a theoretical capacity of 1675 mAh g$^{-1}$ and an impressive energy density of 2567 Wh kg$^{-1}$, lithium-sulfur batteries outshine today's established commercial Li-ion batteries by a factor of five in terms of specific energy density [1]. Hence, lithium-sulfur batteries stand as a remarkable substitute for lithium-ion batteries in the future, with their operational mechanisms closely resembling those of conventional battery technologies [2].

Nevertheless, the commercial implementation of lithium-sulfur continues to face challenges when incorporating their active materials within liquid electrolyte environments. Primarily, the shuttle effect which stems from the dissolution of undesired lithium polysulfide intermediates into the lithium anode through the electrolyte and separator. This occurrence leads to diminished capacity and swift capacity deterioration [3-5].

In recent years, solid-state batteries (SSBs) have emerged as a compelling solution to address the enduring challenges in energy storage [6]. What sets solid-state lithium-sulfur batteries apart from their traditional counterparts is their reliance on a singular, robust sulfide electrolyte characterized by an exceptionally high ionic conductivity, effectively supplanting the conventional combination of liquid electrolytes and separators.

Among these sulfide electrolytes, the "simple" $Li_2S - P_2S$ binary system, collectively known as the $Li_7P_3S_{11}$ family, has garnered significant attention due to its remarkable properties [6]. These $Li_7P_3S_{11}$ materials exhibit extraordinary conductivity levels (> $10^{-4}$ Scm$^{-1}$) without the need for additional elements like Si, Ge, or Al [7]. Various crystalline and amorphous materials within the $Li_7P_3S_{11}$ family have been synthesized using diverse techniques, including the ball milling method, heat treatment, hot pressing, wet chemical treatment [8, 9], and more [10-12]. The key advantages of solid electrolytes lie in their capacity to dramatically enhance the power density of electrochemical cells, primarily due to their exceptional ionic conductivity. Additionally, they offer a heightened level of safety. Moreover, solid electrolytes present a promising solution to mitigate the shuttle effect, a persistent issue in lithium-sulfur batteries [6, 13].

Nevertheless, certain challenges persist, particularly related to lithium-ion diffusion kinetics, the electrode-electrolyte interface, and overall electrochemical performance. The adoption of solid electrolytes may introduce interface challenges between the electrolyte and electrodes, potentially impacting both ionic and electrical conductivity, and thereby potentially affecting the cell's capacity and stability [14].

In the context of this study, we synthesized a high-ionic-conductivity solid electrolyte, $Li_7P_3S_{11}$, using the meticulous blending of specific quantities of $Li_2S$ and $P_2S_5$ constituents through the ball milling method. Subsequent comprehensive structural and electrochemical assessments revealed highly promising results. These findings make a substantial and meaningful contribution to the scientific literature, underscoring the significant potential of $Li_7P_3S_{11}$ for applications in all-solid-state lithium-sulfur batteries.

## 2. EXPERIMENTAL STUDIES

The production of triclinic sulfur-based solid electrolyte $Li_7P_3S_{11}$ was carried out in two stages. $Li_2S$ and $P_2S_5$ powders were mixed into the ball mill at specific ratios (3:7 according to their atomic weights) in a special atmosphere-controlled mortar (in the glovebox) without exposure to air. The synthesis of the triclinic sulfur-based solid electrolyte $Li_7P_3S_{11}$ was carried out in a dual-stage process. $Li_2S$ and $P_2S_5$ powders were meticulously combined in a ball mill, following specific ratios (3:7 based on their atomic weights), within a controlled atmosphere (inside a glovebox) to prevent air exposure. Subsequently, the mechanical activation process was conducted at 600 rpm for a duration of 15 hours. This procedure resulted in the formation of amorphous $Li_7P_3S_{11}$. The ball-milled glassy powders were then placed within a sealed quartz tube and subjected to sintering at 265°C for a span of 2 hours. Finally, the result was the successful production of a crystalline solid electrolyte, $Li_7P_3S_{11}$. Structural analysis of the synthesized glass-ceramic powders was carried out by X-ray diffraction (RigakuD/MAX2000) and Raman with custom-made kapton band-sealed apparatus. DSC analysis was conducted before crystallization heat treatment to characterize the possible exo (endo) thermic reactions during synthesis. Electrochemical tests were conducted at the GAMRY workstation. 100 mg of optimized solid electrolyte powders were put into a PEEK-insulated die with a 10 mm diameter and pressed under 400 Mpa. Solid state cell was then assembled by loading indium on both sides of the $Li_7P_3S_{11}$ pellet and pressing again for the electrochemical impedance test (symmetrical In/$Li_7P_3S_{11}$/In) at a frequency between 1 MHz - 1 Hz with 10 mV amplitude. Cyclic Voltammetry (CV) tests were conducted by asymmetrical Li/$Li_7P_3S_{11}$/Stainless Steel cell between -0.01 V and 4.5 V (vs. Li/Li$^+$) with 1 mV/s step size to evaluate the electrochemical window of the synthesized solid electrolyte.

## 3. RESULTS AND DISCUSSIONS

To investigate the crystallographic properties of the obtained powders, XRD analysis was conducted, shown in Figure 1. Scanning was carried out between 10° and 40° with a scan rate of 1°/min. Compared to the other $Li_7P_3S_{11}$ structures from the reported studies, narrower

peaks were observed in the XRD analyses in this study instead of the wide peaks. The main peak for $Li_7P_3S_{11}$ at 30° after the sintering process, also in agreement with the literature [9, 15]. The phase formation of obtained powder shows crystalline character due to the milling energy of the phase in the (211) plane [16].
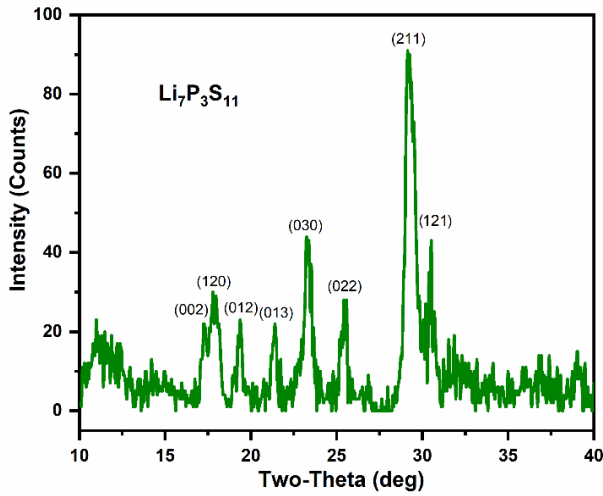


**Figure 1.** XRD analysis of $Li_7P_3S_{11}$ glass ceramic.

To characterize particle morphology and size, SEM analysis was employed, as depicted in Figure 2, providing SEM image of the $Li_7P_3S_{11}$ solid electrolyte. The particle size of $Li_7P_3S_{11}$ was found to exceed 700 nm, indicating that small particles of $Li_2S$ and $P_2S_5$ are incorporated into the larger $Li_7P_3S_{11}$ structure and undergo crystalline transformation, consistent with the XRD results. This observation also suggests a homogeneous mixing of solid electrolyte composites. Thus, the results confirm the uniformity in the blending of $Li_2S$ and $P_2S_5$ materials.
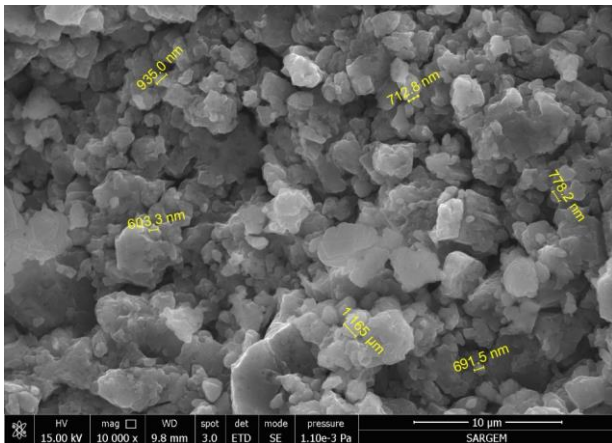


**Figure 2.** SEM image of the $Li_7P_3S_{11}$ solid electrolyte.

DSC analysis was carried out in order to determine the crystallization temperature of amorphous $Li_7P_3S_{11}$ powders, as shown in Figure 3. DSC can measure the amount of absorbed or released energy while the sample is heated, cooled, or kept at a constant temperature [17, 18]. In this technique, the temperature difference between the reference and the sample is shown depending on temperature or time [18]. Amorphous or irregular undesirable structures may occur below or

above the crystallization temperature. Therefore, it is an important step to determine the transition temperature from amorphous to crystalline structure [19, 20]. As a result of the DSC analysis, two peaks are raised between 250 °C and 350 °C, which indicates the existence of two exothermic reactions that characterize the crystallization of the $Li_7P_3S_{11}$ and $Li_4P_2S_6$ phases [21]. It is extremely important to define these peaks in order to know what kind of compounds can be obtained at certain temperatures. The peak of the targeted appropriate structure of $Li_7P_3S_{11}$ formed at about 260 °C.
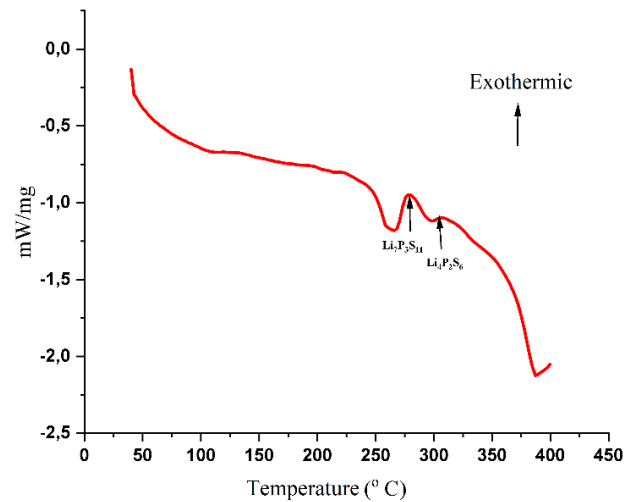


**Figure 3.** DSC analysis of amorphous $Li_7P_3S_{11}$ powders.

Differences in the wavelength of the light interacting with the molecule create Raman shifts [22]. These differences give information about the chemical properties of the molecules. Raman analyses of $Li_7P_3S_{11}$ powders are given in Figure 4. The atomic local environment in the $Li_7P_3S_{11}$ structure consists of $PS_4^{-3}$ tetrahedra and $P_2S_7^{-4}$ ditetrahedra. As is known, $P_2S_7^{-4}$ is a metastable phase and tends to transform into $P_2S_6^{-4}$ [23].

$$P_2S_7^{-4} = P_2S_6^{-4} + 1/8\ S_8 \tag{1}$$



**Figure 4.** Raman analysis of solid electrolyte.

Glass-ceramics in $P_2S_6^{-4}$ form in the low ionic conductivity phase appear to be 385 cm$^{-1}$. These peaks are formed as a result of exot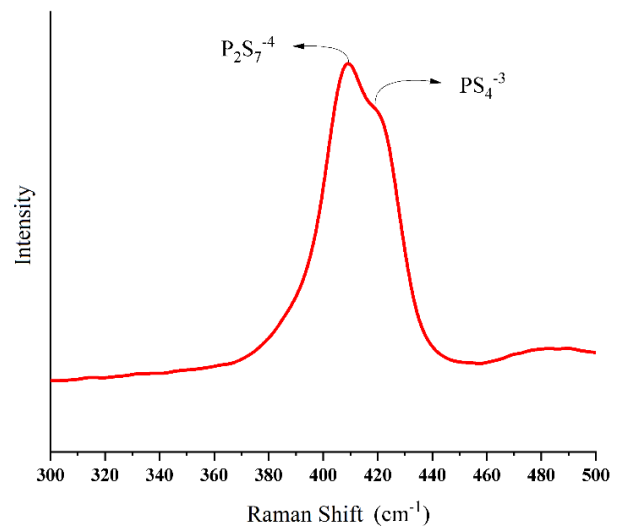hermic reactions. The atomic local environment was determined by Raman analysis. The Raman peaks at 405 cm$^{-1}$ and 420 cm$^{-1}$ confirm the formation of Li$_7$P3S$_{11}$ [9].

Electrochemical impedance spectroscopy (EIS) study was done to measure the ionic conductivity of the obtained solid electrolytes. The molds act as an electrochemical cell at the same time. To avoid air exposure of the materials inside the cell, it is strongly sealed and protected from oxygen or humidity. Impedance measurements were carried out in a symmetrical cell with a solid electrolyte positioned between the two indium (In) electrodes to assess the intrinsic impedance properties of the solid-state electrolyte, unencumbered by the complexities introduced by varying electrode materials or interfaces.

When the impedance curve in Figure 5 is carefully examined, a semicircle and a linear line are clearly seen. Starting point of the semicircle in the X-axis represents the impedance of the solid electrolyte ($R_{bulk}$). The diameter of the semicircular represents the grain boundary ($R_{gb}$) and interface resistance ($R_{if}$) arises between the electrode and electrolyte. The obtainer linear line in the low-frequency region represents the Warburg element ($W_o$). The ionic conductivity is calculated by finding the total resistance (Eq. 2). Li$_7$P$_3$S$_{11}$ powders always have some inclusions that can disrupt the interface and lower the impedance. This resistance is well observed at the intersection at the highest point [9].

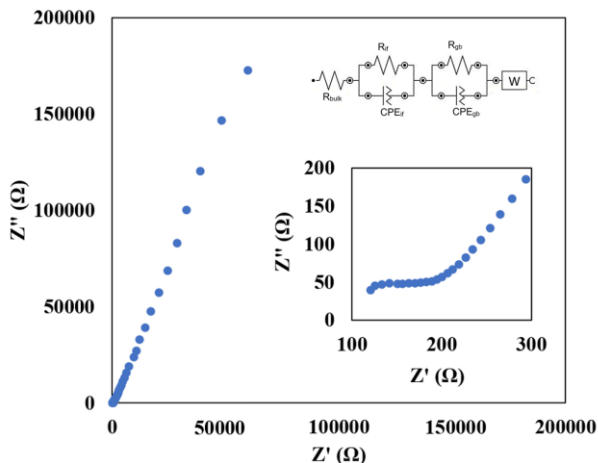$$Total\ Resistance\ R_{total} = R_{bulk} + R_{gb} + R_{if} \qquad (2)$$



**Figure 5.** EIS analysis of Li$_7$P$_3$S$_{11}$ contained symmetrical cell.

Values of $R_{bulk}$, $R_{gb}$, $R_{if}$ calculated using Nova software, were found to be 121.04 Ω, 36.47 Ω, and 27.94 Ω, recpectively. Consequently, the $R_{total}$ was determined to be 185.45 Ω.

The formula for calculating ionic conductivity (σ), as indicated in Eq. 3, is as follows:

$$\sigma = d\ /\ (S \times R_{total}) \qquad (3)$$

Where: d represents the thickness of the solid electrolyte (in this study, 0.2 cm), and S denotes the contact area (1 cm² in this study). Based on these calculations, the total conductivity of the Li$_7$P$_3$S$_{11}$ pellet was determined to be 1.1 mS cm$^{-1}$ at room temperature.

The electrochemical stability of Li$_7$P$_3$S$_{11}$ was determined by Cyclic Voltammetry (CV) at a scanning rate of 0.1 mV s$^{-1}$. Electrochemical measurements were carried out in the voltage range of -0.01 V to 4.5 V (Li/Li$^+$). Cyclic voltammetry curves of Li / Li$_7$P$_3$S$_{11}$/ steel asymmetrical cell are shown in Figure 6. It can be easily observed large oxidation and reduction (redox) reactions peaks. The reduction peak, which corresponds to the metallic lithium deposition process ($Li^+ + e^- \rightarrow Li$), is prominently observed at approximately 0 V. Conversely, the oxidation peak linked to lithium dissolution ($Li \rightarrow Li^+ + e^-$) is evident in the voltage range between 0 V and 1 V, and this peak is attributed to the presence of S$^{2-}$ ions [15]. The positions of these peaks closely align with those observed in Li$_7$P$_3$S$_{11}$ [9, 24]. The CV analysis also shows that the obtained structure has a wide electrochemical window up to at least 5 V.
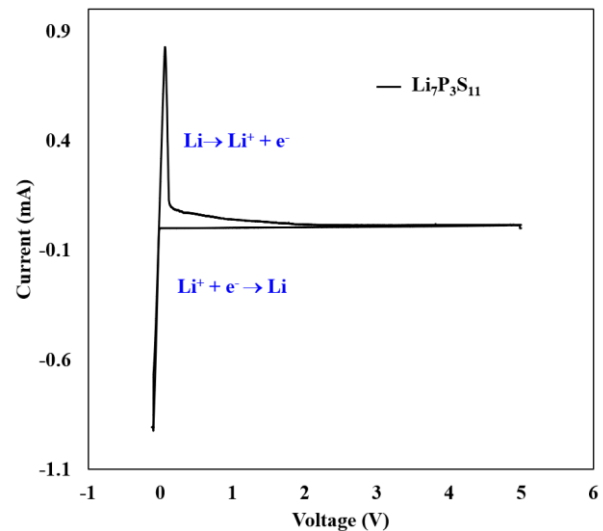


**Figure 6.** CV analysis of asymmetrical solid-state cell.

When compared to previously documented synthesis methods of Li$_7$P$_3$S$_{11}$ solid electrolyte, our approach utilizing ball milling, as illustrated in Table 1, exhibits sufficient ionic conductivity and electrochemical window.

**Table 1.** Comparison for the electrochemical performance of prepared Li$_7$P$_3$S$_{11}$ by ball milling method with other synthesized methods.

| Preparation Method | Electrochemical Window (V) | Ionic Conductivity (mS cm$^{-1}$) | Ref |
|---|---|---|---|
| Ball milling | 5 | 1.1 | This Work |
| dissolution-evaporation | 5 | 0.97 | [25] |
| liquid phase process-ultrasonic irradiation | 5 | 1 | [26] |
| optimal laser | - | 0.7 | [27] |

# 4. CONCLUSIONS

The $Li_7P_3S_{11}$ solid electrolyte intended for use in all-solid-state lithium-sulfur batteries have been effectively synthesized through the mechanical alloying method. Structural analyses were conducted on the acquired powders, revealing that their distinctive properties were consistent with those reported in the literature. Furthermore, the use of thermal analysis methods allowed for accurate determination of crystallization temperatures. Subsequently, the structurally characterized powders were subjected to ionic conductivity testing through impedance measurements within an electrochemical cell. The obtained results have been found to fall within the acceptable thresholds for all-solid-state batteries. Finally, the cell subjected to cyclic voltammetry (CV) testing exhibited reversible oxidation and reduction reactions, maintaining stability across a broad potential range. These findings are anticipated to make a valuable contribution to advancing the commercialization of all-solid-state lithium-sulfur batteries.

## REFERENCES

[1] Gohari, S., et al., Parametric optimization of sulfur@ graphene composites for aqueous and solid-state rechargeable lithium-sulfur batteries. Diamond and Related Materials, 2023: p. 110267.

[2] Olanrele, S.O., et al., Tuning of interactions between cathode and lithium polysulfide in Li-S battery by rational halogenation. Journal of Energy Chemistry, 2020. 49: p. 147-152.

[3] Li, N., et al., From interlayer to lightweight capping layer: Rational design of mesoporous TiO2 threaded with CNTs for advanced Li–S batteries. Carbon, 2019. 143: p. 523-530.

[4] Deng, S., et al., Carbon nanotube-supported polyimide nanoarrays as sulfur host with physical/chemical polysulfide-traps for Li–S batteries. Composites Communications, 2022. 29: p. 101019.

[5] Al Salem, H.I., Electrocatalysis In Li-S Batteries. 2016.

[6] Zhou, J., P. Chen, W. Wang, and X. Zhang, Li7P3S11 electrolyte for all-solid-state lithium-ion batteries: structure, synthesis, and applications. Chemical Engineering Journal, 2022. 446: p. 137041.

[7] Dietrich, C., et al., Lithium ion conductivity in Li 2 S–P 2 S 5 glasses–building units and local structure evolution during the crystallization of superionic conductors Li 3 PS 4, Li 7 P 3 S 11 and Li 4 P 2 S 7. Journal of Materials Chemistry A, 2017. 5(34): p. 18111-18119.

[8] Zhou, J., et al., Wet-chemical synthesis of Li7P3S11 with tailored particle size for solid state electrolytes. Chemical Engineering Journal, 2022. 429: p. 132334.

[9] Xu, R., et al., Preparation of Li7P3S11 glass-ceramic electrolyte by dissolution-evaporation method for all-solid-state lithium ion batteries. Electrochimica Acta, 2016. 219: p. 235-240.

[10] Aoki, Y., et al., Chemical and structural changes of 70Li2S-30P2S5 solid electrolyte during heat treatment. Solid State Ionics, 2017. 310: p. 50-55.

[11] Tsukasaki, H., et al., Direct observation of a non-crystalline state of Li2S–P2S5 solid electrolytes. Scientific reports, 2017. 7(1): p. 4142.

[12] Tsukasaki, H., S. Mori, S. Shiotani, and H. Yamamura, Ionic conductivity and crystallization process in the Li2S–P2S5 glass electrolyte. Solid State Ionics, 2018. 317: p. 122-126.

[13] Kudu, Ö.U., et al., A review of structural properties and synthesis methods of solid electrolyte materials in the Li2S− P2S5 binary system. Journal of Power Sources, 2018. 407: p. 31-43.

[14] Judez, X., et al., Quasi-solid-state electrolytes for lithium sulfur batteries: Advances and perspectives. Journal of Power Sources, 2019. 438: p. 226985.

[15] Rangasamy, E., et al., An iodide-based Li7P2S8I superionic conductor. Journal of the American Chemical Society, 2015. 137(4): p. 1384-1387.

[16] Zhang, Q., et al., Fe 3 S 4@ Li 7 P 3 S 11 nanocomposites as cathode materials for all-solid-state lithium batteries with improved energy density and low cost. Journal of Materials Chemistry A, 2017. 5(45): p. 23919-23925.

[17] Sobolciak, P., M. Karkri, M.A. Al-Maadeed, and I. Krupa, Thermal characterization of phase change materials based on linear low-density polyethylene, paraffin wax and expanded graphite. Renewable Energy, 2016. 88: p. 372-382.

[18] Kissinger, H.E., Differential thermal analysis. J. Res. Natl. Bur. Stand, 1956. 57(4): p. 217.

[19] Borchardt, H.J. and F. Daniels, The application of differential thermal analysis to the study of reaction kinetics1. Journal of the American Chemical Society, 1957. 79(1): p. 41-46.

[20] Smykatz-Kloss, W., Differential thermal analysis: application and results in mineralogy. Vol. 11. 2012: Springer Science & Business Media.

[21] Yersak, T.A., et al., Consolidation of composite cathodes with NCM and sulfide solid-state electrolytes by hot pressing for all-solid-state Li

metal batteries. Journal of Solid State Electrochemistry, 2022. 26(3): p. 709-718.

[22] Long, D.A., The raman effect. 2002: John Wiley & Sons Ltd.

[23] Huang, B., et al., Li3PO4-doped Li7P3S11 glass-ceramic electrolytes with enhanced lithium ion conductivities and application in all-solid-state batteries. Journal of Power Sources, 2015. 284: p. 206-211.

[24] Jung, S.-Y., R. Rajagopal, and K.-S. Ryu, Synthesis and electrochemical performance of (100− x) Li7P3S11-xLi2OHBr composite solid electrolyte for all-solid-state lithium batteries. Journal of Energy Chemistry, 2020. 47: p. 307-316.

[25] Xu, R.C., et al., Preparation of Li7P3S11 glass-ceramic electrolyte by dissolution-evaporation method for all-solid-state lithium ion batteries. Electrochimica Acta, 2016. 219: p. 235-240.

[26] Calpa, M., N.C. Rosero-Navarro, A. Miura, and K. Tadanaga, Instantaneous preparation of high lithium-ion conducting sulfide solid electrolyte Li7P3S11 by a liquid phase process. RSC Advances, 2017. 7(73): p. 46499-46504.

[27] Eatmon, Y., et al., Air Stabilization of Li7P3S11 Solid-State Electrolytes through Laser-Based Processing. Nanomaterials, 2023. 13(15): p. 2210.

**Türk Doğa ve Fen Dergisi**
**Turkish Journal of Nature and Science**

www.dergipark.gov.tr/tdfd

# Retrospective Evaluation of Vitamin D Levels According to Age, Gender and Seasonal Characteristics: Ardahan- Gole

**Ümit YAŞAR¹\*** iD

¹ Ardahan University, Nihat Delibalta Göle Vocational School, Department of Laboratory and Veterinary Health, Ardahan, Türkiye
Ümit YAŞAR ORCID No: 0000-0001-8110-7747

*\*Corresponding author: umityasar@ardahan.edu.tr*

**Abstract:** In recent years, there has been an increase in vitamin D tests in order to determine the prevalence and definition of vitamin D deficiency, which is clinically recognized to be associated with many diseases. The increase in vitamin-supported supplements is also related to this. This deficiency, which is tried to be prevented by taking precautions such as sun exposure, food and diet in local conditions, is tried to be prevented by health professionals with guidance, supervision and drug supplementation. This study covers the period between 2015 and 2022. All patient data were randomly obtained from hospital automation (Göle state hospital) and then 1,25-dihydroxyvitamin D (25(OH)D) levels were retropectively analyzed. The findings of the study showed that vitamin D levels were insufficient ($<20$ng ml$^{-1}$) in male and female populations, there was no significant difference between gender and age groups, and there was a significant seasonal change in vitamin D levels in both genders in summer and winter periods. As a result, it is important to evaluate the prevalence of vitamin D deficiency in Ardahan province and to expand the screening in the whole population and the experience of health professionals.

134

# D Vitamini Düzeylerinin Yaş, Cinsiyet ve Mevsimsel Özelliklerine Göre Retrospektif Değerlendirilmesi: Ardahan- Göle

**Anahtar Kelimeler**
D vitamini,
25(OH)D,
D vitamini
eksikliği

**Öz:** Klinik olarak birçok hastalıkla ilişkili olduğu kabul edilen D vitamini eksikliğinin prevalansını belirlemek ve tanımını yapabilmek amacıyla son yıllarda D vitamin testlerinde artış gözlenmektedir. Vitamin destekli takviyelerin artması da bununla ilişkilidir. Yerel koşullarda güneşe maruziyet, gıda, diyet gibi önlemlerin alınması ile önüne geçilmeye çalışılan bu eksiklik sağlık profesyonelleri tarafından yönlendirme, denetleme ve takviye ile engellenmeye çalışılır. Bu çalışma, 2015- 2022 arası dönemi kapsamaktadır. Tüm hasta verileri rastgele olarak hastane otomasyonundan (Göle devlet hastanesi) elde edildi ve ardından 1,25-dihidroksi vitamin D (25(OH)D) seviyeleri retrospektif olarak analiz edildi. Çalışma bulguları kadın ve erkek popülasyonunda D vitamini seviyelerinin yetersiz düzeyde olduğunu ($<20$ng ml$^{-1}$), cinsiyet ve yaş grupları arasında anlamı bir farkın olmadığını ve her iki cinste de mevsimsel olarak yaz ve kış periyotlarında D vitamini seviyelerinde anlamlı bir değişimin olduğunu göstermiştir. Sonuç olarak Ardahan İli D vitamini eksikliğinin prevalansının değerlendirilip tüm popülasyonda taramaların yaygınlaştırılması ve sağlık profesyonellerin deneyimi önemlidir

## 1. INTRODUCTION

Vitamin D is an essential fat-soluble vitamin obtained from animal and plant food sources, as well as being synthesized by the body from sunlight. There are 2 main forms of vitamin D. These are the vitamin D prohormones, D2 (ergocalciferol) and D3 (cholecalciferol). D2 can be obtained from plant food sources, while D3 can be obtained from animal foods and synthesized by the body through exposure to sunlight[1]. Although there are structural chain differences in these forms of vitamin D, their metabolism and functions within the body are not different. As a result of D2 and D3 metabolizations, they are converted to calcitriol (1,25-dihydroxyvitamin D or 1,25[OH] 2D), which is the active form of vitamin D[2].

1,25(OH)2D is the active metabolite and stimulates calcium absorption in target organs. The active metabolite enters the target cell and then binds to the vitamin D receptor to form a complex. This complex activates the synthesis of proteins such as calcium-binding protein or osteocalcin in the target cell. As a result, calcium is taken into the cell through the proteins in the membrane. This calcium in the target cell is transported to the extracellular fluid by an ATP-dependent mechanism, and then to the blood. Thus, the calcium level in the blood is increased. Target organs for 1,25(OH)2D are bone tissue, intestinal and kidney cells. 1,25(OH)2D acts by stimulating calcium transport from these tissues to the blood. Calcium in the blood functions as the basic component of the functioning mechanism of many systems and tissues in the body, especially bone mineralization and muscle activities [3].

Vitamin D is assessed by determination of 25(OH)D levels in serum. A 25(OH)D level between 20-60 ng mL$^{-1}$ is considered normal in individuals under 65 years of age. Below 20 ng mL$^{-1}$ is defined as 'vitamin D deficiency', and below 12 ng mL$^{-1}$ is defined as 'severe deficiency'. If it is over 100 ng mL$^{-1}$, it may cause hypercalcemia [4, 5].

Vitamin D synthesis begins rapidly when ultraviolet rays (UVB) reach the skin. However, some environmental factors such as different latitude regions of countries, seasonal differences and air pollution also affect the synthesis of vitamin D as they affect UVB wavelengths and exposure times. Age of the individual, clothing, pigment status of the skin, use of sunscreen will also affect the synthesis. On the other hand, the inability to take foods rich in vitamin D into the body disrupts the continuity of homeostasis[6].

Vitamin D is an important component of the endocrine system that regulates calcium homeostasis and stimulates bone development. In addition, vitamin D is effective on immune functions[7, 8].

Additionally, some vitamins, such as vitamin C, vitamin E, and beta-carotene (a form of vitamin A), act as antioxidants in the body. And these antioxidants are molecules that help protect the body's cells from damage caused by harmful molecules called free radicals. Vitamin D is not typically considered an antioxidant in the same way as vitamins C or E, which are well-known antioxidants. However, there is some evidence to suggest that vitamin D may have antioxidant-like properties and play a role in reducing oxidative stress in the body[9-11].

Severe deficiency of vitamin D increases the risk of serious bone and muscle diseases such as rickets and osteomalacia. It has been reported that vitamin D deficiency can also lead to the development of autoimmune diseases. For example, studies have shown that it reduces the risk of multiple sclerosis in cases where they benefit more from sunlight at the age of 6-15 years. Various studies on ecology have also shown

that less exposure to sunlight may be associated with higher cancer prevalence and cancer deaths[3].
Considering this information, vitamin D deficiency is accepted as a general health problem because it can affect all periods of life and individuals in different continents and cause health problems such as serious diseases[12, 13].

Vitamin D synthesis is considered sufficient in individuals living in low latitude regions due to the appropriate wavelength of UVB rays throughout the year, but studies have shown that vitamin D deficiency is high even in these tropical countries[12, 14] . For this reason, a population-based retrospective study was conducted showing the vitamin D levels of individuals living in our region (Ardahan-Gole), taking into account the seasonal periods.

## 2. MATERIAL AND METHOD

### 2.1. Working Order

This retrospective study was conducted with the approval of Ardahan University Scientific Research and Publication Ethics Committee (Protocol No: 2022-2ÖNP-0102, Approval Date: 14.12.2022- Issue: E-67796128-000-2200037489).

This study covers the period between 2015 and 2022. All patient data were obtained from Gole state hospital automation, and then 25(OH)D levels were analyzed retrospectively. The 25(OH)D levels of the individuals were determined by the electrochemiluminescence method, and the values were measured with the Cobas 6000-E601 device. Data from patients with conditions that may affect vitamin D levels, such as metabolic diseases, were not included in the study. Results of the same patient at different times were included. All patients included in the study (n:349) were classified according to age groups, season, gender and vitamin levels.

In the study, 25(OH)D levels obtained from a total of 349 people, 223 women and 126 men, were evaluated. The data were grouped by gender as male and female, by age as (10-19), (20-45), (46-65) and (66+) and by season as autumn, winter, spring and summer.

### 2.2. Statistical Analysis

SPSS 26 and MS-Excel were used for all analyses, calculations and evaluations in this study. Statistical results were evaluated at 95% confidence interval, significance level at $p < 0.05$, and $p < 0.01$ and $p < 0.001$ level of forward significance. In the evaluation of the data, Kruskal Wallis test was used for the comparison of the descriptive statistical methods (mean, standard deviation, median) as well as the non-normally distributed parameters. Mann Whitney U test was used in the evaluations between the two groups.

## 3. RESULTS

The effect of gender difference on serum 25(OH)D levels was not found statistically significant (Table 1).

**Table 1.** 25(OH)D levels by gender

| 25(OH)D (ng mL$^{-1}$) | N | Mean | S.E. | p |
|---|---|---|---|---|
| Female | 223 | 15,92 | 0,65 | > 0.05 |
| Male | 126 | 15,61 | 0,96 | |

When the effects of different age groups on 25(OH)D levels were examined by looking at the gender differences, no statistically significant difference was found (Table 2).

**Table 2.** 25(OH)D levels in different ages and genders.

| 25(OH)D (ng mL$^{-1}$) | Grup | N | Mean | S.E. | p |
|---|---|---|---|---|---|
| 10-19 | Female | 26 | 15,0915 | 1,64 | > 0.05 |
| | Male | 3 | 15,7433 | 1,62 | |
| 20-45 | Female | 83 | 14,8461 | 0,93 | > 0.05 |
| | Male | 62 | 13,8047 | 0,89 | |
| 46-65 | Female | 78 | 16,2818 | 1,11 | > 0.05 |
| | Male | 42 | 17,9083 | 2,30 | |
| ≥66 | Female | 36 | 18,2189 | 2,01 | > 0.05 |
| | Male | 19 | 16,4153 | 2,36 | |

The effect of seasonal changes on the 25(OH)D levels of the population was investigated by taking gender differences into account. When vitamin levels were examined across seasonal periods, no difference was observed between genders. However, seasonal differences caused significant changes in vitamin levels in both genders ($p < 0.01$), (Table 3).

When the 25(OH)D levels in individuals were compared in autumn and winter seasons, it was determined that vitamin values decreased in both male and female groups in a statistically significant way compared to autumn in winter ($p < 0.01$).

When the winter and spring periods were compared in both female and male groups, there was no significant change in vitamin levels.

A significant difference was found in the vitamin levels in the spring and summer seasons ($p < 0.01$). According to this, vitamin levels increase in both men and women in summer compared to spring.

When the summer and autumn periods were compared, although a decrease was observed in the female group, the change in vitamin levels between the groups in both males and females was not statistically significant.

According to the analysis, it was determined that the period with the highest serum vitamin value in women was summer (although there was no significant difference between autumn and summer). In men, this period is the summer-autumn period.

**Table 3.** Serum 25(OH)D levels in different seasons.

| 25(OH)D (ng mL$^{-1}$) | Season | Mean | N | S.E. | p |
|---|---|---|---|---|---|
| Female | autumn | 17,3546 | 54 | 1,06 | < 0.01 |
| | winter | 12,8826 | 61 | 0,91 | |
| | Spring | 14,1970 | 67 | 1,09 | < 0.01 |
| | Summer | 21,3727 | 41 | 02,06 | |
| Male | autumn | 20,6132 | 28 | 3,16 | < 0.01 |
| | winter | 12,6862 | 45 | 1,2 | |
| | Spring | 11,8357 | 30 | 1,02 | < 0.01 |
| | Summer | 20,1757 | 23 | 1,57 | |

## 4. DISCUSSION AND CONCLUSION

25(OH)D deficiency is shown as a social problem by researchers[15]. It has been reported that there is a strong connection between this condition, which is common in society, and the development of the immune system, endocrine system, and acute and chronic diseases[16]. In addition, Karin et al reported that 25(OH)D deficiency is closely related to bone loss, infection and many diseases[17]. There are also studies talking about the relationship between vitamin D deficiency and muscle weakness, cardiovascular diseases, autoimmune diseases and cancer[18].

In this study, it was determined that there was no difference in 25(OH)D values between men and women, but the average 25(OH)D levels in both groups were below 20 ng mL$^{-1}$ (15.92 ng mL$^{-1}$ women; 15.61). ng mL$^{-1}$ male). Clinically, serum 25(OH)D concentrations below 20 ng mL$^{-1}$ have been reported as vitamin D deficiency, and levels below 12 ng mL$^{-1}$ have been reported as severe deficiency. Accordingly, it can be said that individuals in the Ardahan-Gole region have vitamin D deficiency[4, 5].

A study similar to ours was conducted in the Mediterranean region. According to the study, they stated that 24.65% of individuals in the region had 25(OH)D deficiency. In the study, they reported that the mean 25(OH)D for men was approximately 15 ng mL$^{-1}$ (52.95±0.92 nmol L$^{-1}$) and the mean 25(OH)D for women was about 14ng mL$^{-1}$ (48.42±0.54 nmol L$^{-1}$). They also showed that men's 25(OH)D average was higher than women's[15]. In our study, no difference was found between genders.

In another study, they showed that 25(OH)D levels were sufficient in only 8.6% of people. The study also stated that there was no age-related difference as in our study[19].

Serum 25(OH)D levels increase as a result of sun exposure, as 7-dihydrocholesterol in the skin converts to vitamin D. Therefore, 25(OH)D level is affected by many parameters such as skin pigmentation, altitude, latitude and season [20, 21]. In the study by Samefors et al., where they investigated the 25(OH)D level in adults, it was shown that the vitamin level increased significantly in the summer months. According to the study, the average 25(OH)D level of all participants before summer was 45 nmol L$^{-1}$. Participants were encouraged to go outside for half an hour between 11-15:00 every day and As a result, it was shown that 25(OH)D values reached 64 nmol L$^{-1}$ at the end of

136

summer.[22]. In another study, they stated that 25(OH)D deficiency was highly prevalent in high latitude regions [23]. As a result, levels can change with the season, and this variability may differ from population to population[24]. Our study showed that vitamin D levels of both genders are affected by seasonal differences and that this level may be highest in summer in women and in autumn-summer months in men. In addition, it was determined that there was a significant change in autumn and spring months and 25(OH)D levels were higher in autumn. Winter for women, winter-spring for men is the period when the decrease in vitamin D values is highest. According to the results, it was determined that 25(OH)D levels reached normal levels for both genders towards the summer period. In addition, it can be said that the increase in 25(OH)D levels in the summer months continues in the autumn period and the levels that decrease in the winter tend to decrease in the spring as well. This suggests that it is related to seasonal transition processes.

When the effect of age on 25(OH)D levels was examined in the literature, it was reported that there was a significant difference in vitamin levels between age groups and lower 25(OH)D levels were found in those under 65 years of age[19]. However, in the study of the Australian population, the researchers noted that they did not find a significant difference between the age groups[24]. The data obtained in our study were classified according to 4 different age groups, and 25(OH)D levels were evaluated between the groups, and it was determined that the age parameter did not create a significant difference in 25(OH)D levels. As mentioned above, different from our study, some studies reported a significant difference in 25(OH)D levels depending on age[19]. This may be due to the low vitamin D levels of the individuals in our study.

Although many factors affect the 25(OH)D level, according to the results obtained, the vitamin D level of the population living in the province of Ardahan-Gole, which is at high latitude, is generally insufficient. In addition, it can be thought that the 25(OH)D level is low in winter and spring because sun exposure is insufficient, and the 25(OH)D level is high in summer and autumn months because sun exposure is high.

As a result, the reasons for the low 25(OH)D levels in this region should be carefully investigated. It is important that this situation is recognized as a public health problem and that studies are carried out on the whole population. It is also important to make the necessary interventions.

### Limitations of the Study
Due to the insufficient sample and research conducted in the region, the study cannot reflect the entire population. Therefore, further studies are needed.

### Acknowledgement

## REFERENCES

[1] Holick MF. SpringerLink, Vitamin D: Physiology, molecular biology, and clinical applications, Humana Press, Totowa, NJ, 2010.

[2] Miraglia Del Giudice M, Indolfi C, Strisciuglio C. Vitamin D: Immunomodulatory aspects, J Clin Gastroenterol 52 Suppl 1, Proceedings from the 9th Probiotics, Prebiotics and New Foods, Nutraceuticals and Botanicals for Nutrition & Human and Microbiota Health Meeting, held in Rome, Italy from September 10 to 12, 2017 (2018) S86-S88.

[3] Lips P. Vitamin D physiology, Prog Biophys Mol Biol 92(1) (2006) 4-8.

[4] Bilezikian JP, Formenti AM, Adler RA, Binkley N, Bouillon R, Lazaretti-Castro M, et al. Vitamin D: Dosing, levels, form, and route of administration: Does one approach fit all?, Rev Endocr Metab Disord 22(4) (2021) 1201-1218.

[5] Moreira CA, Ferreira C, Madeira M, Silva BCC, Maeda SS, Batista MC, et al. Reference values of 25-hydroxyvitamin D revisited: a position statement from the Brazilian Society of Endocrinology and Metabolism (SBEM) and the Brazilian Society of Clinical Pathology/Laboratory Medicine (SBPC), Arch Endocrinol Metab 64(4) (2020) 462-478.

[6] Silva ICJ, Lazaretti-Castro M. Vitamin D metabolism and extraskeletal outcomes: an update, Arch Endocrinol Metab 66(5) (2022) 748-755.

[7] Ylikomi T, Laaksi I, Lou YR, Martikainen P, Miettinen S, Pennanen P, et al. Antiproliferative action of vitamin D, Vitam Horm 64 (2002) 357-406.

[8] Ceglia L. Vitamin D and its role in skeletal muscle, Curr Opin Clin Nutr Metab Care 12(6) (2009) 628-33.

[9] Bengü AŞ, Adnan A, Özbolat S, Abdullah T, Aykutoğlu G, Çiftci M, et al. Content and antimicrobial activities of bingol royal jelly, Türk Tarım ve Doğa Bilimleri Dergisi 7(2) (2020) 480-486.

[10] Ayna A, Tunc A, Özbolat SN, Bengü AŞ, Aykutoğlu G, Canli D, et al. Anticancer, and antioxidant activities of royal jelly on HT-29 colon cancer cells andmelissopalynological analysis, Turkish Journal of Botany 45(8) (2021) 809-819.

[11] Adnan A. Apoptotic effects of beta-carotene, alpha-tocopherol and ascorbic acid on PC-3 prostate cancer cells, Hacettepe Journal of Biology and Chemistry 48(3) (2020) 211-218.

[12] Pereira-Santos M, Santos J, Carvalho GQ, Santos DBD, Oliveira AM. Epidemiology of vitamin D insufficiency and deficiency in a population in a sunny country: Geospatial meta-analysis in Brazil, Crit Rev Food Sci Nutr 59(13) (2019) 2102-2109.

[13] Maeda SS, Borba VZ, Camargo MB, Silva DM, Borges JL, Bandeira F, et al. Society of, Metabology, Recommendations of the Brazilian Society of Endocrinology and Metabology (SBEM) for the diagnosis and treatment of hypovitaminosis

137

D, Arq Bras Endocrinol Metabol 58(5) (2014) 411-33.

[14] Leal A, Correa MP, Holick MF, Melo EV, Lazaretti-Castro M. Sun-induced production of vitamin D(3) throughout 1 year in tropical and subtropical regions: relationship with latitude, cloudiness, UV-B exposure and solar zenith angle, Photochem Photobiol Sci 20(2) (2021) 265-274.

[15] Matyar S, Dişel NR, Açıkalın A, Kutnu M, İnal T. Çukurova Bölgesinde D vitamini düzeyleri, Cukurova Medical Journal 42(2) (2017) 320-328.

[16] Bouillon R, Carmeliet G, Lieben L, Watanabe M, Perino A, Auwerx J, et al. Vitamin D and energy homeostasis—of mice and men, Nature Reviews Endocrinology 10(2) (2014) 79-87.

[17] Amrein K, Scherkl M, Hoffmann M, Neuwersch-Sommeregger S, Köstenberger M, Tmava Berisha A, et al. Vitamin D deficiency 2.0: an update on the current status worldwide, European journal of clinical nutrition 74(11) (2020) 1498-1513.

[18] Holick MF. Vitamin D deficiency, New England journal of medicine 357(3) (2007) 266-281.

[19] Abdülhalim S, Timur O, Burak I. Rutin sağlık taraması yapılan bireylerde vitamin D düzeyleri, İstanbul Tıp Fakültesi Dergisi 81(4) (2018) 115-118.

[20] Gilchrest BA. Sun exposure and vitamin D sufficiency, The American journal of clinical nutrition 88(2) (2008) 570S-577S.

[21] Braegger C, Campoy C, Colomb V, Decsi T, Domellof M, Fewtrell M, et al. Vitamin D in the healthy European paediatric population, Journal of pediatric gastroenterology and nutrition 56(6) (2013) 692-701.

[22] Samefors M, Tengblad A, Östgren CJ. Sunlight exposure and vitamin D levels in older people-an intervention study in Swedish nursing homes, The journal of nutrition, health & aging 24 (2020) 1047-1052.

[23] Khoo AL, Koenen HJ, Chai LY, Sweep FC, Netea MG, van der Ven AJ, et al. Seasonal variation in vitamin D3 levels is paralleled by changes in the peripheral blood human T cell compartment, PloS one 7(1) (2012) e29250.

[24] Gill TK, Hill CL, Shanahan EM, Taylor AW, Appleton SL, Grant JF, et al. Vitamin D levels in an Australian population, BMC public health 14 (2014) 1-11.

**Türk Doğa ve Fen Dergisi**
**Turkish Journal of Nature and Science**
**www.dergipark.gov.tr/tdfd**

# The Effect of Grass Juice of Cereal Grown in Hydroponic Environment on the Germination of Medicinal and Aromatic Plants

**Banu KADIOĞLU¹\***

¹ Eastern Anatolia Agricultural Research Institute Management Soil and Water Resources Campus, Erzurum, Türkiye
Banu KADIOĞLU ORCID No: 0000-0002-9041-5992

*Corresponding author: banu250@hotmail.com*

**Abstract:** Today, the consumption of water obtained from cereals, which is very important in human nutrition, for health purposes is becoming increasingly common. Various plant extracts are used for this purpose. Soilless farming techniques have long been used as a plant growing medium. In the substrate culture of soilless farming systems, plants are grown in organic (peat, paper, etc.), inorganic (sand, vermiculite, etc.) or synthetic (polyurethane foam, etc.) materials. In our study, The grass juices obtained from barley, wheat and oat were used to determine the effects on seed physiology of medicinal and aromatic plants grown in hydroponic conditions. Medicinal and aromatic plant seeds placed in petri dishes were germinated in vitro. 10 ml of water (control), barley grass juice, wheatgrass juice and oat grass juice were applied to the seeds. The experiment was carried out according to the randomized plots factorial design. In the experiment, the germination physiology and root and stem lengths of the seeds were determined. As a result of the research, it was determined that cereal grass juices applications negatively affected germination physiology, root and stem lengths. It was determined that coriander seeds gave better results than others, and barley grass juice was more effective on germination physiology than wheat grass juice.

## Hidrofonik Ortamda Yetiştirilen Tahılların Çim Sularının Tıbbi ve Aromatik Bitkilerin Çimlenmesi Üzerine Etkileri

**Anahtar Kelimeler**
Arpa,
Buğday,
Yulaf,
Hidroponik
ortam,
Kök ve gövde
uzunluğu,
Çim suyu

**Öz:** Günümüzde insan beslenmesinde oldukça önemli olan tahıllardan elde edilen ekstraktların sağlık amaçlı tüketimi giderek yaygınlaşmaktadır. Bu amaçla çeşitli bitki ekstraktları kullanılmaktadır. Topraksız tarım teknikleri uzun süredir bitki yetiştirme ortamı olarak kullanılmaktadır. Topraksız tarım sistemlerinden substrat kültüründe bitkiler organik (turba, kağıt vb.), inorganik (kum, vermikülit vb.) veya sentetik (poliüretan köpük vb.) materyallerde yetiştirilmektedir. Çalışmamızda hidroponik ortamda yetiştirilen arpa, buğday ve yulaf çim sularının tıbbi ve aromatik bitkilerin tohum fizyolojisi üzerine etkileri araştırılmıştır. Petri kaplarına konulan tıbbi ve aromatik bitki tohumları in vitro koşullarda çimlendirilmiştir. Tohumlara 10 ml su (kontrol), arpa çim suyu, buğday çim suyu ve yulaf çim suyu uygulanmıştır. Deneme tesadüf parselleri faktöryel deneme desenine göre yürütülmüştür. Denemede tohumların çimlenme fizyolojisi ile kök ve gövde uzunlukları belirlenmiştir. Araştırma sonucunda çim suyu uygulamalarının çimlenme fizyolojisi ile kök ve gövde uzunluklarını olumsuz etkilediği belirlenmiştir. Kişniş tohumlarının diğerlerine göre daha iyi sonuç verdiği, arpa çim suyunun çimlenme fizyolojisi üzerine buğday çim suyuna göre daha etkili olduğu belirlenmiştir.

## 1. INTRODUCTION

For many years, cereal grass has been used as food due to its beneficial properties for health. In the last two decades, there has been an increasing trends in laboratory research on the human health benefits of cereal grasses [1]. The young leaves of the cereal grass, which is very rich in antioxidants, are very healthy. For this reason, it has recently received more attention as a natural medicine and scientific studies [2].

Wheat grass, which contains all nutrients, is called a whole food. It has been stated that wheat grass juice has

139

many benefits such as facilitating digestion, cleansing the blood, strengthening the immune system [3]. It has been reported that wheat grass juice has antioxidant and anti-carcinogenic effects and reduces the destructive effect of chemotherapy in breast cancer patients [4]. Barley, which has β-glucon content, contains a high amount of protein and is used as malt and grass juice [5]. It has been stated that barley grass extracts, which are an important source of antioxidants, are beneficial in the treatment of many diseases such as obesity, diabetes, blood circulation system disorders, anemia, joint inflammation, high cholesterol level, kidney diseases and cancer [6]. Oat grass juice is very rich in amino acids, vitamins, minerals, antioxidants and enzymes [7]. In a study in which oat grass juice was applied, it was stated that oat grass water extended the germination period of oil plant seeds and negatively affected seedling growth [8].

Hydroponic system is a method of growing plants using mineral nutrient solutions in water without using soil. In the study, the germination process of barley, wheat and oat seeds was provided by hydroponic system. The roots of the germinating plant interlock and take the appearance of a carpet. On average, the green part can reach 20-25 cm in seven days [9]. Much less water is needed in hydroponic farming therefore the contol of diseases and pests becomes easier. The hydroponic system provides high efficiency and reduces environmental pollution [10]. The yield in the hydroponic system varies depending on the type of seed used, water quality, pH, irrigation duration, presence of plant nutrients, temperature, and light intensity [11].

In the study carried out; It was aimed to determine the effect of barley, wheat and oat grass juices grown in hydroponic environment on the germination physiology and root and stem length of some medicinal and aromatic plants in hydroponic environment.

## 2. MATERIAL AND METHOD

The research was carried out under in vitro conditions (25±1°C) in 2023. In the study sage, fennel, coriander, linen, fenugreek, quinoa and mustard seeds were used. The study was carried out in a total of 140 petri dishes as 7 varieties x 4 applications x 5 replications according to the randomized plots factorial experimental design. To ensure surface sterilization of the seeds, the seeds were sterilized in 5% sodium hypochlorite solution for 10 minutes. Sterilized seeds; It was sown in petri dishes with a diameter of 9 cm and a height of 1.5 cm, 50 seeds in each petri dish, on 2 layers of filter paper (Whatman No: 2) placed on the bottom of the dishes. Grasses were obtained by sowing barley, wheat and oat seeds in 30x50x7 cm plastic tubs in a soilless environment. Harvesting was done with scissors ten days later. Grass juice was obtained by passing the grass through a juice extractor [12]. 10 ml of water (control), barley grass juice (bgj), wheat grass juice (wgj) and oat grass juice (ogj) were added to each petri dish [13]. In the experiment, the seeds were considered as germinated when they had 2 mm rootlets [14]. In the study,

germination rate (%), germination speed (days), mean daily germination (%), peak value (%) and germination value (%) root and stem length were determined based on ISTA rules [12; 15].

Germination percentage: n/Σn x 100      (1)

n = Number of germinated seeds
Σn= Total number of seeds

Germination rate: n1/t1+ n2/t2 +……      (2)

n1, n2, … number of germinated seeds t1, t2, …days

Mean daily germination: Total number of germinated seeds / total number of days      (3)

Peak value: Highest seed count/highest seeding day   (4)

Germination value: Mean daily germination x peak value      (5)

Root and Stem Length: At the end of the germination period of the seeds, the roots and stems of the seedlings were cut with a razor blade from their junctions and their lengths were measured with the help of a millimetric ruler. The average root/stem length was calculated as cm/plant by dividing the sum of root and stem lengths in a nymph by the number of seeds.

Differences between analysis of variance and means were performed in the LSD multiple comparison test by using JMP 5.0.1 program.

## 3. RESULTS

### 3.1 Germination Rate (GP %)

In the germination rate parameter, it was determined that the species and grass juice applications (gja) were important at 1%, and the interaction of species x grass juice application was insignificant. It was determined that coriander seeds (81.11) gave better results than the others (except GJA0-Control). It was determined that the applications had a negative effect on the germination rate compared to the control, and in the species x gja interaction, coriander seed had the highest value with 93.3 in wheat grass juice application (Figure 1).



**Figure 1.** The effect of species x grass juice applications on GP
GJA0= control, GJA1= coriander x bgj, GJA2= fennel x bgj, GJA3= sage x bgj, GJA4= linen x bgj,GJA5= fenugreek x bgj, GJA6= quinoa x bgj, GJA7= mustard x bgj, GJA8= coriander x wgj, GJA9= fennel x wgj, GJA10= sage x wgj, GJA11= linen x wgj, GJA12= fenugreek x wgj, GJA13= quinoa x wgj, GJA14= mustard x wgj, GJA15= coriander x bgj+wgj, GJA16= fennel x bgj+wgj, GJA17= sage x bgj+wgj, GJA18= linen x bgj+wgj, GJA19= enugreek x bgj+wgj, GJA20= quinoa x bgj+wgj, GJA21 = mustard x bgj+wgj

## 3.2 Germination Speed (GS days)

It was determined that species, grass juice applications and species x gja interaction were important at 1% during the germination period. It has been found that mustard seeds, whose germination speed has a negative effect on the species, are more sensitive. It was determined that grass juice applications decreased GS compared to the control. It was determined that ogj application got the lowest value with 2.78. Mustard seeds were found in barley grass juice with the lowest value of 0.78 in the species x gja interaction during the germination period (Figure 2).
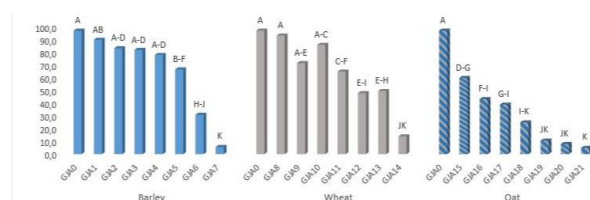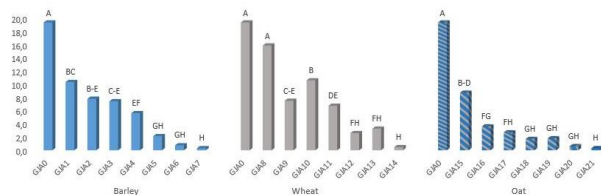
**Figure 2.** The effect of species x grass juice applications on GS
GJA0= control, GJA1= coriander x bgj, GJA2= fennel x bgj, GJA3= sage x bgj, GJA4= linen x bgj,GJA5= fenugreek x bgj, GJA6= quinoa x bgj, GJA7= mustard x bgj, GJA8= coriander x wgj, GJA9= fennel x wgj, GJA10= sage x wgj, GJA11= linen x wgj, GJA12= fenugreek x wgj, GJA13= quinoa x wgj, GJA14= mustard x wgj, GJA15= coriander x bgj+wgj, GJA16= fennel x bgj+wgj, GJA17= sage x bgj+wgj, GJA18= linen x bgj+wgj, GJA19= enugreek x bgj+wgj, GJA20= quinoa x bgj+wgj, GJA21 = mustard x bgj+wgj

## 3.3. Mean Daily Germination (MDG days)

When the mean daily germination parameter was examined, it was determined that the grass juice applications and species x gja interaction was insignificant, and it was significant in 1% of the species. Among the species, coriander seeds had the highest value with 7.04% and mustard seeds had the lowest value with 0.35. In the study, although the application of wgj (2.90) on the mean daily germination was more effective, it was not found to be statistically significant (Figure 3).
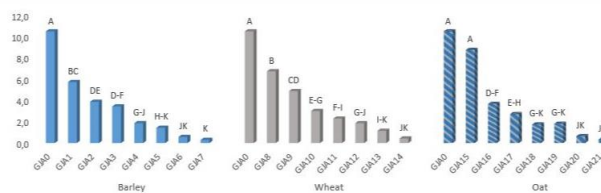
**Figure 3.** The effect of species x grass juice applications on MDG
GJA0= control, GJA1= coriander x bgj, GJA2= fennel x bgj, GJA3= sage x bgj, GJA4= linen x bgj,GJA5= fenugreek x bgj, GJA6= quinoa x bgj, GJA7= mustard x bgj, GJA8= coriander x wgj, GJA9= fennel x wgj, GJA10= sage x wgj, GJA11= linen x wgj, GJA12= fenugreek x wgj, GJA13= quinoa x wgj, GJA14= mustard x wgj, GJA15= coriander x bgj+wgj, GJA16= fennel x bgj+wgj, GJA17= sage x bgj+wgj, GJA18= linen x bgj+wgj, GJA19= enugreek x bgj+wgj, GJA20= quinoa x bgj+wgj, GJA21 = mustard x bgj+wgj

## 3.4. Peak Value (PV %)

When the peak value was examined, it was determined that the species and grass juice applications were important at 1%. Species x gja interaction was determined to be significant at 5%. In the study, it was determined that there were differences between the species, and sage seeds had the highest peak value with 1.67. It was determined that it was followed by fennel seeds with 1.55, coriander with 1.45, linen seeds with 1.42, fenugreek with 0.76, quinoa with 0.61 and mustard seeds with 0.35, respectively. In the grass juice application, the ogj application got the lowest value with 0.91. Coriander seeds had the highest value with 2.4 in the species x gja interaction in barley grass juice. It was determined that grass juice applications affected the investigated parameter negatively (Figure 4).
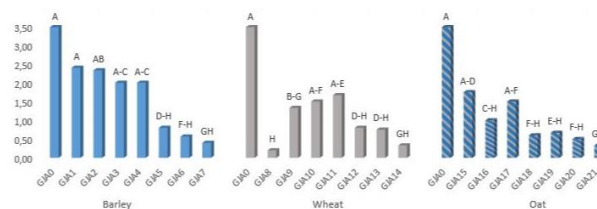
**Figure 4.** The effect of species x grass juice applications on PV
GJA0= control, GJA1= coriander x bgj, GJA2= fennel x bgj, GJA3= sage x bgj, GJA4= linen x bgj,GJA5= fenugreek x bgj, GJA6= quinoa x bgj, GJA7= mustard x bgj, GJA8= coriander x wgj, GJA9= fennel x wgj, GJA10= sage x wgj, GJA11= linen x wgj, GJA12= fenugreek x wgj, GJA13= quinoa x wgj, GJA14= mustard x wgj, GJA15= coriander x bgj+wgj, GJA16= fennel x bgj+wgj, GJA17= sage x bgj+wgj, GJA18= linen x bgj+wgj, GJA19= enugreek x bgj+wgj, GJA20= quinoa x bgj+wgj, GJA21 = mustard x bgj+wgj

## 3.5 Germination Value (GV %)

In the GV value, the species, gja and species x gja interaction was found to be significant at 1%. Among the species, coriander (7.52) had the best values barley grass juice with 4.98 compared to control in grass juice applications. It was determined that the coriander x barley grass juice interaction gave the best result with 13.71 in the species x gja interaction (Figure 5).
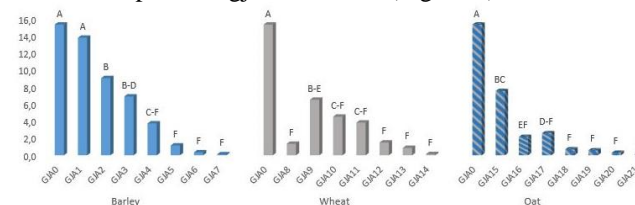
**Figure 5.** The effect of species x grass juice applications on GV
GJA0= control, GJA1= coriander x bgj, GJA2= fennel x bgj, GJA3= sage x bgj, GJA4= linen x bgj,GJA5= fenugreek x bgj, GJA6= quinoa x bgj, GJA7= mustard x bgj, GJA8= coriander x wgj, GJA9= fennel x wgj, GJA10= sage x wgj, GJA11= linen x wgj, GJA12= fenugreek x wgj, GJA13= quinoa x wgj, GJA14= mustard x wgj, GJA15= coriander x bgj+wgj, GJA16= fennel x bgj+wgj, GJA17= sage x bgj+wgj, GJA18= linen x bgj+wgj, GJA19= enugreek x bgj+wgj, GJA20= quinoa x bgj+wgj, GJA21 = mustard x bgj+wgj

## 3.6 Root and Stem Length (cm/plant)

In our study, in which we investigated the effect of grass juices on sage, fennel, coriander, linen, fenugreek, quinoa and mustard seeds, it was determined that the species, gja and species x gja interaction in root length was significant at 1%. In stem length, while the species and species x gja interaction was significant at 1%, grass juice applications were found to be insignificant. Fenugreek (0.61) got the best value in root length parameter. The barley grass juice with 0.51 and fenugreek x bgj interaction with 1.31 had the best values

141

compared to the control (Figure 6a). When we examine the stem length, mustard has the lowest value with 1.93. It was determined that quinoa x barley grass juice had the highest value with 3.33 in the species x gja interaction (Figure 6b).
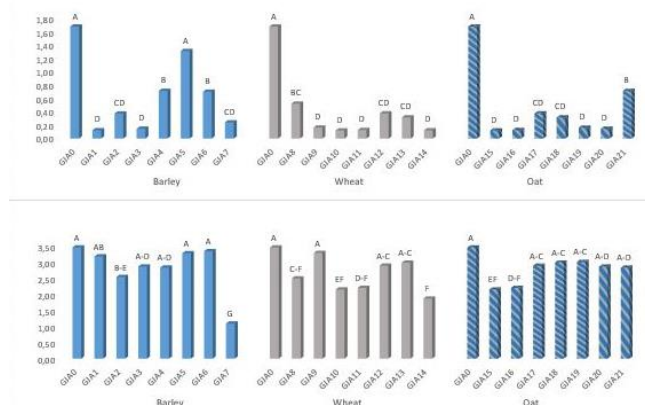


**Figure 6.** The effect of species x grass juice applications on root and stem length

GJA0= control, GJA1= coriander x bgj, GJA2= fennel x bgj, GJA3= sage x bgj, GJA4= linen x bgj,GJA5= fenugreek x bgj, GJA6= quinoa x bgj, GJA7= mustard x bgj, GJA8= coriander x wgj, GJA9= fennel x wgj, GJA10= sage x wgj, GJA11= linen x wgj, GJA12= fenugreek x wgj, GJA13= quinoa x wgj, GJA14= mustard x wgj, GJA15= coriander x bgj+wgj, GJA16= fennel x bgj+wgj, GJA17= sage x bgj+wgj, GJA18= linen x bgj+wgj, GJA19= enugreek x bgj+wgj, GJA20= quinoa x bgj+wgj, GJA21 = mustard x bgj+wgj

## 4. DISCUSSION AND CONCLUSION

Today, the consumption of plants for health purposes is increasing and cereals and cereal products are also consumed for this purpose. More grass juices are consumed for health purposes. Grass juices are very rich in terms of nutrients and vitamins [12]. Different studies are carried out such as the nutritional values of grass juices, their effects on health and other plants. In the study in which different doses (25, 50, 75 and 100%) of oat grass juice were applied, the germination of barley, wheat, oats, beans, lentils, sugar beet, sunflower, Italian grass, red clover, clover, cockscomb and wild mustard seeds rate, germination index, average germination time, shoot and root length were examined and it was stated that the effects of oat grass juice application and grass juice doses on germination and seedling development were negative [16]. In the study in which wheat grass juice was applied, barley (*Hordeum vulgare*), corn (*Zea mays*), wheat (*Triticum aestivum*), beans (*Phaseolus vulgaris*), clover (*Medicago sativa*), perennial grass (*Lolium perene*), sheep's ball (*Festuca ovina*) and the germination index, germination rate, and root and stem length of sugar beet (*Beta vulgaris*) seeds were examined and it was stated that wheat grass juice reduced the investigated properties [12]. According to the results we obtained from our research in parallel, it was determined that barley, wheat and oat grass juice applications had a negative effect on germination physiology, root and stem development. Grain juice contains alkaloid, saponin, gum, mucilage, protein and amino acid [17]. Because it contains these substances, it is thought to have an allelopathic effect on the germination and development of other plant species. The allelopathic effect can affect plant growth by affecting metabolic events such as

photosynthesis, respiration and ion uptake mechanisms in plants [18]. In the study where the effects of different doses of carbon dioxide applications on turf water yield and nutritional values in hydroponic wheat (*Triticum aestivum* L.) grass juice production were determined, three different carbon dioxide doses (Control; 0, D1; 750, D2; 1500 and D3; 2000 ppm) were applied to the growing medium. The effects on plant yield, seed rate, plant and grass yield, grass juice yield and pH, plant height and root length were investigated. It was stated that the highest plant, grass and grass juice yields and plant height values were obtained from D1 application, while the highest root length values were obtained from D1 and D3 applications [19]. In our study, the highest root and plant length were obtained from the barley grass juice application, and the lowest values were obtained from the wheat grass juice application. In another study conducted in hydroponic environment, the yield and nutritional values of barley, wheat and corn grass juice were examined, plant height and root length were examined and it was determined that the highest root length belonged to the corn plant [20]. Karaman et al. [21] investigated the effects of essential oil doses obtained from lavender plant on culture and foreign plants and reported that with the increase of lavender oil doses, germination and seedling properties decreased. In a study examining the effects of 6% plant extract doses (20, 40, 80 and 100%) of vinegar weed on germination and abnormal grass formation characteristics of rapeseed seeds, it was stated that 100% vinegar plant extract caused the lowest germination and the highest abnormal seedling percentage [22]. In our study, it has been determined that the mustard species, in which the responses of plant species to grass juice are different, are more sensitive to grass juice applications. In the study in which the effect of plant extracts on the germination and seedling growth of pepper was determined, it was stated that the inhibition effect and rate of plant extracts changed depending on the species and doses [23]. In a study in which the plant extract doses obtained from radish species and turnip plants were applied to cockscomb, barren wild oats, purslane, wild mustard, it was reported that there was a significant decrease in germination and shoot and root lengths in parallel with increasing doses [24]. In another study, it was determined that the sap obtained from squash shoots applied to cockscomb and vinegar weed seeds inhibited germination [25]. In another study, it was reported that the extract obtained from the leaves of salvia and celery plant had a negative effect on lentil seed germination and seedling growth, and inhibited root development [26].

The young leaves of cereal grass juices are very beneficial for human health, as they are rich in antioxidants. There has been an increasing interest in the use of grain juices, which contain all nutrients, as a natural medicine. Plant growing technique without using soil is called soilless farming technique. Media and water culture are used in soilless agriculture. In the study used in two cultures, it was determined that medicinal and aromatic plant seeds using barley, wheat and oat grass juices grown in hydroponic conditions have a negative effect on germination physiology and root and stem lengths. It was determined that coriander seeds

142

gave better results than others, and barley grass juice was more effective on germination physiology than wheat grass juice. The effects of different plant extracts on different plants should be determined in the future studies.

## REFERENCES

[1] Yadav M, Sethi J, Dahyia K, Sood S, Gupta V, Singh V, et al. Effect of *Triticum aestivium* on physiological and biochemical parameters in high fat diet fed rabbits. JK Practitioner. (2013); 18 (3-4): 39-42.

[2] Urbonaviciute A, Samuoliene G, Brazaityte A, Duchovskisukauskas A. The effect of variety and lighting qualityon wheatgrass antioxidant properties. Zemdirbyste-Agriculture. (2009); 96 (3): 119-128.

[3] Anonymous [Internet]. Miracle superfood: wheatgrass benefits; 2022 [cited 2022 May 25]. Available from: https://www.fhi.no/nettpub/utbruddsveilederen/

[4] Ashish S, Shilpa K, Singh RR, Sanjav K, Rajendran N. Wheatgrass: an alternative household nutritional food security. International Research Journal of Pharmacy. (2012); 3 (7): 246-250.

[5] Altuner F, Oral E, Ülker M. Determination of yield and quality components of some barley (*Hordeum vulgare* L.) cultivars. Journal of Bahri Dagdas Crop Research. (2018); 7 (2): 11-22.

[6] Paulickova I, Ehrenbergerova J, Fiedlerova V, Gabrovska D, Havlova P, Holasova M, et al. Evaluation of barley grass as a potential source of some nutritional substances. Czech Journal of Food Science. (2007); 25: 65–72.

[7] Rexhepi-Hasani A, Renata K. Consumer acceptance and readiness to pay for green juices containing grain grass juices in Kosovo. Journal of the Association-Institute for English Language and American Studies. (2015); 4 (6): 49-57.

[8] Ergin N, Kaya MD. Bazı yağ bitkileri tohumlarının çimlenme ve fide gelişimi üzerine iki yulaf çeşidinin allelopatik etkileri. Iğdır Üniversitesi Fen Bilimleri Enstitüsü Dergisi. (2020); 10 (2): 1419-1428.

[9] Karasahin M. Green fodder production in hydroponic medium. Harman Time Magazine. (2014); 12: 2-4.

[10] Uyeda J, Cox LJ, Radovich TJ. An Economic comparison of commercially available organic and inorganic fertilizers for hydroponic lettuce production. Sustainable Agriculture. (2011); 5: 1-4.

[11] Fazaeli H, Golmohammadi HA, Tabatabayee SN, Asgari-Tabrizi M. Productivity and nutritive value of barley gren fodder yield in hydroponic system. World Applied Science Journal. (2012); 16 (4): 531-539.

[12] Akgun İ, Ayata R, Karaman R. Effect of wheat grass (*Triticum aestivum* l.) juice on seed germination. Academia Journal of Engineering and Applied Sciences. (2018); 1 (4): 19-24.

[13] Prodo FE, Boero C, Gallardo M, Gon-zalez JA. Effect of NaCl on germination growth and soluble sugar content in che-nopodium quinoa (Wild) seeds. Bot. Bull. Acad. Sin. (2000); 41: 27-34.

[14] ISTA. The Rules: International Rules for Seed Testing, ISTA, Zürih, Switzerland; 1996.

[15] Kadioglu B. Effect of different bacterial strains on the germination forage pea (*Pisum sativum* ssp. arvense L.) under salt stress. Legume Research. (2021); 44 (11): 1333-1337.

[16] Karaman R, Turkay C, Akgun İ. Effects of oat grass juice on germination and seedling characteristics of certain weeds and cultivated plants. Journal of Tekirdag Agricultural Faculty. (2021); 18 (2): 312-321.

[17] Ashok AS. Phytohemıcal and pharmacologıal screenıng of wheatgrass juice (*Triticum aestivum* L.). International Journal of Pharmaceutical Sciences. (2011); 9(1): 159-164.

[18] Terzi İ. Effects of walnut fruıt hull extracts on muskmelon seed germınatıon, seedlıngs elongatıon and dry weıghts. Anadolu Unıversıty Journal of Scıence and Technology. (2007); 8 (2): 355-360.

[19] Karasahin M. Grass juice yield and nutritional values of some cereals ın soilless culture. Iğdır Univ. J. Inst. Sci. &Tech. (2015); 5 (4): 57-64.

[20] Karasahin M. The effects of different carbon dioxide doses on yield and nutritional values of hydroponic wheat (*Triticum aestivum* L.) grass juice. International Journal of Agriculture and Wildlife Science (IJAWS). (2015a); 1 (2): 78 – 84.

[21] Karaman R, Erbaş S, Baydar H, Kaya M. Allelopathic effect of lavandin (Lavandula x intermedia Emeric ex Loisel. var. Super A) oil on germination and seedling development of some weed and field crops. Harran Journal of Agricultural and Food Sciences. (2014); 18 (4): 35-41.

[22] Ghiyasi M, Ozdemir FA, Amirnia R, Tajbakhsh M, Rahimi A. Allelopathic effect of chenopodium album l. on germination and abnormal seedling of canola (*Brassica napus* L.). BEU Journal of Science. (2016); 5 (2): 225-228.

[23] Ozbay N. Allelopathic Effects of some Herbs and Medicinal Plants' Extracts on Seed Germination and Seedling Growth of Pepper. Turkısh Journal of Agrıcultural and Natural Scıences. (2018); 5 (1): 81-85.

[24] Ozdemir S. Investıgatıons of bıo herbıcıdal potentıal of plant extracts obtaıned from some crops in brassıcaceae famıly for weed control. [Master's Thesis]. Antakya: Mustafa Kemal University Institute of Science and Technology; 2007.

[25] Qasem LR, Issa NN. Allelopathic effects of squash (*Cucurbita pepo* L. Cv. Scarlette) on ceratain common weed species in Jordan. Proceedings of the 4th World Congress on Allelopathy, "Establishing the Scientific Base", Wagga Wagga, New South Wales, Australia: 2005. p. 258-262.

[26] Stratu A, Toma D, Costica N. The effect of extracts from Apium graveolens L. and Evisticum officinale koch leaves on the germination of certain dicotyledons species. An. Stiint. Univ. Al. I. Cuza Iasi, Sect. II a. Biol. Veget. (2012); 58 (2): 73-79.

143

**Türk Doğa ve Fen Dergisi**
**Turkish Journal of Nature and Science**
www.dergipark.gov.tr/tdfd

# Brain Extraction from Magnetic Resonance Images Using UNet modified with Residual and Dense Layers

## Kali GÜRKAHRAMAN[1*] ⓘD, Çağrı DAŞGIN[2] ⓘD

[1] Sivas Cumhuriyet University, Faculty of Engineering, Department of Computer Engineering, Sivas, Türkiye
[2] Sivas Cumhuriyet University, Institute of Science, Department of Computer Engineering, Sivas, Türkiye
Kali GÜRKAHRAMAN ORCID No: 0000-0002-0697-125X
Çağrı DAŞGIN ORCID No: 0009-0006-9932-5789

*\*Corresponding author: abc@bingol.edu.tr*

**Abstract:** The main goal of brain extraction is to separate the brain from non-brain parts, which enables accurate detection or classification of abnormalities within the brain region. The precise brain extraction process significantly influences the quality of successive neuroimaging analyses. Brain extraction is a challenging task mainly due to the similarity of intensity values between brain and non-brain structure. In this study, a UNet model improved with ResNet50 or DenseNet121 feature extraction layers was proposed for brain extraction from Magnetic Resonance Imaging (MRI) images. Three publicly available datasets (IBSR, NFBS and CC-359) were used for training the deep learning models. The findings of a comparison between different feature extraction layer types added to UNet shows that residual connections taken from ResNet50 is more successful across all datasets. The ResNet50 connections proved effective in enhancing the distinction of weak but significant gradient values in brain boundary regions. In addition, the best results were obtained for CC-359. The improvement achieved with CC-359 can be attributed to its larger number of samples with more slices, indicating that the model learned better. The performance of our proposed model, evaluated using test data, is found to be comparable to the results obtained in the literature.

144

# Artık ve Yoğun Katmanlarla Değiştirilmiş UNet Kullanılarak Manyetik Rezonans Görüntülerinden Beyin Çıkarımı

**Öz:** Beyin çıkarımının temel amacı, beyni beyin dışı kısımlardan ayırarak beyin bölgesi içindeki anormalliklerin doğru tespitini veya sınıflandırılmasını mümkün kılmaktır. Hassas beyin çıkarma işlemi, ardışık nörogörüntüleme analizlerinin kalitesini önemli ölçüde etkiler. Beyin çıkarımı, beyin ve beyin dışı yapılar arasındaki yoğunluk değerlerinin benzerliği nedeniyle zorlu bir görevdir. Bu çalışmada, Manyetik Rezonans Görüntüleme (MRG) görüntülerinden beyin çıkarımı için ResNet50 veya DenseNet121 öznitelik çıkarma katmanları ile geliştirilmiş bir UNet modeli önerilmiştir. Derin öğrenme modellerini eğitmek için IBSR, NFBS ve CC-359 adlı üç halka açık veri kümesi kullanılmıştır. UNet'e eklenen öznitelik çıkarma katman türleri arasındaki karşılaştırma sonuçları, ResNet50'den alınan artık bağlantıların tüm veri kümelerinde daha başarılı olduğunu göstermektedir. ResNet50 bağlantılarının, beyin sınır bölgelerindeki zayıf ancak önemli gradyan değerlerinin ayrımını artırmada etkili olduğu anlaşılmaktadır. Ayrıca, en iyi sonuçlar CC-359 için elde edilmiştir. CC-359 ile elde edilen gelişme, verisetinin daha fazla kesit ve örnek içermesinden dolayı modelin daha iyi öğrenmesinden kaynaklanmıştır. Önerilen modelin performansı, test verileri kullanılarak değerlendirildiğinde, literatürde elde edilen sonuçlarla karşılaştırılabilir bulunmuştur.

# 1. INTRODUCTION

The non-invasive Magnetic Resonance Imaging (MRI) technique provides rich information about the examined anatomical structure due to its high spatial resolution. It is widely used in the early diagnosis and assessment of many diseases, since it provides the detection of changes in brain structures that may develop even in micro dimensions over time. However, due to its high resolution, it also causes the detailed presence of non-brain structures such as skull, scalp and eyeballs in the MRI scans [1]. The removal of non-brain structures may have a significant impact on the subsequent analyses related to the brain.

Brain extraction, also known as skull stripping, is the initial step in analyzing MRI and other neuroimaging data, involving the separation of the brain from non-brain parts [2-3]. Its primary goal is to remove the skull and provide leverage in obtaining high accuracy for the detection or classification of any abnormalities within the relevant brain region [3, 4]. Accurate brain extraction significantly impacts the quality of neuroimaging studies, including image registration, brain tumor or lesion segmentation, measurement of brain regions of interest for global and neurodegenerative diseases, detection of cortical thickness, and planning neurosurgical interventions [2].

Brain extraction is a challenging task mainly due to the similarity of intensity values between brain and non-brain structure [3]. The partial volume effect blurs the boundaries between two tissues, making it difficult to distinguish structures especially in low contrast brain images. Interpreting brain structures that lack sharp edges in brain images, and the presence of unwanted signals (artifacts) at air/tissue boundaries in brain images, further adds to the complexity. Moreover, motion artifacts from the patient and noise from the imaging environment can reduce image quality and increase the difficulty of brain extraction [1].

In the literature, manual segmentation is considered the "gold standard" for brain extraction [5-6]. However, this method is not only labor intensive and time consuming, but also exhibits significant inter-individual variability, potentially introducing analysis bias and thus impeding the reproducibility of clinical studies [2]. Therefore, in recent years, many semi-automatic or fully automatic brain extraction techniques have been proposed with the aim of overcoming the drawbacks encountered in manual segmentation [1].

In the morphological and intensity-based initial brain extraction methods, selecting the most appropriate threshold value(s) to separate foreground and background is often challenging [1, 3]. Brain Extraction Tool (BET) and BET2 techniques developed by Smith [5] and Jenkinson et al. [7], define an initial sphere by determining the center of gravity of the head and deforming it until it reaches the brain edge. Brain Surface Extraction (BSE) technique developed by Shattuck et al. [8] uses an edge-based approach with anisotropic

diffusion filtering. It has been reported that BET works poorly on neck-intense images and BSE has lower performance on low-resolution images [1]. Moreover, BET and BSE techniques require parameters to be optimized for each image, making them challenging to use in large-scale studies [1, 6].

Atlas/template-based brain extraction methods involve adapting an atlas/template MRI brain image to reveal relationships between brain regions, thereby separating structures with no relationship into brain and non-brain. The widely used atlas-based Brain Extraction using Nonlocal Segmentation Technique (BEaST) is fast and achieved successful performance on T1-weighted MRI images of both healthy individuals and Alzheimer's patients [9]. However, this method requires parameter optimization depending on the dataset used.

Hybrid techniques for brain extraction involve combining the results of multiple methods. Souza et al. [6] prepared a dataset called Calgary-Campinas-359 (CC-359), which contains 359 T1-weighted MRI images of healthy individuals. In their study, the images were segmented with eight different methods, and the segmentation error was reduced by evaluating the results of multiple methods using the expectation-maximization technique. However, the hybrid technique benefits from results of techniques like BEaST, BET, and BSE, which require parameter optimization [6].

Recently, deep learning (DL) techniques, which have achieved successful results in medical image analysis and imaging, have demonstrated the potential to outperform medical experts in solving specific problems [4, 10-12]. DL models proposed for brain extraction are also available in the literature [13]. Kleesiek et al. [14] developed a deep convolutional neural network (CNN) model for brain extraction from MRI images in three different open datasets and achieved high-performance results. Isensee et al. [2] developed a 3D-UNet-based method called HD-BET, which performed brain extraction by examining brain images of healthy individuals as well as those with various pathologies, apart from MRI images of healthy individuals. They trained the DL model with images obtained from different sequences (T1, T2, and FLAIR) and MRI devices, and tested it on open brain image datasets, achieving successful results. Similarly, Hwang et al. [15] used a modified 3D-UNet model from a 2D-UNet model for brain extraction from T1-weighted MRI images. The developed DL model achieved high performance compared to traditional models, but its performance on MRI images obtained from different devices is uncertain. Zhang et al. [16] modified the 3D-UNet model and developed the FRNET model, in which residual layers were added between encoder and decoder blocks, and a new boundary loss function was used during model training. FRNET was tested only on infant MRI dataset and achieved high dice score values for brain extraction. Similarly, Dasgin and Gurkahraman [17] showed the effectiveness of the 3D-UNet model modified with residual connections in brain extraction. Hoopes et al. [18] used generative DL model to synthesize medical images

and then generalized real brain images from these synthesized images using a 3D-UNet model, which they called SynthStrip. SynthStrip significantly improved performance values obtained by traditional methods for different datasets.

In summary, DL-based automatic brain extraction techniques are faster than traditional methods and do not require parameter optimization. However, the selection of the brain extraction method depends on the problem and is influenced by the characteristics of MRI images. Therefore, when choosing a brain extraction technique, factors such as the model of the MRI scanner and magnetic field intensity (Tesla) should be taken into account. In image segmentation studies, previous studies have shown that the 3D- UNet model outperformed CNN models and that enriching the latent layer of the 3D- UNet model with residual and dense connections between encoder and decoder blocks improved accuracy performance. Therefore, this study aims to perform brain extraction on MRI images obtained from different MRI scanners with different magnetic field intensity values by adding feature extraction layers of ResNet and DenseNet architectures to the UNet model.

## 2. MATERIAL AND METHOD

In this study, a UNet model improved with residual and dense connections was proposed for brain extraction from MRI images. In the following subsections, the details of the datasets used and the developed method are presented.

### 2.1. Datasets

In this study, three different publicly available datasets, The Internet Brain Segmentation Repository (IBSR) [19], The Neurofeedback Skull-stripped (NFBS) [20], and CC-359 [6], were utilized for training and testing the 3D-DL model.

The IBSR dataset [19] includes 3D-T1 weighted gray images acquired from 18 healthy subjects using a 1.5 Tesla Siemens Magnetom MRI scanner, along with manually segmented brain mask images by experts.
The NFBS dataset [20] consists of images from 125 participants with various clinical and psychiatric histories, acquired using a 3T Siemens Magnetom TIM Trio scanner with a resolution of $1 \times 1 \times 1$ mm³. The brain mask images were also manually segmented by experts.

The CC-359 dataset [6] includes brain images with a slice thickness of $1 \times 1 \times 1$ mm³ from 359 healthy individuals aged between 29 and 80 years, acquired using 1.5/3.0

Tesla Philips, Siemens, and GE MRI scanners. In this study, the images were saved in NIfTI (.nii) format without data loss, and both gray and mask images were created. Note that not all images in the dataset have manual segmentations available. Thus, the brain mask images recommended as the silver standard by Souza et al. [6], using the Simultaneous Truth and Performance Level Estimation (STAPLE) technique, were used as ground truth in this study.

### 2.2. UNet-based 3D Deep Learning Model

Autoencoder is a data compression algorithm that automatically perform compression and decompression functions specific to the data, and the autoencoder in the DL model implements these functions using neural networks. To create an autoencoder, a coding function, a decoding function, and an error function showing the information loss between the compressed and uncompressed representations of the data are required [21]. The UNet model, fundamentally an autoencoder, consists of an encoder that encodes the input image into low-level features at multiple levels and a decoder that reflects these features into pixel space. With its symmetrical structure, UNet uses skip connections between the encoder and decoder to preserve image information in greater detail [22, 23].

Figure 1 shows the 3D UNet model modified with the feature extraction layers of the ResNet50 [24] and DenseNet121 [25] models proposed for ImageNet. The model consists of two different blocks, encoder, and decoder, each containing convolution and deconvolution layers. In the middle part of this general structure, the residual/dense blocks of ResNet50 and DenseNet121 models were adapted to achieve better compression of information, and the brain extraction results were compared.

In the encoder blocks, four convolution blocks with filter sizes of 8, 32, 64, and 64 were used, respectively. Each block consists of a 3x3x3 convolution operation, followed by batch normalization (BN) and ReLU activation. This process is repeated twice, and finally, the feature maps' dimensions are reduced using max pooling. In the decoder blocks, there are four upsampling blocks with filter sizes of 64, 64, 32, and 8, respectively. The operations in the decoder blocks consist of upsampling (transposed convolution), followed by two repetitions of Convolution, BN, and ReLU. The activation function used in the final block is sigmoid.
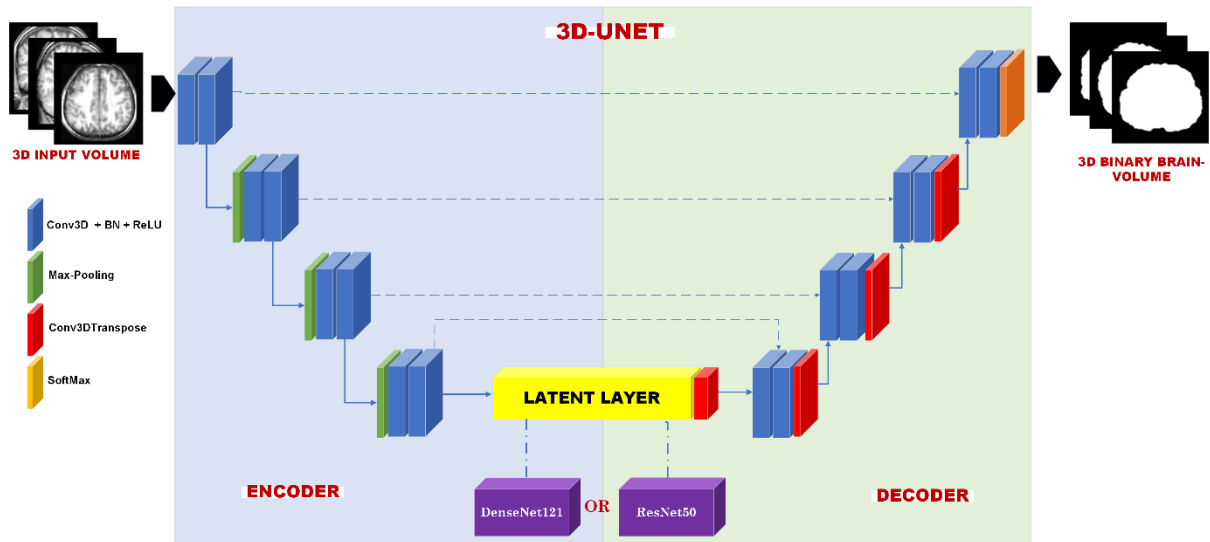
**Figure 1.** 3D-UNet model modified with feature layers of the DenseNet121 and ResNet50.

For the experiments, due to the limited number of samples in the IBSR dataset (only 18 samples), the datasets were split into 80% for training and 20% for testing, with the test set also serving as the validation set. A dataset's optimal train-test split ratio for DL applications is not clearly defined. In this study, we adopted the widely favored experimental train-test ratio of 80%-20%, as commonly seen in the DL medical image analysis literature [26-27]. The optimization technique used during training was ADAM, with a learning rate of 0.0002 and a momentum coefficient of 0.8. The number of epochs was set to 500 for IBSR and 100 for the other datasets, with early stopping as an option. The batch size was set to 4 due to hardware limitations for training the 3D model. The 3D-UNet model was implemented using the Keras library in Python 3.9 based on Tensorflow. The experiments were conducted on a PC with a NVIDIA RTX A6000 48 GB GPU, Intel i9 12900 KS @ 3.40 Hz CPU, and 64 GB RAM.

To compare the performances of the dense and residual blocks in the latent layer of the model under the same conditions, the rest of the architecture was designed to be the same, and the traditional loss function, binary-cross entropy, was used.

### 2.3. Performance Metrics

The segmentation performance of the UNet model was assessed using the Dice coefficient, sensitivity, and specificity metrics. The Dice coefficient, as given in Equation 1, is calculated by dividing twice the intersection of the real (R) and predicted (P) masks by the sum of the areas of both masks.

$$Dice = \frac{2|P \cap R|}{|P|+|R|} = \frac{2TP}{2TP+FP+FN} \qquad (1)$$

where TP, FP, and FN represent True Positive, False Positive, and False Negative, respectively.

Sensitivity, also known as recall, assesses the proportion of brain tissue that is successfully included in the segmentation. Specificity gauges the proportion of non-brain tissue that is accurately excluded from the segmentation (Equation 2).

$$Sensitivity = \frac{TN}{TN+FP} \qquad (2)$$

$$Specificity = \frac{TP}{TP+FN} \qquad (3)$$

### 3. EXPERIMENTAL RESULTS AND DISCUSSION

147

The experiments were performed by training and testing two separate UNet architectures modified with DenseNet121 and ResNet50 feature extraction layers. Both architectures were trained and tested on the IBSR, NFBS, and CC359 datasets. The training and testing datasets were randomly split to ensure the model was tested on data it had not seen during the training process. The training and testing procedures were repeated five times, and the average performance values were computed.

The results of all experiments are presented in Table 1. Each cell in the table shows the average and standard deviation of five test results. When comparing the different feature extraction layer types added to the UNet architecture, the most successful results were achieved with ResNet50 across all datasets. However, when considering individual datasets, the most successful outcomes were obtained with CC-359. The residual connections in the ResNet50 architecture particularly improved the distinction of weak but important gradient values in the brain boundary regions. On the other hand, according to the datasets, the improvement can be attributed to the larger number of samples and more slices in the CC-359 dataset, indicating that the model learned better.

**Table 1.** Average performance values of modified UNet models.

| Dataset | Models | Dice Coefficient | Sensitivity | Specificity |
|---------|--------|-----------------|-------------|-------------|
| IBSR | ResNet50 | 0.9613 (±0.0036) | 0.9590 (±0.0017) | 0.9931 (±0.0010) |
| | DenseNet121 | 0.9473 (±0.0063) | 0.9211 (±0.0230) | 0.9955 (±0.0016) |
| NFBS | ResNet50 | 0.9875 (±0.0018) | 0.9840 (±0.0048) | 0.9990 (±0.0005) |
| | DenseNet121 | 0.9838 (±0.0067) | 0.9812 (±0.0146) | 0.9985 (±0.0010) |
| CC-359 | ResNet50 | 0.9887 (±0.0028) | 0.9899 (±0.0058) | 0.9985 (±0.0009) |
| | DenseNet121 | 0.9872 (±0.0025) | 0.9874 (±0.0069) | 0.9985 (±0.0011) |

The sample results obtained with the IBSR, NFBS, and CC-359 datasets are presented in Figure 2-4. Upon examining the generated binary segmentation masks, they demonstrate consistency with the Dice scores given in Table 1. It is evident that the key factor influencing the segmentation performance is how well the model has learned the boundary regions. Across all cases, the most successful segmentation masks are produced by the model with residual connections. Comparing the results from all figures, the most promising outcomes are achieved for the CC-359 dataset, as shown in Figure 4. Our observation that the model learned better with the CC-359 dataset due to more samples and more slices is also supported by the segmentation results.
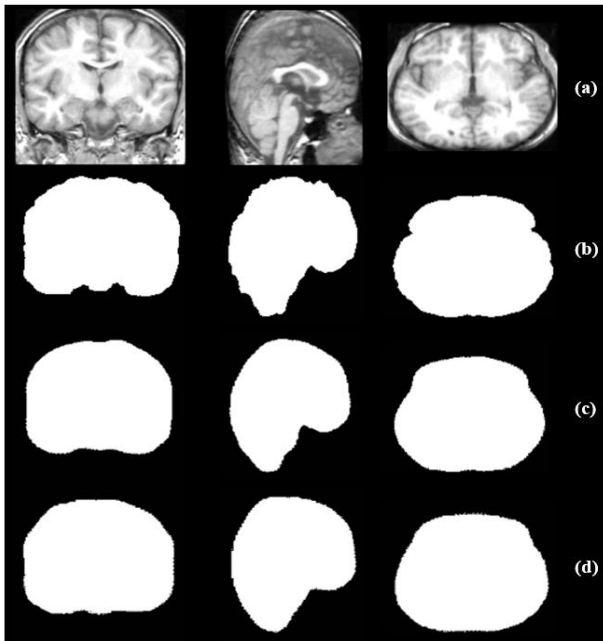


**Figure 2.** IBSR results, a) original gray, b) binary ground-truth, c) UNet with ResNet binary result, d) UNet with DenseNet binary result



**Figure 3.** NFBS results, a) original gray, b) binary ground-truth, c) UNet with ResNet binary result, d) UNet with DenseNet binary result
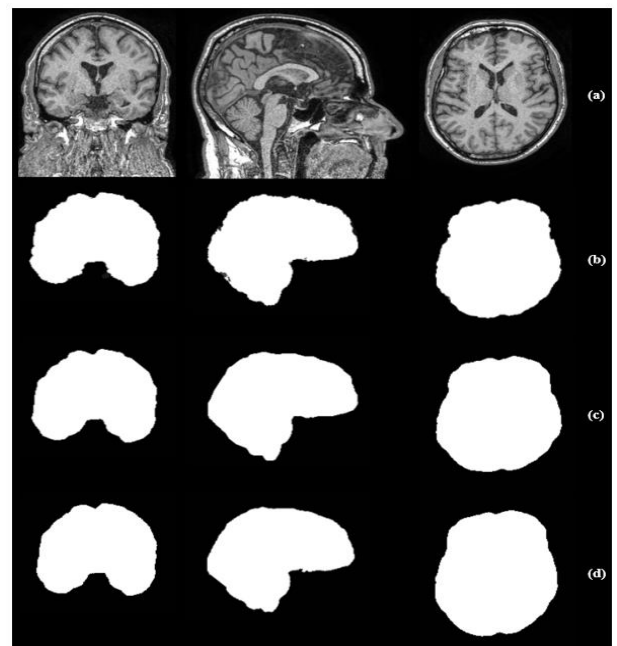


**Figure 4.** CC-359 results, a) original gray, b) binary ground-truth, c) UNet with ResNet binary result, d) UNet with DenseNet binary result

Table 2 provides a comparison of our model with the studies from the literature which used DL architecture and the same datasets. The comparisons were performed using the results of the 3D-UNet model based on ResNet50, which yielded better results than the DenseNet-based architecture. Kleesiek et al. [14] achieved Dice scores, sensitivity, and specificity values of 0.9632, 0.9501, and 0.9961, respectively, for the IBSR dataset using their proposed CNN model. Hwang et al. [15] compared their 3D-UNet architecture results, obtained for the NFBS dataset, with traditional techniques such as BSE [8], Robust Brain Extraction (ROBEX) [28], and CNN model's results [14], demonstrating superior performance

values. As evident from Table 2, the performance values obtained in this study for the IBSR dataset are competitive with Kleesiek et al.'s [14] results. For the NFBS dataset, the average Dice and sensitivity values are comparable to those of Hwang et al. [15], while our specificity value is higher. Moreover, the Dice values obtained for the NFBS and CC-359 datasets are higher than those achieved by Isensee et al.'s [2] HD-BET method, which reported Dice coefficient values of 0.9820 for NFBS and 0.9690 for CC-359 datasets. Although this study exclusively used NFBS and CC-359 datasets for testing, the model was trained on a large dataset consisting of 6586 samples collected from 25 different institutions.

**Table 2.** Literature comparison

| Study | Model | Dataset | Dice | Sensitivity | Specificity |
|-------|-------|---------|------|-------------|-------------|
| Kleesiek et al. [14] | CNN | IBSR | 0.9632 (±0.0100) | 0.9501 (±0.0200) | 0.9961 (±0.0030) |
| Hwang et al. [15] | 3D-UNet | NFBS | 0.9903 (±0.0016) | 0.9853 (±0.0040) | 0.9953 (±0.0022) |
| Isensee et al. [2] | HD-BET | NFBS | 0.9820(±0.0020) | - | - |
| | (3D-UNet) | CC-359 | 0.9690(±0.0020) | - | - |
| **This study** | **ResNet-based** | IBSR | 0.9613 (±0.0036) | 0.9590 (±0.0017) | 0.9931 (±0.0010) |
| | **3D-UNet** | NFBS | **0.9875 (±0.0018)** | 0.9840 (±0.0048) | **0.9990 (±0.0005)** |
| | | CC-359 | **0.9887 (±0.0028)** | **0.9899 (±0.0058)** | **0.9985 (±0.0009)** |

The process of refining brain images by eliminating non-brain regions is crucial for improving the performance of artificial intelligence (AI) algorithms, particularly in medical applications like classification and disease analysis. It offers several advantages: Firstly, it enhances accuracy by ensuring AI algorithms focus exclusively on pertinent brain structures, minimizing diagnostic errors. Secondly, it boosts efficiency by simplifying data, enabling faster processing, which is vital for real-time healthcare applications. Additionally, it promotes better generalization, helping AI models perform well on new cases without being affected by irrelevant data. Its clinical value lies in facilitating precise and timely diagnoses, aiding healthcare professionals in informed decision-making. Lastly, purified brain data advances neuroscience and medical research, allowing for a deeper understanding of neurological conditions. In essence, the purification of brain images by excluding non-brain regions is a critical preprocessing step that enhances AI algorithms' performance in medical fields, benefiting clinical practice and scientific research.

DL-based brain extraction has potential to improve the accuracy and efficiency of clinical applications significantly. It not only saves time but also reduces the risk of human error, making it a valuable tool in modern healthcare for diagnosing, monitoring, and researching neurological conditions and brain function. As DL algorithms continue to evolve, we can expect even greater advancements in the field of brain image analysis such as disease diagnosis and monitoring, functional brain imaging, and treatment planning. Disease diagnosis and monitoring includes such as tumor detection and analysis, stroke assessment, and neurodegenerative diseases. Accurate brain extraction helps in identifying and characterizing brain tumors. It can aid in tumor volume measurement and tracking changes over time, which is crucial for treatment planning and monitoring. In stroke diagnosis, it's important to accurately segment the brain to identify regions affected by ischemia or hemorrhage. This information assists in determining the extent of brain

damage and guiding treatment decisions. DL-based brain extraction can improve the accuracy of identifying brain regions affected by neurodegenerative diseases like Alzheimer's and Parkinson's. It can facilitate early diagnosis and disease progression monitoring. For the treatment planning, in both neurosurgery and radiation therapy for brain tumors, accurate brain segmentation plays a pivotal role. Precise brain segmentation provides surgeons with a clear view of the brain's structure, enabling them to plan the safest and most effective approach for tumor removal or other procedures in neurosurgical interventions. In radiation therapy, knowing the exact boundaries of the brain is essential to prevent damage to healthy tissue, and accurate brain extraction helps define the treatment target.

## 4. CONCLUSION

This study proposed an improved UNet architecture including residual and dense feature extraction layers to address the challenging problem of extracting brain from surrounding structures, primarily due to pixel intensity similarities. The obtained results demonstrate that the model's performance is particularly dependent on its ability to accurately segment the boundary regions of the brain and other structures. The superior performance of the architecture with residual connections can be attributed to its capability to preserve weak gradient values in deep layers. The findings also emphasize the importance of large-scale training data, as evidenced by the best results obtained for the CC-359 dataset. It highlights the significance of extensive training data for achieving improved performance. Comparing our proposed model to relevant literature studies utilizing the same dataset and UNet-based models, it yields comparable performance results.

In conclusion, for future research in this domain, focusing on architectures and loss function selection that target the distinguishing ability of boundary regions could be a

realistic approach, given its significant impact on the model's performance.

## Conflict of Interest Statement

There is no conflict of interest between the authors.

## REFERENCES

[1] Kalavathi P, Prasath VS. Methods on skull stripping of MRI head scan images-a review. Journal of Digital Imaging. 2016; 29: 365-379.

[2] Isensee F, Schell M, Pflueger I, Brugnara G, Bonekamp D, Neuberger U, et al. Automated brain extraction of multisequence MRI using artificial neural networks. Human Brain Mapping. 2019; 40(17): 4952-4964, 2019.

[3] Bhat SY, Naqshbandi A, Abulaish M. Skull stripping on multimodal brain MRI scans using thresholding and morphology. The Imaging Science Journal, 2023; 1-13.

[4] Karakis R, Gurkahraman K, Mitsis GD, Boudrias MH. Deep learning prediction of motor performance in stroke individuals using neuroimaging data. Journal of Biomedical Informatics. 2023; 141: article number 104357.

[5] Smith SM. Fast robust automated brain extraction. Human Brain Mapping. 2002; 17: 143-155.

[6] Souza R, Lucena O, Garrafa J, Gobbi D, Saluzzi M, Appenzeller S, et al. An open, multi-vendor, multi-field-strength brain MR dataset and analysis of publicly available skull stripping methods agreement. NeuroImage. 2018; 170: 482-494.

[7] Jenkinson M, Pechaud M, Smith S. BET2 - MR-based estimation of brain, skull and scalp surfaces. Oxford Centre for Functional Magnetic Resonance Imaging of the Brain (FMRIB), Oxford, 2005.

[8] Shattuck DW, Sandor-Leahy SR, Schaper KA, Rottenberg DA, Leahy RM. Magnetic resonance image tissue classification using a partial volume model. NeuroImage, 2001; 13 (5): 856-876.

[9] Eskildsen SF, Coupe P, Fonov V, Manjon JV, Leung KK, Guizard N, et al. BEaST: brain extraction based on Non-local segmentation technique. NeuroImage. 2012; 59 (3): 2362-2373.

[10] Litjens G, Kooi T, Bejnordi BE, Setio AAA, Ciompi F, Ghafoorian M., et al. A survey on deep learning in medical image analysis. Medical Image Analysis. 2017; 42: 60-88.

[11] Yapici M, Karakis R, Gurkahraman K. Improving Brain Tumor Classification with Deep Learning Using Synthetic Data. Computers, Materials and Continua. 2023; 74 (3): 5049-5067.

[12] Gurkahraman K, Karakis R. Brain tumors classification with deep learning using data augmentation. Journal of the Faculty of Engineering and Architecture of Gazi University. 2021; 36 (2): 997-1011.

[13] Rehman HZU, Hwang H, Lee S. Conventional and deep learning methods for skull stripping in brain MRI. Applied Sciences. vol. 10, no. 5, article number 1773, 2020.

[14] Kleesiek J, Urban G, Hubert A, Schwarz D, Maier-Hein K, Bendszus M, et al. Deep MRI brain extraction: A 3D convolutional neural network for skull stripping. Neuroimage. 2016; 129: 460-469.

[15] Hwang H, Rehman HZU, Lee S. 3D U-Net for skull stripping in brain MRI. Applied Sciences. 2019; 9 (3): article number 569.

[16] Zhang Q, Wang L, Zong X, Lin W, Li G, Shen D. FRNET: Flattened Residual Network for Infant MRI Skull Stripping. arXiv 2019; arXiv:1904.05578.

[17] Daşgın Ç, Gürkahraman K. Artık Bağlantılar ile Düzenlenen U-Net Mimarisi Kullanarak Beyin Çıkarımı. International Conference on Applied Engineering and Natural Sciences ICAENS 2023. Konya, Turkey: 2023. p.348.

[18] Hoopes A, Mora JS, Dalca AV, Fischl B, Hoffmann M. SynthStrip: Skull-stripping for any brain image. NeuroImage. 2022; 260: article number 119474.

[19] IBSR [Internet]. The Internet Brain Segmentation Repository (IBSR) [cited 2023 July 27]. Available from: https://www.nitrc.org/projects/ibsr

[20] Puccio B, Pooley JP, Pellman JS, Taverna EC, Craddock RC. The preprocessed connectomes project repository of manually corrected skull-stripped T1-weighted anatomical MRI data. GigaScience. 2016; 5: article number 45.

[21] Kingma DP, Welling M. Auto-encoding variational bayes. 2013; arXiv preprint, arXiv:1312.6114.

[22] Ronneberger O, Fischer P, Brox T. U-net: Convolutional networks for biomedical image segmentation. Medical Image Computing and Computer-Assisted Intervention–MICCAI 2015: 18th International Conference. Munich, Germany: 2015, Proceedings, Part III 18, Springer International Publishing; 2015. p. 234-241.

[23] Çiçek Ö, Abdulkadir A, Lienkamp SS, Brox T, Ronneberger O. 3D U-Net: learning dense volumetric segmentation from sparse annotation. Medical Image Computing and Computer-Assisted Intervention–MICCAI 2016: 19th International Conference. Athens, Greece: 2016, Proceedings, Part II 19, Springer International Publishing; 2016. p. 424-432.

[24] He K, Zhang X, Ren S, Sun J. Deep residual learning for image recognition. Proceedings of the IEEE Conference on Computer Vision and Pattern Recognition. Las Vegas, NV, USA; 2016. p. 770-778.

[25] Huang G, Liu Z, Van Der Maaten L, Weinberger KQ. Densely connected convolutional networks. Proceedings of the IEEE Conference on Computer Vision and Pattern Recognition. Honolulu, HI, USA; 2017. p. 4700-4708.

[26] Montagnon E, Cerny M, Cadrin-Chênevert A, Hamilton V, Derennes T, Ilinca A, et al. Deep learning workflow in radiology: a primer. Insights into Imaging. 2020; 11: 1-15.

[27] Rana M, Bhushan M. Machine learning and deep learning approach for medical image analysis:

diagnosis to detection. Multimedia Tools and Applications. 2023; 82(17): 26731-26769.

[28] Iglesias JE, Liu CY, Thompson PM, Tu Z. Robust brain extraction across datasets and comparison with publicly available methods. IEEE Transactions on Medical Imaging, 2011; 30 (9): 1617-1634.

151